



Defense Threat Reduction Agency
8725 John J. Kingman Road, MS 6201
Fort Belvoir, VA 22060-6201



DTRA-TR-14-4

TECHNICAL REPORT

Effects of Rock Joints on Failure of Tunnels Subject to Blast Loading

Approved for public release, distribution is unlimited.

November 2013

HDTRA01-03-D-0009

Deborah Sulsky and Howard
Schreyer

Prepared by:
OVPR/University Strategic
Partnership
MSC02 1660
1 University of New Mexico
Albuquerque, NM 87131

DESTRUCTION NOTICE:

Destroy this report when it is no longer needed.
Do not return to sender.

PLEASE NOTIFY THE DEFENSE THREAT REDUCTION
AGENCY, ATTN: DTRIAC/ J9STT, 8725 JOHN J. KINGMAN ROAD,
MS-6201, FT BELVOIR, VA 22060-6201, IF YOUR ADDRESS
IS INCORRECT, IF YOU WISH THAT IT BE DELETED FROM THE
DISTRIBUTION LIST, OR IF THE ADDRESSEE IS NO
LONGER EMPLOYED BY YOUR ORGANIZATION.

REPORT DOCUMENTATION PAGE				<i>Form Approved</i> OMB No. 0704-0188	
Public reporting burden for this collection of information is estimated to average 1 hour per response, including the time for reviewing instructions, searching existing data sources, gathering and maintaining the data needed, and completing and reviewing this collection of information. Send comments regarding this burden estimate or any other aspect of this collection of information, including suggestions for reducing this burden to Department of Defense, Washington Headquarters Services, Directorate for Information Operations and Reports (0704-0188), 1215 Jefferson Davis Highway, Suite 1204, Arlington, VA 22202-4302. Respondents should be aware that notwithstanding any other provision of law, no person shall be subject to any penalty for failing to comply with a collection of information if it does not display a currently valid OMB control number. PLEASE DO NOT RETURN YOUR FORM TO THE ABOVE ADDRESS.					
1. REPORT DATE (DD-MM-YYYY) 00-11-2013		2. REPORT TYPE Technical		3. DATES COVERED (From - To) 07/21/2010 - 4/30/2012	
4. TITLE AND SUBTITLE Effect of Rock Joints on Failure of Tunnels Subject to Blast Loading				5a. CONTRACT NUMBER DTRA01-03-D-0009-0026	
				5b. GRANT NUMBER	
				5c. PROGRAM ELEMENT NUMBER	
6. AUTHOR(S) Deborah Sulsky and Howard Schreyer				5d. PROJECT NUMBER	
				5e. TASK NUMBER 26	
				5f. WORK UNIT NUMBER	
7. PERFORMING ORGANIZATION NAME(S) AND ADDRESS(ES) OVPR/University Strategic Partnership MSC02 1660 1 University of New Mexico Albuquerque, NM 87131				8. PERFORMING ORGANIZATION REPORT NUMBER OVPRED 798B	
9. SPONSORING / MONITORING AGENCY NAME(S) AND ADDRESS(ES) Defense Threat Reduction Agency 8725 John J. Kingman Road STOP 6201 Fort Belvoir, VA 22060 PM/James Reed				10. SPONSOR/MONITOR'S ACRONYM(S) DTRA	
				11. SPONSOR/MONITOR'S REPORT NUMBER(S) DTRA-TR-14-4	
12. DISTRIBUTION / AVAILABILITY STATEMENT Approved for public release, distribution is unlimited.					
13. SUPPLEMENTARY NOTES					
14. ABSTRACT This project provided the basis for numerical simulations of tunnel failure under blast loads. The challenges included handling large deformations, complex failure modes, multiple failure planes and rock joints with various orientations. Meeting these challenges depended critically on developing appropriate constitutive equations for rock, and a robust, efficient numerical procedure for studying failure induced by waves in the host rock interacting with a tunnel. This research formulated constitutive equations that combined continuum and discontinuum aspects of material response in order to capture essential physical features of rock, such as joints and faults with variable strength and orientation, multiple failure orientations, and a spectrum of failure modes that includes axial splitting and various combinations of shear and opening modes. The numerical approach was based on the material-point method (MPM) that handles large continuum deformations. A constitutive model that predicts fractures was combined with MPM to study rock failure in the vicinity of a tunnel. Moreover, a one-dimensional study of the effect of joints on a propagating wave pulse was performed showing the net transmission through a joint set.					
15. SUBJECT TERMS Tunnel, blast, material point method, joints					
16. SECURITY CLASSIFICATION OF:			17. LIMITATION OF ABSTRACT UU	18. NUMBER OF PAGES	19a. NAME OF RESPONSIBLE PERSON James Reed
a. REPORT Unclassified	b. ABSTRACT Unclassified	c. THIS PAGE Unclassified			19b. TELEPHONE NUMBER (include area code) 703-767-8793

CONVERSION TABLE

Conversion Factors for U.S. Customary to metric (SI) units of measurement.

MULTIPLY → BY → TO GET
TO GET ← BY ← DIVIDE

angstrom	1.000 000 x E -10	meters (m)
atmosphere (normal)	1.013 25 x E +2	kilo pascal (kPa)
bar	1.000 000 x E +2	kilo pascal (kPa)
barn	1.000 000 x E -28	meter ² (m ²)
British thermal unit (thermochemical)	1.054 350 x E +3	joule (J)
calorie (thermochemical)	4.184 000	joule (J)
cal (thermochemical/cm ²)	4.184 000 x E -2	mega joule/m ² (MJ/m ²)
curie	3.700 000 x E +1	*giga bacquerel (GBq)
degree (angle)	1.745 329 x E -2	radian (rad)
degree Fahrenheit	$t_k = (t^{\circ}f + 459.67) / 1.8$	degree kelvin (K)
electron volt	1.602 19 x E -19	joule (J)
erg	1.000 000 x E -7	joule (J)
erg/second	1.000 000 x E -7	watt (W)
foot	3.048 000 x E -1	meter (m)
foot-pound-force	1.355 818	joule (J)
gallon (U.S. liquid)	3.785 412 x E -3	meter ³ (m ³)
inch	2.540 000 x E -2	meter (m)
jerk	1.000 000 x E +9	joule (J)
joule/kilogram (J/kg) radiation dose absorbed	1.000 000	Gray (Gy)
kilotons	4.183	terajoules
kip (1000 lbf)	4.448 222 x E +3	newton (N)
kip/inch ² (ksi)	6.894 757 x E +3	kilo pascal (kPa)
ktap	1.000 000 x E +2	newton-second/m ² (N-s/m ²)
micron	1.000 000 x E -6	meter (m)
mil	2.540 000 x E -5	meter (m)
mile (international)	1.609 344 x E +3	meter (m)
ounce	2.834 952 x E -2	kilogram (kg)
pound-force (lbs avoirdupois)	4.448 222	newton (N)
pound-force inch	1.129 848 x E -1	newton-meter (N-m)
pound-force/inch	1.751 268 x E +2	newton/meter (N/m)
pound-force/foot ²	4.788 026 x E -2	kilo pascal (kPa)
pound-force/inch ² (psi)	6.894 757	kilo pascal (kPa)
pound-mass (lbm avoirdupois)	4.535 924 x E -1	kilogram (kg)
pound-mass-foot ² (moment of inertia)	4.214 011 x E -2	kilogram-meter ² (kg-m ²)
pound-mass/foot ³	1.601 846 x E +1	kilogram-meter ³ (kg/m ³)
rad (radiation dose absorbed)	1.000 000 x E -2	**Gray (Gy)
roentgen	2.579 760 x E -4	coulomb/kilogram (C/kg)
shake	1.000 000 x E -8	second (s)
slug	1.459 390 x E +1	kilogram (kg)
torr (mm Hg, 0° C)	1.333 22 x E -1	kilo pascal (kPa)

*The bacquerel (Bq) is the SI unit of radioactivity; 1 Bq = 1 event/s.

**The Gray (GY) is the SI unit of absorbed radiation.

Contents

1	Executive Summary	1
2	Abbreviated Report with Recommendations	4
2.1	Introduction and Literature Survey	4
2.2	Key Results	7
2.2.1	Preliminary Comments	7
2.2.2	Blast Induced Waves Impacting Tunnels	7
2.2.3	One-dimensional Waves Passing through Joints	9
2.2.4	Constitutive Equation for Joints and Faults	11
2.3	Recommendations	15
3	Rock Fractures Near Tunnels due to a Blast	16
3.1	Introduction	16
3.2	Classical Models For Failure	17
3.2.1	Essential Aspects of Failure in Plane Stress or Plane Strain	17
3.2.2	Classical Models of Failure	18
3.2.3	Proposed Form for the Failure Criterion	21
3.2.4	Analytical Form of the Critical Direction	22
3.2.5	Effect of Material Parameters on the Failure Surface	24
3.2.6	Selection of Values for Material Parameters	25
3.3	Evolution of Failure	25
3.3.1	Displacement Discontinuity and Softening	25
3.3.2	Evolution Equations	27
3.4	Elastic-Decohesion Model	28
3.4.1	Combined Elasticity and Decohesion	28
3.4.2	Numerical Treatment of Elastic Decohesion Equations	29
3.5	2D Simulations of a Tunnel in a Blast	33
3.5.1	Parameter Study	41
3.6	Summary	45
4	One-Dimensional Joint Analysis	47
4.1	Introduction	47
4.2	One-Dimensional Constitutive Models for Joints	48
4.2.1	Preliminary Comments	48

4.2.2	1D Joint Modeling Formulation	49
4.2.2.1	Basic Notation	49
4.2.2.2	Joint Closure	49
4.2.2.3	Joint Opening	50
4.2.3	Numerical Implementation of 1D Joint Model	52
4.2.3.1	Stress and Strain Within an Element	52
4.2.3.2	Joint Closure and Unloading	53
4.2.3.3	Joint Opening	54
4.2.3.4	Other loading scenarios and summary	55
4.2.3.5	Results of Driver Program for 1D Joint Model	55
4.2.4	Gap Constitutive Model	56
4.2.4.1	Gap Constitutive Equation	56
4.2.4.2	Results of Driver Program for 1D Gap Model	56
4.2.5	1D Joint Model for Plasticity and Elasticity	57
4.2.5.1	Formulation that Includes Joint Elasticity	57
4.2.5.2	Numerical Implementation of the Elastic-Plastic Joint Model	58
4.2.5.3	Calculation of E_g	59
4.2.5.4	Results of Driver Program for 1D Elastic-Plastic Joint Model	59
4.2.6	Experimental Validation of 1D Joint Model	59
4.2.7	MPM Code, Gap Model, and Analytical Solution	61
4.2.7.1	Numerical Procedure and Model Problem	61
4.2.7.2	Gap Model Analysis	62
4.2.7.3	Analytical Solution to Determine Closure Potential	62
4.2.7.4	Proposed Boundary Condition Characterization	63
4.3	Basic Features of Wave Propagation through a Joint	65
4.3.1	Preliminary Comments	65
4.3.2	One-Dimensional Bar Problem	65
4.3.3	Gap, Plastic Joint, and Elastic-Plastic Joint Comparison	66
4.3.3.1	Description of Model Problem	66
4.3.3.2	No Discontinuity	66
4.3.3.3	Gap Discontinuity	67
4.3.3.4	Plastic Joint Discontinuity	69
4.3.3.5	Elastic-Plastic Joint Discontinuity	70
4.3.4	Summary	72
4.4	Effects of Parameters on Wave Propagation through Single Joint	72
4.4.1	Program of Single Joint Study	72
4.4.1.1	Study Parameters	73
4.4.2	Single Discontinuity Study	74
4.4.2.1	Gap	74
4.4.2.2	Plastic Joint	75
4.4.2.3	Elastic-Plastic Joint	78
4.4.3	Single Joint Conclusions	78
4.5	Effects of Parameters on Wave Propagation through Two Joints	80

4.5.1	Preliminary Comments	80
4.5.1.1	Lumping Joints Study	80
4.5.1.2	Joint Spacing Study	81
4.5.2	Study of Wave Propagation Through Two Gaps	81
4.5.2.1	Illustrative Results	81
4.5.2.2	In-Depth Details for Two Joints	84
4.5.3	Propagation of a Wave Through Two Plastic Joints	86
4.5.3.1	Illustrative Results	86
4.5.3.2	In-Depth Details for Two Joints	89
4.5.4	Summary of Multiple Joints	92
4.6	The Utility of Lumping Gaps and Joints	92
4.6.1	Objective of the Chapter	92
4.6.2	Gaps	93
4.6.3	Joints	95
4.6.4	Summary	96
4.7	Conclusion	97
	Appendices	97
A	Convergence Study with a Single Gap	97
B	Convergence Study with Two Gaps	99
C	Nondimensionalization Scheme	101
C.1	Dimensioned Quantities	101
C.2	Equations	101
C.3	Proposed Dimensionless Quantities	102
D	Material Point Placement	103
E	Complete Figures	108
E.1	Single Gap	108
E.2	Single Plastic Joint	109
E.3	Single Elastic-Plastic Joint	110
F	Lumping Joints Study	111
F.1	Gaps, $u_{g0} = 1.5\text{mm}$	112
F.2	Gaps, $u_{g0} = 0.5\text{mm}$	113
F.3	Plastic Joints, $u_{g0} = 1.5\text{mm}$	114
F.4	Plastic Joints, $u_{g0} = 0.5\text{mm}$	115
F.5	Elastic-Plastic Joints, $u_{g0} = 1.5\text{mm}$	116
F.6	Elastic-Plastic Joints, $u_{g0} = 0.5\text{mm}$	117
G	Joint Spacing Study	117
G.1	Gaps	119
G.2	Plastic Joints	120
H	Axisymmetric Wave Propagation	120
H.1	Problem Layout	121
H.2	Results	123
H.2.1	Parameters	123
H.2.2	Plots	123

H.3	Discussion	128
5	Modeling of Joints and Faults	129
5.1	Introduction	129
5.2	Outline of the Basic Constitutive Approach	131
5.2.1	Preliminary Remarks	131
5.2.2	Material between Joints Faults	131
5.2.3	Joints and Faults	132
5.2.4	Combination of Joints and Faults and the Surrounding Medium . . .	132
5.3	Constitutive Model for Joints and Faults	132
5.3.1	Initial Comments	132
5.3.2	Notation	133
5.3.3	Assumed Features for Joint Behavior	134
5.3.4	Basic Formulation for Compaction	136
5.3.5	Elasticity	138
5.3.6	Plasticity	140
5.3.7	Composite Yield Function	147
5.3.8	Closing Comments	148
5.4	Strains Related to the Use of Finite Elements	150
5.4.1	Preliminary Remarks	150
5.4.2	Strain and Stress Associated with Joints, Continuum Elements . . .	150
5.4.3	Tangent Components	152
5.5	Numerical Procedure for Constitutive Equation	157
5.5.1	Preliminary Remarks	157
5.5.2	Initial Step to Obtain a Trial Stress	159
5.5.3	Case where the Compressive Gap Governs	161
5.5.4	Case where Shear Governs	162
5.5.5	Case of Zero Normal Traction	164
5.5.6	Concluding Remarks	165
5.6	Constitutive Equation Algorithm Features	166
5.6.1	Preliminary Remarks	166
5.6.2	Features of the Assumed Response Functions	166
5.6.3	Concluding Remarks	174
5.7	Summary	175

List of Figures

2.1	The computational domain is 105m by 100m with x and y coordinates between $-50 < x < 55$ and $-50 < y < 50$. The region representing the blast zone is shown in red, the rock is colored cyan and the tunnel is shown in green. The center of the blast is 39m from the left wall of the tunnel.	8
2.2	(a) Stress as a function of time at the point (38.8125, 0.0625). The plot in (a) shows free propagation of a wave from a cylindrical source that applies a pulse with $\sigma_0 = -3.8 \times 10^8$ Pa to a domain made up of rock modeled elastically, and with no tunnel in the rock. In (b) the elastic-decohesive model is invoked and the distribution and orientation of cracks around the tunnel with normal opening u_n greater than $0.005u_0$ at $t = 11$ msec is shown.	9
2.3	Notation for the problem of a bar with a single discontinuity	9
2.4	Stress as a function of x for various values of prescribed time.	11
2.5	Results of wave propagation through a bar with a plastic joint	12
2.6	Results of wave propagation through a bar with an elastic-plastic joint . . .	13
2.7	Notation associated with a joint or fault and corresponding yield surface. . .	14
2.8	Plots of stress and strain for uniaxial strain with gap formation and closing. . .	14
3.1	Generic aspects of a failure surface in plane stress or plane strain, and the orientation of the surface of material cracking (failure).	18
3.2	Sketches of curves showing failure initiation including orientations of the normal to surfaces of material failure as predicted by classical models (a) Rankine, (b) Tresca and (c) Mohr-Coulomb. (The normal lies within the plane only for the solid portions of each curve.)	20
3.3	Plots of failure surfaces in $\tau_n - \tau_t$ space.	22
3.4	Effects of material parameters on shape of decohesion surface for plane stress, (a) effect of τ_{sf} for $\tau_{nf} = 0.1$ and $f'_c = 1.0$; (b) effect of f'_c for $\tau_{nf} = 0.1$ and $\tau_{sf} = 0.3$	24
3.5	Effect of the value of the softening function on the decohesion surface in the $\tau_n - \tau_t$ space for $\sigma_{tt}^2/f'_c = 0.5$	27
3.6	Relationship between original square element and equivalent element used to define decohesive strains.	30

3.7	(a) The computational domain is 105m by 100m with x and y coordinates between $-50 < x < 55$ and $-50 < y < 50$. The region representing the blast zone is shown in red, the rock is colored cyan and the tunnel is shown in green. The center of the blast is 39m from the left wall of the tunnel. (b) A schematic plot of wave propagation. A compressive wave is generated from the blast source and propagates radially.	34
3.8	Stress as a function of time at the point (38.8125, 0.0625). The plot shows free propagation of a wave from a cylindrical source that applies a pulse with $\sigma_0 = -3.8 \times 10^8$ Pa to a domain made up of rock modeled as elastic, and with no tunnel in the rock.	35
3.9	Contours of (a) maximum principle stress σ_{\max} , (b) maximum principle stress σ_{\max} around the tunnel and (c) minimum principle stress σ_{\min} around the tunnel at $t = 11$ msec. The rock is modeled as elastic.	36
3.10	(a) Location of an observation point (38.8125, 0.0625) and values of stress components vs. time in (b) the $x - y$ coordinates and in (c) the principle coordinates, at that point, using the elastic model.	37
3.11	Contours of (a) maximum principle stress σ_{\max} , (b) maximum principle stress σ_{\max} around the tunnel, (c) minimum principle stress σ_{\min} around the tunnel and (d) width of cracks around the tunnel at $t = 11$ msec. The rock is modeled as elastic-decohesive.	38
3.12	Distribution and orientation of cracks with normal opening u_n (a) greater than $0.005u_0$ (b) greater than $0.1u_0$ and (c) greater than u_0 at $t = 11$ msec. .	38
3.13	Values of stress components vs. time at (38.8125, 0.0625) in (a) the $x - y$ coordinates and in (b) the principle coordinates using the elastic-decohesive model.	39
3.14	(a) Location of the observation point (41.9375, 3.0625), and values of stress components vs. time in (b) the $x - y$ coordinates and in (c) the principle coordinates, at that point, using the elastic model.	39
3.15	Evolution of stress components in (a) $x - y$ coordinates and in (b) principle stress components at the location (41.9375, 3.0625). The rock is modeled as elastic-decohesive. The vertical black line indicates when cracks begin to form.	40
3.16	Contours of maximum principle stress at 11 msec due to a load of magnitude (a) -3.8×10^8 Pa and (b) -1.9×10^8 Pa.	41
3.17	The distribution and orientation of cracks with normal opening u_n greater than $0.1u_0$ around the tunnel at 11 msec due to a load of magnitude (a) -3.8×10^8 Pa and (b) -1.9×10^8 Pa.	41
3.18	The computational domain for two examples where the blast is located closer to the tunnel. The distance from the center of the blast zone (red) is 21m to (a) the left wall of the tunnel and (b) the top of the tunnel. The tunnel is shown in green.	42
3.19	Free elastic waves from a source (a) to the left of the observation point at (20.8125, 0.0625) and (b) above the observation point at (0.0625, -20.8125) with $\sigma_0 = -2.68 \times 10^8$	43

3.20	Contours of maximum principle stress at $t = 7\text{msec}$ for two different orientations of the blast with respect to the tunnel. The blast has $\sigma_0 = -2.68 \times 10^8$ Pa and the distance between the blast center and the tunnel is 21m. The rock is modeled as elastic-decohesive.	44
3.21	Distribution and orientation of cracks near the tunnel with effective normal opening greater than $0.1u_0$ at $t = 7$ msec for two different orientations of the blast with respect to the tunnel.	44
4.1	Wave propagating towards a joint set	48
4.2	The joint “hardening” function $g(\bar{u}_g)$ when $\bar{u}_g \leq 1$	50
4.3	Impact of m on the shape of the joint “hardening” function $g(\bar{u}_g)$	51
4.4	Joint with prescribed positive strain increments	51
4.5	Joint Driver Loading Cycle	55
4.6	Gap Driver Loading Cycle	56
4.7	Elastic-Plastic Joint Driver Loading Cycle	60
4.8	Experimental configuration	60
4.9	Driver output	61
4.10	Verification run where the green dot represents a gap in the middle of the bar.	62
4.11	Gap Model Verification	64
4.12	Notation for the problem of a bar with a single discontinuity	65
4.13	Results of wave propagation through a bar without a discontinuity	67
4.14	Results of wave propagation through a bar with a gap	68
4.15	Results of wave propagation through a bar with a plastic joint	69
4.16	Results of wave propagation through a bar with an elastic-plastic joint	71
4.17	Single Discontinuity Study	72
4.18	Plots of results for wave propagation through a single gap with $u_p = 1.5\text{mm}$	75
4.19	Plots of results for a wave transmitted through a single plastic joint with $u_p = 1.5\text{mm}$	77
4.20	Plots of results for a wave transmitted through a single, elastic-plastic joint with $u_p = 1.5\text{mm}$	79
4.21	Transmitted energy results for multiple gap study	80
4.22	Plots of stress for different gap spacings (blue dots denote locations of gaps)	82
4.23	Results for transmitted energy due to gap spacing	83
4.24	Stress plots at various time of wave propagation through two gaps spaced 40 material points apart (blue dots denote gap locations)	85
4.25	\bar{u} versus time for each gap	85
4.26	Plots of material point stress for multiple joint spacing (blue dots denote joint locations)	87
4.27	Energy versus time plots for multiple joint spacings	88
4.28	Energy transmission of multiple joint spacings	89
4.29	Material point stress plotted at different times (blue dots denote joint locations)	91
4.30	\bar{u} versus time for each joint	92
4.31	Plots of stress for a single lumped gap and two separate gaps. Blue dots denote gap locations.	93

4.32	Plots of energy for a single lumped gap and two separate gaps	94
4.33	Plots of transmitted energy for a single lumped gap and two separate gaps .	94
4.34	Plots of stress for a single lumped joint and two separate joints. Blue dots denote joint locations.	95
4.35	Plots of energy for a single lumped joint and two separate joints	96
4.36	Plots of transmitted energy for a single lumped joint and two separate joints	96
A.1	Mesh refinement for wave propagation through a gap, 1 material point per cell	98
A.2	Mesh refinement for wave propagation through a gap, 1 material point per cell	98
A.3	Mesh refinement for wave propagation through a gap, 1 material point per cell	99
A.4	Mesh refinement for wave propagation through a gap, 1 material point per cell	99
B.1	Mesh refinement for wave propagation through two gaps, 1 material point per cell	100
B.2	Mesh refinement for wave propagation through 2 gaps, 1 material point per cell	100
B.3	\bar{u} versus time for first gap	100
B.4	\bar{u} versus time for second gap	101
D.1	Stress as a function of x for different times using 50 material points located close to the cell boundary to discretize the bar	105
D.2	Stress as a function of x for different times using 128 material points centered in the cells to discretize the bar	106
D.3	Stress as a function of x for different times using 50 material points located close to the cell boundary to discretize the bar with a gap in the center of the bar	106
D.4	Stress as a function of x for different times using 128 material points centered in the cells to discretize the bar with a gap in the center of the bar	107
E.1	Results of single gap study, $u_p = 1.5\text{mm}$	108
E.2	Results of single plastic joint study, $u_p = 1.5\text{mm}$	109
E.3	Results of single elastic-plastic joint study, $u_p = 1.5\text{mm}$	110
F.1	Layout of Discontinuity Lumping Study	111
F.2	Results of lumping multiple gaps, $u_{g0} = 1.5\text{mm}$	112
F.3	Results of lumping multiple gaps, $u_{g0} = 0.5\text{mm}$	113
F.4	Results of lumping multiple plastic joints, $u_{g0} = 1.5\text{mm}$	114
F.5	Results of lumping multiple plastic joints, $u_{g0} = 0.5\text{mm}$	115
F.6	Results of lumping multiple elastic-plastic joints, $u_{g0} = 1.5\text{mm}$	116
F.7	Results of lumping multiple elastic-plastic joints, $u_{g0} = 0.5\text{mm}$	117
G.1	Layout of Discontinuity Spacing Study	118
G.2	Results of spacing two gaps, $u_{g0} = 1.5\text{mm}$	119
G.3	Results of spacing two plastic joints, $u_{g0} = 1.5\text{mm}$	120
H.1	Axisymmetric bar	122
H.2	Axisymmetric bar with joint parallel to radius	122
H.3	Axisymmetric bar with joint perpendicular to radius	123
H.4	Comparison of σ_{rr} when r values are large, t_{prop} is the length of time of wave propagation for the length of the bar, both cases are plotted at the same times where t_{prop} is the time of one wave propagation along the bar	124

H.5	Comparison of σ_{tt} when r values are large, tprop is the length of time of wave propagation for the length of the bar, both cases are plotted at the same times where tprop is the time of one wave propagation along the bar	124
H.6	Comparison of σ_{rr} when radial joint runs along bar, dashed lines are case with no joint, tprop is the length of time of wave propagation for the length of the bar, both cases are plotted at the same times	125
H.7	Comparison of $\sigma_{\theta\theta}$ when radial joint runs along bar, dashed lines are case with no joint, tprop is the length of time of wave propagation for the length of the bar, both cases are plotted at the same times	125
H.8	Gap size versus σ_{rr} when a joint is perpendicular to r -axis in middle of bar .	126
H.9	Comparison of σ_{rr} when radial perpendicular to bar in middle of bar, dashed lines are case with no joint, tprop is the length of time of wave propagation for the length of the bar, both cases are plotted at the same times	126
H.10	Comparison of $\sigma_{\theta\theta}$ when joint perpendicular to bar in middle of bar, dashed lines are case with no joint, tprop is the length of time of wave propagation for the length of the bar, both cases are plotted at the same times	127
5.1	Jointed Rock	129
5.2	Notation for a joint.	134
5.3	Observed features for normal compaction and unloading of a joint.	135
5.4	Closure of a joint.	137
5.5	Yield surface for joint in space of traction components.	140
5.6	Evolution of yield surfaces in space of traction components.	149
5.7	Yield surface with and without asperities.	149
5.8	Notation associated with joint and element.	151
5.9	Path showing compaction, unloading and re-compaction.	167
5.10	Plots of stress and strain for uniaxial strain with gap formation and closing.	168
5.11	Plot of stress versus strain for a path similar to that of Example 1 but with $[u_0^p] = 0.5[u_{j0}]$	169
5.12	Path showing the interactive effects of shear and normal stress.	170
5.13	Path showing compaction, unloading into gap opening with shear, and reloading in compression with shear.	171
5.14	Path showing compaction, unloading to include a gap formation, and reloading in compression for a joint half the width of an element.	172
5.15	Path showing compaction, unloading to include a gap formation, and reloading in compression for a joint one-tenth the width of an element.	173
5.16	Path showing compaction, unloading to include a gap formation, and reloading in compression for a joint one-tenth the width of an element.	174

List of Tables

2.1	Parameters that are used in the elastic-decohesive formulation.	8
3.1	Parameters that are used in the elastic-decohesive formulation.	25
4.1	Inputs used for the single joint sets	73
4.2	Inputs used for gap spacing	81
4.3	Energy dissipated in closing the joints	88
F.1	Inputs used for multiple joints	111
G.1	Inputs used for joint spacing	118

1

Executive Summary

The objective of this research is to provide the capability to numerically simulate the effect of blast loads on tunnels located in jointed rock media. A successful procedure must include the capability for handling large deformations, complex failure modes, multiple failure planes and rock joints with various orientations. The key is to have appropriate constitutive equations that can reproduce the essential aspects of joint behavior, and that can capture a spectrum of failure modes including the possibility of axial splitting and various combinations of shear and opening motion. The numerical procedure must also be capable of handling the movement of failed rock into the tunnel cavity.

The study was separated into three phases. The first phase examined wave propagation from a cylindrical source, the interaction of the wave with a tunnel cavity and the prediction of potential failure scenarios. The second phase consisted of a one-dimensional investigation of wave propagation through one or more joints, and the effect of various choices of constitutive parameters describing joints. The final phase developed a three-dimensional constitutive equation that reflects the essential features of both joint and fault behavior. Because of the restricted time frame under which the research was conducted, the synthesis of the three-dimensional formulation of joints into the numerical simulations of wave propagation was not conducted. Nevertheless, each phase of the research provided important insight into the nature of the problem. These results are summarized next.

The effect of blast waves on tunnels was modeled as two-dimensional with the source consisting of a stress pulse on the boundary of a cylindrical cavity. No attempt was made to model the damage that occurs in the rock immediately adjacent to the source. Instead the size of the cylindrical source was taken to be sufficiently large so that the emanating waves could be considered as propagating through an elastic medium. The tunnel was also considered to be cylindrical but not circular as indicated in Fig. 1. Numerical results were obtained for rock modeled as purely elastic and for rock allowed to fracture using an oriented failure criterion to predict the formation of one or more cracks at points in the vicinity of both the source and the tunnel. The results of the first phase demonstrated the capability of the numerical algorithm based on the material-point method (MPM) to handle large deformations and of the constitutive equation to handle oriented failure.

The first observation of note is that a wave consisting of a single pulse, traveling radially from a cylindrical source, evolves a significant tensile tail behind the compressive segment

of the wave. In some cases, this tensile phase can be sufficiently large to initiate cracking. Secondly, when the compressive part reflects off the free surface of a tunnel wall, a second component of tensile stress is introduced. These two aspects, tensile tail and reflected wave can superimpose to cause significant cracking in a region close to the tunnel wall first met by the wave. These fractures in tension are due to the radial component of the stress. In addition, there is a tensile contribution of the circumferential component of the stress wave that can cause failure, so there is the possibility of a zone of failure with a distribution of two orthogonal cracks. Furthermore, there are the effects of refraction of waves around the tunnel, and tunnel geometry plays a role. In particular, with a blast on the side, there is a significant stress enhancement near the top of the tunnel, possibly resulting in material being forced into the tunnel. This phenomenon is strictly due to stress from the waves since gravity was not considered. Failure around the bottom and even in the region behind the tunnel is also noted. There is less damage to the tunnel ceiling from a blast located directly above, rather than on the side.

The second phase of the research consisted of studying the effects of one or more joints on a pulse introduced at the boundary of a one-dimensional domain in Cartesian and cylindrical coordinates. The basic assumption of all joint models is that the tensile-carrying capability of a joint is insignificant and is, therefore, taken to be zero. Two limiting cases for modeling a joint were first considered. If the joint simply consists of two perfect surfaces with zero spacing, then a compressive pulse will transmit with no alteration. On the other hand, if the joint is modeled as a gap, two possibilities exist. If the gap is sufficiently large, a compressive pulse will simply reflect from the free surface as a tensile pulse with no transmission through the gap. If the gap width is sufficiently small, a part of the original compressive pulse will reflect as a tensile pulse, the gap will close, and a portion of the original pulse will transmit through the joint. If a second joint exists, a reflection will occur at the second joint until the joint closes, a reflection will occur, a second reflection from the first joint will occur and the second reflected compressive pulse will transmit through the second joint. The net effect of a set of joints on a compressive pulse is that part of the original wave is reflected, and the remaining part, after one or more reflections between joints, will eventually be transmitted; however, the travel time through the joint set is much longer than through intact rock due to the multiple reflections.

If cylindrical geometry holds, there is the additional complication since dispersion is a natural occurrence - including the formation of a tensile tail. Even for a joint that is initially closed, the tensile tail cannot be propagated. Typically joints consist of a certain amount of aggregate between the two surfaces defining the joint. Compaction of such a joint is highly nonlinear with the initial tangent modulus close to zero and the tangent modulus of a compacted joint very high. The result is that reflected and transmitted waves through realistic joints can be expected to be a smooth combination of the idealized models of perfect joints and joints as gaps. Representative examples of reflected and transmitted waves due to joints with nonlinear constitutive equations are provided in the main body of the report.

An important aspect of this phase of the study is that if the discontinuity in displacement implicitly inherent in a joint is handled numerically as part of the constitutive equation, there is no need to use discrete methods that involve contact and impact algorithms. Constitutive

equations specifically tailored to represent experimental data reflecting nonlinear compaction of joints are easily incorporated within the numerical procedure, whether it be the material point method or the finite element method.

The final phase of the project involved a theoretical formulation and a corresponding numerical algorithm for predicting the response of a joint to compaction, to opening, and to shear or tangential motion. The approach is also believed applicable to the treatment of faults, which have features similar to joints with the understanding that faults are considerably wider than joints and the middle plane of a fault can cover an area several orders of magnitude larger than the corresponding plane defined by a joint.

The essential observed features of both joints and faults are considered to be the following: (i) compaction, which is nonlinear, can be modeled as a combination of plasticity and nonlinear elasticity, (ii) the tangent modulus for compaction can vary by several orders of magnitude according to the degree of compaction, (iii) upon unloading the compressive stress reduces to zero, (iv) with further unloading no tensile stress is sustained and a physical gap develops, (v) provided there is some normal compressive stress, there is resistance to shear motion that is due to a combination of Mohr-Coulomb friction and the presence of surface roughness, or asperities, (vi) shear motion in the presence of asperities causes dilatation, or opening of the joint, (vii) dilatation due to shear affects the plastic response of joint compaction, (viii) with sufficient shear motion, the asperities are obliterated and from then on only Mohr-Coulomb friction occurs with no additional dilatation, and (ix) the in-plane normal components of strain and transverse shear strain are assumed to be governed by the adjacent rock mass.

In addition to the constitutive equation algorithm for joints and faults, a formulation is provided for incorporating the algorithm with a finite element or material point method with the sides of elements assumed to be aligned with the plane of the joint or fault. Example results are provided for assumed strain paths. The algorithm is of a form easily implemented in a program used for large-scale simulations of wave propagation in rock media with joints and faults.

In conclusion, this project has provided the foundation and theoretical understanding for numerical simulations of waves from blast loading impinging on a tunnel or other buried structure. The existence of tensile waves due to reflections or geometrical effects may cause a number of physical fracture planes of various orientations in several regions in the vicinity of a tunnel. In addition, large compressive stresses can assist in failure akin to axial splitting. It is suggested that the presence of joints and faults may cause either a shielding or a magnifying effect depending upon the orientation of planes defining joints and faults. Similar to the observations of one-dimensional trapping, shear waves may become trapped between joint planes and travel with significant amplitude much further than expected with a homogeneous medium. On the other hand, in the vicinity of a tunnel, joints can be considered as pre-existing failure planes so that zones of damage can be enhanced.

The capacity to handle large deformations with the material point method, together with constitutive equations for handling discontinuities associated with existing joints and faults and with the creation of new planes of failure, provides a unique capability for large-scale numerical simulations of tunnels in jointed rock subjected to large dynamic loads.

2

Abbreviated Report with Recommendations

2.1 Introduction and Literature Survey

The focus of this project is to determine the effect of jointed or faulted rock on stress waves propagated through the system and the consequence these joints or faults can have on the failure of tunnels subjected to blast loads. Joints in rocks are features observed widely in nature. In fact, it is probably more difficult to find rocks with no joints than to observe jointed rock. Experimental evidence suggests strongly that joints behave in a highly nonlinear fashion, even for small stresses. Thus, it is essential that the features of joints be included in large-scale analyses involving either static or dynamic loads on underground or partially embedded structures such as tunnels or foundations for power plants.

Joints typically appear as planes of tensile failure that have experienced no shear and occur as sets of parallel joints Goodman [1989] with each joint defining a surface area of moderate extent. On the other hand, a fault is also a surface of material failure but with the important distinction that a fault typically occurs as a single surface and exhibits pre-existing large shear or tangential relative motion between the surfaces defining the fault. As a consequence of the large motion, a fault is typically many orders of magnitude larger in area than a joint and the volume defining the fault is filled with debris consisting of crushed aggregate. Nevertheless, there are certain features that joints and faults have in common. Among these are the following: (i) neither a joint nor a fault exhibits any significant tensile strength, (ii) when a compressive stress is applied to both, the stress versus closure displacement is highly nonlinear, (iii) upon unloading both exhibit a stress versus displacement relation that is nonlinear with a significant permanent displacement when the compressive stress is reduced to zero, (iv) asperities in both can provide a significant inherent strength in shear, and (v) for large shearing motion under a constant applied compressive stress, a Mohr-Coulomb frictional relation obtains. Because of these similarities, a constitutive model for a joint is considered to be applicable to a fault as well.

Previous work by the authors has focused on the development of a decohesive model for predicting the onset of failure with an emphasis on providing the state of stress at which

failure initiates, on the orientation of the failure surface, on the mode of failure and on providing the correct fracture energy [Schreyer et al., 2002b; Sulsky and Schreyer, 2004; Schreyer et al., 2006; Schreyer, 2007]. The approach involves a discrete constitutive relation between surface traction and discontinuity in displacement. Several applications of the decohesive model to large scale simulations of Arctic ice [Sulsky et al., 2007; Peterson and Sulsky, 2011] have been obtained using the material point method (MPM). The great advantage of MPM is that the positive aspects of both Eulerian and Lagrangian frames are combined to form a seamless method for handling problems with large deformations [Sulsky et al., 1994, 1995; Sulsky and Schreyer, 1996].

The potential value of this decohesive formulation is illustrated in the first task of this project in which a cylindrically symmetric impulsive stress wave is introduced into a homogeneous medium. Instead of modeling the severe damage in the immediate vicinity of the blast, we model the effect of the blast by imposing a load at a large radial distance from the center of the blast. Comparison is made between wave propagation in rock that is unnaturally restricted to isotropic elasticity, with rock governed by a combination of isotropic elasticity and the decohesive failure model. With the decohesive model, radial microcracks are formed around the source. Once micro cracks are introduced, the medium is no longer isotropic. Therefore, the nature of the propagated wave in comparison with the purely elastic case is affected at the outset. Cylindrical wave propagation is accompanied by both compressive and tensile phases of both the radial and circumferential components of the stress. The interaction of such a wave with the free surface defined by the front wall of a tunnel is significantly more complex than the reflection of a planar wave. The result is the initiation of both horizontal and vertical cracks in a region in front of the tunnel. Furthermore, if the blast is located to the side of a tunnel, horizontal cracks are formed near the top of the tunnel due to axial splitting. These details of crack formation in unjointed media are made available only with the use of appropriate decohesive failure models and MPM.

An important by-product of the development of decohesive failure is that pre-existing planes of weakness can be accommodated by simply prescribing the orientation of a surface through a unit normal vector and an initial value of effective discontinuity. Both joints and faults can be considered as surfaces (typically planar) of pre-existing failure. The distinction is that newly-formed cracks provide small resistance to closure and only frictional resistance to shear whereas joints and faults exhibit nonlinear resistance to closure and provide an additional resistance to shear that is not often present in freshly formed cracks. Therefore, the previous development on decohesive modeling forms a natural starting point for formulating a discrete model for joints and faults. The new development is the addition of elastic-plastic closure and shear to the previous decohesive model.

An alternative approach to the discrete modeling of joints and faults is to consider the joint or fault to be part of a representative volume with the remaining part consisting of the continuum on either side of the joint or fault. The effect of the joint or fault is smeared over the representative volume which is modeled as an equivalent continuum. Examples of this approach are given by Lee [1998], Cai and Horii [1992], and, Brannon [2010]. As indicated by Chalhoub and Pouya [2008], even determining the size of a representative volume element can be difficult. The model provided by Cai and Horri is limited to compressive states up to

the limit (critical) state. The other models have similar constraints. The one condition that none consider is the possibility of tensile stress, tensile failure and the possibilities of gap formation and shear motion with no shear and normal stress. Most often, these approaches attempt to place the equivalent continuum within the context of a constitutive framework based on isotropic elasticity and plasticity. The problem with such an approach is that it does not consider the anisotropy inherent with nonlinear joint or fault closure. Moreover, opening with failure in which traction on a single joint or fault plane cannot be supported is also not included.

Discrete models for joints can be separated into two categories: one for which the joint is considered to have finite width, in which case a continuum theory is used, and one in which the joint is idealized as zero width which requires a formulation involving traction and displacement discontinuity. The latter approach can utilize directly many of the concepts from continuum theory and has been studied extensively by Barton [1972], Desai and Ma [1992], who apply a "disturbed-state" or interpolation plasticity model. Plesha [1987], Grasselli and Egger [2003], and Huang et al. [2002], made a great effort to include the effects of surface roughness which produces dilatation under shear and a reduction in shear strength with shearing motion.

In evaluating these contributions, a balanced approach is necessary. First, if an attempt is made to include all details then the result will be a very complex three-dimensional model that is computationally expensive. On the other hand, essential features must be included. Getting an appropriate balance between detail and the essence of the overall response characteristics is one of the objectives of this research. The proposed approach is in the spirit of the work of Wang et al. [2003], with the additional feature of allowing for arbitrary loading paths including gap opening and closing.

A serious problem with modeling rock joints for application to wave propagation is that experimental data are often obtained from manufactured joints [Li and Ma, 2009; Chitty, 2010] rather than *in situ* joints. In addition, the need for capturing the details of joint behavior is questionable in light of the variability of properties that likely exist in the field. Therefore, the focus here is on capturing the essential features of joint behavior rather than attempting to match experimental features for any one joint. A study can be performed for various values of material parameters to determine if results for the problem at hand is particularly sensitive to a particular feature.

The approach adopted herein is to develop a discrete constitutive model for the joint or fault and to use a conventional continuum constitutive model for the material between the joints or on either side of a fault. The formulation is given for a joint within an element in which equilibrium is enforced for stress components identified with the joint surface, and a kinematic constraint of equal values for the orthogonal set of strains is invoked.

2.2 Key Results

2.2.1 Preliminary Comments

Within the limited time allocated for the project, it was decided that the most efficient allocation of resources and available personnel was to work simultaneously on three phases. These phases consist of (i) a two-dimensional study of wave propagation from a cylindrical source and predictions of failure in the vicinity of a tunnel, (ii) a one-dimensional study of the effect of joints on a propagating wave pulse, and (iii) the development of a three-dimensional model for joints and fault and the corresponding numerical algorithm. The full report of these phases is given as Chaps. 3, 4 and 5, respectively. Since each of these chapters is relatively long and somewhat dense, a brief description of each phase and the most important results are summarized in this section. This chapter also serves as an overview that helps to place the following material in perspective.

2.2.2 Blast Induced Waves Impacting Tunnels

An elastic-decohesive model is used to predict fracture patterns around a tunnel induced by a blast. The constitutive model is used to specifically indicate when a crack is initiated, to provide the orientation of the crack, to give the mode of failure, and to allow for the numerical determination of the width of cracks. The model can predict multiple failure planes, a feature that is necessary to simulate crack branching. Pre-existing planes of weakness such as those formed from previous cracks, joints and gaps can also be accommodated. The elastic-decohesive model has been implemented in the material-point method (MPM) [Sulsky et al., 1995; Sulsky and Schreyer, 2004]. In order to scope out the effect of an elastic-decohesive model on the propagation of a blast wave through rock, the rock is first modeled as elastic and then, in subsequent simulations, the rock is allowed to fracture using the elastic-decohesive formulation.

Figure 2.1 shows the computational domain for the first simulation. The computation is done in two space dimensions, assuming plane strain. The computational domain is 105m by 100m with x and y coordinates between $-50 < x < 55$ and $-50 < y < 50$. A circular region centered at the origin, with a radius of 3m, is non-deformable. This region (colored red in the figure) represents the blast zone and is used to numerically impose a prescribed traction boundary condition on the surrounding region to model the effect of the blast wave. No attempt is made to model the damage that occurs in the rock immediately adjacent to the blast source. Instead the size of the cylindrical source was taken to be sufficiently large so that the emanating waves could be considered as propagating through an elastic medium. Exterior to this circular region, we model the rock material through which the blast propagates, using the material properties given in Table 2.1. These parameters are representative of granite.

The radially symmetric, compressive pulse modeling the blast is taken to be $\sigma(t) = \sigma_0(1 - \cos(2t/t_d))H(t_d - t)$ as a function of time, for $t > 0$, where $H(t)$ is the Heaviside function. We use a magnitude $\sigma_0 = -380\text{MPa}$ and a duration $t_d = 1.3$ msec for the pulse. This pulse is the boundary condition imposed on the radial component of stress at the

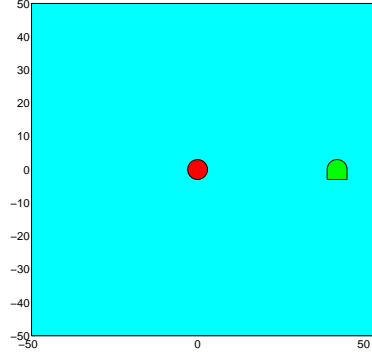


Figure 2.1: The computational domain is 105m by 100m with x and y coordinates between $-50 < x < 55$ and $-50 < y < 50$. The region representing the blast zone is shown in red, the rock is colored cyan and the tunnel is shown in green. The center of the blast is 39m from the left wall of the tunnel.

Young's modulus (Pa)	Poisson's ratio	density (kg/m ³)	τ_{nf} (Pa)	τ_{tf} (Pa)	u_0 (m)	s_m	f'_c (Pa)
53.3×10^9	0.21	2658	5.4×10^6	16×10^6	0.01	4	54×10^6

Table 2.1: Parameters that are used in the elastic-decohesive formulation.

boundary of the non-deformable region at a radius $r = 3$. Note that stress is negative in compression and positive in tension. The simulations are performed using the material-point method with a square mesh, 0.25m on a side. Thus, the domain has 420×400 elements, with 4 material points per element initially. Simulations are run for times between zero and 13 msec with a time step of 0.05 msec. For reference, Figure 2.2(a) shows stress as a function of time at the point (38.8125, 0.0625) if there is no tunnel. This point is just to the left of the center of the left face of the tunnel. We see that a compressive pulse initiated in a cylindrical cavity propagates outward and reaches the point at time 7.5msec, after traveling a distance 35.8m with speed 4751m/s. In this cylindrical geometry, a tensile tail develops behind the initial compressive pulse. At this point in the domain, the maximum amplitude of the tensile tail is roughly the same as the maximum amplitude of the compressive pulse.

Now, invoking the elastic-decohesive model allows fractures to form. Figure 2.2(b) shows the crack distribution and orientation around the tunnel with normal opening u_n greater than $0.005u_0$. The tunnel profile is outlined in green. The decohesion model can allow multiple cracks to occur at a point so that crack branching can be studied. In this simulation, three cracks are allowed, colored in this figure with black, blue and red line segments, respectively. The orientation of the line segments is tangent to the crack surface. The rock is most likely to fail in a region in front of the tunnel and in a region near the tunnel top and near the lower left corner. Not surprisingly, when the initially compressive blast wave hits the tunnel wall, it reflects from the free surface as a tensile wave which causes a peak in the maximum principle stress to the left of the tunnel. Although, some cracks appear on the right side

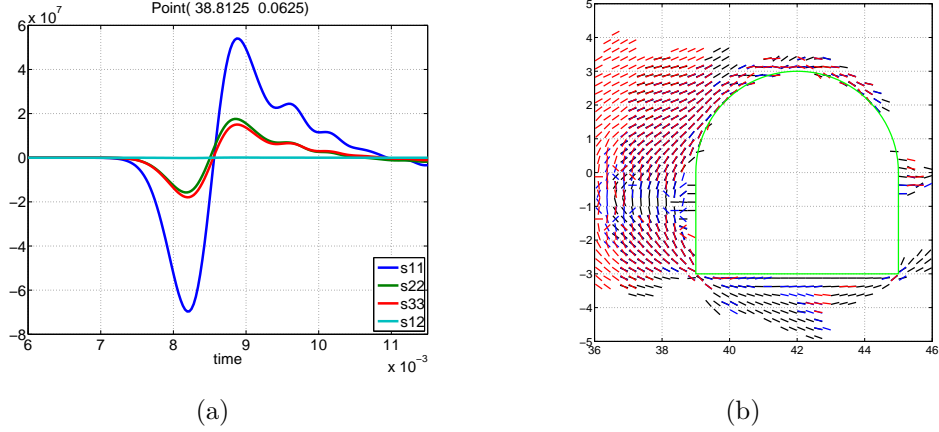


Figure 2.2: (a) Stress as a function of time at the point (38.8125, 0.0625). The plot in (a) shows free propagation of a wave from a cylindrical source that applies a pulse with $\sigma_0 = -3.8 \times 10^8$ Pa to a domain made up of rock modeled elastically, and with no tunnel in the rock. In (b) the elastic-decohesive model is invoked and the distribution and orientation of cracks around the tunnel with normal opening u_n greater than $0.005u_0$ at $t = 11$ msec is shown.

of the tunnel as well - the side away from the blast. An unexpected result occurs when the compressive wave passes around the tunnel top and bottom, the rock is under large compression and axial splitting occurs.

2.2.3 One-dimensional Waves Passing through Joints

To determine the effect of a wave in the form of a stress pulse transmitting through a joint or a set of joints, a model problem was considered. The problem consisted of a sinusoidal pulse of stress applied at the left end of a bar (represented as either uniaxial stress or uniaxial strain) that contains one or more joints. The situation is illustrated in Fig. 4.12. The bar is considered to be long enough, and the time duration sufficiently limited, so that reflections off the right end are not a factor. The bar is considered to be elastic while the joint is modeled as (i) a gap, (ii) a purely plastic material, or (iii) an elastic-plastic material.

With use of the one-dimensional dynamic code, numerical solutions are obtained for the bar problem shown in Fig. 4.12.

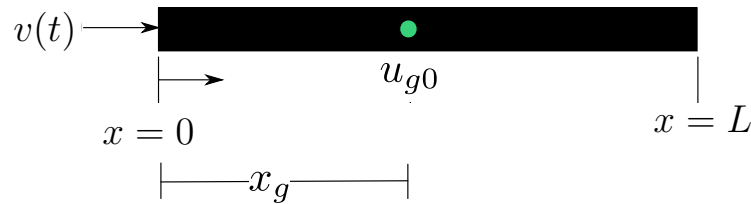


Figure 2.3: Notation for the problem of a bar with a single discontinuity

Whether single or multiple discontinuities are prescribed, the first discontinuity will be located in the middle of the bar at $x_g = \frac{L}{2}$. A discontinuity of length u_{g0} is prescribed as a single discontinuity or the sum of multiple discontinuities. The bar has a velocity boundary condition imposed at $x = 0$ and a free surface boundary condition imposed at $x = L$. Initially, the bar is at rest with no prestress. The velocity boundary condition is imposed in the form of a sinusoidal pulse as follows:

$$v(t) = \frac{v_{max}}{2} \left(1 - \cos\left(\frac{2\pi t}{t_{wave}}\right) \right) H[t_{wave} - t]H[t]. \quad (2.1)$$

in which $H[]$ denotes the Heaviside function. The prescribed velocity pulse contains two parameters consisting of: v_{max} , the peak particle velocity of the imposed wave, and t_{wave} , the duration of the sinusoidal pulse.

If there is no joint, the pulse will propagate along the bar with no distortion. Therefore, we look at the cases representing the various models for a joint as examples of the effects of joints covered in considerable detail in Chapt. 4. If the joint is modeled as a gap, the pulse must be of sufficient magnitude and duration to close the gap. Prior to closure the joint represents a free surface boundary so that the pulse will be reflected. After closure, the remainder of the pulse transmits with no distortion. The numerical representation of such a scenario is not so simple because the instance of gap closure implies an abrupt rise from a stress of zero to a finite stress that is transmitted through the joint. The result is that spurious oscillations are introduced into the numerical solution.

A numerical solution of dimensionless stress, σ , as a function of the dimensionless spatial coordinate, x , at various values of dimensionless times is shown in Fig. 4.14(a). Here, t denotes time and t_0 is a reference time chosen for convenience. When the compressive pulse has transmitted into the bar. At the later time t_1 , part of the wave has reflected as a tensile segment, the gap has closed and the remaining part of the original pulse has transmitted through the joint. At the later time t_2 , the reflected and transmitted parts have merely progressed further in their respective directions.

Next, suppose the material in the joint is modeled as a strain-hardening, plastic material. Now the response is much smoother and a portion of the incoming pulse is immediately transmitted through the joint as illustrated in Fig. 4.15(a). There is a reflected tensile pulse and the transmitted pulse is only a slight modification of the original pulse. However, as the red line in Fig. 4.15(b) indicates, there is energy dissipation associated with the closure of the joint. Other forms of energy including the kinetic, strain, total, and input (work) energies are plotted as well. The response of the joint as a plastic material is illustrated in Fig. 4.15(c). Notice that unloading is vertical indicating no elastic component.

Finally, elastic unloading is included as illustrated in Fig. 4.16(c). The corresponding plots of stress at various times, as shown in Fig. 4.16(a), show little difference from the previous case involving no joint elasticity with the exception of a small compressive tail in the reflected wave.

These examples illustrate the important information that can be obtained through the use of one-dimensional simulations of waves transmitted through joints. The extreme models for a joint consist of a purely elastic model with the elastic modulus identical to the adjacent

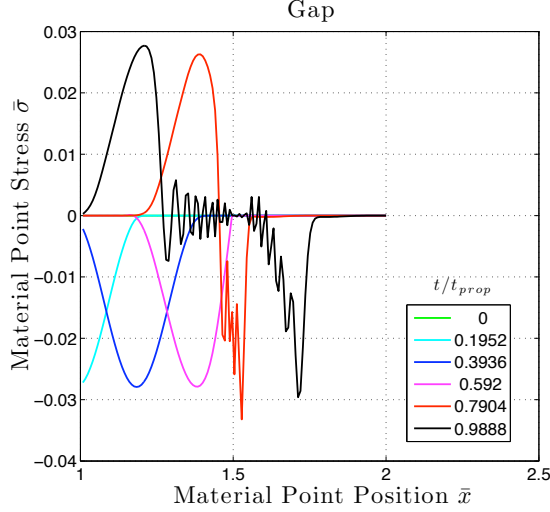


Figure 2.4: Stress as a function of x for various values of prescribed time.

continuum and of a gap that provides no resistance to closure. An elastic-plastic model provides intermediate representations between these two extreme cases. It is seen immediately that, in general, joints provide dissipation and cause dispersion. If there is more than one joint, there is the possibility of a certain amount of wave trapping as a portion of a wave transmitted through the first joint will be reflected from a second joint. This suggests the question as to whether or not a constitutive approach involving the smearing of joint behavior within a composite constitutive equation can reflect sufficiently accurately the features of waves transmitting through jointed rock.

2.2.4 Constitutive Equation for Joints and Faults

A joint is modeled as a reference surface with unit normal \mathbf{n} and with physical surfaces separated by a discontinuity in displacement, $[\mathbf{u}_J]$. If two additional orthogonal unit vectors, \mathbf{t} and \mathbf{p} , lie in the plane, then the view of the joint in the \mathbf{n} - \mathbf{t} plane is illustrated in Fig. 2.7(a). If the \mathbf{p} -component is insignificant, then the displacement discontinuity is $[\mathbf{u}_J] = [u_{Jn}]\mathbf{n} + [u_{Jt}]\mathbf{t}$. A normal component of strain is defined to be $e_{Jnn} = \{[u_{Jn}] - [u_{Jn0}]\} / [u_{Jn0}]$ in which $[u_{Jn0}]$ represents the initial normal component of discontinuity. Similarly, the traction vector is $\boldsymbol{\tau} = \tau_n\mathbf{n} + \tau_t\mathbf{t}$. The proposed plasticity model consists of nonlinear elasticity for the normal component of traction versus normal strain and plasticity in which the yield surface consists of the union of three separate yield surfaces identified by $F_C = 0$, $F_S = 0$, and $F_T = 0$, in which F_C , F_S and F_T are yield functions for compaction, shear and zero tensile strength, respectively. The resulting yield surface for the joint, $F_J = 0$, is shown in Fig. 2.7(b).

The joint is assumed to be a crack with an initial discontinuity in the normal direction. Closure, or compaction, is resisted by material within the joint. Resistance to opening, or to tension is small or nonexistent. Shearing motion produces tangential discontinuities. Resistance to shear may exist due to a combination of frictional resistance and the presence of asperities.

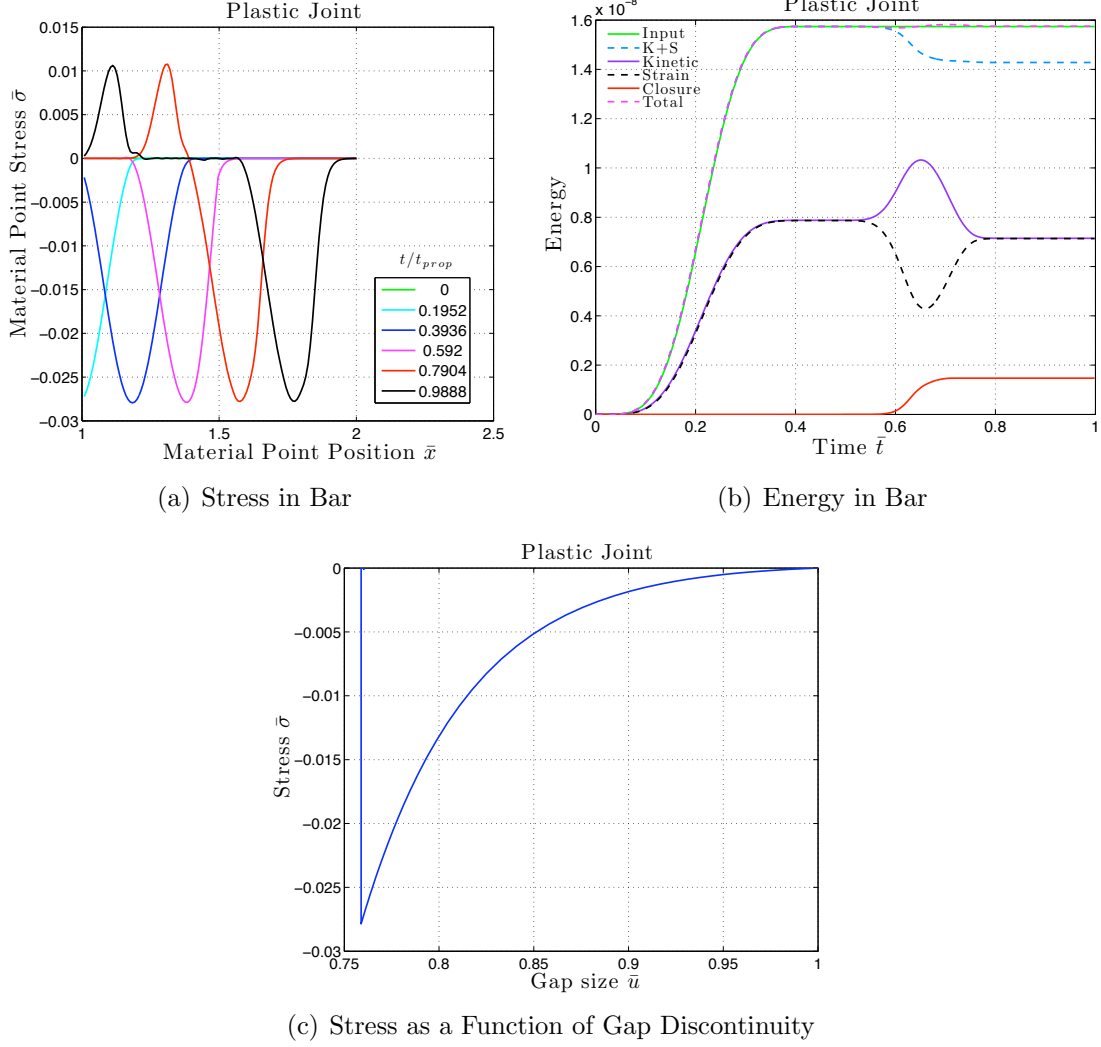


Figure 2.5: Results of wave propagation through a bar with a plastic joint

The model is based on the following assumed features of joint and fault behavior.

Direct Closing and Opening

1. Under uniaxial compression, the compressive joint stress is a highly nonlinear function of the amount of closure.
2. The features of stress versus closure for different joints can be reflected reasonably well by a single analytical expression if dimensionless forms of stress and closure are used.
3. Upon unloading in the compressive regime, a nonlinear elastic response is exhibited.
4. A joint or fault exhibits no strength in tension.

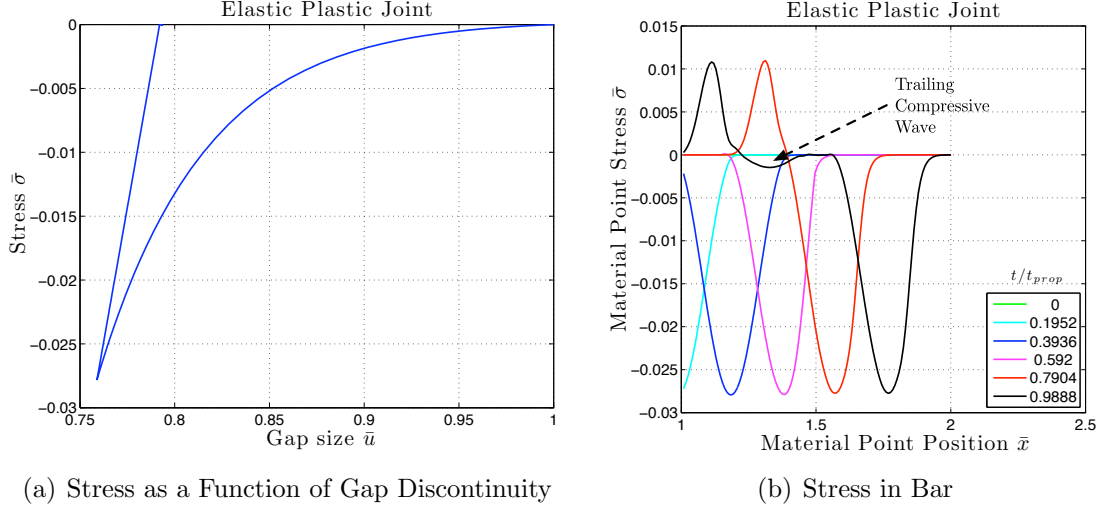


Figure 2.6: Results of wave propagation through a bar with an elastic-plastic joint

Direct Shear

5. The amount of tangential motion may be several orders of magnitude larger than the amount of normal compaction.
6. After sufficiently large shear motion, the response is governed by Coulomb's friction criterion.
7. Even with no compressive component of traction, joints exhibit resistance to shear due to the surface roughness in the form of asperities between the mating surfaces.
8. After a certain amount of shear the asperities wear down and any accompanying cohesive strength is lost.

Combined Shear and Normal Deformation

9. Compressive traction enhances the apparent strength in shear due to asperities.
10. Asperities cause dilatation under shear.

A constitutive equation algorithm has been written under the assumption that strain increments are prescribed. One example provided here is uniaxial compaction, release, extension into the joint-opening regime and reclosing. The strain path is shown in Fig. 2.8(a) and the corresponding stress-strain path in Fig. 2.8(b). The sample is first compacted as illustrated by segment O-A, and then unloaded to zero stress at point B. The nonlinear loading phase is governed by elasticity and plasticity based on a small initial yield stress. The unloading phase is governed by nonlinear elasticity. With additional positive increments in strain, the joint is unloaded to its original configuration at point C. With further positive

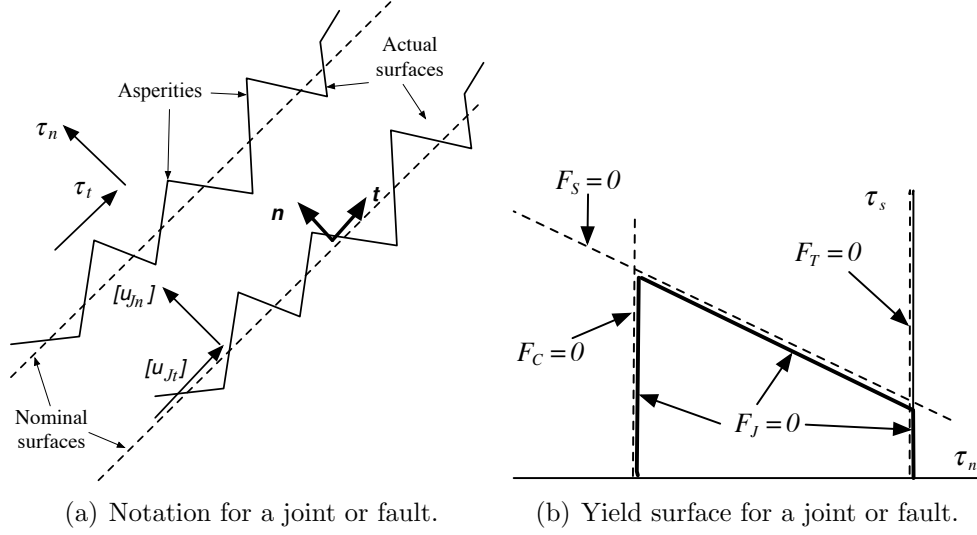


Figure 2.7: Notation associated with a joint or fault and corresponding yield surface.

increments, a gap is formed to the maximum value illustrated by the normal strain at point D. The width of the gap is tracked using a positive joint plastic strain. Note that the normal component of traction remains zero. Then the strain increments are reversed and the gap is closed at point E, making the joint plastic strain zero. The model has been formulated so that re-compaction follows the original loading curve as indicated by the segment E-F.

This example illustrates that the model exhibits plasticity immediately upon loading without shear, and nonlinear elasticity for unloading. The numerical procedure also handles gap formation and closure within the constitutive equation without requiring a separate algorithm to handle impact of two free surfaces. Other examples with different values of material parameters and for paths that include shear are given in the body of the report.

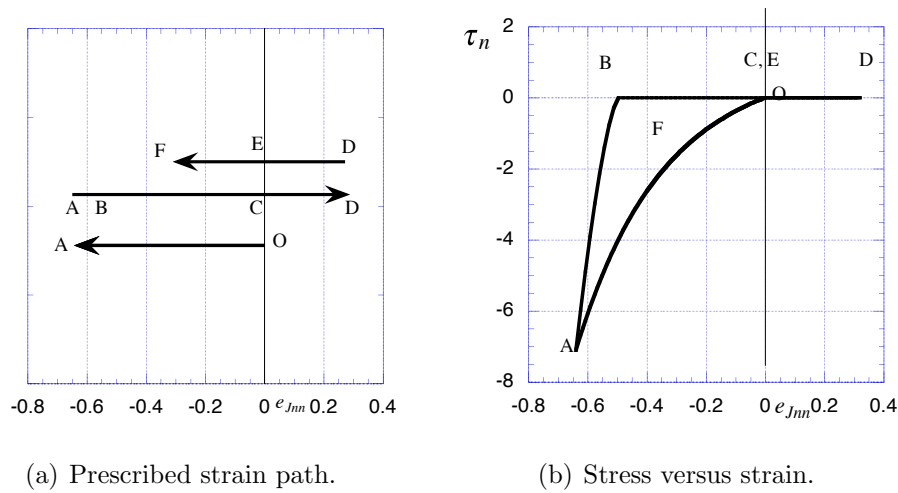


Figure 2.8: Plots of stress and strain for uniaxial strain with gap formation and closing.

2.3 Recommendations

The following recommendations for in-depth investigations are warranted as a consequence of the insight provided by research conducted under this project.

Spherical Waves: The restriction to a two-dimensional study implied that the source was cylindrical. The resulting propagated wave showed the development of a significant tensile tail, a result with important implications regarding material failure. The tensile part is magnified when the compressive head of the wave also reflected in tension from the free surface formed by a tunnel wall. It is expected that a similar phenomenon exists for waves emanating from a spherical rather than a cylindrical source. The specific nature of a tensile tail and superposition of tensile stress due to reflection of spherical waves should be investigated.

Axial Splitting: The analysis of a compressive stress pulse enveloping a tunnel indicates that in addition to tensile failure at one location, a high compressive stress can cause axial failure at a different location in the vicinity of the tunnel. Field data should be studied to determine whether or not such failures are observed.

Dispersion and Dissipation Associated with Joints and Faults: The one-dimensional analysis indicates that joints and faults cause dissipation and changes in wave shape (dispersion) both of which may significantly reduce the potential for damage around a tunnel. A study should be performed to determine the dissipation and dispersion associated with waves impinging at an angle to a fault and on one or more joints.

Parameter Study of Joint Constitutive Model: A three-dimensional constitutive model and associated numerical algorithm has been developed to represent the response of joints and faults to a number of prescribed strain paths. There are a limited number of material parameters incorporated within the model. A set of paths should be conducted for a representative range of values for these parameters to determine which parameters are of most importance for a given class of paths and to provide guidance for matching experimental data.

Full Three-Dimensional Numerical Simulations: The results of this research include new insights and the development of the capability to perform a complete three dimensional numerical analysis of the potential failure of a tunnel due to waves in jointed media. The resolution must be sufficiently complete to capture tensile tails of an initial compressive pulse. The inclusion of the constitutive equation for joints and faults provides a unique capability for studying the potential failure of tunnels. The orientation of joints with respect to the direction of wave propagation may be important for either focusing the wave energy towards a tunnel, or, conversely, diverting some of the wave energy away. Finally, the combination of the joint-fault constitutive equation together with the existing cohesive failure model provides a powerful numerical approach for studying the complete problem of wave propagation towards and around a tunnel, and the evolution of failure in zones adjacent to the tunnel, all occurring within a computational domain that includes joints and faults.

3

Rock Fractures Near Tunnels due to a Blast

3.1 Introduction

We have developed a decohesive crack model to be used to study the formation of fractures near a tunnel in rock due to a blast load. A problem with many existing decohesion models is that they are studied as academic exercises and often do not reflect features shown by experimental data. The proposed decohesion model is an attempt to reflect the essential fracture characteristics of rock without the overwhelming detail that would be impossible to handle numerically. Of these characteristics, it is believed that the stress at which failure initiates, the orientation of failure, and the fracture energy represent the essential features. With the assumption that the effect of a crack can be smeared over an element, the result is a constitutive numerical algorithm that is both efficient and that captures the induced anisotropy associated with failure.

The model is phenomenological and relatively simple since applications to large-scale numerical simulations represent the intended use. Nevertheless, there is an attempt to reflect the essential aspects of both experimental data and micro-structural properties within the formulation. The primary focus is on predicting correctly the stress at which a crack initiates or re-activates, and the orientation of the crack.

Section 3.2 reviews classical failure models and sets up the notation and ideas arising in our proposed new model. This section also lays out the criterion we use to detect when failure is initiated. Section 3.3 describes how cracks open once failure is detected and initiated. Then, based on the assumption that the continuum deformation of rock is sufficiently small so that elasticity can be invoked, Section 3.4 provides an explanation of how decohesion can be combined with elasticity to obtain a constitutive equation subroutine for use in large-scale numerical simulations. For simplicity, this report focuses on two-dimensional problems in plane stress or plane strain. Section 3.5 applies the elastic-decohesive model to examine fracture patterns around a tunnel induced by a blast, modeled as a pressure pulse imparted to the surrounding rock. We find that the tunnel geometry plays a role in the fracture pattern. In particular, fractures emanate from a corner. Moreover, the arched top of a

tunnel is subject to a large compressive load when a blast originates from the side. Our model predicts that the compression results in axial splitting and thus, horizontal cracks form near the arched tunnel ceiling. In contrast, if the blast originates above the arch, damage to the ceiling is reduced. Section 3.6 provides a summary of these findings and some concluding remarks.

3.2 Classical Models For Failure

3.2.1 Essential Aspects of Failure in Plane Stress or Plane Strain

Let $\boldsymbol{\sigma}$ denote the stress tensor with components σ_{11} , σ_{22} and σ_{12} for an orthonormal basis \mathbf{e}_1 and \mathbf{e}_2 in the plane of interest. The out of plane component of stress, if present, is denoted by σ_{33} , associated with an orthonormal basis vector \mathbf{e}_3 . The principal directions of stress, \mathbf{p}_1 and \mathbf{p}_2 , also form an orthonormal basis associated with principal values σ_1 and σ_2 in the plane. Failure in plane stress or plane strain is often described by a failure surface in terms of principal stresses. A generic failure surface is sketched in Fig. 3.1. The figure depicts the failure surface in stress space. That is, if material is loaded from zero stress with σ_1 proportional to σ_2 , failure will occur when σ_1 and σ_2 reach the values indicated on the failure surface. Failure in equal biaxial tension is identified as point (a), failure in uniaxial tension by point (b), failure in pure shear at (c) (one principal value of stress is the negative of the other), while failure in uniaxial compression is identified as (d). The value of the uniaxial compressive stress is typically an order of magnitude larger than the failure stress in uniaxial tension. As the stress state is extended into the regime where both principal stresses are compressive, the failure surface extends from (d) to a maximum at point (e). The remaining regime for compressive stresses is given as the segment of the curve shown as a dotted line from (e) to equal biaxial compression at point (f). With the assumption of initial isotropy in the plane, the remainder of the curve is merely a reflection about the symmetry line (a-f).

Next, the generic features associated with the orientation of the normal to the plane of material failure will be discussed. As indicated in Fig. 3.1, suppose a unit normal vector \mathbf{n} lies within the plane of stress or strain, and forms an angle, θ , with respect to the first principal direction \mathbf{p}_1 . Define the normal vector to the surface of material failure by the critical angle, θ_c . For the regime (a), (b), (c)-(d), \mathbf{n} is equal to \mathbf{p}_1 , the direction of maximum principal stress, or $\theta_c = 0$. Such an orientation is typically associated with brittle materials. In particular, if $\theta_c = 0$ for uniaxial compression, the resulting feature is called axial splitting and is seen in some experimental specimens formed from concrete. However, in the regime (d)-(e), two orientations of failure exist $\theta_c = \pm\alpha$, with α increasing smoothly from zero at (d) to a maximum of about 30° at (e). Finally, for the dotted segment of the failure curve, the normal is out of the plane and, again, is in the direction of maximum principal stress which is zero (from a three-dimensional viewpoint) with the other two principal stresses in the plane being negative.

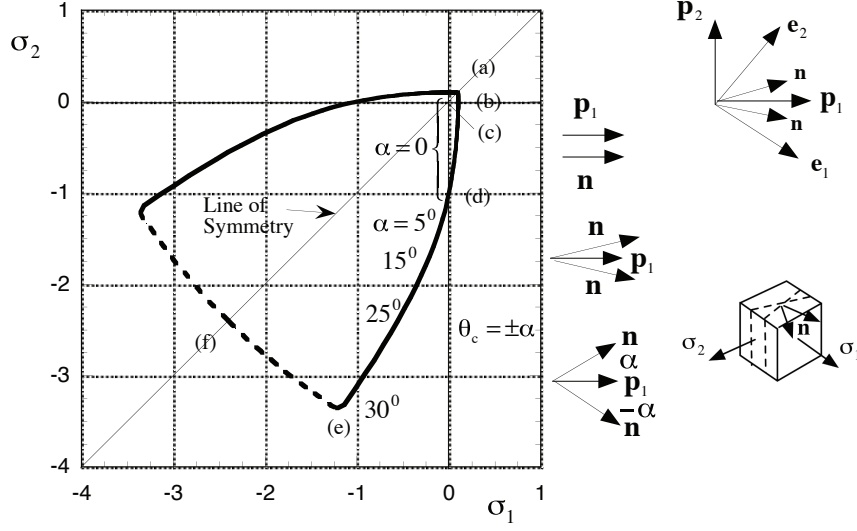


Figure 3.1: Generic aspects of a failure surface in plane stress or plane strain, and the orientation of the surface of material cracking (failure).

3.2.2 Classical Models of Failure

In order to describe various models in a succinct manner, and for future use, a standard notation is now introduced. Small deformations are assumed so there is no need to differentiate among the various stress and strain tensors. The traction on any surface with normal \mathbf{n} is

$$\boldsymbol{\tau} = \boldsymbol{\sigma} \cdot \mathbf{n}. \quad (3.1)$$

Introduce another orthonormal pair of base vectors consisting of \mathbf{n} and \mathbf{t} , normal and tangent unit vectors to the plane of material failure. Then $\tau_n = \sigma_{nn}$ and $\tau_t = \sigma_{nt}$ are the normal and shear components of traction, respectively, and the remaining component of stress in the plane is σ_{tt} .

In order to describe the classical models, it is assumed that failure on a material surface with given orientation, \mathbf{n} , can be described through the use of a decohesion function, F_n^D , which depends on material properties and the traction vector. The latter dependence implies that the function depends on the orientation of the particular material surface being considered. The function is constructed so that $F_n^D < 0$ indicates failure is not occurring, $F_n^D = 0$ identifies the onset of failure, and $F_n^D > 0$ is not allowed. To determine if failure is initiated at a point, all possible orientations must be considered with the critical direction being the one that maximizes F_n^D .

As described for Fig. 3.1, a point on the decohesive surface, $F_n^D = 0$, can be obtained by incrementing radially from the origin in stress space. Each point on the radial path defines

a state of stress which must be evaluated to determine if decohesion has occurred. A search for the critical orientation of \mathbf{n} is performed by maximizing F_n^D with respect to the angle θ where

$$\mathbf{n} = \cos \theta \mathbf{p}_1 + \sin \theta \mathbf{p}_2 \quad 0 \leq \theta < \pi. \quad (3.2)$$

Once the stress path has been extended so that the maximum value of F_n^D is zero, one point on the decohesion surface has been defined. The unit vector \mathbf{n} defined by the corresponding critical value, $\theta = \theta_c$, provides the orientation of the physical surface where a crack initiates. The process is repeated for different radial paths until the complete decohesion surface is obtained.

The classical criteria for failure are simple enough so that analytical expressions are available for both the decohesion surface and the orientation of crack initiation. However, the general approach described above provides a common framework for both classical models and the alternative formulation that will be introduced later.

In summary, a classical decohesion function, F^D , is defined as follows:

$$F^D = \max_{\mathbf{n}} F_n^D \quad F_n^D \equiv F_n^D(\boldsymbol{\tau}) \quad (3.3)$$

with failure indicated when $F_n^D = 0$. The decohesion functions of Rankine, F_n^R , and Tresca, F_n^T , each depend on only one component of the traction, $\boldsymbol{\tau}$, as follows:

$$F_n^R = \frac{\tau_n}{\tau_{nf}^R} - 1 \quad F_n^T = \frac{\tau_t^2}{(\tau_{sf}^T)^2} - 1. \quad (3.4)$$

The material parameters τ_{nf}^R and τ_{sf}^T are the critical values of normal and shear traction, respectively, and are associated with these specific criteria. The surface $F^R = 0$ denotes the maximum tensile stress criterion of Rankine and is shown in Fig. 3.2a for plane stress in terms of principal components. The critical orientations for the surfaces of material failure are unique and these directions are also given ($\theta_c = 0$ for plane stress). Similarly, the surface $F^T = 0$, shown in Fig. 3.2b, is the maximum shear-stress criterion of Tresca. However, now for each point of failure there are two possible orientations of the failure surface whereby \mathbf{n} makes equal angles with the direction of maximum principal stress and $\theta_c = \pm 45^\circ$. The two possible surfaces of material failure are orthogonal to each other. On the dotted segment of the surface, the normal does not lie in the plane of stress.

Another criterion, which is often used for geologic materials, is that of Mohr-Coulomb which involves both the normal and shear components of traction as follows:

$$F_n^{MC} = \frac{\tau_t}{\tau_{sf}^{MC}} + \frac{\tau_n}{\tau_{nf}^{MC}} - 1. \quad (3.5)$$

The essential idea is a generalization of the Tresca criterion in that failure in shear on a given surface is assumed to depend on the amount of normal traction. If τ_{nf}^{MC} is infinite, the criterion is that of Tresca; if τ_{sf}^{MC} is infinite, the result is Rankine's criterion. Similarly to the Tresca criterion, there are two possible orientations for material failure but, instead of $\theta_c = \pm 45^\circ$, the normal to the surface of failure is now $\theta_c = \pm \alpha$ with respect to the direction of maximum principal stress in the plane of maximum and minimum principal directions of

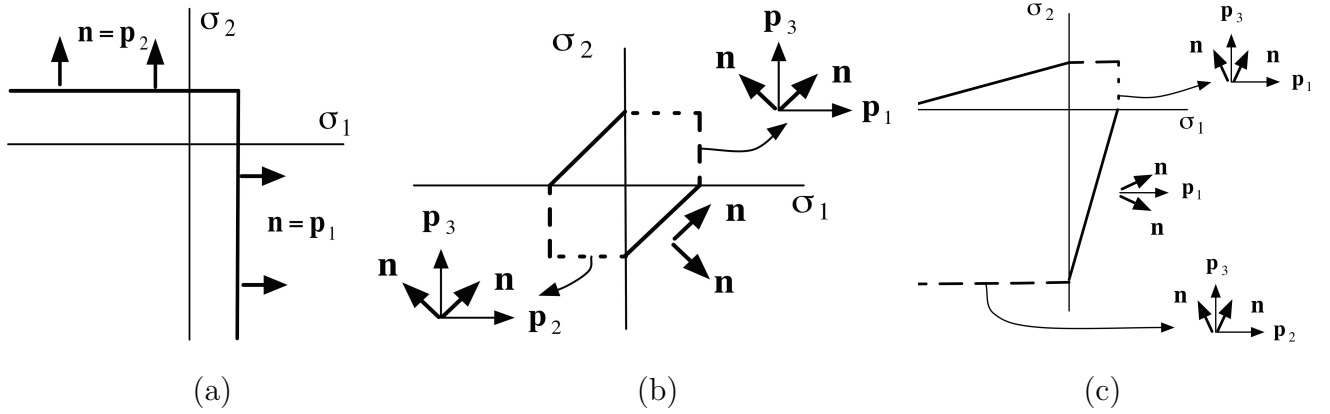


Figure 3.2: Sketches of curves showing failure initiation including orientations of the normal to surfaces of material failure as predicted by classical models (a) Rankine, (b) Tresca and (c) Mohr-Coulomb. (The normal lies within the plane only for the solid portions of each curve.)

stress and $\tan 2\alpha = \tau_{nf}^{MC} / \tau_{sf}^{MC}$. The surface $F^{MC} = 0$ is shown in Fig. 3.2c for plane stress. For example, if $\tau_{sf}^{MC} = 1.4\tau_{nf}^{MC}$ the positive intercept of the σ_1 axis for $\sigma_2 = 0$ is $\sigma_1 = 0.9\tau_{nf}^{MC}$. Similarly, if $\sigma_1 = 0$, the intercept is $\sigma_2 = -8.75\tau_{nf}^{MC}$ which yields a ratio of approximately 10 between the tensile and compressive failure stresses, a ratio often observed for concrete and geologic materials. The orientation of the normal of material failure with respect to the direction of maximum principal stress is $\theta_c = \pm 18^\circ$ for all points of failure. The Mohr-Coulomb criterion, which is often used for geologic materials, predicts only one value of α with $\theta_c = \pm\alpha$ for all states of stress that satisfy the failure criterion. Although reasonable for some of the failure domain, such an angle is not representative for all states of stress at the initiation of failure. Again, the dotted portion of the surface in Fig. 3.2 indicates that an out-of-plane component exists for the normal vector.

Each criterion has had considerable success in predicting failure, the Rankine criterion for brittle materials, Tresca for ductile materials, and Mohr-Coulomb for concrete and geologic materials such as rock and ice. However, as the Schulson [2004] data show for ice, and similarly for many other materials, materials often fail according to one criterion for one regime of stress, and to another criterion for a different regime. Specifically, the Rankine criterion is often suitable for tensile states of stress, Mohr-Coulomb for intermediate states, and the Tresca criterion for large compressive states. Not one of these classical criteria has the flexibility to accurately reflect simultaneously both the state of stress at failure and the orientation of the surface of material failure for all paths in plane stress or plane strain. In particular, none predicts axial splitting. Next, a new model is proposed that attempts to remedy this situation.

3.2.3 Proposed Form for the Failure Criterion

A mathematically attractive approach for indicating when failure initiates is one based on loss of ellipticity as indicated by Schreyer [2001]. Such a criterion might be used to suggest when a decohesive model should be implemented. However, it is considerably simpler to just use the value of a decohesive function to indicate when failure initiates and this is the approach adopted here. The key new feature in the proposed decohesion function is to allow for the possibility that, in addition to the traction, failure may depend on the component of the stress σ_{tt} , as suggested but not implemented by Planas et al. [2003]. The decohesion function is similar to the Mohr-Coulomb function in that both the shear and normal components of the traction are included. If it is believed that the strength in shear should reach a limiting value for large negative values of τ_n , then an exponential form can be utilized to relate the brittle and shear contributions:

$$F = \max F_n(\boldsymbol{\tau}, \sigma_{tt}) \quad F_n = \frac{\tau_t^2}{(s_m \tau_{sf})^2} + \exp \left(\kappa \left(\frac{\tau_n}{\tau_{nf}} + \frac{\langle -\sigma_{tt} \rangle^2}{(f'_c)^2} - 1 \right) \right) - 1 \quad (3.6)$$

The ramp function is defined so that $\langle x \rangle = x$ if x is positive; otherwise $\langle x \rangle$ is zero. The material parameter f'_c denotes the failure stress in uniaxial compression. Two additional material parameters are s_m and κ , defined below. The form (3.6) has been used in numerical simulations by Sulsky et al. [2007].

The failure surface is defined by $F = 0$. The parameter τ_{sf} is the shear failure strength when $\tau_n = 0$ and must be interpreted differently from the corresponding parameter in the Tresca and Mohr-Coulomb criteria. In particular, τ_{sf} is not the maximum possible shear strength, but the shear strength in pure shear, as we will see below. First, note that if the shear parameter, τ_{sf} , is infinite then (3.6) reduces to

$$B = \max_{\mathbf{n}} B_n \quad B_n = \frac{\tau_n}{\tau_{nf}} + \frac{\langle -\sigma_{tt} \rangle^2}{(f'_c)^2} - 1. \quad (3.7)$$

The surface $B = 0$ is one for which \mathbf{n} is always in the direction of maximum principal stress and, consequently, represents a brittle criterion. With the use of (3.7), the decohesion function of (3.6) can be rewritten as a combination of shear and brittle parts as follows:

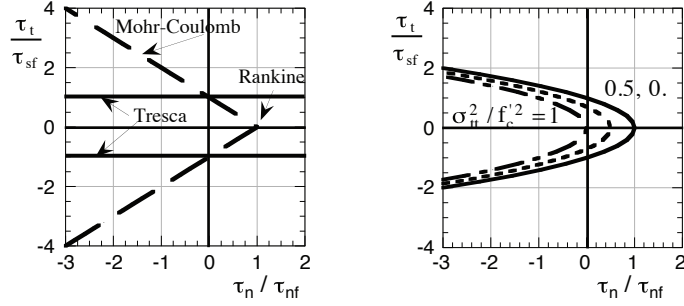
$$F_n = \frac{\tau_t^2}{(s_m \tau_{sf})^2} + \exp \left(\kappa B_n \right) - 1. \quad (3.8)$$

Note that $B_n \leq 0$ because no solution to $F_n = 0$ exists for $B_n > 0$.

In pure shear, $B_n = -1$, and failure occurs when $\tau_t = s_m \tau_{sf} \sqrt{1 - e^{-\kappa}}$. If τ_{sf} is defined as the failure stress under pure shear, then we have the identity

$$s_m^2 (1 - e^{-\kappa}) = 1 \quad \text{or} \quad \kappa = \ln s_m^2 - \ln(s_m^2 - 1). \quad (3.9)$$

This equation relates κ to s_m . The parameter s_m can be determined by considering a compressive normal stress component so that $\tau_n < 0$. In the limit of a large negative value of τ_n , F reduces to $F = (\tau_t / (s_m \tau_{sf}))^2 - 1$. Thus, under this circumstance, failure would occur



(a) Classical surfaces

(b) Proposed surfaces

Figure 3.3: Plots of failure surfaces in $\tau_n - \tau_t$ space.

when the shear traction is $s_m \tau_{sf}$. Therefore, s_m multiplied by the shear failure at zero normal stress, is the maximum possible value for the shear failure under large normal compressive stress. It is reasonable to assume $s_m > 1$. We typically use $s_m = 4$.

The classical surfaces and the proposed decohesion surface of (3.6) are displayed in the space of τ_t and τ_n in Figs. 3.3a and 3.3b, respectively. Note that the shear contribution must be zero for the Rankine criterion because, by definition, the normal to the failure surface is a direction of maximum principal stress so any shear component associated with this surface is zero. As indicated in Fig.3.3b, the quadratic term for shear in (3.6) provides a smooth transition at $\tau_t = 0$ whereas the Mohr-Coulomb criterion introduces a discontinuity in slope. When the normal component of traction is sufficiently compressive, the quadratic form indicates a failure stress in shear that is intermediate to those given by the Mohr-Coulomb and Tresca criteria. Also, when the in-plane stress becomes $\sigma_{tt} = -f'_c$, failure is predicted even if τ_n and τ_t are zero.

3.2.4 Analytical Form of the Critical Direction

Performing a numerical search to find the maximum value of F with respect to θ is computationally intensive and might result in unacceptable run times for large-scale simulations involving failure. Because of the relatively simple form of (3.6) it is almost possible to find analytically the critical value of θ by setting $\partial F / \partial \theta = 0$. As a first step, it is convenient to transform to the principal basis of stress with principal stresses ordered such that $\sigma_1 \geq \sigma_2$. The transformation relations for the components in the local $\mathbf{n} - \mathbf{t}$ system reduce to

$$\begin{aligned}\tau_n &= \sigma_1 \cos^2 \theta + \sigma_2 \sin^2 \theta \\ \sigma_{tt} &= \sigma_1 \sin^2 \theta + \sigma_2 \cos^2 \theta \\ \tau_t &= (\sigma_2 - \sigma_1) \cos \theta \sin \theta.\end{aligned}\tag{3.10}$$

Using the definition of F , (3.6), and the relationship between principal components and $\mathbf{n} - \mathbf{t}$ components, (3.10), we can write the equation for F as

$$F(\theta) = k_1 \sin^2 \theta \cos^2 \theta - 1 + e^{g(\theta)}\tag{3.11}$$

where

$$k_1 = \frac{(\sigma_1 - \sigma_2)^2}{s_m^2 \tau_{sf}^2} \geq 0, \quad (3.12)$$

$$g(\theta) = \kappa \left[\frac{\sigma_1}{\tau_{nf}} \cos^2 \theta + \frac{\sigma_2}{\tau_{nf}} \sin^2 \theta - 1 + \frac{1}{f_c^2} \langle -\sigma_1 \sin^2 \theta - \sigma_2 \cos^2 \theta \rangle^2 \right].$$

Note that $F(\theta) = F(\pi - \theta)$. The expression for F can be simplified if we substitute $\xi = \sin^2 \theta$, then

$$F(\xi) = k_1 \xi(1 - \xi) - 1 + e^{g(\xi)} \quad (3.13)$$

where

$$g(\xi) = \kappa \left[\frac{\sigma_1}{\tau_{nf}}(1 - \xi) + \frac{\sigma_2}{\tau_{nf}}\xi - 1 + \frac{1}{f_c^2} \langle -\sigma_1 \xi - \sigma_2(1 - \xi) \rangle^2 \right]. \quad (3.14)$$

To maximize F , first obtain the derivatives

$$\begin{aligned} \frac{dF}{d\theta} &= \frac{dF}{d\xi} \frac{d\xi}{d\theta}, & \frac{d\xi}{d\theta} &= 2 \sin \theta \cos \theta = \sin 2\theta, \\ \frac{dF}{d\xi} &= k_1(1 - 2\xi) + g'(\xi)e^{g(\xi)}. \end{aligned} \quad (3.15)$$

The derivative, $dF/d\theta$, is zero when $\theta = \theta_1 = 0$, $\theta = \theta_2 = \pi/2$, and when $\theta = \theta_3$ where

$$k_1(1 - 2\xi^*) + g'(\xi^*)e^{g(\xi^*)} = 0, \quad \xi^* = \sin^2 \theta_3. \quad (3.16)$$

Note that if θ_3 exists, then so does a fourth solution, $\theta_4 = \pi - \theta_3$. A meaningful solution to (3.16) must have $0 \leq \xi^* \leq 1$. We next examine when ξ^* exists.

To examine the roots of equation (3.16), first compute the derivatives of $g(\xi)$,

$$g'(\xi) = -\kappa \left[\frac{\sigma_1 - \sigma_2}{\tau_{nf}} + \frac{2}{f_c^2} (\sigma_1 - \sigma_2) \langle -\sigma_1 \xi - \sigma_2(1 - \xi) \rangle \right] \leq 0 \quad (3.17)$$

$$g''(\xi) = \kappa \frac{2}{f_c^2} (\sigma_1 - \sigma_2)^2 H[-\sigma_1 \xi - \sigma_2(1 - \xi)] \geq 0. \quad (3.18)$$

Now consider the function $h(\xi) = g'(\xi)e^{g(\xi)}$, which is non-positive. Its derivative is $h'(\xi) = [g''(\xi) + (g'(\xi))^2]e^{g(\xi)}$. Since $h'(\xi) \geq 0$, $h(\xi)$ is non-decreasing. Since $-k_1(1 - 2\xi)$ is an increasing function, there can be at most one root $\xi^* \in (0, 1)$ of equation (3.16).

Thus, there are three possible critical points. When $\theta = 0$, $F(0) = -1 + e^{g(0)}$ and when $\theta = \pi/2$, $F(\pi/2) = -1 + e^{g(\pi/2)}$. Since $dg/d\theta = g'(\xi) \sin 2\theta$, g is a decreasing function of θ for $\theta \in [0, \pi/2]$, and therefore we always have $F(0) > F(\pi/2)$. Now examine $dF/d\xi$, in equation (3.15). Since $g'(\xi) \leq 0$, $dF/d\xi$ can change sign at most once, and the root of the equation $dF/d\xi = 0$ must occur for $\xi^* \in [0, 1/2]$. Thus, $dF/d\xi$ is either always negative, in which case ξ^* does not exist, or $dF/d\xi$ changes from positive to negative for $\xi \in [0, 1/2]$, and $F(\xi^*)$ will be the maximum value. To summarize, if ξ^* does not exist, the maximum of F occurs when $\theta_c = \xi_c = 0$. If ξ^* , a solution to (3.16), exists, then the maximum of F occurs at ξ^* . To test if ξ^* exists, compute $dF/d\xi$ at $\xi = 0$ and $dF/d\xi$ at $\xi = 1/2$. If these have the same sign then no solution exists. If these have opposite sign then ξ^* exists and can be found by bisection.

3.2.5 Effect of Material Parameters on the Failure Surface

The results of the previous subsection can be used as a guide for choosing material parameters if sufficient experimental data are available. First, suppose $\tau_{nf} = 0.1$ and $f'_c = 1.0 = 10\tau_{nf}$. Figure 3.4a shows a sequence of surfaces based on different values for τ_{sf} as specified on the left side of the plot. The orientation of the normal as defined by θ_c is given on the right side. Only positive values are stated even though negative signs for the values shown are also solutions. When $\tau_{sf} = 3.0$, the outer surface is obtained and $\theta_c = 0$ for all points on the surface, i.e., the normal is in the direction of maximum principal stress. When $\tau_{sf} = 0.3$, the next surface is obtained. For the regime from equal biaxial tension down to uniaxial compression $\theta_c = 0$ so uniaxial compressive splitting is still predicted. However, when both components become compressive, θ_c quickly increases from zero. For the other two cases identified by $\tau_{sf} = 0.2$ and $\tau_{sf} = 0.1$ the normal is still $\theta_c = 0$ when both principal stresses are tensile, but the transition to large values of θ_c is rather abrupt.

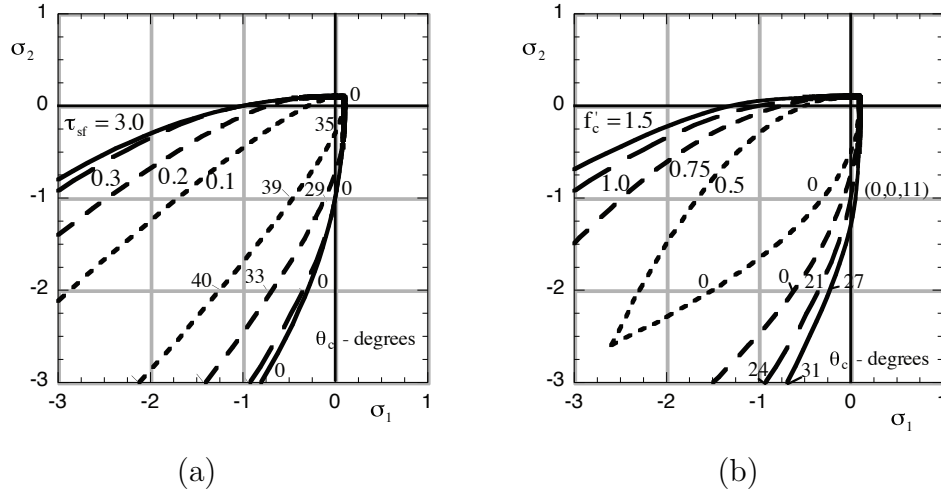


Figure 3.4: Effects of material parameters on shape of decohesion surface for plane stress, (a) effect of τ_{sf} for $\tau_{nf} = 0.1$ and $f'_c = 1.0$; (b) effect of f'_c for $\tau_{nf} = 0.1$ and $\tau_{sf} = 0.3$

The situation is somewhat different when τ_{nf} and τ_{sf} are fixed and f'_c is allowed to change as shown in Fig. 3.4b. For these surfaces, $\tau_{nf} = 0.1$ and $\tau_{sf} = 0.3$. For the two innermost surfaces identified as $f'_c = 0.5$ and $f'_c = 0.75$, the normal is in the direction of maximum principal stress ($\theta_c = 0$). The fact that these surfaces come together for large pressure is considered to be irrelevant because there is no evidence of failure in rock for a stress state in the regime of large equal biaxial compressive stresses. Evidence of such a failure would be a material failure surface with a normal predominately out of the plane. The last two surfaces associated with $f'_c = 1.0$ and $f'_c = 1.5$ in Fig. 3.4b show rather abrupt transitions to nonzero values of θ_c as the value of either principal stress decreases from the tensile regime.

3.2.6 Selection of Values for Material Parameters

The proposed model can be viewed as a generalization of classical models with an important distinction. The proposed formulation includes the in-plane normal stress which provides a prediction of the orientation of the surface of material failure that can vary with the state of stress. Such a variation is in accord with experimental evidence for many geologic materials [Lade, 2001].

As a rough rule of thumb for quasi-brittle materials such as rock, the following relationships hold

$$f'_c = Y/1000 \quad (3.19)$$

$$\tau_{nf} = f'_c/10 \quad (3.20)$$

$$\tau_{sf} = 3.5\tau_{nf} \quad (3.21)$$

where the Young's modulus is denoted by Y . The coefficient 3.5 for the shear failure is relatively large and the large value forces the failure to be mode I. Lower values of this coefficient allows a transition to mixed mode failure and ultimately to purely shear failure. The rock is modeled with properties representative of granite using a Young's modulus of 53.3 GPa, a Poisson's ratio of 0.21 and a density of 2658 kg/m³. The guidelines listed above lead to the decohesive parameters given in Table 3.1.

τ_{nf} (Pa)	τ_{tf} (Pa)	u_0 (m)	s_m	κ	f'_c (Pa)
5.4×10^6	16×10^6	0.01	4	$\ln s_m^2 - \ln(s_m^2 - 1)$	54×10^6

Table 3.1: Parameters that are used in the elastic-decohesive formulation.

After determining the initiation of failure and the orientation of the material surface of failure, the next issue is that of determining the mode of failure and of providing a method for describing the evolution of failure, the topic of the following section.

3.3 Evolution of Failure

3.3.1 Displacement Discontinuity and Softening

The basic assumption inherent with a decohesive approach to modeling failure is that a discontinuity in displacement, $[\mathbf{u}]$, develops simultaneously with a reduction in traction. Decohesion is defined to be the loss of strength that occurs with an increase in a suitable norm of the displacement discontinuity. Such an approach is inherently different from classical fracture mechanics for which a stress singularity exists and the issue of whether or not a crack propagates is associated with a critical stress intensity factor. A decohesive or discrete framework implies that propagation is identified with failure initiation provided by a critical value of a decohesion function.

For the planar problem considered here, it is convenient to express the displacement discontinuity in terms of normal and tangential components

$$[\mathbf{u}] = u_n \mathbf{n} + u_t \mathbf{t}. \quad (3.22)$$

In analogy with some models of plasticity, it is assumed that a single scalar parameter, \bar{u} , called the effective decohesion, can be used to quantify the degree of decohesion that has occurred. The parameter, \bar{u} , is monotonically increasing and obtained as an integral of its time derivative which is defined in terms of the rate of the displacement discontinuity as follows

$$\dot{\bar{u}} = \left([\dot{\mathbf{u}}] \cdot \mathbf{D} \cdot [\dot{\mathbf{u}}] \right)^{1/2}. \quad (3.23)$$

The positive definite, second-order tensor, \mathbf{D} , depends on the material and is defined to yield the correct ratio of fracture energy for modes I (pure opening) and II (pure shear).

Under uniaxial tension, it is assumed that decohesion does not begin until the normal component of traction τ_n attains the critical value τ_{nf} . Then τ_n decreases as u_n increases until a critical value $u_n = u_0$ is reached at which point all traction-carrying capability is lost and two free surfaces are created. It is assumed that a purely shear mode of failure does not exist or, in other words, u_n always increases during failure. Then, for simplicity, \mathbf{D} is chosen so that, (3.23) yields an effective decohesion, \bar{u} , that involves only the normal component scaled by the length scale induced by u_0 , $\bar{u} = u_n/u_0$. In this work, issues of closing when a crack has only partially formed will not be considered so that u_n is, itself, a monotonically increasing parameter.

Again, for simplicity a linear decay is assumed so that $\tau_n = \tau_{\text{nf}} f_n$ in which f_n is a softening function associated with the direction \mathbf{n} as follows:

$$f_n = \langle 1 - \bar{u}_n \rangle. \quad (3.24)$$

The result is that for uniaxial tension, the normal traction is related linearly to the normal component of displacement discontinuity as follows:

$$\tau_n = \tau_{\text{nf}} \langle 1 - \bar{u}_n \rangle. \quad (3.25)$$

For the sake of simplicity, if the internal energy associated with the material failure surface is ignored, then the fracture energy, g_f , is obtained from the relation

$$g_f = \int_0^{u_0} \tau_n du_n = \frac{1}{2} \tau_{\text{nf}} u_0. \quad (3.26)$$

The parameter u_0 can be determined if τ_{nf} and g_f are given as material constants. Schreyer et al. [2002a] provide a more general formulation.

In order to consider any state of stress, not just one of uniaxial tension, the softening function is included in the decohesion function in such a manner that if τ_n is positive, then both components of traction τ_n and τ_t should approach zero as f_n goes to zero. Such a property is obtained if the decohesion function of (3.6) is changed to the following:

$$F = \max_{\forall \mathbf{n}} F_n \quad F_n = \frac{\tau_t^2}{(s_m \tau_{\text{sf}})^2} + \exp \left(\kappa \left(\frac{\tau_n}{\tau_{\text{nf}}} + f_n \left(\frac{\langle -\sigma_{tt} \rangle^2}{(f'_c)^2} - 1 \right) \right) \right) - 1. \quad (3.27)$$

In essence, we redefine B_n in (3.8) to be

$$B_n = \frac{\tau_n}{\tau_{\text{nf}}} + f_n \left(\frac{\langle -\sigma_{tt} \rangle^2}{(f'_c)^2} - 1 \right). \quad (3.28)$$

The effect of f_n on the decohesion surface, $F = 0$, in the $\tau_n - \tau_t$ space is shown in Fig. 3.5 for $(\sigma_{tt}/f'_c)^2 = 0.5$. In particular, when failure is complete, then $f_n = 0$, and shear can still be sustained when τ_n is negative.

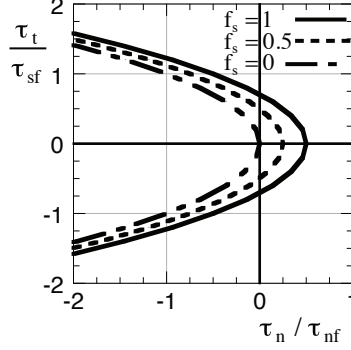


Figure 3.5: Effect of the value of the softening function on the decohesion surface in the $\tau_n - \tau_t$ space for $\sigma_{tt}^2/f'_c = 0.5$.

3.3.2 Evolution Equations

The mode of failure, \mathbf{m} , is defined to be the direction of the discontinuity in displacement:

$$\mathbf{m} = [\mathbf{u}]/|[\mathbf{u}]|. \quad (3.29)$$

An associated evolution equation is proposed with ω defined to be a monotonically increasing parameter that is a measure of the amount of decohesion. With a scale factor $u_0\tau_{nf}$ chosen to render ω dimensionless, an associated rule is

$$\dot{u}_n = \dot{\omega}u_0\tau_{nf}\frac{\partial F_n}{\partial \tau_n} \quad \dot{u}_t = \dot{\omega}u_0\tau_{nf}\frac{\partial F_n}{\partial \tau_t} \quad (3.30)$$

in which superposed dots denote derivatives with respect to time. Because the time derivative appears linearly on both the left and right sides of each equation, any variable that increases monotonically with time can also be used as a time variable. Expressed another way, the formulation is rate independent. The derivatives of F with respect to its stress arguments are easily computed from (3.27)

$$\frac{\partial F}{\partial \tau_n} = \frac{\kappa}{\tau_{nf}}e^{\kappa B_n} \quad \frac{\partial F}{\partial \tau_t} = \frac{2\tau_t}{(s_m\tau_{sf})^2}, \quad (3.31)$$

and then (3.30) becomes

$$\dot{u}_n = \dot{\omega}\kappa e^{\kappa B_n} \quad \dot{u}_t = \dot{\omega}\frac{2\tau_t}{s_m\tau_{sf}}\frac{\tau_{nf}}{s_m\tau_{sf}}, \quad (3.32)$$

where we have introduced the dimensionless normal and tangential opening rate,

$$\dot{\bar{u}}_n = \dot{u}_n/u_0 \quad \dot{\bar{u}}_t = \dot{u}_t/u_0. \quad (3.33)$$

An important attribute of the formulation is that the normal component of displacement discontinuity continues to increase for all states of stress satisfying the decohesion condition, in particular for uniaxial compression in which case the normal component of traction, τ_n , is zero. This is considered to be a desirable and unique feature of the model and is a consequence of incorporating τ_n linearly in the expression for the decohesion function given by (3.27).

In addition to (3.32), one other equation is necessary for determining $\dot{\omega}$. The equation necessary for closure is that of consistency which states that the decohesion condition $F_n = 0$ must continue to be satisfied or, expressed in rate form,

$$\dot{F}_n = 0. \quad (3.34)$$

At this time, it is noted that if the normal to the failure surface is in the direction of maximum principal stress, then $\tau_t = 0$ and (3.32) implies that the mode of deformation is in the direction of the normal, a situation that is typical for brittle failure. This is the reason why the decohesion function of (3.7) is characterized as a brittle one. Once a complete crack, as reflected by $f_n = 0$, has been established the evolution equations of (3.32) can no longer be applied. Instead, alternative equations must be invoked. Nonzero traction is physically unacceptable if the free surfaces of a crack have separated so the appropriate condition then is to adjust the decohesion strains so that $\tau_n = 0$ and $\tau_t = 0$. If the crack is forced closed, the value of the modified decohesion function

$$F_n^* \equiv F_n|_{f_n=0} = \frac{\tau_t^2}{(s_m \tau_{sf})^2} + \exp\left(\kappa\left(\frac{\tau_n}{\tau_{nf}}\right)\right) - 1 \quad (3.35)$$

must be checked. If $F_n^* \leq 0$, no further action is required. However, if $F_n^* > 0$ then the shear decohesion strain should be increased or decreased in order to adjust the magnitude of τ_t and force F_n^* back to zero.

3.4 Elastic-Decohesion Model

3.4.1 Combined Elasticity and Decohesion

Any continuum constitutive equation that is considered appropriate prior to failure can be used to describe the rock. For the sake of simplicity it is assumed that linear, isotropic elasticity is adequate. For plane stress in the $x_1 - x_2$ plane, the relations between stress and strain rate in component form are

$$\begin{aligned} \dot{\sigma}_{11} &= E_1 \dot{\epsilon}_{11} + E_2 \dot{\epsilon}_{22} + E_2 \dot{\epsilon}_{33} \\ \dot{\sigma}_{22} &= E_2 \dot{\epsilon}_{11} + E_1 \dot{\epsilon}_{22} + E_2 \dot{\epsilon}_{33} \\ \dot{\sigma}_{12} &= 2G \dot{\epsilon}_{12} \end{aligned} \quad (3.36)$$

in which the elasticity parameters are

$$E_1 = Y \frac{1}{1 - \nu^2} \quad E_2 = Y \frac{\nu}{1 - \nu^2} \quad 2G = Y \frac{1}{1 + \nu}, \quad (3.37)$$

and Y denotes Young's modulus, ν the Poisson's ratio and G the shear modulus. For plane strain, the relations are

$$\begin{aligned} \dot{\sigma}_{11} &= E_1 \dot{\epsilon}_{11} + E_2 \dot{\epsilon}_{22} \\ \dot{\sigma}_{22} &= E_2 \dot{\epsilon}_{11} + E_1 \dot{\epsilon}_{22} \\ \dot{\sigma}_{33} &= E_2 \dot{\epsilon}_{11} + E_2 \dot{\epsilon}_{22} \\ \dot{\sigma}_{12} &= 2G \dot{\epsilon}_{12} \end{aligned} \quad (3.38)$$

in which the elasticity parameters are

$$E_1 = Y \frac{1 - \nu}{(1 + \nu)(1 - 2\nu)} \quad E_2 = Y \frac{\nu}{(1 + \nu)(1 - 2\nu)} \quad 2G = Y \frac{1}{1 + \nu}. \quad (3.39)$$

For a material point at which failure is occurring, the object is to solve (3.36) or (3.38) subject to the constraint that the consistency condition and the evolution equations of (3.32) are satisfied. This combination of equations is what is meant by the phrase elastic-decohesive constitutive equations.

3.4.2 Numerical Treatment of Elastic Decohesion Equations

Although the constitutive equations have been given, there remains the question of how these equations are combined and implemented with an algorithm for solving the equations of motion and of deformation. Discontinuities in displacement represent a relatively new area of analysis and a general consensus on the most appropriate method has not been achieved.

Even for the finite element method, which is widely used in the engineering community, there are several methods for kinematically representing jumps in displacement. In what is called the extended finite element method, one approach is to use enhanced basis functions so that the discontinuity across element boundaries is modeled explicitly of which representative examples are given by Moes et al. [1999]; Wells and Sluys [2001a,b,c]; Alfaiate et al. [2003]. An alternative procedure is to introduce a localized band within an element [Larsson and Runesson, 1996]. A more elementary method is to assume that a crack displacement field is constant over an element and to smear the effect over the element [Rashid, 1968] an approach that is almost as old as finite element method itself. The smeared crack approach has been subject to considerable criticism but it is believed that some of the noted shortcomings should actually be attributed to limitations of the constitutive equations and not the method itself. Because the smeared crack method has many positive attributes, not least of which is its simplicity, the procedure described next is based on the method. For the limited range of applications considered here, the method is considered to be adequate.

Consider an active crack with current components of discontinuity u_n and u_t , assumed to be constant across a square element of side h as indicated in Fig. 3.6. For a crack with a

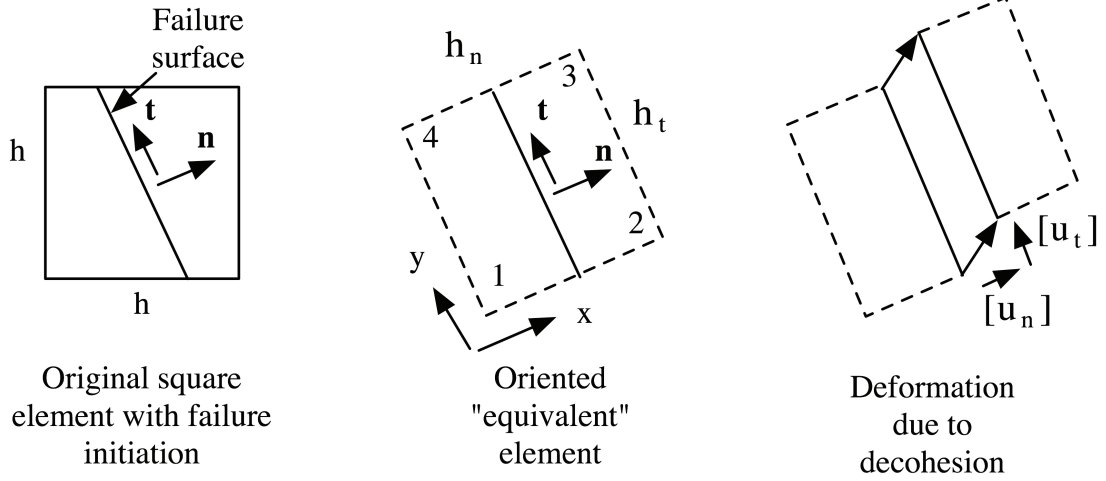


Figure 3.6: Relationship between original square element and equivalent element used to define decohesive strains.

normal \mathbf{n} oriented at an angle to the x_1 -axis, the length of the crack is denoted by h_t where

$$\begin{aligned} h_t &= \frac{h}{\cos \theta} & -\frac{\pi}{4} \leq \theta \leq \frac{\pi}{4}, \\ h_t &= \frac{h}{\sin \theta} & \frac{\pi}{4} \leq \theta \leq \frac{3\pi}{4}. \end{aligned} \quad (3.40)$$

A general expression for the rate of decohesive strain tensor within a representative strip of material of width L^d containing the crack is

$$\dot{\mathbf{e}}^d = \frac{1}{L^d} ([\dot{\mathbf{u}}] \otimes \mathbf{n})_{\text{sym}} \quad \dot{\mathbf{e}}_{ij}^d = \frac{1}{L^d} (\dot{u}_i n_j + \dot{u}_j n_i) \quad (3.41)$$

The expression on the left is in direct notation and involves the tensor product, \otimes , which is defined such that the corresponding expression in indicial notation is shown on the right. For an element, the parameter, L^d , is determined by equating the rate of dissipation considering the effect of the discontinuity as smeared over the element to the rate of dissipation performed by the traction acting on the surface discontinuity. If Ω denotes the area of the element, dA a differential of area, and dr a differential of crack length, equating dissipation rates yields

$$\int_{\Omega} \boldsymbol{\sigma} : \frac{1}{L^d} ([\dot{\mathbf{u}}] \otimes \mathbf{n})_{\text{sym}} dA = \int_{h_t} \boldsymbol{\tau} \cdot [\mathbf{u}] dr. \quad (3.42)$$

Now, assume the discontinuity is constant along the crack within an element, and the decohesive crack strain and stress are constant over an element. The result is

$$L^d \equiv h_n = \frac{h^2}{h_t}, \quad (3.43)$$

and (3.41) yields specific expressions for components of decohesive strain in the $\mathbf{n-t}$ basis as follows:

$$e_{nn}^d = \frac{u_n}{h_n} \quad e_{nt}^d = \frac{u_t}{2h_n} \quad e_{tt}^d = 0. \quad (3.44)$$

An alternative way of viewing the development is to visualize a rotated rectangular element (dotted lines in Fig. 3.6) with sides of length h_n and h_t and an area equal to the original element. For this dotted element with the deformation due only to a uniform discontinuity in displacement, the displacement components at the nodes for the local coordinate system are

$$\begin{aligned} u_x^1 &= 0 & u_x^2 &= u_n & u_x^3 &= u_n & u_x^4 &= 0 \\ u_y^1 &= 0 & u_y^2 &= u_t & u_y^3 &= u_t & u_y^4 &= 0 \end{aligned} \quad (3.45)$$

in which superscripts denote the node number and the subscript indicates the component. The basis functions for a 4-noded, rectangular element are

$$\begin{aligned} N_1 &= (1 - x/h_n)(1 - y/h_t) & N_2 &= (x/h_n)(1 - y/h_t) \\ N_3 &= (x/h_n)(y/h_t) & N_4 &= (1 - x/h_n)(y/h_t). \end{aligned} \quad (3.46)$$

If the displacement field is smeared over the element in the conventional continuous form, then

$$\begin{aligned} u_x &= u_x^1 N_1 + u_x^2 N_2 + u_x^3 N_3 + u_x^4 N_4 \\ u_y &= u_y^1 N_1 + u_y^2 N_2 + u_y^3 N_3 + u_y^4 N_4. \end{aligned} \quad (3.47)$$

The linear strain-displacement relations are

$$e_{xx} = \frac{\partial u_x}{\partial x}, \quad e_{yy} = \frac{\partial u_y}{\partial y}, \quad e_{xy} = \frac{1}{2} \left(\frac{\partial u_x}{\partial y} + \frac{\partial u_y}{\partial x} \right). \quad (3.48)$$

If x and y are associated with the unit vectors \mathbf{n} and \mathbf{t} , respectively, and the strain components are evaluated at the center of the element after (3.45), (3.46) and (3.47) are substituted in (3.48), the result is identical to the components of the decohesive strain tensor given in (3.44).

If there is no decohesion, the stress rates will simply be those given by (3.36) or (3.38). If there is decohesion, the stress rate must be relaxed in a manner such that traction continuity is maintained across the crack within the element. The result is an effective stress rate defined as follows for plane stress

$$\begin{aligned} \dot{\sigma}_{11} &= E_1(\dot{e}_{11} - \dot{e}_{11}^d) + E_2(\dot{e}_{22} - \dot{e}_{22}^d) + E_2(\dot{e}_{33} - \dot{e}_{33}^d) \\ \dot{\sigma}_{22} &= E_2(\dot{e}_{11} - \dot{e}_{11}^d) + E_1(\dot{e}_{22} - \dot{e}_{22}^d) + E_2(\dot{e}_{33} - \dot{e}_{33}^d) \\ \dot{\sigma}_{12} &= 2G(\dot{e}_{12} - \dot{e}_{12}^d) \end{aligned} \quad (3.49)$$

or plane strain

$$\begin{aligned} \dot{\sigma}_{11} &= E_1(\dot{e}_{11} - \dot{e}_{11}^d) + E_2(\dot{e}_{22} - \dot{e}_{22}^d) \\ \dot{\sigma}_{22} &= E_2(\dot{e}_{11} - \dot{e}_{11}^d) + E_1(\dot{e}_{22} - \dot{e}_{22}^d) \\ \dot{\sigma}_{33} &= E_2(\dot{e}_{11} - \dot{e}_{11}^d) + E_2(\dot{e}_{22} - \dot{e}_{22}^d) \\ \dot{\sigma}_{12} &= 2G(\dot{e}_{12} - \dot{e}_{12}^d) \end{aligned} \quad (3.50)$$

in which the components of decohesive strain are obtained through the transformation relations from the component forms given in (3.44). Given the strain rates, \dot{e}_{11} , \dot{e}_{22} , \dot{e}_{33} , and \dot{e}_{12} , it is the role of a constitutive equation subroutine to provide the stress rates, and the decohesive rates \dot{u}_n , \dot{u}_t and $\dot{\omega}$ such that (3.32) and (3.49) or (3.50) are satisfied simultaneously. The procedure is completely analogous to that used with computational plasticity.

With computational algorithms, time steps and, hence, strain increments are finite and it is generally not feasible to maintain consistency for all time. Instead it is customary to assume that a step in prescribed strain is elastic and obtain a trial stress. The decohesion function is evaluated with the new values of stress (traction). If the value of the decohesion function is negative or zero, the step was truly elastic and no further modifications are necessary. If, on the other hand, $F_n > 0$ then it is assumed to be satisfactory if displacement discontinuity and decohesive strains are increased according to the evolution equations until the value of the decohesion function is forced to zero only at the end of the step. One method for zero finding is the Newton-Raphson procedure which states that increments in the decohesion parameter are given by

$$\Delta\omega = -\frac{F_n}{\partial F_n/\partial\omega}. \quad (3.51)$$

It has been assumed that ω is a monotonically increasing parameter, and since F_n is being forced to zero from above, it follows that $\partial F_n/\partial\omega$ must be negative, a condition called a stability criterion. To evaluate $\partial F_n/\partial\omega$, the equation

$$\dot{F}_n = \dot{\omega}\partial F_n/\partial\omega \quad (3.52)$$

is used. First, note that as a consequence of isotropy, the elastic constitutive equations in the **n-t** system are of the same form as (3.49) or (3.50), or

$$\begin{aligned} \dot{\tau}_n &= E_1(\dot{e}_{nn} - \dot{e}_{nn}^d) + E_2(\dot{e}_{tt} - \dot{e}_{tt}^d) + E_2\dot{e}_{33} \\ \dot{\sigma}_{tt} &= E_2(\dot{e}_{nn} - \dot{e}_{nn}^d) + E_1(\dot{e}_{tt} - \dot{e}_{tt}^d) + E_2\dot{e}_{33} \\ \dot{\tau}_t &= 2G(\dot{e}_{nt} - \dot{e}_{nt}^d) \end{aligned} \quad (3.53)$$

or plane strain

$$\begin{aligned} \dot{\tau}_n &= E_1(\dot{e}_{nn} - \dot{e}_{nn}^d) + E_2(\dot{e}_{tt} - \dot{e}_{tt}^d) \\ \dot{\sigma}_{tt} &= E_1(\dot{e}_{tt} - \dot{e}_{tt}^d) + E_2(\dot{e}_{nn} - \dot{e}_{nn}^d) \\ \dot{\sigma}_{33} &= E_2(\dot{e}_{nn} - \dot{e}_{nn}^d) + E_2(\dot{e}_{tt} - \dot{e}_{tt}^d) \\ \dot{\tau}_{12} &= 2G(\dot{e}_{nt} - \dot{e}_{nt}^d) \end{aligned} \quad (3.54)$$

For this part of the algorithm, it is assumed that the total strains are fixed with the result that \dot{e}_{nn} , \dot{e}_{tt} , \dot{e}_{33} and \dot{e}_{nt} are zero. Furthermore, e_{nt}^d is identically zero so (3.49) or (3.50) reduces to

$$\dot{\tau}_n = -E_1\dot{e}_{nn}^d \quad \dot{\sigma}_{tt} = -E_2\dot{e}_{nn}^d \quad \dot{\tau}_t = -2G\dot{e}_{nt}^d \quad (3.55)$$

or

$$\dot{\tau}_n = -E_1\dot{e}_{nn}^d \quad \dot{\sigma}_{tt} = -E_2\dot{e}_{nn}^d \quad \dot{\sigma}_{33} = -E_2\dot{e}_{nn}^d \quad \dot{\tau}_{12} = -2G\dot{e}_{nt}^d \quad (3.56)$$

respectively.

The evolution equations of (3.32) and the decohesive strain relations of (3.44) yield

$$\dot{\epsilon}_{nn}^d = \frac{\dot{u}_n}{h_n} = \dot{\omega} \frac{u_0}{h_n} \kappa e^{\kappa B_n} \quad \dot{\epsilon}_{nt}^d = \frac{\dot{u}_t}{2h_n} = \dot{\omega} \frac{u_0}{h_n} \frac{\tau_t}{s_m \tau_{sf}} \frac{\tau_{nf}}{s_m \tau_{sf}}. \quad (3.57)$$

The use of (3.24) yields $\dot{f}_n = -\langle \dot{u}_n \rangle$. It follows from (3.27), (3.53) or (3.54) with (3.57) that

$$\frac{\partial F_n}{\partial \omega} = -A \quad (3.58)$$

with

$$A = \frac{u_0}{h_n} \left(\frac{4G}{s_m \tau_{sf}} \frac{\tau_t^2}{(s_m \tau_{sf})^2} \frac{\tau_{nf}}{s_m \tau_{sf}} + \kappa^2 e^{2\kappa B_n} \left(\frac{E_1}{\tau_{nf}} - 2f_n \frac{\langle -\sigma_{tt} \rangle}{f'_c} \frac{E_2}{f'_c} + \frac{h_n}{u_0} H(1 - \bar{u}_n) \left(\frac{\langle -\sigma_{tt} \rangle^2}{f_c'^2} - 1 \right) \right) \right) \quad (3.59)$$

The stability criterion is $A > 0$.

To consider the implications of the stability criterion, first consider uniaxial tension so that $\tau_t = 0$ and $\sigma_{tt} = 0$. During decohesion, stability is satisfied provided

$$\frac{u_0}{h_n} \frac{E_1}{\tau_{nf}} > 1, \quad (3.60)$$

with the implication that the element size h_n must be less than a critical value. For the case of $\tau_t = 0$ and $\sigma_{tt} < 0$, A is a minimum during decohesion if

$$\sigma_{tt} = -f_n \frac{u_0}{h_n} \frac{E_1}{\tau_{nf}} \frac{E_2}{E_1} \tau_{nf} \quad (3.61)$$

and

$$A_{\min} = \kappa^2 e^{2\kappa B_n} \left(\frac{u_0}{h_n} \frac{E_1}{\tau_{nf}} - 1 - f_n^2 \left(\frac{u_0}{h_n} \frac{E_1}{\tau_{nf}} \right)^2 \left(\frac{\tau_{nf}}{f'_c} \right)^2 \left(\frac{E_2}{E_1} \right)^2 \right). \quad (3.62)$$

The last term does have an adverse effect on stability but since $E_2/E_1 < 1$ and, typically, $\tau_{nf}/f'_c \approx 0.1$ the effect on the critical value for h_n will be small. Because the first term in (3.59) is non-negative, the addition of shear can only increase the critical value for h_n .

3.5 2D Simulations of a Tunnel in a Blast

The elastic-decohesive model has been implemented in the material-point method (MPM) [Sulsky et al., 1995; Sulsky and Schreyer, 2004]. In order to scope out the effect of an elastic-decohesive model on the propagation of a blast wave through rock, the rock is first modeled as elastic and then, in subsequent simulations, the rock is allowed to fracture using the elastic-decohesive formulation. Figure 3.7 shows the computational domain for the first simulation. The computation is done in two space dimensions, assuming plane strain. The computational domain is 105m by 100m with x and y coordinates between $-50 < x < 55$

and $-50 < y < 50$. A circular region centered at the origin, with a radius of 3m, is non-deformable. This region (colored red in the figure) represents the blast zone and is used to numerically impose a prescribed traction boundary condition on the surrounding region to model the effect of the blast wave. Exterior to this circular region, we model the rock material through which the blast propagates, using the material properties given in Section 3.2.6. As noted, these parameters are representative of granite.

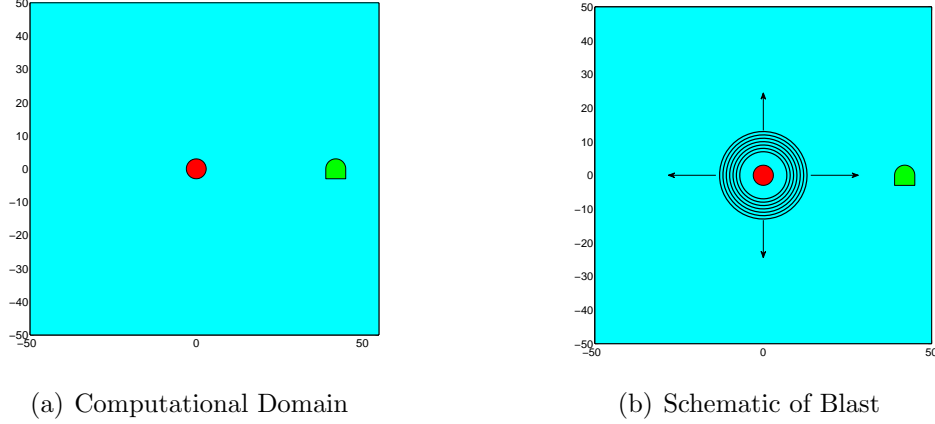


Figure 3.7: (a) The computational domain is 105m by 100m with x and y coordinates between $-50 < x < 55$ and $-50 < y < 50$. The region representing the blast zone is shown in red, the rock is colored cyan and the tunnel is shown in green. The center of the blast is 39m from the left wall of the tunnel. (b) A schematic plot of wave propagation. A compressive wave is generated from the blast source and propagates radially.

The green region shown in Figure 3.7 indicates the presence of a tunnel in the rock. The tunnel is rectangular along three sides, capped with a circular arc. The rectangular part is 6m wide ($39 < x < 45$) and 3m high ($-3 < y < 0$). The circular arc is part of a circle centered at (42, 0) with radius 3m. The distance between the center of the blast source and the left tunnel wall is 39m. Zero displacement is imposed on the computational domain boundaries. However, the computational domain is large enough so that for the duration of the simulations, the pressure wave that emanates from the blast zone barely impinges on the domain boundary.

The radially symmetric, compressive pulse modeling the blast is taken to be $\sigma(t) = \sigma_0(1 - \cos(2t/t_d))H(t_d - t)$ as a function of time, for $t > 0$, where $H(t)$ is the Heaviside function. We use a magnitude $\sigma_0 = -380\text{MPa}$ and a duration $t_d = 1.3$ msec for the pulse. This pulse is the boundary condition imposed on the radial component of stress at the boundary of the non-deformable region at a radius $r = 3$. Note that stress is negative in compression and positive in tension. The simulations are performed using the material-point method with a square mesh, 0.25m on a side. Thus, the domain has 420×400 elements, with 4 material points per element initially. Simulations are run for times between zero and 13 msec with a time step of 0.05 msec. For reference, Figure 3.8 shows stress as a function of time at the point (38.8125, 0.0625) if there is no tunnel. We see that a compressive pulse initiated in a cylindrical cavity propagates outward and reaches the point at time

7.5msec, after traveling a distance 35.8m with speed 4751m/s. In this cylindrical geometry, a tensile tail develops behind the initial compressive pulse. At this point in the domain, the maximum amplitude of the tensile tail is roughly the same as the maximum amplitude of the compressive pulse.

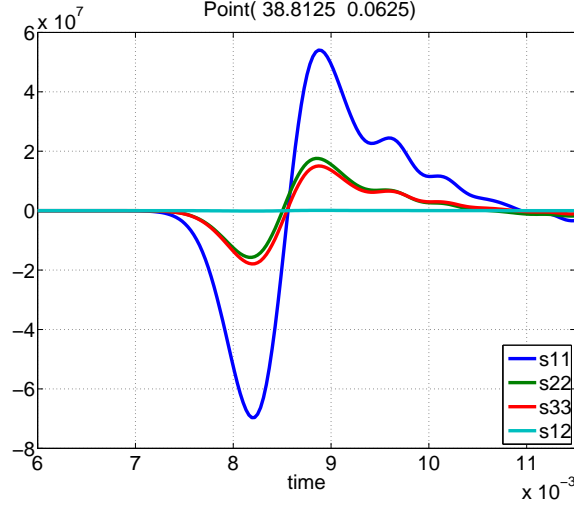


Figure 3.8: Stress as a function of time at the point (38.8125,0.0625). The plot shows free propagation of a wave from a cylindrical source that applies a pulse with $\sigma_0 = -3.8 \times 10^8$ Pa to a domain made up of rock modeled as elastic, and with no tunnel in the rock.

Figure 3.9 shows results at 11 msec from the simulation of waves interacting with a tunnel using an elastic constitutive model for the rock. We show contours of the magnitude of the maximum principal stress over the whole domain in (a). The plot shows a radially expanding wave from the centrally located blast zone that impinges on the tunnel, causing reflected waves. Note the loss of symmetry after reflection due to the asymmetric tunnel geometry. The maximum and minimum principle stress over an area near the tunnel is shown in Figure 3.9b and Figure 3.9c. Blue areas are regions where the stress is in tension while the red indicates compression. The original compressive pulse is followed by a tensile tail that develops behind that pulse. The compressive pulse reflects from the free surface of the tunnel wall as a tensile wave. One would expect fracture to occur in regions of large tensile stress, although axial splitting is a possibility if the compressive stress is large enough. In order to explore the likelihood of failure, a test point located at the coordinates (38.8125,0.0625), right in front of the tunnel, is examined. This point is shown as the red asterisk in Figure 3.10a. Figures 3.10b,c show the values of stress components vs. time at this point. Notice that the reflected tensile wave has a magnitude that exceeds τ_{nf} so that we expect fracture if decohesion is activated.

The effect of allowing the rock to fracture is evident in Figure 3.11 where we again show contours of the magnitude of maximum principal stress at 11 msec, but with the rock modeled using the elastic-decohesive model. Figure 3.11a shows internal wave reflections that occur from waves interacting with partially fractured rock. The microcracking occurs due

to the tensile tail that develops behind the main compressive pulse in cylindrical geometry. Fully opened cracks form near the blast zone and near the tunnel. Figure 3.11d shows the magnitude of the effective jump in displacement, \bar{u}_n , representing cracks that are produced as part of the decohesive model. The jump in displacement is normalized by the decohesion length scale, u_0 . Only normalized values greater than one indicate the complete formation of cracks. Complete cracks occur predominantly near the tunnel, with some smaller cracks around the blast zone (not shown). When the initially compressive blast wave hits the tunnel wall, it reflects off the free surface as a tensile wave causing fractures to occur on the top and near the lower left corner of the tunnel, as shown in Figure 3.11d.

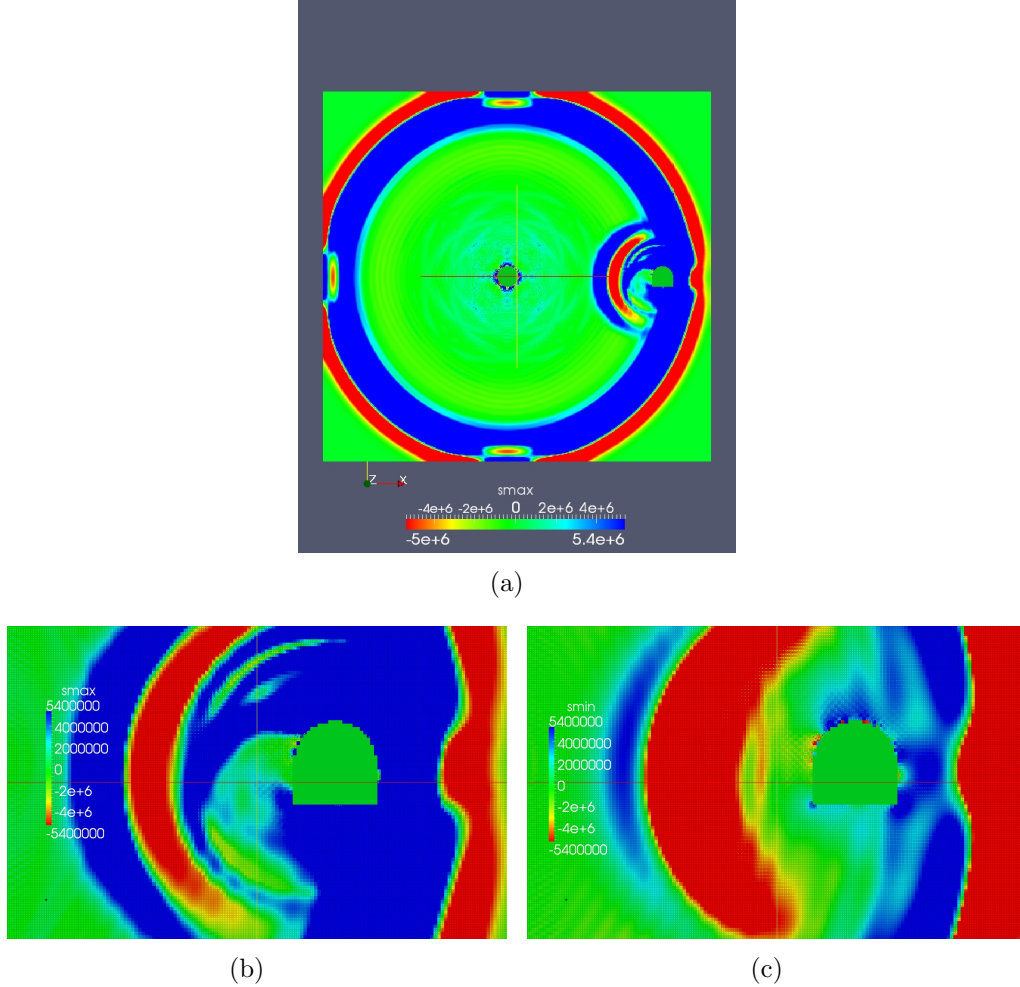


Figure 3.9: Contours of (a) maximum principle stress σ_{\max} , (b) maximum principle stress σ_{\max} around the tunnel and (c) minimum principle stress σ_{\min} around the tunnel at $t = 11$ msec. The rock is modeled as elastic.

Figure 3.12 shows the crack distribution and orientation around the tunnel. The tunnel profile is outlined in green. The decohesion model can allow multiple cracks to occur at a point so that crack branching can be studied. In this simulation, three cracks are allowed, colored in this figure with black, blue and red line segments, respectively. The orientation of

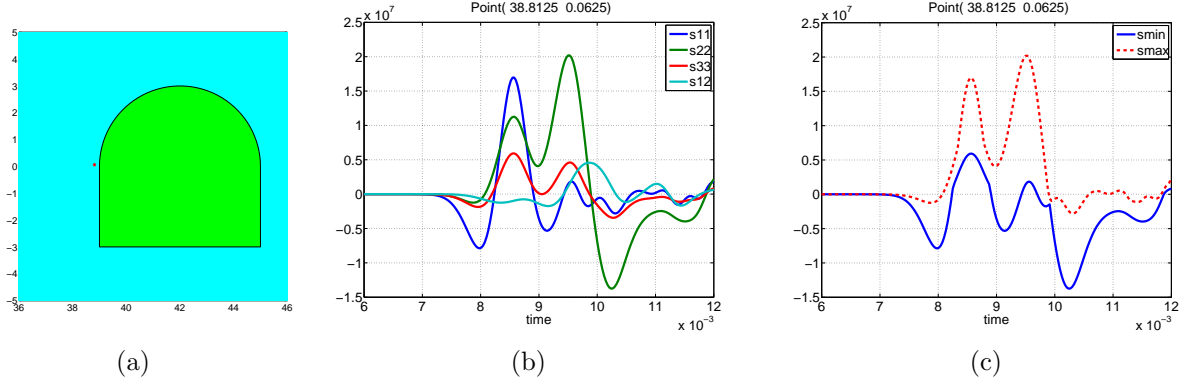
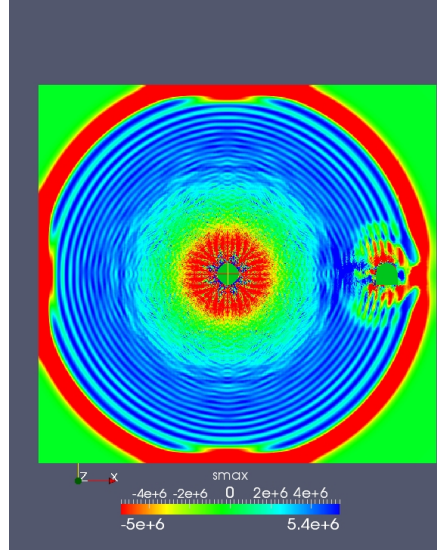


Figure 3.10: (a) Location of an observation point (38.8125,0.0625) and values of stress components vs. time in (b) the $x - y$ coordinates and in (c) the principle coordinates, at that point, using the elastic model.

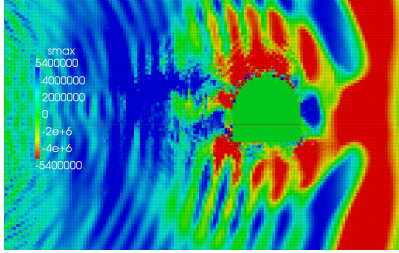
the line segments is tangent to the crack surface. Figure 3.12 shows the distribution of cracks with normal opening u_n (a) greater than $0.005u_0$, (b) greater than $0.1u_0$ and (c) greater than u_0 . There are many micro cracks shown in Figure 3.12a. The rock is most likely to fail in a region in front of the tunnel and in a region near the tunnel top and near the lower left corner. Not surprisingly, when the initially compressive blast wave hits the tunnel wall, it reflects from the free surface as a tensile wave which causes a peak in the maximum principle stress to the left of the tunnel. Although, some cracks appear on the right side of the tunnel as well - the side away from the blast. An unexpected result occurs when the compressive wave passes around the tunnel top and bottom, the rock is under large compression and axial splitting occurs.

To examine the failure in more detail, compare the stress components as a function of time, at the observation point (38.8125,0.0625) to the left of the tunnel using the elastic-decohesive model, Figure 3.13, with the stress as a function of time for an elastic model, with the tunnel, Figure 3.10, and without the tunnel, Figure 3.8. In the elastic case, the reflected tensile wave is reinforced by the tensile tail. A local maximum in tension is first reached at time about 8.5 msec in the σ_{xx} (s11) component. According to the decohesive parameter τ_{nf} which controls failure in tension, decohesion will initiate. Figure 3.12a shows that cracks are indeed present around the location of the observation point. The parameter τ_{nf} controls the maximum value in tension, and this is consistent with the figures 3.13a,b in which the maximum tension does not exceed the value of $\tau_{nf} = 5.4 \times 10^6$ Pa.

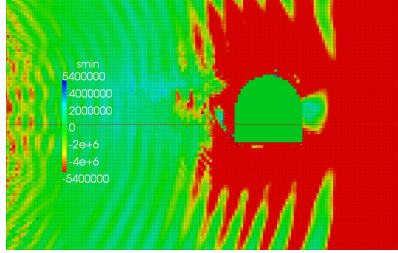
Another observation point is chosen at the top of the tunnel, (41.9375,3.0625), shown as a red asterisk in Figure 3.14a, to study the presence of the horizontal cracks at this location. We first examine the elastic response. Without the tunnel, the freely propagating elastic wave is almost identical to what is seen at the first observation point, Figure 3.8, because the radial distance from the blast is similar. However, the interaction of the elastic waves at the top of the tunnel is quite different than what is seen with the almost normal incidence of the waves at the side of the tunnel; compare Figure 3.10 and Figure 3.14. At the top of the tunnel the incident compressive pulse is enhanced and the tensile tail is reduced. The peak



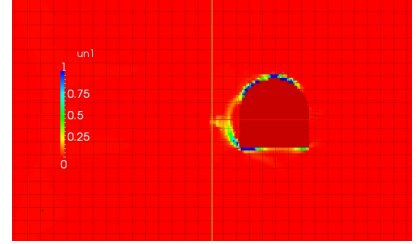
(a)



(b)

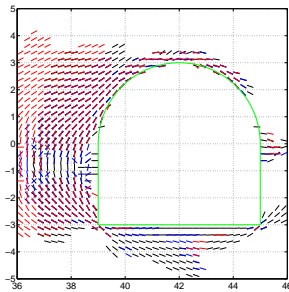


(c)

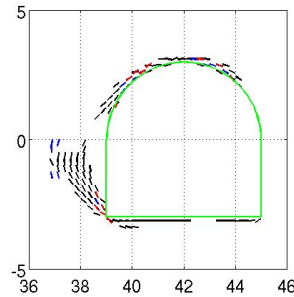


(d)

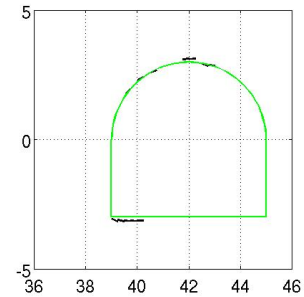
Figure 3.11: Contours of (a) maximum principle stress σ_{\max} , (b) maximum principle stress σ_{\max} around the tunnel, (c) minimum principle stress σ_{\min} around the tunnel and (d) width of cracks around the tunnel at $t = 11$ msec. The rock is modeled as elastic-decohesive.



(a)



(b)



(c)

Figure 3.12: Distribution and orientation of cracks with normal opening u_n (a) greater than $0.005u_0$ (b) greater than $0.1u_0$ and (c) greater than u_0 at $t = 11$ msec.

compressive stress reaches a value of approximately -10^8 Pa which exceeds the assumed

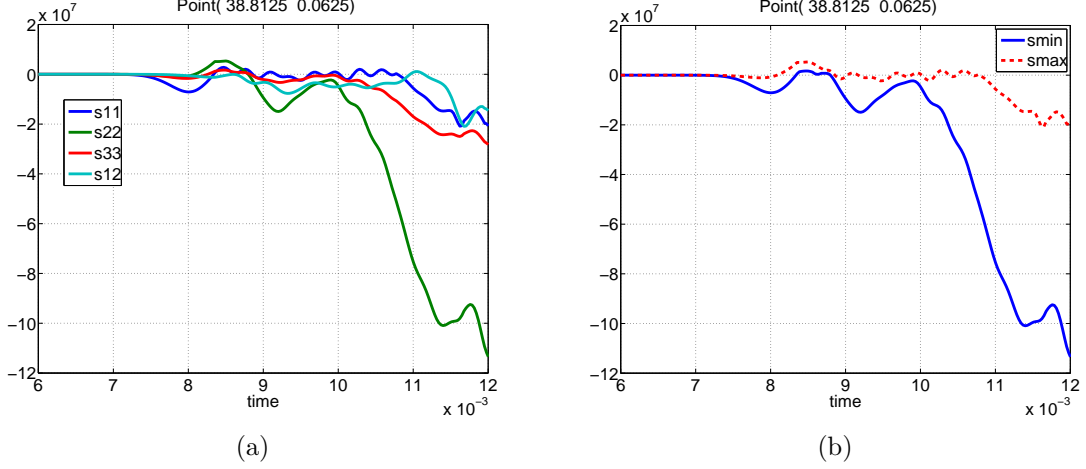


Figure 3.13: Values of stress components vs. time at (38.8125, 0.0625) in (a) the $x - y$ coordinates and in (b) the principle coordinates using the elastic-decohesive model.

compressive strength $f'_c = 5.4 \times 10^7$ Pa. Thus, we expect axial splitting at the top of the tunnel, leading to horizontal cracks.

The stress components observed at the point (41.9375, 3.0625) as a function of time when the elastic-decohesive model is used, are shown in Figure 3.15. The black vertical line indicates the time when the rock starts to fracture. The stress xx -component of stress (s11) is large in compression during the time period [8.5, 9.5] msec. Axial splitting occurs when the σ_{xx} (s11) = σ_{\min} reaches -6×10^8 Pa which is close to the value of $f'_c = 5.4 \times 10^7$ Pa. A complete crack (i.e. $\bar{u}_n > 1$) forms around time 10.5 msec. Axial splitting does not reduce the magnitude of the compressive stress.

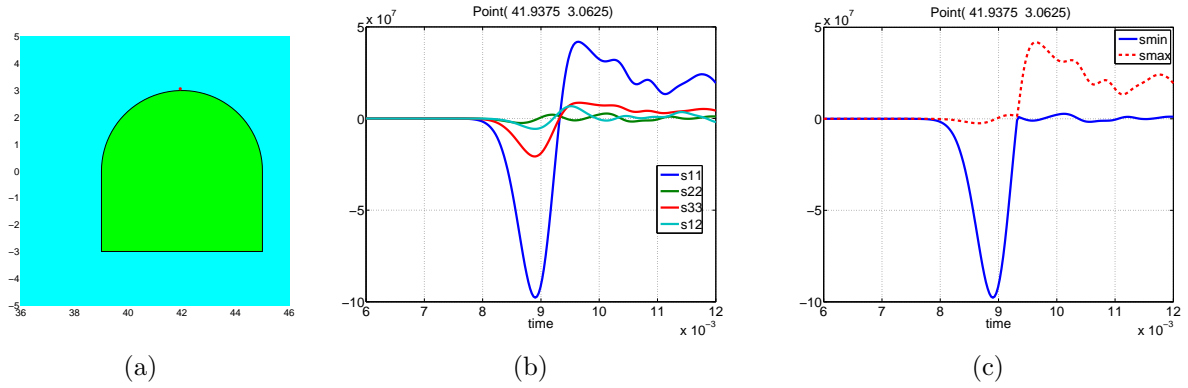


Figure 3.14: (a) Location of the observation point (41.9375, 3.0625), and values of stress components vs. time in (b) the $x - y$ coordinates and in (c) the principle coordinates, at that point, using the elastic model.

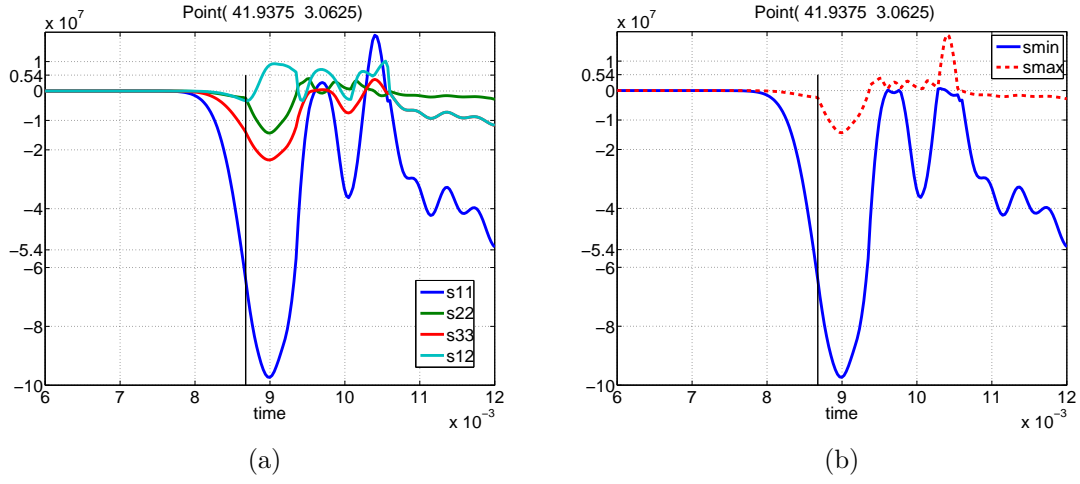


Figure 3.15: Evolution of stress components in (a) $x-y$ coordinates and in (b) principle stress components at the location (41.9375, 3.0625). The rock is modeled as elastic-decohesive. The vertical black line indicates when cracks begin to form.

3.5.1 Parameter Study

In this section, we examine the results when we vary the size of the blast, the distance between the blast and the tunnel and the blast location relative to the tunnel. First, we reduce the magnitude of the blast by reducing σ_0 by 50% to a value of $\sigma_0 = -1.9 \times 10^8 \text{ Pa}$. Figure 3.16 shows contours of maximum principle stress and Figure 3.17 shows the distribution and orientation of cracks using two values for the blast magnitude. As one would expect, the larger the blast, the more fracturing occurs in the rock. One common feature is that the rock first opens in an area in front of the tunnel wall and along a band forming a curved region emanating the lower left corner. This region is where the local peak in tension occurs. The presence of a geometric corner tends to enhance the failure in rock.

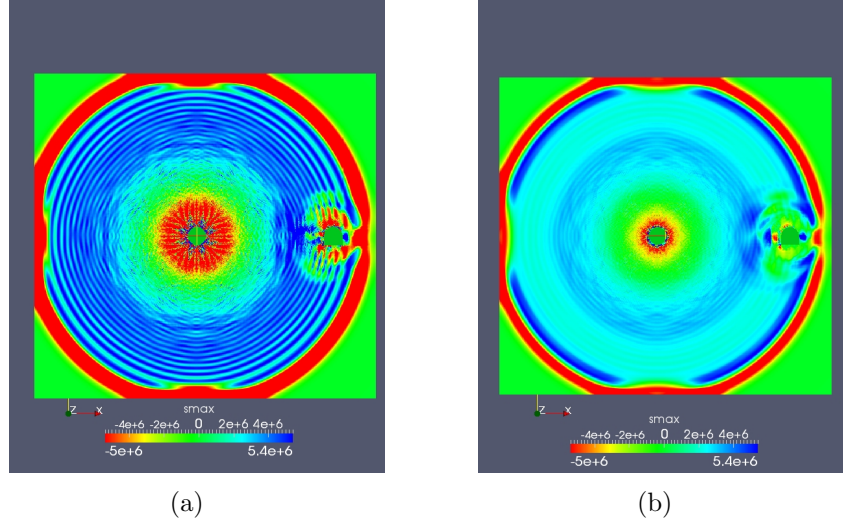


Figure 3.16: Contours of maximum principle stress at 11 msec due to a load of magnitude (a) $-3.8 \times 10^8 \text{ Pa}$ and (b) $-1.9 \times 10^8 \text{ Pa}$.

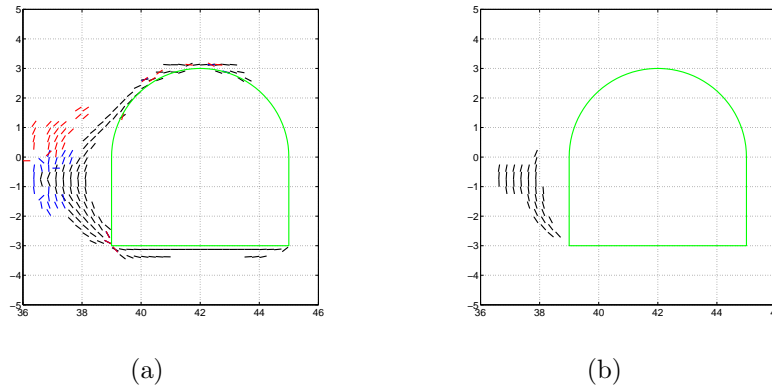


Figure 3.17: The distribution and orientation of cracks with normal opening u_n greater than $0.1u_0$ around the tunnel at 11 msec due to a load of magnitude (a) $-3.8 \times 10^8 \text{ Pa}$ and (b) $-1.9 \times 10^8 \text{ Pa}$.

In the next two examples, we keep the blast zone and tunnel the same size as in the previous simulations, but reduce the distance between them. The distance from the center of the blast zone to the left edge of the tunnel is reduced from 39m as shown in Figure 3.7, to 21m as shown in Figure 3.18. For these examples, the computational domain is $-50 < x < 50$ and $-50 < y < 50$. The mesh size is still 0.25m making the number of elements 400×400 , with 4 material points per element initially. Simulations are run for times between zero and 8 msec with a time step of 0.05 msec. Material parameters are the same as those used previously and listed in Section 3.2.6.

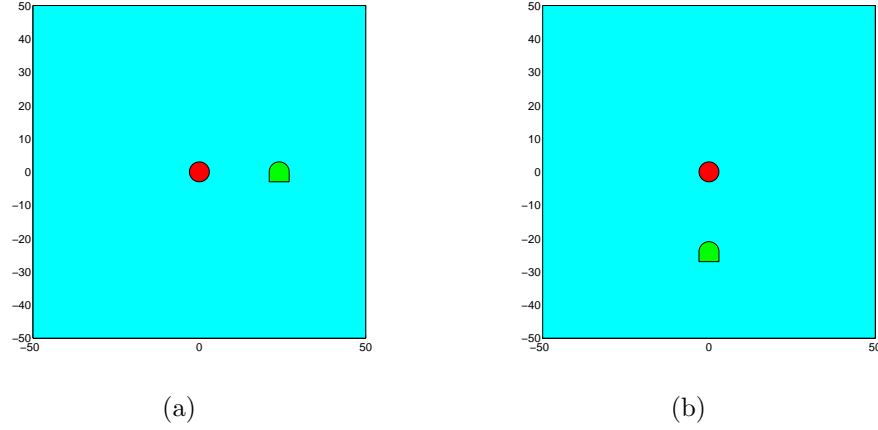


Figure 3.18: The computational domain for two examples where the blast is located closer to the tunnel. The distance from the center of the blast zone (red) is 21m to (a) the left wall of the tunnel and (b) the top of the tunnel. The tunnel is shown in green.

If we keep the magnitude of the blast the same but move the blast closer to the tunnel, we expect the blast to cause more damage. As shown in Schreyer [1976], the magnitude of stress components in cylindrical waves emanating from a disturbance applied on the surface of a cylindrical cavity of radius a varies with the radius r according to the factor $\sqrt{a/r}$. Thus, to have the same impact in terms of the size of the compressive wave hitting the tunnel, we should scale the magnitude of the blast. Thus, for the shorter distance of 21m between the blast and the tunnel, we use $\sigma_0 = -2.68 \times 10^8$ Pa instead of $\sigma_0 = -3.8 \times 10^8$ Pa. For these examples, we place an observation point at the side of the tunnel closest to the blast with coordinates (20.8125, 0.0625) when the blast is to the left of the tunnel, and an observation point with coordinates (0.0625, -20.8125) at the top of the tunnel when the blast is above the tunnel. Figure 3.19 shows the values of stress vs. time at those points when the tunnel is absent. These free waves are very similar in shape and close in value at the peak in compression and the peak in tension to that shown in Figure 3.8 for a larger pulse further from the tunnel. In Figure 3.19a the σ_{xx} (s11) component is large and compressive because the tunnel is to the right of the blast zone while in Figure 3.19b the σ_{yy} (s22) is large and compressive because the tunnel is below the blast zone. For the new examples of this section, we will examine results at time 7 msec and compare with the previous results at 11 msec in order to account for the shorter travel time to the tunnel when the blast is closer.

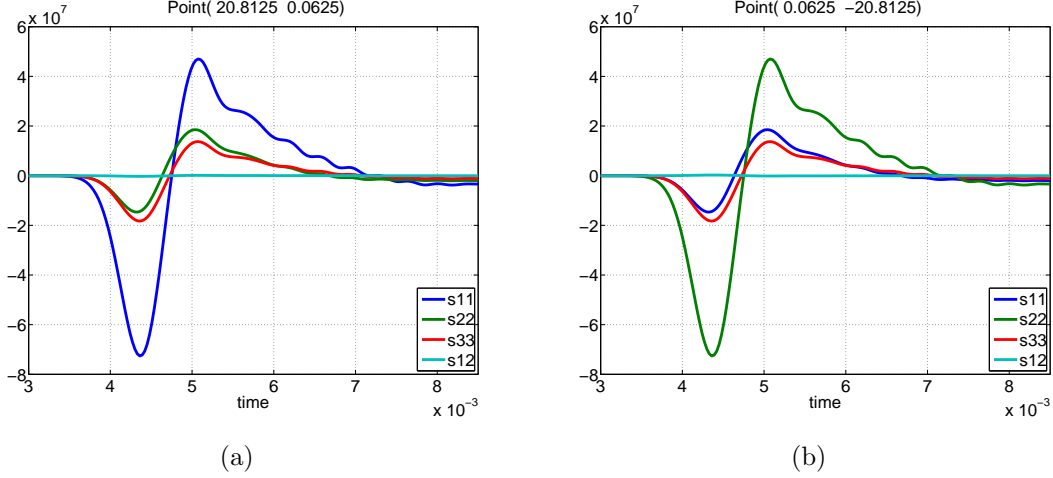


Figure 3.19: Free elastic waves from a source (a) to the left of the observation point at $(20.8125, 0.0625)$ and (b) above the observation point at $(0.0625, -20.8125)$ with $\sigma_0 = -2.68 \times 10^8$.

Even though the waves hitting the tunnel are similar in amplitude, the cylindrical geometry can and does provide a means for the blast to have a differing effect on the tunnel as the distance between blast and tunnel is varied. Figure 3.20 shows contours of maximum principal stress at 7 msec when the elastic-decohesive model is invoked in the rock. There appears to be more micro cracking throughout the domain in Figure 3.11 where the blast is further from the tunnel. The reason for this effect is that the tensile tail increases as a function of distance traveled from the source. Next, we look closer at the fracture patterns near the tunnel.

Figure 3.21 shows the distribution and orientation of cracks whose displacements are greater than $0.1u_0$ near the tunnel. The damage to the tunnel is similar in Figure 3.21a and Figure 3.13b because in both cases the incoming stress waves are similar and the structure of the tunnel is identical. However, Figure 3.21a shows the beginning formation of a spall plane at $x = 18$. This plane is about $1/2$ wavelength from the tunnel wall and the location of the maximum tensile stress. Moreover, the nearly horizontal cracks on the top of the tunnel in Figure 3.21a are due to axial splitting as was seen previously. In Figure 3.21b the tunnel is below the blast. In this case, the cracks form a symmetric pattern around the tunnel due to a symmetry in the domain and in the stress wave. Interestingly, there is the beginning of a spall plane at $y = -18$, where local peaks in tension occur. Complete fracture, with effective normal opening greater than u_0 occur at the top of the tunnel and along the bottom near the corner, when the blast is located to the left. When the blast is above the tunnel, complete cracks do not form at this time for these parameters. The microcracks that form around the tunnel are due to different failure modes because of varying stress states at different positions. The modes of failure can be determined by examining the stress state at points near the tunnel. Three points are examined with coordinates $(0.0625, -20.8125)$, $(1.5625, -21.4375)$ and $(3.0625, -24.4375)$. The region around $(0.0625, -20.8125)$ has microcracks caused by tensile failure. The rock fractures around $(1.5625, -21.4375)$ are due to shear failure and the

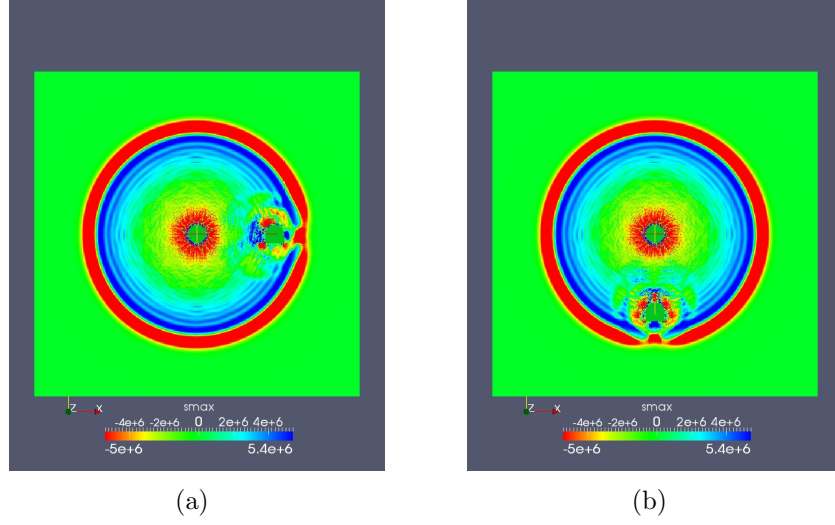


Figure 3.20: Contours of maximum principle stress at $t = 7$ msec for two different orientations of the blast with respect to the tunnel. The blast has $\sigma_0 = -2.68 \times 10^8$ Pa and the distance between the blast center and the tunnel is 21m. The rock is modeled as elastic-decohesive.

rock fractures around $(3.0625, -24.4375)$ are due to axial splitting under large compressive stress.

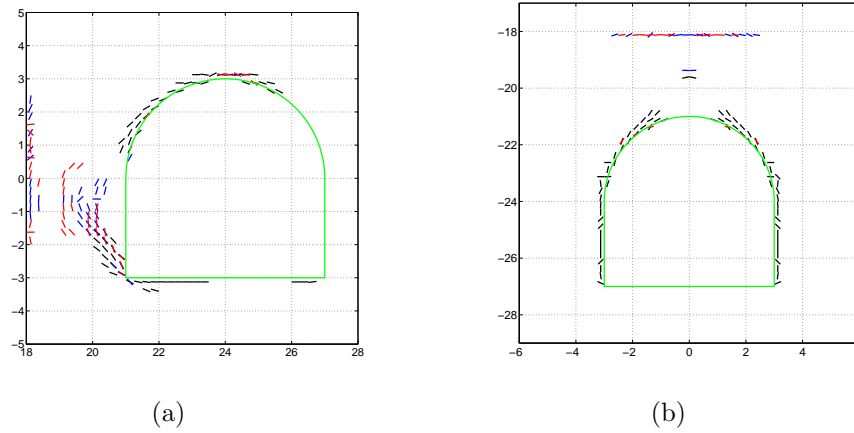


Figure 3.21: Distribution and orientation of cracks near the tunnel with effective normal opening greater than $0.1u_0$ at $t = 7$ msec for two different orientations of the blast with respect to the tunnel.

3.6 Summary

A decohesive approach has been proposed for modeling the initiation and evolution of cracks in rock which otherwise can be represented as an elastic continuum. Such an approach is different from the more common procedure of using a continuum constitutive equation with a failure criterion to simulate cracks. The decohesive model offers advantages in that interpretation of material parameters is simpler, the basic variables of the formulation such as normal and tangential components of crack-displacement discontinuity are more in tune with observations, and weaknesses associated with previous cracks can be easily accommodated. Important features of the model include the following: (i) A crack can initiate and evolve even if the stress is one of uniaxial compression. (ii) The orientation of the crack and the mode of failure depend on the state of stress. (iii) Crack branching can be predicted. (iv) A variety of pre-existing lines of weakness can be accommodated through the choice of initial values for material parameters. In conclusion, it is believed that the ability to specifically model the failure of rock as reflected by the orientation and location of cracks and crack opening represents a significant enhancement to existing approaches. As indicated by preliminary analyses performed by Sulsky et al. [2007], and as part of this project, numerical solutions to boundary value problems can be obtained at a computational cost comparable to the most efficient methods being used currently.

In applying the elastic-decohesive model to study crack formation in rock surrounding a tunnel, we observe that the tunnel geometry plays a role in the pattern of material failure. With a blast on the side of a tunnel, fractures form when the incoming compressive pulse reflects from the tunnel wall (a free surface) as a tensile wave. In cylindrical geometry, the reflected tensile wave is enhanced by interaction with a tensile tail that forms behind the incoming compressive pulse. This tensile tail can be large, since it grows with distance traveled from the source, a feature not found in the propagation of plane waves. The geometric singularity at the corner of the tunnel also induces fractures. We found it surprising that the top arch of the tunnel is subject to a large compressive load when the blast originates from the side. Our model predicts axial splitting near the arched tunnel ceiling due to the large compression. In contrast, if the blast originates above the arch, damage to the ceiling is reduced. In this case, cracks form around the sides of the tunnel. Various modes of failure are observed due to the varying stress states at different points along the tunnel. However, even with the same size blast, complete failure does not occur when the blast is above the tunnel, but does occur when the blast is to the side.

The cylindrical geometry used in this study plays an interesting role in fracture formation. The presence of a tensile tail behind the initial compressive pulse can enhance failure, as noted above. Moreover, if the distance between the blast and the tunnel is reduced, the tensile tail is reduced, and less cracking occurs, since the tensile tail grows with distance from the source. The elastic-decohesive model, and its implementation in the material-point method, provides an efficient tool to study these effects, and other effects such as blast size, relative distance between the blast and the tunnel, and orientation of the blast with respect to the tunnel. If combined with the capability documented in this report to model gaps and joints in rock, this modeling and simulation proficiency has the potential to increase our

understanding of the complex interactions between waves and rock features and the impact these have on tunnel failure.

4

One-Dimensional Joint Analysis

4.1 Introduction

A joint can be considered a pre-existing discontinuity in displacement of rock that is normally considered to be a continuum. Typically joints display nonlinear elastic and plastic behavior in compression and exhibit little or no strength in tension. Such features have the potential to modify significantly stress waves propagating through jointed media. This phase of the study provides a description of a discrete one-dimensional constitutive model for rock joints and describes the effects of joints on waves propagating through rock media. Included in the investigation are details of how the peak stress, the energy, and the impulse of a sinusoidal pulse are altered by values of the various material parameters. Also the effects of multiple joints on these same features are provided. In connection with large-scale numerical simulations, this latter phase is of importance in determining if two or more joints can be replaced by a single equivalent joint. In addition, this development provides the framework for a corresponding investigation of three-dimensional waves impinging on a single joint or multiple joints oriented obliquely to the direction of wave propagation.

The problem for the one-dimensional study of rock joint behavior is a compressive wave propagating through a rock joint or joint set oriented normally to the direction of wave travel (Figure 4.1). The study determines the characteristics of the wave after propagating through a joint or a joint set. The features of interest are energy dissipation, wave reflection, and change of shape. The parent rock, modeled as a linear elastic medium, is assumed to contain either a single joint or sets of joints.

Since the constitutive equation used to describe the joint involves plasticity, one result of joint-wave interaction is the dissipation of energy. The portion of the wave that reflects off the joint travels opposite to the initial direction and becomes a tensile wave. This reflected portion can also be calculated to properly determine the effects of joints. A part of the wave propagates through the joint as a compressive wave.

The amount of energy dissipation is dependent on the joint properties. A weathered joint filled with gouge and mineralization has a resistance to joint closure. Energy is dissipated during closure because the gouge resists closure and does not allow the intact rock faces to come fully into contact. A fresh joint, called a gap, with no relative shear motion closes with

no resistance because the asperities of the rock faces line up. All of the energy remains in the parent rock. Some energy reflects off the joint and some passes through the joint if the free surfaces come into contact. Until the two faces of intact rock come into contact, a fresh, unfilled joint acts as a free surface and the wave is reflected.

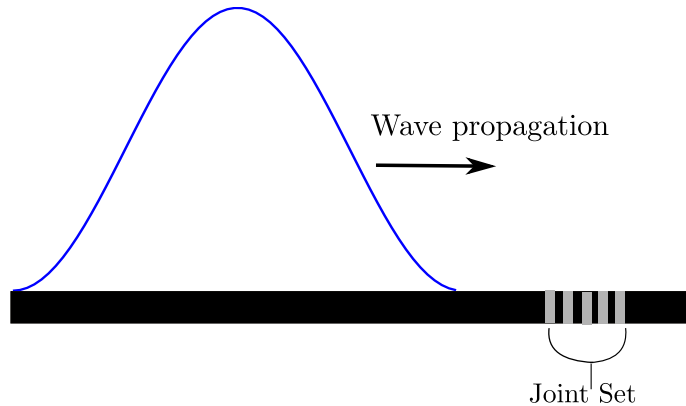


Figure 4.1: Wave propagating towards a joint set

The research objective is to numerically model the characteristics of wave-joint interaction in jointed rock. The main focus is the proper representation of wave-joint interaction for one-dimensional motion. The features that are studied include the amount of energy transmitted through a joint, the impulse of the transmitted wave in comparison with the impulse provided by the initial wave, and the reduction of peak stress in an initial wave altered by a joint. The results of modeling two joints sequentially are obtained and compared with modeling the joint set as an equivalent joint.

4.2 One-Dimensional Constitutive Models for Joints

4.2.1 Preliminary Comments

The term “joint” will be used to describe a discontinuity of the parent rock that has some resistance to closure of the discontinuity. A joint is physically understood as a rock with fractures that have weathered and accumulated gouge and mineralization between the two parent rock faces defining each fracture. This accumulated material provides resistance if the fracture is compressed. The term “gap” will be used to describe a discontinuity of the parent rock that has no resistance to closure. A gap is a fresh rock fracture that has had no shearing motion. Therefore, the parent rock faces of a gap can come into contact with no resistance to closure.

The subsequent sections of this chapter outline the formulation for the 1D joint models. Experimental data are provided with the development of the 1D model.

4.2.2 1D Joint Modeling Formulation

4.2.2.1 Basic Notation

Consider a segment of rock, called a bar, composed primarily of material governed by linear elasticity. All motion in the bar is constrained to be in the axial, or normal, direction. Along the bar are one or more perpendicular cracks. Each crack may undergo compaction, or joint closure, and opening, or gap formation. The only component of stress is the axial, or normal, component which is also called the normal component of traction.

To begin, suppose there is one joint described as a displacement discontinuity of initial length u_{g0} . At any later time the size of the discontinuity may change to a generic length u_g . Prior to any deformation, $u_g = u_{g0}$. This existing discontinuity is a joint composed of gouge, which is sediment and mineral particles that coalesced within the crack after its initial formation. The joint resists compaction in compression and is assumed to have no strength in tension. A non dimensional length of the discontinuity u_{g0} is defined to be $\bar{u}_g = u_g/u_{g0}$. Later on, \bar{u}_g will be referred to as the dimensionless size of the discontinuity. If the joint has opened beyond its initial size u_{g0} , then $\bar{u}_g > 1$ and the result indicates the joint has opened. If the joint has closed from its initial size u_{g0} , then $\bar{u}_g < 1$ and the process is joint closure. By definition, \bar{u}_g has an initial value of 1.

A joint function $F(\sigma_{el}, \bar{u}_g)$ is defined to indicate the current state of the joint with regard to whether or not additional closure is imminent. The stress is σ_{el} and a joint “hardening” function $g(\bar{u}_g)$ relates joint closure to stress. The hardening function has parameters that will be given values to match experimental data for normal loading of joints. The joint function is chosen to be of the form

$$F = -\sigma_{el} + g(\bar{u}_g). \quad (4.1)$$

If $F < 0$, no joint closure occurs. If $F = 0$, the joint may close. And, $F > 0$ is not allowed. A distinction must be made in regimes of joint closure or joint opening. As noted earlier, joints resist compression but have no strength in tension.

4.2.2.2 Joint Closure

The state of joint closure is governed by the joint function $F(\sigma_{el}, \bar{u}_g)$ as defined in Equation (4.1). The “hardening” function is chosen to be of the form

$$g(\bar{u}_g) = \sigma_g \left(1 - \frac{1}{\bar{u}_g^m} \right) e^{\bar{u}_g^m}, \quad (4.2)$$

where σ_g is a material parameter with dimensions of stress and m is another material parameter that is dimensionless. Such a form gives qualitative joint closure characteristics consistent with experimental data for a granular filled joint (Li and Ma [2009]). Assume the joint is at its initial state prior to any loading. For a given increment in joint closure $\Delta \bar{u}_g < 0$, $\bar{u}_g < 1$. The stress in the joint is $\sigma_{joint} = g(\bar{u}_g)$. Figure 4.2 shows the characteristics of the joint closure function $g(\bar{u}_g)$. Li and Ma’s publication will be used to calibrate the

constitutive model to their published data. The existence of a gap implies the stress is zero which is modeled simply by requiring the joint “hardening” function to satisfy

$$g(\bar{u}_g) = 0 \quad \text{when} \quad \bar{u}_g > 1. \quad (4.3)$$

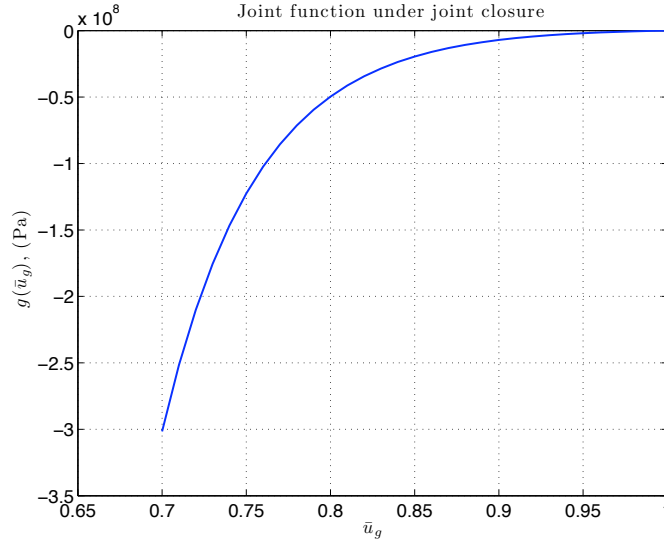


Figure 4.2: The joint “hardening” function $g(\bar{u}_g)$ when $\bar{u}_g \leq 1$

An investigation was conducted to illustrate the effects of different values of m in the joint closure function $g(\bar{u}_g)$. In Figure 4.3, various values of m are prescribed to show the effect of the characteristic material parameter on the shape of $g(\bar{u}_g)$. The importance of this investigation is to demonstrate that as the value of m grows larger, the joint will have less resistance to closure. The parameter m can be used to better match the constitutive model predictions to experimental data.

4.2.2.3 Joint Opening

Joint opening is simpler than joint closure because the experimental data suggest joints do not have any tensile strength. When a joint is put under a tensile load from a zero stress state, the load cannot be sustained and the joint will immediately open up. The need for a decohesion function is unnecessary whenever a tensile load is applied from a zero stress state. The joint will open up immediately and have zero stress. Suppose a joint is again at its initial size u_{g0} and a tensile load is applied. Figure 4.4 illustrates this process and relates \bar{u}_g to the stress σ , at the gap. The notion that rock joints have zero tensile strength does not appear plausible intuitively. However, the joint gouge between fractured rock faces is a granular media. Granular media do have zero tensile strength. Yet, jointed rock can allow for tensile waves to propagate through in physical testing. The hypothesis for this phenomenon is that there is an “in situ” stress consisting of confining pressure so that rock joints do not simply open up during underground wave propagation.

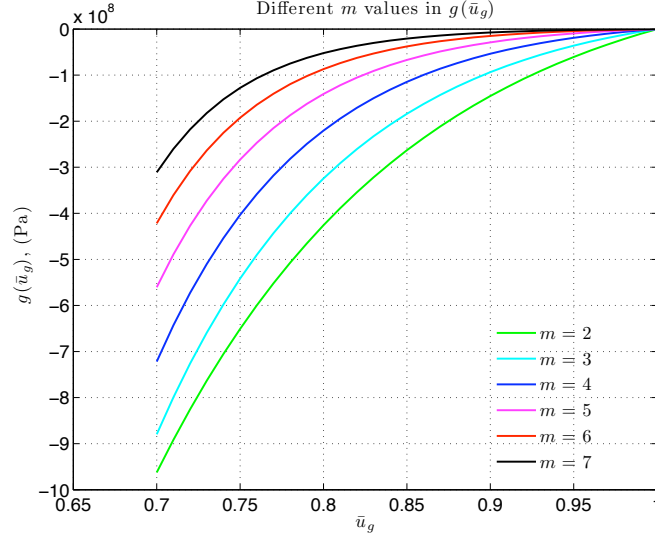


Figure 4.3: Impact of m on the shape of the joint “hardening” function $g(\bar{u}_g)$

Consider a joint under a compressive load that has intact rock on either side of its plane of discontinuity. The numerical implementation of a joint spreads its effect over a portion of the parent rock containing the joint, so the intact rock must also be considered. If a positive (tensile) increment in strain is applied from a compressive state, the magnitude of the strain increment matters. If the strain increment is large enough that the intact rock returns to zero strain and the joint returns to its initial joint size u_{g0} , the element containing the joint will have zero stress. If the strain increment is not large enough to unload the joint and intact rock to a zero stress state, then the joint closure routine will be followed with a positive strain increment.

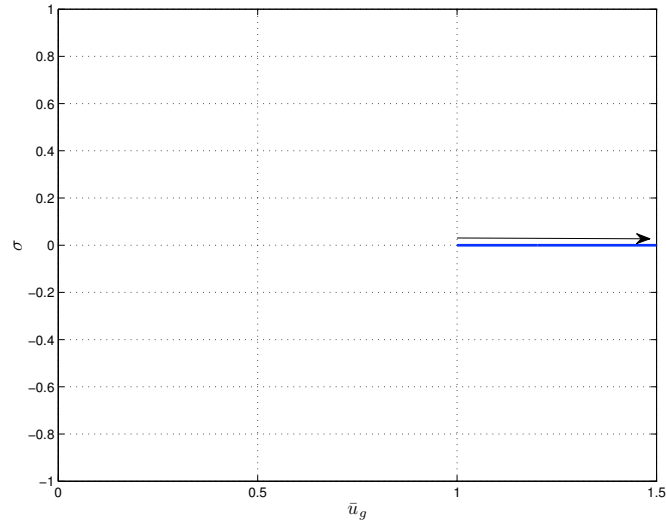


Figure 4.4: Joint with prescribed positive strain increments

4.2.3 Numerical Implementation of 1D Joint Model

4.2.3.1 Stress and Strain Within an Element

Begin by considering an element of length h . The element represents a domain consisting of an elastic region and a joint discontinuity of initial size u_{g0} , where $u_{g0} \ll h$. Within the element, the stress (σ_{el}) is a single value for both segments consisting of a continuum and a joint. Over the element, there is both an elastic strain (ϵ_{el}) governing the continuum and a joint strain (ϵ_g). The elastic region has a Young's Modulus of Y . The continuum and joint strains combine to form the total strain ϵ_{tot} . The total strain and total strain increments are given by

$$\epsilon_{tot} = \epsilon_{el} + \epsilon_g \quad (4.4)$$

$$\Delta\epsilon_{tot} = \Delta\epsilon_{el} + \Delta\epsilon_g. \quad (4.5)$$

The numerical scheme provides an increment in total strain ($\Delta\epsilon_{tot}$) at the current time step and the element under consideration. For the purpose of explaining the numerical implementation, the current time step is the k -th time step. The state of stress and strain of the element is known at the k -th time step. The numerical implementation will determine the state of stress and strain at the element at the $(k+1)$ -th time step, the next time step. Therefore, stress and strain values with an superscript k denote the values at the current time step and values with an superscript $k+1$ denote the values at the next time step. Also, the joint will be non-dimensionalized as shown earlier, where $\bar{u}_g^k = \frac{u_g^k}{u_{g0}}$.

Given the basic description of joint behavior under normal loading in 1D, the numerical implementation of the joint model is detailed. The implementation for the model is based upon the following:

1. The element is of length h and contains one joint.
2. The element has nodal displacements u_2 and u_1 . The total strain across the element is $\epsilon_{tot} = \frac{u_2 - u_1}{h}$.
3. The joint strain is defined to be $\epsilon_g = \frac{u_g}{h}$.
4. Every joint starts with an initial discontinuity size u_{g0} . Therefore, the element also has an initial total strain equal to the initial joint strain $\epsilon_{tot,0} = \epsilon_{g0} = \frac{u_{g0}}{h}$.
5. During joint closure, the stress equals the hardening function $g(\bar{u}_g)$.
6. After joint closure and upon unloading the joint strain remains fixed. The elastic strain, and hence the stress, reduces to provide the prescribed reduction in total strain.
7. During joint opening, the stress is zero and the joint simply opens to accommodate the given strain increment.
8. The stress is constant over the element.

4.2.3.2 Joint Closure and Unloading

For the element under consideration suppose the existing state of stress is negative (compressive). At the discrete time t^k , suppose an increment in total strain $\Delta\epsilon_{tot}^k$ is negative. The updated total strain is

$$\epsilon_{tot}^{k+1} = \epsilon_{tot}^k + \Delta\epsilon_{tot}. \quad (4.6)$$

The total strain is held fixed. The problem becomes one of determining the appropriate increments in elastic rock strain and inelastic joint strain so that the sum of elastic and joint strain equals the total strain, and the stress in the continuum rock equals the stress in the joint.

To begin, assume that the increment in the elastic strain equals the increment of total strain. The result will be a value of the joint function that is positive. The task is to decrease the elastic strain and simultaneously increase the joint strain until the joint function is zero, the condition that implies the stress in the rock equals the stress in the joint.

The procedure that is proposed is that of Newton-Raphson to force the joint function to zero. We drop the superscript "k" designating the discrete time for the moment. The proposed Newton-Raphson procedure is an iterative one. Suppose the iterative count is designated by "i". The initial state (i = 0) is given by

$$\epsilon_{el}^{(0)} = \epsilon_{el}^k + \Delta\epsilon_{tot} \quad (4.7)$$

$$\epsilon_g^{(0)} = \epsilon_g^k \quad (4.8)$$

$$\bar{u}_g^{(0)} = \bar{u}_g^k. \quad (4.9)$$

These values for strains are used for the first iteration of the Newton-Raphson scheme to solve for the joint discontinuity over the material point domain. The iterative procedure starts with i = 0. First the stress is found in the rock continuum which is elastic:

$$\sigma_{el}^i = Y\epsilon_{el}^i \quad (4.10)$$

The joint function $F^{(i)}(\sigma_{el}, \bar{u}_g)$ is then calculated as follows:

$$F^{(i)} = -\sigma_{el}^i + g(\bar{u}_g^i). \quad (4.11)$$

The starting value for the decohesion function is greater than zero. Now, the joint is allowed to close in a procedure that forces F to zero. In the implementation, requiring F to be zero is too strict for a reasonable number of iterations. The actual requirement becomes that of enforcing F to be a small positive number ε . The Newton-Raphson scheme requires the increment in the decohesion function given as follows:

$$\delta F^{(i)} = -\frac{\partial \sigma_{el}}{\partial \epsilon_{el}} \delta \epsilon_{el}^{(i)} + \frac{\partial g(\bar{u}_g)}{\partial \bar{u}_g} \delta \bar{u}_g^{(i)} \quad (4.12)$$

where

$$\frac{\partial g}{\partial \bar{u}_g} = \frac{\sigma_g m}{e^{\bar{u}_g m} (\bar{u}_g)^{(m+1)} (\bar{u}_g)^{(m+1)}} \quad (4.13)$$

$$\frac{\partial \sigma_{el}}{\partial \epsilon_{el}} = -Y \quad (4.14)$$

According to the Newton-Raphson algorithm, $\bar{u}_g^{(i+1)}$ is obtained from

$$\delta \bar{u}_g^{(i+1)} = -\frac{F^{(i)}}{\delta F^{(i)}} \quad (4.15)$$

$$\bar{u}_g^{(i+1)} = \bar{u}_g^{(i)} + \delta \bar{u}_g^{(i+1)}. \quad (4.16)$$

For the new value of $\bar{u}_g^{(i+1)}$, a new joint strain is found by

$$\epsilon_g^{(i+1)} = \frac{\bar{u}_g^{(i+1)} u_{g0}}{h}. \quad (4.17)$$

and a corresponding new value in elastic strain.

$$\epsilon_{el}^{(i+1)} = \epsilon_{tot}^{k+1} - \epsilon_g^{(i+1)} \quad (4.18)$$

It follows that

$$\delta \epsilon_{el}^{(i+1)} = -\delta \epsilon_g^{(i+1)} = -\frac{\delta \bar{u}_g^{(i+1)} u_{g0}}{h} \quad (4.19)$$

Using these new values of strain, the process can be repeated, whereby the stresses in the elastic region and the joint region are found. If F does not meet the requirement of having a value less than a small positive number, the process is repeated until $F^{(i+1)}$ does meet the requirement. The corresponding values for ϵ_g^{k+1} and ϵ_{el}^{k+1} become the strains associated with the element at time t^{k+1} once the Newton-Raphson scheme is complete.

Unloading from a compressive state is achieved simply by holding the joint strain constant, allowing the elastic rock strain to absorb the positive increment in total strain, and setting the joint stress equal to the rock stress obtained from the elastic relation.

4.2.3.3 Joint Opening

For the material point under consideration at time t^k , suppose an increment in total strain $\Delta \epsilon_{tot}^k$ is positive and that the strain in the element is due solely to the joint discontinuity. Therefore, $\epsilon_{tot}^k = \epsilon_g^k = u_{g0}/h$ and $\epsilon_{el}^k = 0$. Because joints cannot withstand any tensile loading, the stress across the material point will be initially discontinuous and must be resolved. The elastic region of the element will have zero stress because all of the strain increment is automatically put onto the joint and the stress is continuous. In summary, given a positive total strain increment from an initial zero stress, all strain will be applied to the jointed region of the element.

$$\epsilon_{tot}^{k+1} = \epsilon_{tot}^k + \Delta \epsilon_{tot}^k \quad (4.20)$$

$$\epsilon_{el}^{k+1} = 0 \quad (4.21)$$

$$\epsilon_g^{k+1} = \epsilon_g^k + \Delta \epsilon_{tot}^k \quad (4.22)$$

4.2.3.4 Other loading scenarios and summary

Consideration must be given to the loading scenario where a joint is in compression and a positive strain increment is prescribed at time t^{k+1} . Assume the total prescribed increment in strain $\Delta\epsilon_{tot}^{k+1}$ has a large enough magnitude that when initially prescribed to the elastic region ϵ_{el}^{k+1} is greater than zero (under tension). This could satisfy the condition that $F \leq 0$ but there would be a discontinuity in stress between the elastic and joint regions of the material point. Therefore, a check is performed at the end of the Newton-Raphson scheme to check if $\sigma^{k+1} = Y\epsilon_{el}^{k+1} > 0$. Assuming $\sigma^{k+1} > 0$, the strains are modified as follows:

$$\epsilon_g^{k+1} = \epsilon_g^{k+1} + \epsilon_{el}^{k+1} \geq \frac{u_{g0}}{h} \quad (4.23)$$

$$\epsilon_{el}^{k+1} = 0 \quad (4.24)$$

$$\sigma^{k+1} = 0. \quad (4.25)$$

4.2.3.5 Results of Driver Program for 1D Joint Model

A driver program was used to prescribe increments in strain for a joint and its associated elastic region. A load-unload-load path was prescribed to demonstrate how the model deals with unloading. The results of the run are shown in Figure 4.5.

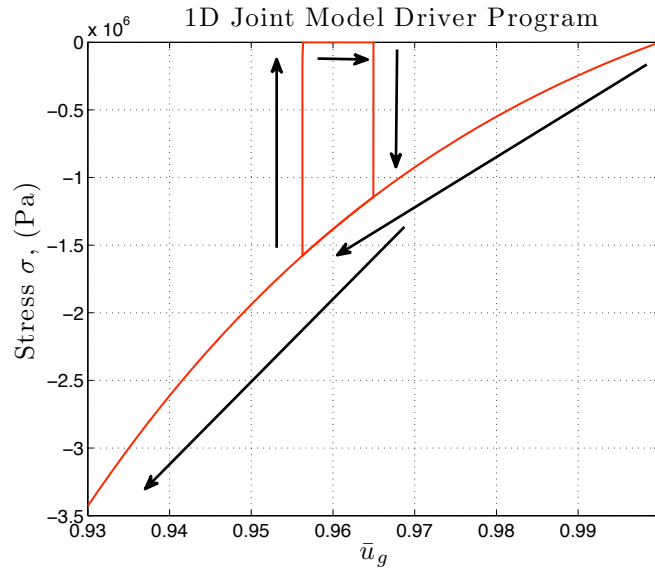


Figure 4.5: Stress as a function of displacement discontinuity for a joint going through a load-unload-load cycle.

The results demonstrate that the joint constitutive model unloads vertically, as outlined in Section 4.2.3.3. The physical meaning is that all of the joint deformation is plastic deformation. The joint unloads vertically from the value of stress when the function $F = 0$ and then loads vertically back to the value of stress when $F = 0$. During unloading, all of the positive strain increments ($\Delta\epsilon_{tot}$) are allocated to the strain ($\Delta\epsilon_{el}$) of the elastic region.

4.2.4 Gap Constitutive Model

4.2.4.1 Gap Constitutive Equation

A gap is a discontinuity in displacement with no resistance to closure. A gap is simply a joint that has not had any coalescence of gouge or mineralization to resist closure back to its initial state prior to the initial fracturing. For one-dimension, with no resistance to closure or opening, a gap simply closes or opens based on the the increment in strain $\Delta\epsilon_{tot}^{k+1}$.

To simplify the explanation of the implementation of the gap constitutive model, consider the parameters used to describe the behavior of a joint in Section 4.2.2. The gap has an initial size u_{g0} . A dimensionless gap size describes the gap at a time t^k as $\bar{u}_g^k = u_g^k/u_{g0}$. The initial total strain in the gap is $\epsilon_g^0 = u_{g0}/h$, where h is the size of the element containing the gap. The total strain in the element ϵ_{tot}^k is the sum of the gap strain and elastic strain ($\epsilon_g^k + \epsilon_{el}^k$). A decohesion function F governs the gap and is the same as the function used in a joint (Equation 4.1). The difference is that the “hardening” function $g(\bar{u}_g)$ for a gap is now

$$g(\bar{u}_g) = 0. \quad (4.26)$$

The modification to the “hardening” function is the only difference between a joint and a gap. The formulation and numerical implementation is otherwise identical to the joint formulation described in Sections 4.2.2 and 4.2.3.

4.2.4.2 Results of Driver Program for 1D Gap Model

The gap constitutive model was used through the same load-unload-load cycle in Figure 4.5. The gap cannot sustain any load whether in tension or compression (Fig 4.6). The different legs of the loading path overlap because nonzero stress does not appear until the gap fully closes.

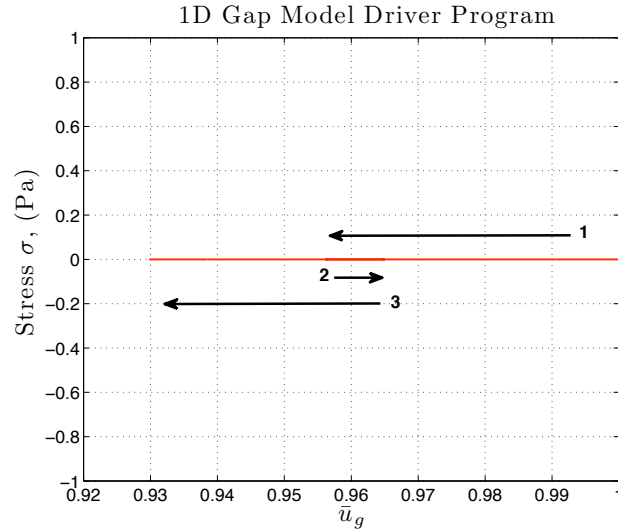


Figure 4.6: Driver program results for a gap going through load-unload-load cycle with each leg labelled sequentially.

4.2.5 1D Joint Model for Plasticity and Elasticity

4.2.5.1 Formulation that Includes Joint Elasticity

The 1D Joint Model of Section 4.2.2 is altered to allow for a portion of joint closure to be associated with linear elasticity. For a joint without linear elasticity, the dimensionless joint size \bar{u}_g closes along the “hardening” function $g(\bar{u}_g)$ and unloads vertically. All of the initial strain increment $\Delta\epsilon_{tot}^k$ at time t^k is first allocated to the elastic region of the element with which the joint is associated. With the decohesion function (4.1), the constraints on the decohesion function are not violated when the total increment in strain is allocated to the elastic region of the joint. This constitutive algorithm represents a plastic joint. Its formulation will be modified to create a constitutive algorithm for an elastic-plastic joint.

Based on the formulation of the 1D joint model, consider an initial joint discontinuity u_{g0} within an element of length h . The element also has a linearly elastic continuum of length $h_c = h - u_{g0}$. At time t^k , the continuum portion of the element has a strain ϵ_c and the joint has a current discontinuity of length u_g^k . The stress in the element is $\sigma^k = E_c \epsilon_c^k$ and continuity of the stress across the element σ^k is maintained. E_c is the modulus of elasticity for the the continuum portion of the element. In other words, the stress at the joint is also σ^k . The kinematic condition for strain across the element is

$$\epsilon_{tot}^k h = \epsilon_c^k h_c + \epsilon_g^k u_{g0}. \quad (4.27)$$

The strains are defined as

$$\epsilon_g^k = \frac{u_g^k}{u_{g0}} \quad (4.28)$$

$$\epsilon_c^k = \frac{h_c - u_c^k}{h_c}, \quad (4.29)$$

where u_c^k is the amount of displacement that has occurred within the linearly elastic continuum portion of the element.

For the next time step, an increment in total strain $\Delta\epsilon_{tot}^{k+1}$ is prescribed. The increment in total strain in terms of an increment in displacement Δu_{tot}^{k+1} and the length of the element h is

$$\epsilon_{tot}^{k+1} = \frac{\Delta u_{tot}^{k+1}}{h}. \quad (4.30)$$

The total strain increment is a sum of the increment in continuum strain as well as joint strain:

$$\Delta\epsilon_{tot}^{k+1} = \frac{\Delta\epsilon_c^{k+1} h_c + \Delta\epsilon_g^{k+1} u_{g0}}{h} \quad (4.31)$$

Assume a linearly elastic constitutive relation for both the continuum and the joint. The modulus of elasticity of the joint E_g is not necessarily equal to the modulus of elasticity of the continuum E_c . To maintain continuity of stress, the following is enforced

$$\Delta\sigma = E_c \Delta\epsilon_c^{k+1} = E_g \Delta\epsilon_g^{k+1}. \quad (4.32)$$

Propose a dimensionless parameter α_g derived from (4.31) and (4.32), where

$$\Delta \varepsilon_g^{k+1} = \frac{\Delta \varepsilon_{tot}^{k+1} h}{(1 + \alpha_g) u_{g0}}. \quad (4.33)$$

α_g expresses the strain in the continuum as,

$$\begin{aligned} \Delta \varepsilon_c^{k+1} &= \alpha_g \frac{\Delta \varepsilon_g^{k+1} u_{g0}}{h_c} \\ &= \frac{\alpha_g}{1 + \alpha_g} \frac{\Delta \varepsilon_{tot}^{k+1} h}{h_c}. \end{aligned} \quad (4.34)$$

From Equations (4.32), (4.33), and (4.34), the dimensionless parameter α_g is,

$$\alpha_g = \frac{E_g h_c}{E_c u_{g0}}. \quad (4.35)$$

Propose an effective modulus E^* for the entirety of the element, such that $\Delta \sigma = E^* \Delta \varepsilon_{tot}^{k+1}$. To find E^* , solve the stress continuity equation of $\Delta \sigma$ for the entire element and the continuum.

$$E^* \Delta \varepsilon_{tot}^{k+1} = E_c \Delta \varepsilon_c^{k+1} \quad (4.36)$$

Substitute (4.34) into (4.36) and solve for E^* . The expression for E^* is,

$$E^* = \frac{\alpha_g}{1 + \alpha_g} \frac{h}{h_c} E_c. \quad (4.37)$$

4.2.5.2 Numerical Implementation of the Elastic-Plastic Joint Model

To implement the elastic-plastic joint model, the process is almost the same as that of the plastic-only joint model implementation in Section 4.2.3. The difference is that before calculating the value of the decohesion F function, the trial increments in strain for both the joint and the continuum regions are calculated. This differs from the fully plastic joint, where the total increment in strain is initially allocated to the elastic region. Assume an increment in total strain $\Delta \varepsilon_{tot}^{k+1}$ is prescribed at time t^{k+1} . First, the equivalent modulus of elasticity is calculated following (4.37). The equivalent modulus E^* is then used from this point forward as the modulus of elasticity Y used in Section 4.2.3. The term α_g is calculated following (4.35). The trial increments in strain for the joint and the continuum region are

$$\Delta \varepsilon_g^{k+1} = \frac{1}{1 + \alpha_g} \Delta \varepsilon_{tot}^{k+1}, \quad (4.38)$$

$$\Delta \varepsilon_c^{k+1} = \frac{\alpha_g}{1 + \alpha_g} \Delta \varepsilon_{tot}^{k+1}. \quad (4.39)$$

With these as the trial increments in strain, the F function is calculated and the Newton-Raphson solver is followed if necessary just as outlined in Section 4.2.3. The modulus of elasticity used for the Newton-Raphson solver is E^* .

4.2.5.3 Calculation of E_g

The modulus of elasticity for the joint can be allowed to vary with closure or be held constant. This is an option specifically implemented so as to better match the experimental data. Non-linear elasticity has been allowed but won't be presented. E_g can be a constant prescribed initially as a function of the joint function $g(\bar{u}_{g,pres})$, where $\bar{u}_{g,pres}$ is a prescribed value of \bar{u}_g . Then, E_g is

$$E_g = \frac{\partial g(\bar{u}_{g,pres})}{\partial \bar{u}_{g,pres}}. \quad (4.40)$$

One possibility is to set E_g constant with a value equal to the modulus of elasticity for the continuum.

$$E_g = E_c \quad (4.41)$$

The reason is that the elastic behavior of a joint composed of fractured parent rock particulate would have the same elastic behavior as the parent rock.

Alternatively, E_g can be calculated to change through joint deformation based on the minimum joint size reached. As a joint closes, the minimum value of \bar{u}_g is captured as $\bar{u}_{g,min}$. The joint modulus is calculated as

$$E_g = b \frac{\partial g(\bar{u}_{g,min})}{\partial \bar{u}_{g,min}}. \quad (4.42)$$

b is a non-dimensional factor that can be used to better fit experimental data and ensure that both elastic and plastic closure is occurring. If the joint was to unload, then E_g would be held constant during unloading. After the joint is closed to a stress less than $\bar{u}_{g,min}$, E_g would change.

4.2.5.4 Results of Driver Program for 1D Elastic-Plastic Joint Model

A driver program was used to prescribe increments in strain for a joint and its associated elastic region. A load-unload-load routine was prescribed to demonstrate how the elastic-plastic model unloads. The results of the run are shown in Figure 4.7.

The plot shows that the elastic-plastic joint unloads linearly and elastically. The physical meaning is that as the joint closes both elastic and plastic deformation occurs. Elastic unloading will occur within the joint because of the equivalent modulus E^* . For the second load cycle, once the deformation causes F to increase to the value $F = 0$, then elastic-plastic deformation will resume. The elastic unloading is the reason for the difference between the elastic-plastic joint model and the purely plastic joint model shown in Figure 4.5.

4.2.6 Experimental Validation of 1D Joint Model

The parameters used in the constitutive model have been chosen based on experimental data from a published experimental study of wave propagation across a filled rock joint Li and

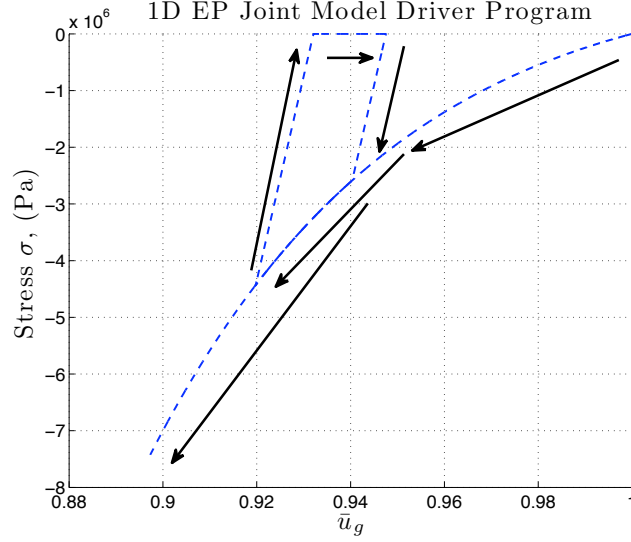


Figure 4.7: Driver program results for an elastic-plastic joint going through a load-unload-load cycle.

Ma [2009]. The authors used a Split-Hopkinson bar with a granular-filled joint between the incident and transmission bars confined by a PVC sleeve. The experimental set up is shown in Figure 4.8. The properties of the incident and transmission bars are a Young's modulus of 60 GPa, a density ρ of 2650 kg/m³, length L of 2 m, and a diameter of 50 mm. The material properties will be used in subsequent numerical simulations.

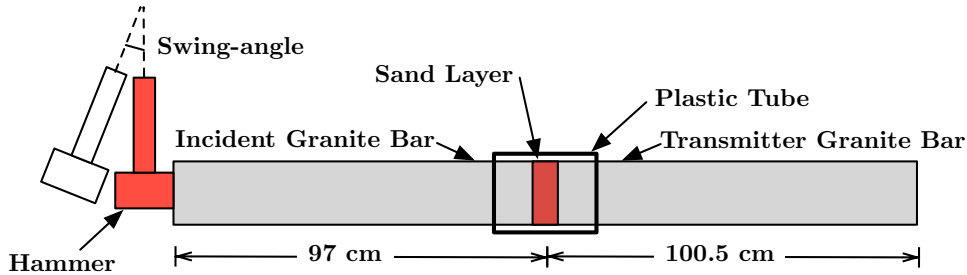


Figure 4.8: Experimental configuration

Using different hammer swing angles, Li and Ma found the stress-strain data lies on the same curve regardless of swing angle. The curve fit provided by the experimentalists is shown in Figure 4.9.

The developed constitutive model coincides with experimental data for a closure function $g(\bar{u}_g)$ of the form:

$$g(\bar{u}_g) = \sigma_g \left(1 - \frac{1}{\bar{u}_g^m} \right) (e^{-\bar{u}_g^m}). \quad (4.43)$$

The parameters σ_g and m best fit at values of 3.75 GPa and 7.1, respectively. Using a

driver program prescribing strain increments, the stress-strain curve was recreated with the constitutive model (Fig 4.9).

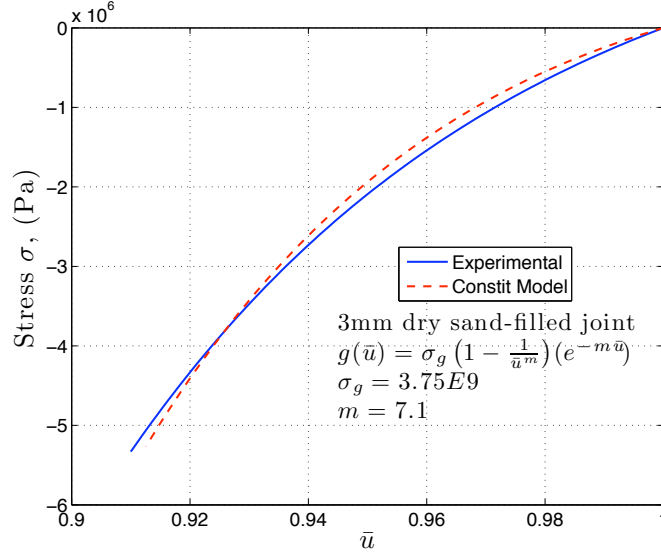


Figure 4.9: Driver output

These values of σ_g and m are used in the subsequent studies of joints with strength in closure. The experimental data do not give an indication of the joint behavior during unloading, so it is assumed that a joint could be modeled accurately with either an elastic-plastic model (linear joint unloading) or a fully plastic model (vertical joint unloading).

4.2.7 MPM Code, Gap Model, and Analytical Solution

4.2.7.1 Numerical Procedure and Model Problem

Each of the three different constitutive models has been implemented into a one-dimensional Material Point Method (MPM) dynamic code. The studies conducted on these different models use the same code. To test the code and gap model, a one-dimensional solution was found for a bar with a gap in the middle. The bar is initially at rest with zero initial stress. The problem set up is that shown in Figure 4.10. A single gap exists at the middle of the bar, and the gap has an initial discontinuity of u_0 . A sinusoidal velocity $v(t)$ is prescribed at the left boundary. The assumed function is

$$v(t) = \frac{v_{max}}{2} \left(1 - \cos\left(\frac{2\pi t}{t_{wave}}\right) \right) H[t_{wave} - t]H[t]. \quad (4.44)$$

$H[t]$ denotes a Heaviside function, t_{wave} is the time span of the pulse, and v_{max} is the peak particle velocity of the pulse. The function has zero derivative at $t = 0$ and $t = t_{wave}$. This “smoothness” tends to reduce numerical error.

For the run, a gap of initial discontinuity $u_0 = 3mm$ was chosen. The peak particle velocity v_{max} is $1m/s$. The time span of the wave $t_{wave} = 2.1e-4s$ (or $1/2$ the length of time for a wave front to travel from one end of the bar to the other). The bar is discretized using 50 elements and one material point is assigned initially to be at the center of each element.

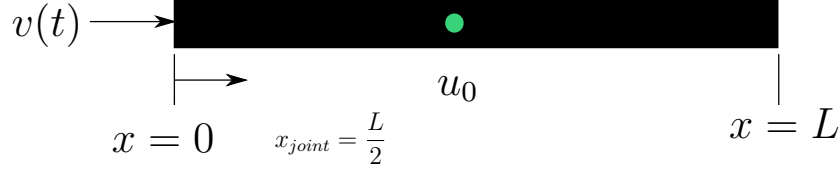


Figure 4.10: Verification run where the green dot represents a gap in the middle of the bar.

4.2.7.2 Gap Model Analysis

The behavior of a gap should be full wave reflection until total closure occurs. Once the gap width reduces to 0, the remaining portion of the pulse should propagate past the gap. The first example is one for which the pulse is not large enough to close the gap with the reflected wave shown in (Fig 4.11(a)).

No displacement occurs at material points located beyond the joint because none of the wave propagates through (Fig 4.11(b)). The energy in the bar does not decrease because a gap has no resistance to closure so no energy is dissipated during closure (Fig 4.11(c)). Referring to the legend of Figure 4.11(c), the input energy is the energy introduced into the bar by the velocity boundary condition. The strain energy is the elastic energy in the material point summed along the bar, including the elastic energy in the parent rock for the region associated with the gap. The kinetic energy is calculated using the velocity of each material point. The closure energy is the energy dissipated at the gap due to the a resistance to closure and is zero. The results in Figure 4.11 substantiate the intuitive behavior of the gap constitutive model, discussed below.

4.2.7.3 Analytical Solution to Determine Closure Potential

The analytical solution for a continuum modeled as an elastic bar is used to determine the maximum displacement that will occur for a sinusoidal wave reflecting off a free surface of a one-dimensional bar. This maximum displacement is then compared to the maximum closure of a gap having the same sinusoidal wave reflection. The gap closes the same amount as the motion of the free surface if the initial gap is large enough.

The governing partial differential equation to the one-dimensional elastic bar problem without body forces is

$$(Yu_{,x})_{,x} = \rho u_{,tt}. \quad (4.45)$$

The analytical solution to Equation (4.45) for the problem set up shown in Figure 4.10

(ignoring the gap) is

$$u(x, t) = v_{max} \left\{ \left(t - \frac{x}{c} \right) - \frac{1}{\omega} \sin \left(\omega \left(t - \frac{x}{c} \right) \right) \right\} \left\{ H \left[t - \frac{x}{c} \right] - H \left[t - \frac{2\pi}{\omega} - \frac{x}{c} \right] \right\} \\ + v_{max} \left\{ \left(t + \frac{x}{c} \right) + \frac{1}{\omega} \sin \left(\omega \left(t + \frac{x}{c} \right) \right) \right\} \left\{ H \left[t - \frac{2L}{c} + \frac{x}{c} \right] - H \left[t - \frac{2L}{c} - \frac{2\pi}{\omega} + \frac{x}{c} \right] \right\}, \quad (4.46)$$

where

$$\omega = \frac{2\pi}{t_{wave}}, \quad (4.47)$$

$$c = \sqrt{\frac{Y}{\rho}}. \quad (4.48)$$

This solution is valid for time $0 \leq t \leq 2t_{prop}$, where $t_{prop} = L/c$.

The maximum displacement u_p at $x = L$ occurs at time $t_{prop} + t_{wave}$ and is called the closure potential where

$$u_p = v_{max}(2\pi)/\omega \quad (4.49)$$

or

$$u_p = v_{max}t_{wave}. \quad (4.50)$$

The expression in Equation (4.50) is also valid for an open gap. The displacement u_p is a function of the velocity boundary condition and can be used to characterize the initial velocity pulse. As long as the gap does not fully close, the maximum displacement at the gap after wave reflection is equal to u_p . For the boundary condition of Eq. (4.44), u_p is calculated to be $0.21mm$. If the initial gap width is larger than this value, no portion of the wave is transmitted through the gap.

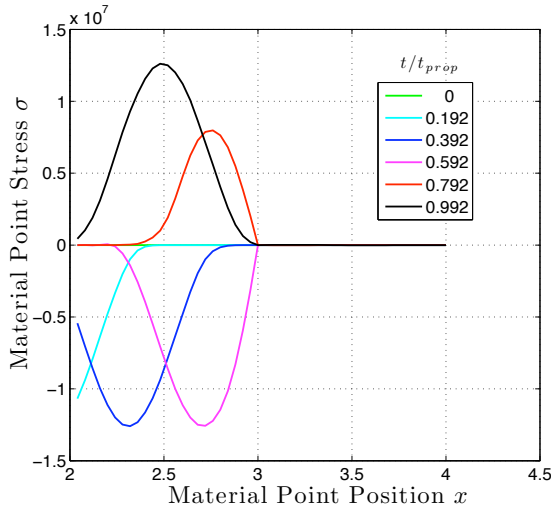
Further, the analytical peak stress of the rightward propagating compressive wave is $\sigma_{max} = -\rho cv_{max}$. Using the imposed boundary condition, the peak stress is -12.6 MPa. This value agrees with the peak compressive stress of the sinusoidal wave before interacting with the gap in Figure 4.11(a).

4.2.7.4 Proposed Boundary Condition Characterization

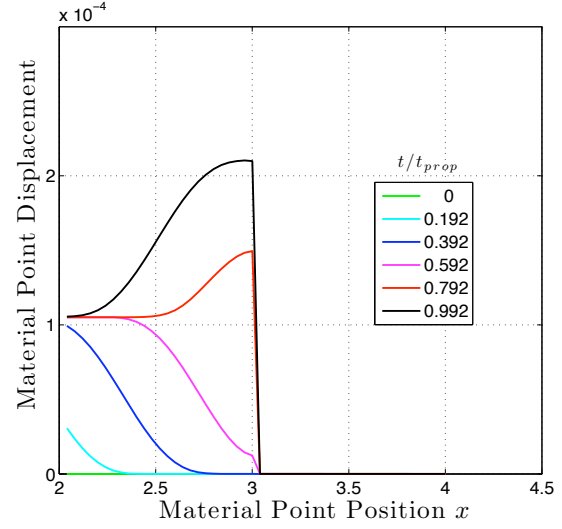
It is proposed that the expression for u_p from Equation (4.50) be used to define the potential for closure of a gap from the effect of the input wave. A gap of size u_{g0} with no resistance to closure will close an amount u_p for one sinusoidal wave reflecting off of it when $u_{g0} > u_p$. If $u_p/u_{g0} > 1$, the gap will fully close and some energy will be transmitted. If $u_p/u_{g0} < 1$, the gap will not close in a single wave reflection.

Next consider a joint filled with rubble that offers resistance to closure. The resistance of a joint implies that if u_p is equal to u_{g0} , the joint will not fully close because a portion of the wave is reflected off of the joint, another portion is propagated past the joint, and the remaining portion is dissipated in closing the joint.

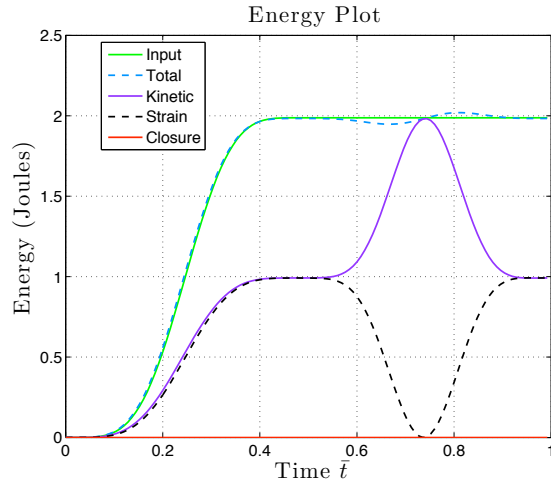
Nevertheless, it is suggested that u_p/u_{g0} be used as a non-dimensional variable to characterize the potential for closure for both gaps and joints.



(a) Material Point Stress



(b) Material Point Displacement



(c) Energy in Bar

Figure 4.11: Response of the bar due to a velocity pulse as defined in Equation (4.44). Figure 4.11(a) is a plot of stress as a function of x for various times. Figure 4.11(b) is a plot of displacement as a function of x for various times. Figure 4.11(c) is a plot of various measures of energy as a function of time.

4.3 Basic Features of Wave Propagation through a Joint

4.3.1 Preliminary Comments

Three constitutive models are proposed in Chapter 4.2. The gap, plastic joint, and elastic plastic joint constitutive algorithms have each been implemented into a dynamic MPM code. The one-dimensional bar is discretized using elements with each element containing one material point. The location of the material points within cells is discussed further in Appendix D because it has an impact on the smoothness of the results. The purpose of the basic features study is to determine the qualitative characteristics of a gap or joint on wave propagation.

4.3.2 One-Dimensional Bar Problem

With use of the one-dimensional dynamic code, numerical solutions are obtained for the bar problem shown in Figure 4.12. Whether single or multiple discontinuities are prescribed,

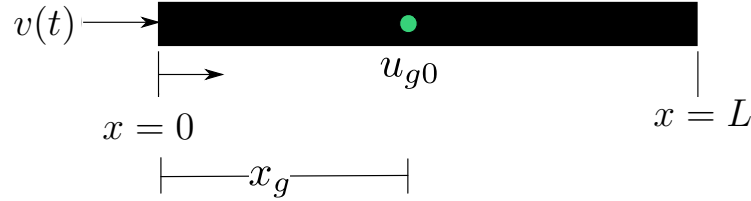


Figure 4.12: Notation for the problem of a bar with a single discontinuity

the first discontinuity will be located in the middle of the bar at $x_g = \frac{L}{2}$. A discontinuity of length u_{g0} is prescribed as a single discontinuity or the sum of multiple discontinuities. The bar has a velocity boundary condition imposed at $x = 0$ and a free surface boundary condition imposed at $x = L$. Initially, the bar is at rest with no prestress. The velocity boundary condition is imposed in the form of a sinusoidal pulse as follows:

$$v(t) = \frac{v_{max}}{2} \left(1 - \cos\left(\frac{2\pi t}{t_{wave}}\right) \right) H[t_{wave} - t]H[t]. \quad (4.51)$$

The prescribed velocity pulse contains two parameters consisting of: v_{max} , the peak particle velocity of the imposed wave, and t_{wave} , the duration of the sinusoidal pulse. As given in Eq. (4.50), u_p is the potential for closure as reflected through the dimensionless variable u_p/u_{g0} .

The parameters of the bar are:

- Length $L = 2$ m,
- Density $\rho = 2650$ kg/m³,
- Youngs modulus $Y = 60$ GPa,
- Circular cross-sectional area $A = 2$ mm²,

- Elastic wave speed $c = \sqrt{\frac{Y}{\rho}} = 4758 \text{ m/s}$,
- Location of the joint is $x_g = \frac{L}{2}$. For multiple joint studies, the first joint is located at x_g and subsequent joints are at specified points greater than x_g ,
- The spatial domain of the bar is discretized using 125 elements with one material point per element. 125 elements presents reasonable convergence with less noise, as shown in Appendix A.

The results of each study and bar parameters are nondimensionalized based on the scheme in Appendix C. Parameters with an over bar denote the dimensionless value. For example, \bar{t} is the dimensionless time. The nondimensionalizing scheme results in a dimensionless elastic wave speed, \bar{c} , of unit value and the dimensionless length of the bar, \bar{L} , of unit value. This ensures the dimensionless propagation time, \bar{t}_{prop} , of an elastic wave traveling from one end of the bar to the other is also of unit value.

$$\bar{t}_{prop} = \frac{\bar{L}}{\bar{c}} = 1 \quad (4.52)$$

The parameters m and σ_g for $g(\bar{u}_g)$ and the stated values of both are shown in Figure 4.9 and used for each numerical solution.

4.3.3 Gap, Plastic Joint, and Elastic-Plastic Joint Comparison

4.3.3.1 Description of Model Problem

To illustrate the effects of the constitutive equations on the solution, consider a bar with a single discontinuity in the middle, as presented in Figure 4.12 and Section 4.3.2. The discontinuity can be characterized as a gap, a plastic joint, or an elastic plastic joint. The initial size of the discontinuity, u_{g0} , is 1 mm. An imposed sinusoidal velocity boundary condition has a peak particle velocity, v_{max} , of 8.31 m/s and a dimensionless wave time $\bar{t}_{wave} = 0.43$. The dimensionless wave time is large enough so that numerical dispersion is minimal for the numerical solution. The potential for closure of a discontinuity u_p is 1.5 mm for this boundary condition (Eqn (4.50)). This implies that a gap with no resistance to closure of initial discontinuity 1 mm will fully close from the propagated wave. A series of four computational runs, including a bar without a discontinuity, are presented to illustrate the impact of each constitutive algorithm on discontinuity behavior and wave propagation. The discontinuity is located halfway along the bar length at approximately $\bar{x} = 1.5$. The dimensionless bar length is of unit value and is centered in a computational domain of length 3.

4.3.3.2 No Discontinuity

Figures 4.13(a) and 4.13(b) show results for the elastic bar with no discontinuity. The compressive wave travels the length of the bar with no interruption, as one would expect. The sum of the kinetic and strain energies in the bar remain constant after the wave is fully

into the bar. The red line of Figure 4.13(b) is the energy that would be dissipated in closing a discontinuity and is zero throughout the run because of the homogenous elastic bar.

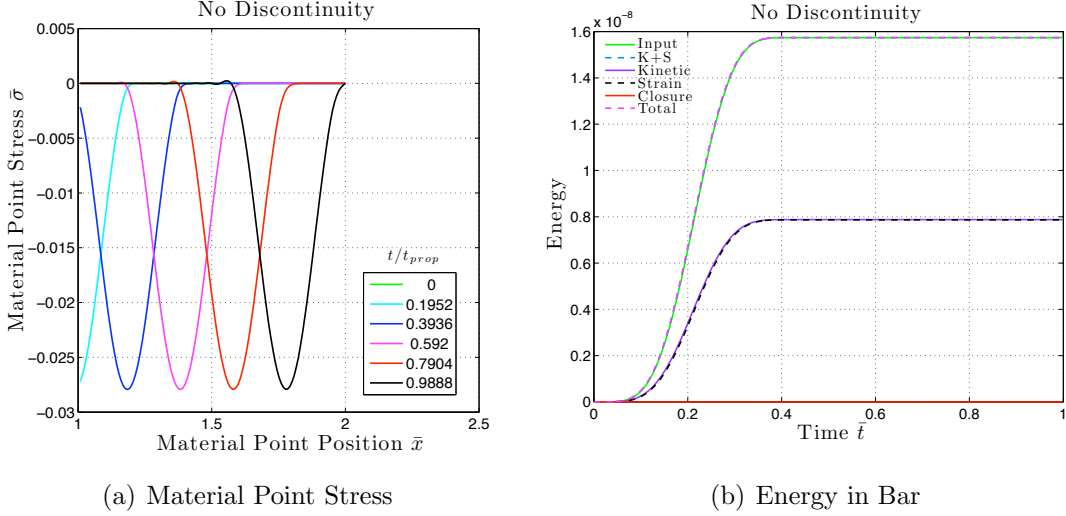


Figure 4.13: Results of wave propagation through a bar without a discontinuity

4.3.3.3 Gap Discontinuity

Figure 4.14 shows results for a bar with a gap. The gap has no resistance to closure and is identical to a free surface. The compressive wave will reflect off of it as a leftward traveling tensile wave until full closure occurs (Fig 4.14(a)). At time $\bar{t} \approx 0.8$, the discontinuity fully closes and no longer acts as a free surface. The remaining portion of the wave can then propagate through the discontinuity continuing as a compressive wave. The numerical procedure cannot resolve the abrupt change that occurs with gap closure with the consequence of small, spurious oscillations after gap closure (plotted times $\bar{t} \approx 0.8$ and 1 (the black and red lines)). The tail end of the reflected tensile wave moving left of $\bar{t} \approx 0.8$ oscillates around zero stress for the same reason. Therefore, once the joint fully closes, the tail of the reflected tensile wave will drop to zero and whatever remains of the initial compressive wave will propagate through the gap. The rightward portion of the compressive wave at \bar{t} of 0.8 is noisy but has the form of the pulse with an almost vertical front face and a tail that has the sinusoidal form of the initial compressive wave. When full closure of the gap occurs, the wave is split at the discontinuity. The front portion of the wave that was reflected as a tensile wave sharply drops to zero stress but its front moving face maintains the shape of the initial pulse. The front face of the continuing compressive wave is steep but the tail assumes the shape of the initial pulse.

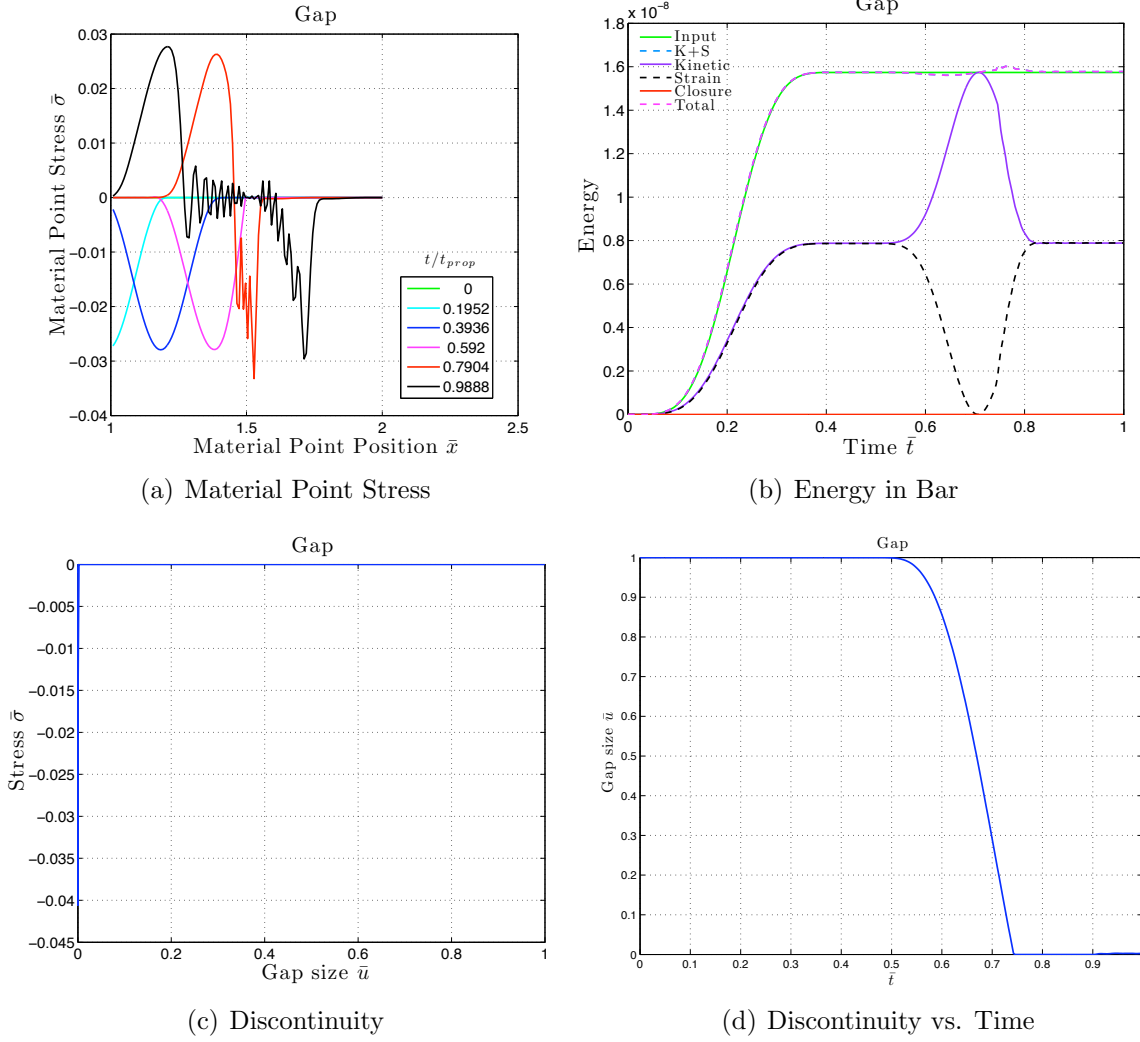


Figure 4.14: Results of wave propagation through a bar with a gap

The energy plot behaves as expected, as shown in Figure 4.14(b). The sum of the kinetic and strain energies remain constant after the wave is fully introduced and equal to that of the input energy. The reflection of the wave at the discontinuity starting initially at $\bar{t} \approx 0.5$ causes equal increases in kinetic and decreases in strain energy so that the sum of the two values remains constant. This is identical to free surface reflection. The closure energy remains zero throughout because the gap dissipates no energy from the compressive wave.

Figure 4.14(c) is the plot of stress versus dimensionless discontinuity \bar{u} . The discontinuity is initially equal to 1. As the compressive wave interacts with it, the gap closes while not withstanding any compressive load. During this period, the wave is fully reflecting off of the discontinuity in the form of a leftward traveling tensile wave. At a discontinuity size \bar{u} equal to zero, the bar becomes continuous, which allows the remainder of the initial compressive wave to propagate past the gap. Figure 4.14(d) is a plot of \bar{u} versus time and is more

insightful than Figure 4.14(c). At time $\bar{t} \approx 0.5$, the gap begins closing, and when $\bar{t} \approx 0.75$, the gap is completely closed.

4.3.3.4 Plastic Joint Discontinuity

Figure 4.15 shows the results of wave propagation through a plastic joint. The discontinuity has resistance to closure and allows part of the initial compressive wave to propagate immediately through the joint. The stress plot in Figure 4.15(a) shows the wave propagating through the joint with very little attenuation. The peak compressive stress after the joint appears to be approximately the same as the peak stress before the joint. A portion of the wave is reflected off of the joint as a tensile wave but the behavior is much smoother than the results for the gap shown in Figure 4.14(a). The majority of the tensile reflection occurs when the wave first interacts with the joint. The nonlinear resistance to closure is much less for a joint closing from $\bar{u}_g = 1$ to $\bar{u}_g = 0.9$ compared to a joint closing from $\bar{u}_g = 0.7$ to $\bar{u}_g = 0.6$. Therefore, more of the front of the compressive wave will reflect off of the joint as a tensile wave because of the initially weaker resistance to closure of the joint.

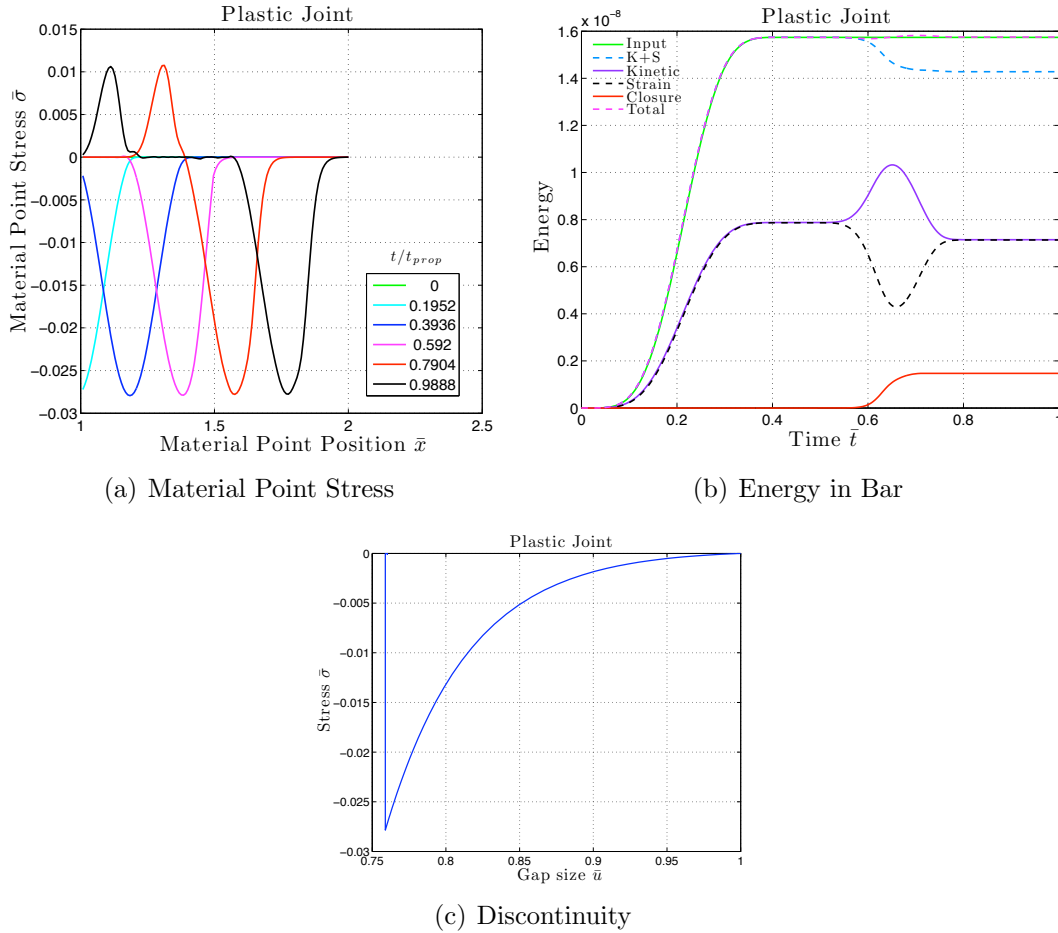


Figure 4.15: Results of wave propagation through a bar with a plastic joint

Once the joint has closed enough to resist any further closure, the majority of the compressive wave will propagate through the joint with little reflection. The length of the wave propagated through the joint is approximately the same length as the initial wave. The reflected tensile wave is much shorter because the joint closed quickly to a state of stress allowing the majority of the wave to continue through as a compressive wave with no further tensile reflection and no further increase in closure.

The plot of energy shown in Figure 4.15(b) demonstrates that the joint dissipates some energy during closure. The blue dotted line is the sum of the strain and kinetic energies in the bar. At dimensionless time $\bar{t} \approx 0.5$, the wave first interacts with the joint. The joint begins to close but not until $\bar{t} \approx 0.6$ does the dissipated energy accumulate enough to be seen on the plot. For \bar{t} between 0.5 and 0.6, the joint is closing but its resistance to closure is small enough that some of the wave reflects off of the joint as a tensile wave. The joint continues closing which requires an increase in energy dissipation until the stiffness of the joint is large enough that no more closure occurs. The closure energy increases while the sum of the strain and kinetic energies decreases. The total energy in the bar defined as the sum of the elastic, kinetic and closure energies remains constant during the joint interaction (the magenta dashed line in Fig 4.15(b)).

Figure 4.15(c) plots the stress at the joint as a function of \bar{u} . As the joint closes, the stress follows the gap function $g(\bar{u}_g)$. The joint closes to a minimum value of $\bar{u} \approx 0.76$ and then unloads to a zero stress state. The unloading is plastic (\bar{u} remains constant), which produces a vertical unloading path. Correspondingly, the surrounding parent rock unloads elastically until zero stress is reached. The peak stress of the gap prior to unloading is $\bar{\sigma} \approx -0.027$. This is also the peak value of stress for the wave after propagating through the joint (Fig 4.15(a)).

4.3.3.5 Elastic-Plastic Joint Discontinuity

For the elastic-plastic joint, the modulus of elasticity for the joint was taken to be constant and is the slope of the function $g(\bar{u}_g)$ when \bar{u}_g is 0.7. The reason for this choice is that for the assumed force on the boundary, the joint will not close below $\bar{u}_g = 0.7$ and an unloading curve with a tangent to the loading cycle seems to agree with the experimental behavior of joints. The ratio of the elastic modulus of the parent rock to the joint modulus is,

$$\frac{E_j}{E_c} = 0.091. \quad (4.53)$$

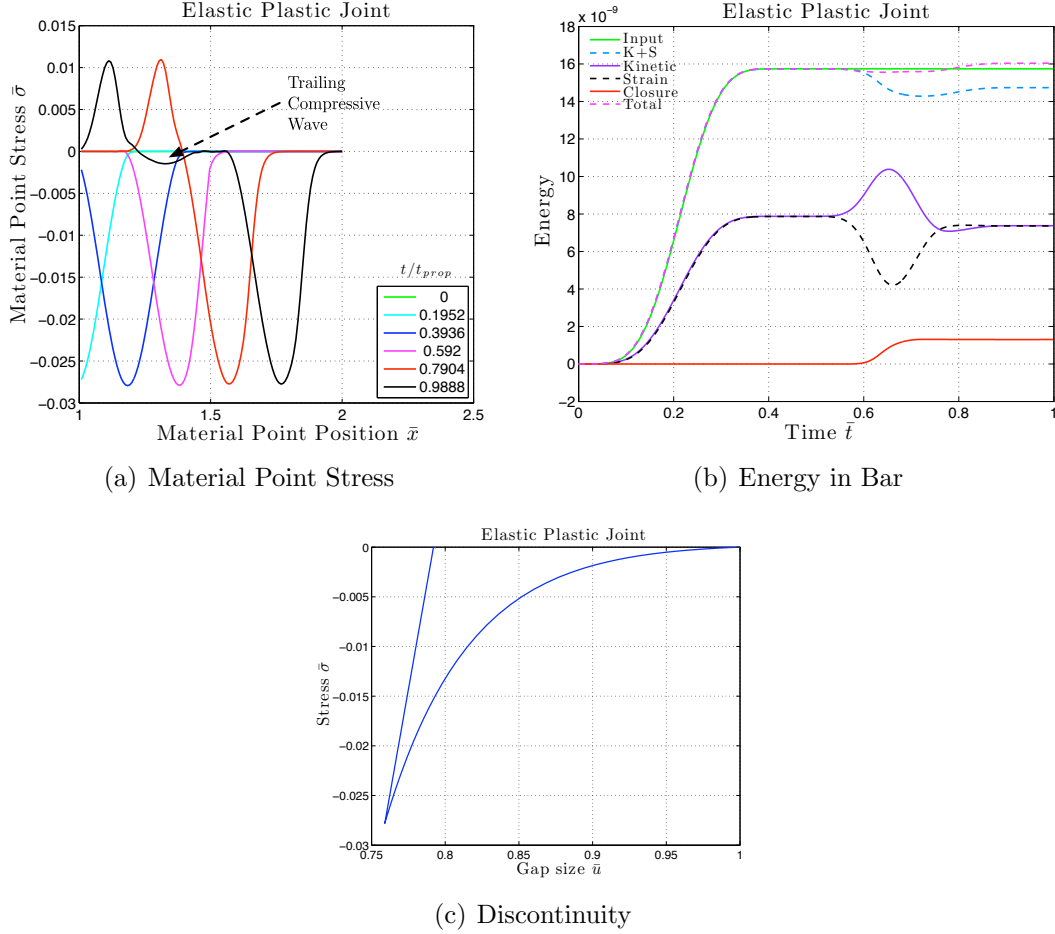


Figure 4.16: Results of wave propagation through a bar with an elastic-plastic joint

Figure 4.16 provides plots of results obtained with an elastic-plastic joint in the bar. The elastic-plastic behavior is very similar to the plastic joint in Section 4.3.3.4. Comparing the stress plots of Figures 4.15(a) and 4.16(a), the compressive wave propagates towards the joint with a portion of the wave reflecting off of it and another portion propagating past and continuing on as a compressive wave. The peak values of the waves in each scenario are approximately the same. The key difference is the plastic joint does not have a compressive wave trailing the reflected tensile wave from the joint. However, the elastic-plastic joint at time $\bar{t} \approx 1$ has a leftward moving compressive wave traveling behind the reflected tensile wave, indicated in Figure 4.16(a). The source of this phenomenon is likely the joint unloading elastically. The modulus of elasticity of the joint is less than the modulus of the parent rock. The discontinuity in moduli might create a separate wave during unloading. Nonetheless, the impact of specifying an elastic-plastic joint as opposed to a plastic joint appears to be minimal.

The energy plot of Figure 4.16(b) does have some slight variance from the plastic joint energy plot. The total energy does move slightly above the input energy of the bar after the

wave propagates through the joint. The scheme of using an effective modulus might be the source of the discrepancy. Nonetheless, the discrepancy is minimal.

The joint behavior in Figure 4.16(c) is almost identical to the plastic joint (Fig 4.15(c)). The peak stress at the joint and the shape of the loading curve is the same. Elasticity causes non-vertical unloading. The joint length \bar{u} does not remain constant due to elasticity as the joint stress unloads fully to zero strain.

4.3.4 Summary

A single discontinuity, whether a gap or joint, causes an attenuation of the input stress wave. As a gap closes, the wave will reflect off of it until full closure occurs. Once the gap fully closes, the remainder of the stress pulse will propagate through the gap. Numerical dispersion occurs during gap closure because of the strong discontinuity in stress caused by the gap. A plastic joint yields a smoother attenuation of the stress pulse in comparison of the results for a gap. As the joint closes, a portion of the wave will reflect off and a portion will propagate through. However, the strong discontinuity in stress is not present for the plastic joint. An elastic-plastic joint behaves almost identically to a plastic joint. The only difference is a small trailing compressive wave that follows the initial tensile reflection off of the elastic-plastic joint.

4.4 Effects of Parameters on Wave Propagation through Single Joint

4.4.1 Program of Single Joint Study

The focus of the one-dimensional study is to qualitatively determine the impact of each constitutive model on wave propagation for a single joint. Figure 4.17 illustrates the single joint study. A joint is placed in the middle of the bar with an initial discontinuity length u_{g0} . A wave is propagated down the bar as shown in Figure 4.12. The wave impulse, peak stress, and energy transmitted through the discontinuity are considered to determine the impact of the discontinuity on wave propagation. The form of the pulse is varied by the wave time t_{wave} and peak particle velocity v_{max} to give the same potential for closure u_p . Also, the initial discontinuity size is varied. The values of the size of initial joint width and parameters of the propagated wave are shown in Table 4.1.



Figure 4.17: Single Discontinuity Study

(a) Boundary Conditions, $u_p = 1.5\text{mm}$

Set	v_{max}	\bar{t}_{wave}
1	7.14 m/s	0.5
2	7.68 m/s	0.465
3	8.31 m/s	0.43
4	9.04 m/s	0.395
5	9.92 m/s	0.36
6	10.99 m/s	0.325
7	12.32 m/s	0.29
8	14.01 m/s	0.255
9	16.23 m/s	0.22
10	19.31 m/s	0.185
11	23.81 m/s	0.15

(b) Initial Discontinuity Size u_{g0}

Set	u_{g0}
1	0 mm
2	0.15 mm
3	0.3 mm
4	0.45 mm
5	0.6 mm
6	0.75 mm
7	0.9 mm
8	1.05 mm
9	1.2 mm
10	1.35 mm
11	1.5 mm

Table 4.1: Inputs used for the single joint sets

4.4.1.1 Study Parameters

Each study uses the same parameters to draw conclusions about wave-joint interaction. The parameters considered are the peak stress, the impulse of the wave, and the energy transmitted past the discontinuity. The peak stress past the discontinuity is related to the peak stress before the discontinuity by

$$\bar{\sigma}_{ratio} = \frac{\bar{\sigma}_{min,right}}{\bar{\sigma}_{min,left}}. \quad (4.54)$$

$\bar{\sigma}_{min,right}$ is the minimum peak stress after the wave has propagated beyond the discontinuity. $\bar{\sigma}_{min,left}$ is the minimum peak stress before the wave has propagated through the discontinuity. Each of these is non-dimensionalized. The impulse value is calculated as

$$I_{ratio} = \frac{\bar{I}_{right}}{\bar{I}_{left}}. \quad (4.55)$$

Again, the subscript *left* and *right* denote the value before propagating past the discontinuity and after propagating past the discontinuity. Both the impulse and peak stress are values found at the material points and are more likely to display unrealistic values because of numerical dispersion. The energy summed across the entire bar is \bar{E}_{total} and is the sum of the kinetic and strain energies for each material point in the bar. The transmitted energy \bar{E}_{trans} is the sum of the kinetic and strain energies only for the material points to the right of the discontinuity. The energy is plotted with the expression

$$E_{ratio} = \frac{\bar{E}_{trans}}{\bar{E}_{total}}. \quad (4.56)$$

The energy values are less susceptible to dispersion because energy is a summed quantity of the the material point values.

4.4.2 Single Discontinuity Study

The first study is a single discontinuity. The gap, plastic joint, and elastic-plastic joint constitutive algorithms are each used for the discontinuity in the middle of the bar. The problem layout is shown in Figure 4.17. The input parameters in Table 4.1 are used for the closure potential u_p of 1.5 mm and the initial joint sizes.

4.4.2.1 Gap

The single discontinuity study begins with the gap. The corresponding results are shown in Figure 4.18. The gap enables intuitive expectations of the discontinuity behavior to be confirmed. When the initial discontinuity u_{g0} is zero, all of the wave energy should propagate past the gap. The peak stress and impulse should be the same on either side of the gap. Conversely, when u_{g0} is equal to u_p , the wave should not propagate past the gap. The impulse and peak stress should be zero past the gap. And, no energy should be transmitted through the gap.

In Figure 4.18(a), when u_{g0}/u_p is equal to one no energy is transmitted because total gap closure occurs at the end of the wave reflection. For $u_{g0}/u_p = 0$, all of the energy is transmitted past the gap. This behavior is the same for the impulse and peak stress in Figures 4.18(c) and 4.18(b), respectively.

The wave characteristics seem to have little impact on the amount of transmitted energy. Regardless of v_{max} and \bar{t}_{wave} , the results of transmitted energy plot on top of one another (Fig 4.18(a)). This does not hold for the impulse or peak stress. The results for peak stress and impulse of each run are not fully shown in Figure 4.18. The wave impulse for each wave input lay close to one another (Fig 4.18(c)). But, the peak stress does not. For smaller \bar{t}_{wave} values, a larger peak stress occurs past the gap than before the gap. These results do not seem plausible and are due to numerical dispersion associated with a jump in stress once the gap closes. Individual material point quantities are particularly susceptible to numerical dispersion and make the results without much dispersion difficult to interpret on the same axis. The forcing function with small values of \bar{t}_{wave} result in significant dispersion. Peak stress and impulse are plotted for every run and shown in Figure E.1 in Appendix E.

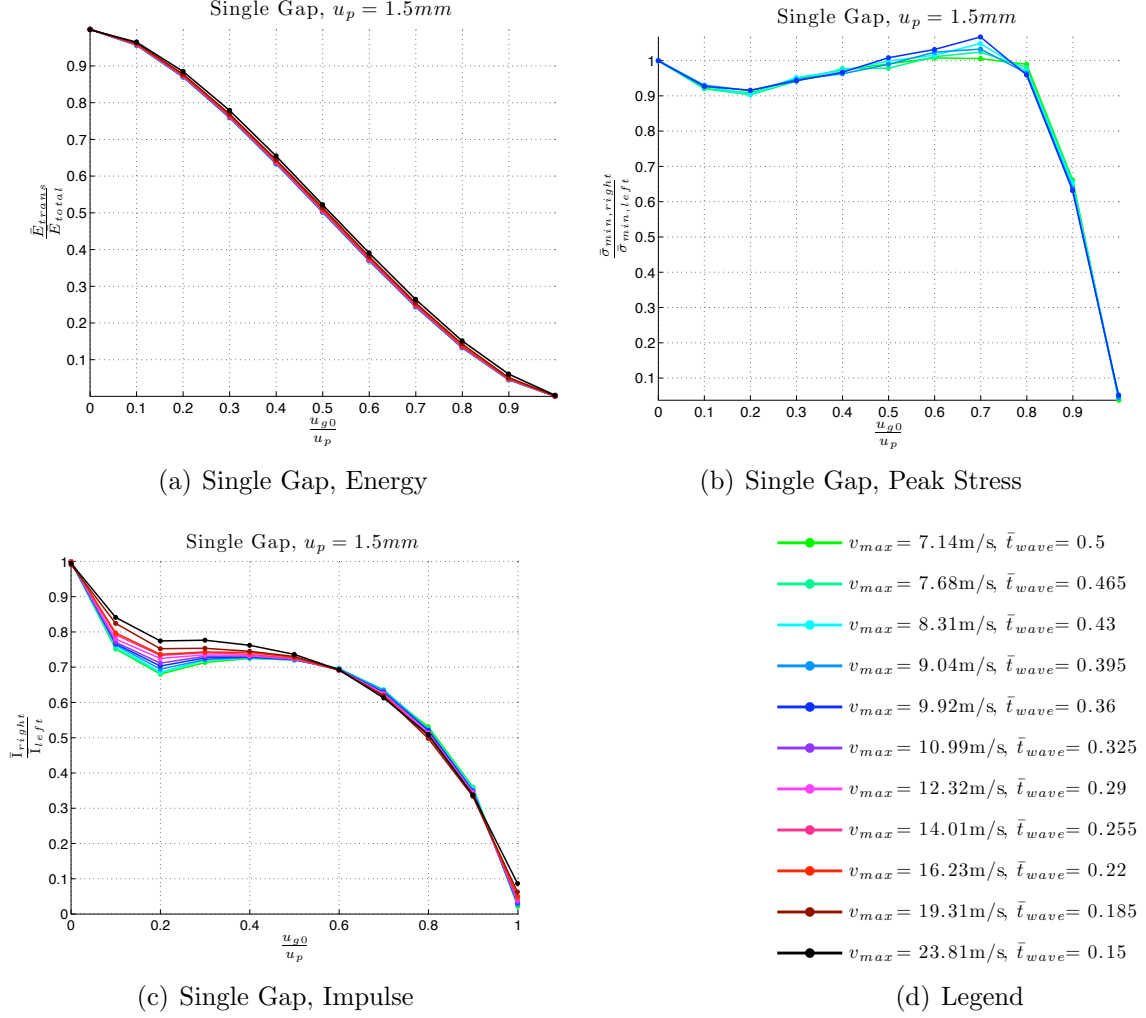


Figure 4.18: Plots of results for wave propagation through a single gap with $u_p = 1.5\text{mm}$

Conclusions of Single Gap Study

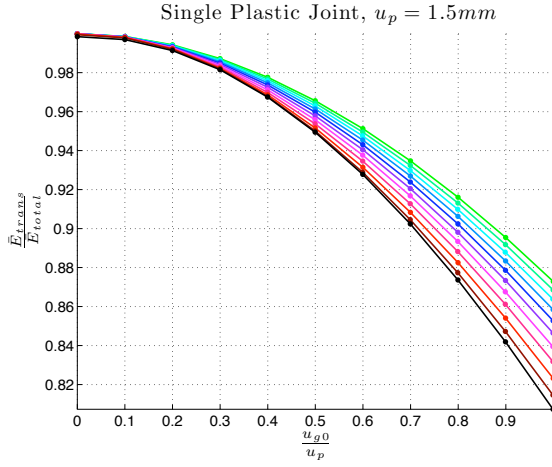
- The significant parameter for wave propagation through a single gap is u_{g0}/u_p .
- The energy transmitted past a gap is approximately constant regardless of the wave characteristics. As long as u_p is the same for a sinusoidal pulse, v_{max} and \bar{t}_{wave} do not impact the transmitted energy.
- The peak stress is very close to one when u_{g0}/u_p is less than one. This only applies to waves of $\bar{t}_{wave} \geq 0.395$.

4.4.2.2 Plastic Joint

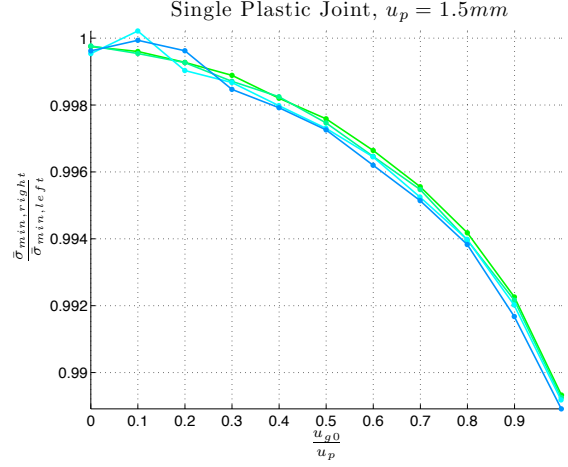
The inputs of the single plastic joint study are the same as the single gap study. The results are presented in the same manner as well, shown in Figure 4.19. For an initial gap size

of zero, the transmitted energy, peak stress, and wave impulse are the same for each wave input and are either one or close to one. These results are expected. The energy plot of Figure 4.19(a) shows that more energy is transmitted past the plastic joint for a longer wave time \bar{t}_{wave} for all values of u_{g0}/u_p . This conclusion is expected because a long wave interacts with a joint for a longer period of time allowing it to propagate more energy as opposed to reflecting off the joint quickly. The peak stress curves in Figure 4.19(b) lie on top of one another for the input parameters of \bar{t}_{wave} 0.5, 0.465, 0.43, and 0.395. The peak stress drops slightly as u_{g0}/u_p is closer to one. The result is intuitive because the larger the joint, the more energy will be dissipated in closing it before a large portion of the energy can propagate through. However, for other input parameters, the peak stress result is greater than one. This should not occur with the constitutive algorithm. The behavior comes from numerical dispersion and the results are omitted. The full results are shown in Figure E.2. The peak stress grows for smaller wave times and appears to peak when u_{g0}/u_p is between 0.6 and 0.8 for the smaller wave times. The wave impulse decreases with larger u_{g0} (Fig 4.19(c)). The longer the wave the larger the impulse transmitted for wave times between 0.5 and 0.36. For wave times shorter than this, the characteristic breaks down due to numerical error.

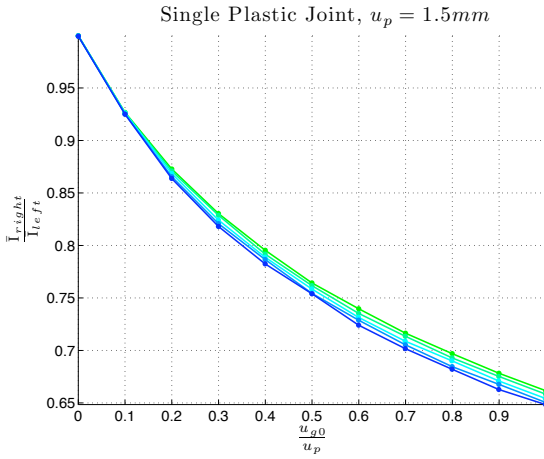
The results for peak stress and impulse of each run are not fully shown in Figure E.2 of Appendix E. Individual material point quantities are particularly susceptible to numerical dispersion, which can skew the results. The input boundary conditions with small values of \bar{t}_{wave} result in significant errors. For \bar{t}_{wave} less than 0.36, the characteristic features break down due to numerical error.



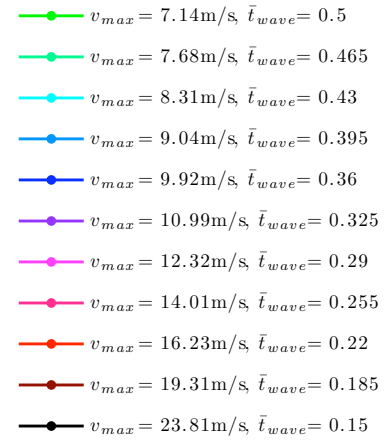
(a) Single Plastic Joint, Energy



(b) Single Plastic Joint, Peak Stress



(c) Single Plastic Joint, Impulse



(d) Legend

Figure 4.19: Plots of results for a wave transmitted through a single plastic joint with $u_p = 1.5\text{mm}$.

Conclusions of Single Plastic Joint Study

- The longer the wave time, the more energy is transmitted past the plastic joint.
- The larger the initial discontinuity size, the less the peak stress transmitted past the joint. This only holds for wave times greater than 0.395 because numerical error makes determining the characteristics difficult.
- The wave impulse decreases with larger initial discontinuity size for wave times greater than 0.36.

4.4.2.3 Elastic-Plastic Joint

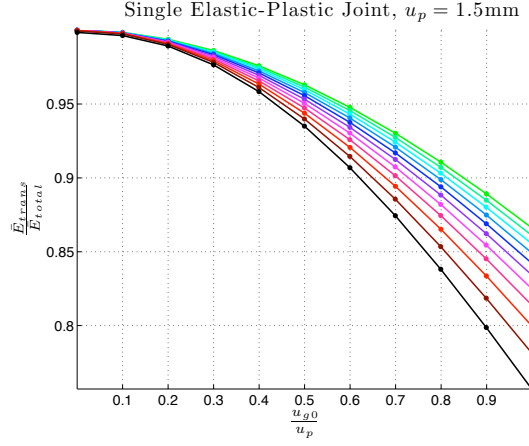
The characteristic behavior of the single elastic-plastic joint is very similar to the plastic joint. The results of Figure 4.20 present similar qualitative characteristics as Figure 4.19.

Conclusions of Single Elastic-Plastic Joint Study

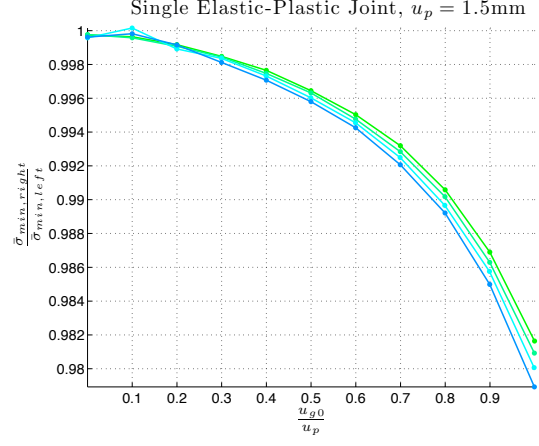
- The wave-joint interaction of an elastic-plastic joint has similar characteristics of a plastic joint.
- Slightly less energy is transmitted past an elastic-plastic joint than a plastic joint. The qualitative characteristics of both are the same.
- Slightly less peak stress is transmitted past an elastic-plastic joint than a plastic joint. The impact of wave characteristics on peak transmitted stress is the same.
- Slightly less impulse is transmitted past an elastic-plastic joint than a plastic joint. The impact of wave characteristics on wave impulse is the same.

4.4.3 Single Joint Conclusions

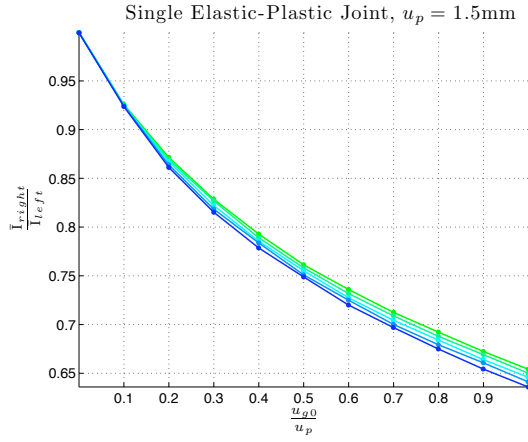
Overall, the study of single gaps and single joints yielded several conclusive results. The goal of the study was to determine the impact of wave parameters and initial joint size on energy transmission, impulse, and peak stress. Due to numerical errors introduced that are more pronounced by small values of \bar{t}_{wave} , the impulse and peak stress could not be concretely determined because each value is calculated at a material point. This was the case for a gap, a plastic joint, and an elastic-plastic joint. The results for energy transmission were less effected by numerical error because the energy is summed over multiple material points. For a gap, energy transmission was the same for values of u_{g0}/u_p , and the wave parameters v_{max} and \bar{t}_{wave} had no impact. For a plastic joint, more energy was transmitted through the discontinuity for larger values of \bar{t}_{wave} . The reason for this is that a longer wave spends a longer period of time interacting with the joint. Because the joint has nonlinear resistance to closure, a longer wave-joint interaction time forces the joint to a stress state that can allow the remainder of the wave to propagate past. For an elastic-plastic joint, the results led to the same conclusion. The elastic-plastic joint does not behave significantly different from a plastic joint. The key difference between the two is that the amount of energy transmitted



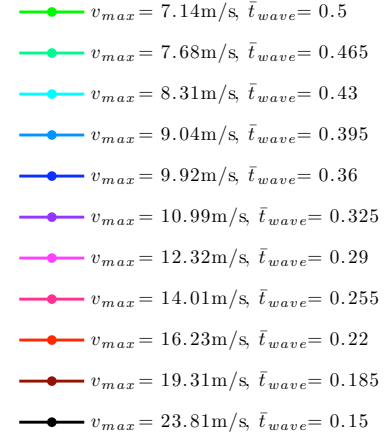
(a) Single Elastic-Plastic Joint, Energy



(b) Single Elastic-Plastic Joint, Peak Stress



(c) Single Elastic-Plastic Joint, Impulse



(d) Legend

Figure 4.20: Plots of results for a wave transmitted through a single, elastic-plastic joint with $u_p = 1.5\text{mm}$.

through an elastic-plastic joint is slightly less than that of a plastic joint for identical values of initial discontinuity size and wave parameters \bar{t}_{wave} and v_{max} .

4.5 Effects of Parameters on Wave Propagation through Two Joints

4.5.1 Preliminary Comments

Appendices F and G present two studies (and numerical results), which motivate this chapter. The intent of those studies was to find the impact of lumping joints into fewer joints and the spacing of two joints on wave propagation. After analyzing the results of the lumping gaps (Fig F.1), the issue arose that n gaps of equal initial size u_p/n allowed energy to be transmitted through the gaps. Whereas, a single gap of initial size u_p does not allow any energy to be transmitted past. Intuitively, whether a gap with no resistance to closure or two gaps with no resistance to closure, one would expect that no energy would be transmitted past them.

The results of the lumping gap study are plotted in Figure 4.21 (also included in Appendix F). One would expect no energy to propagate past the set of gaps when the sum of initial gap sizes u_{g0} is equal to the potential for closure of the input wave u_p . For a single gap, the results are as expected and satisfactory, as the entire compressive wave is reflected off of the gap. But, for multiple gaps, energy does propagate past the gaps. Further exploration is conducted to understand the impact of these unexpected results by increasing the distance between two gaps and analyzing the propagating wave.

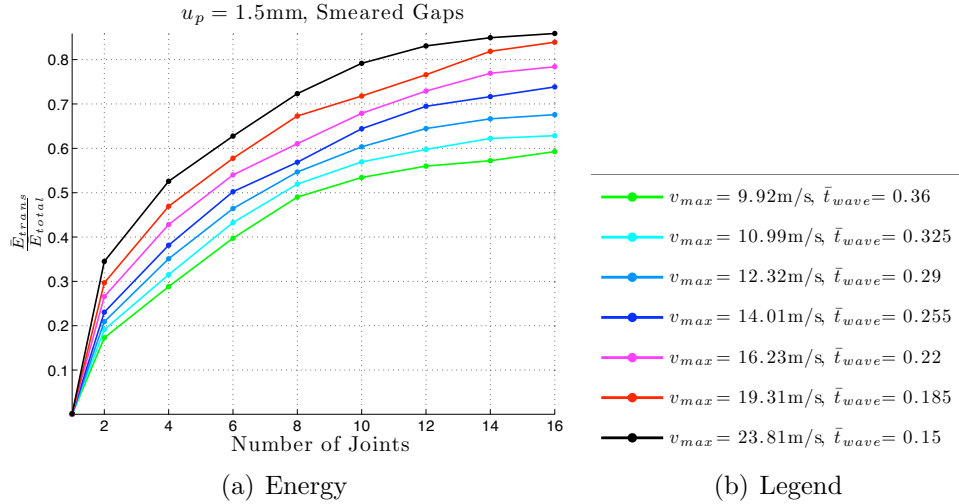


Figure 4.21: Transmitted energy results for multiple gap study

4.5.1.1 Lumping Joints Study

As discussed above, the study of lumping multiple joints illustrated in Figure F.1 warranted further exploration. The results are provided in Appendix F. The key result is that more energy is transmitted through multiple joints than transmitted through one equivalent joint

with the same total potential for closure. The study was conducted on gaps, plastic joints, and elastic-plastic joints with prescribed $u_{g0} = 1.5\text{mm}$ and $u_{g0} = 0.5\text{mm}$.

4.5.1.2 Joint Spacing Study

The numerical solutions to the study are provided in Appendix G. Two joints were prescribed in the middle of the bar, and the distance between the two was varied for each run. The tentative conclusion is that the more spacing between gaps, the less energy is transmitted. The results for plastic joints are not as susceptible to spacing issues as gaps. However, these results may not be conclusive because of wave trapping discussed below.

4.5.2 Study of Wave Propagation Through Two Gaps

4.5.2.1 Illustrative Results

To produce clearer numerical results, 250 material points and one material point per cell were prescribed to discretize the bar (rather than the previously proposed 125). The finer mesh was chosen because dispersion introduced by two discontinuities is less prominent with 250 versus 125 material points (Appendix B presents a convergence study for two gaps). The spacing between two gaps is varied by specifying the number of material points between the two gaps. The gaps have equal initial discontinuities of size $u_{g0}/2$, where u_{g0} is 1.5mm. The sinusoidal pulse is defined by parameter values of $v_{max} = 9.92\text{m/s}$ and $\bar{t}_{wave} = 0.36$, which produces a value of $u_p = 1.5\text{mm}$. The initial total discontinuity size is $u_{g0} = 1.5\text{mm}$. The value of \bar{t}_{wave} was chosen to allow the full length of the wave to fit in the length of the bar to the right of the second discontinuity. The value of v_{max} produces a wave that has a potential for closure equal to the total initial discontinuity size. These values are reported in Table 4.1(a). The gaps are spaced by specifying the number of material points separating them. As shown in Table 4.1(b), the material point spacing is equivalent to $\Delta\bar{x}_{gap}$, which is the dimensionless length between the two material points with prescribed gaps. The dimensionless value $\Delta\bar{x}_{gap}/\bar{t}_{wave}$ relates the gap spacing to the length of the wave. This value was chosen to better determine the relationship between gap spacing and wave length.

(a) Boundary Conditions, $u_p = 1.5\text{mm}$

v_{max}	\bar{t}_{wave}
9.92 m/s	0.36

(b) Discontinuity Spacing

MP Spacing	$\Delta\bar{x}_{gap}$	$\Delta\bar{x}_{gap}/\bar{t}_{wave}$
10	0.04	0.111
20	0.08	0.222
30	0.12	0.333
40	0.16	0.444

Table 4.2: Inputs used for gap spacing

Stress at each material point is plotted at various times for each spacing in Figure 4.22. In each run, the results are similar regardless of gap spacing. The initial compressive pulse propagates to the first gap as expected. The first (left-most) gap will close upon wave-joint

interaction. The closure introduces numerical dispersion because of the discontinuity in stress. The first portion of the wave reflects off the gap as a leftward traveling tensile pulse and the remainder propagates through the gap. The continuing compressive wave interacts with the second gap. Because the size of initial discontinuity of both gaps is $u_p/2$, the second gap also closes. During closure of the second gap, the compressive wave is reflected as a tensile wave traveling left. Gaps have no strength in tension, therefore, the now leftward traveling wave between the two gaps will reflect off of the first gap, which opens, and the pulse becomes a rightward traveling compressive wave. This event will be referred to as wave trapping. At this point, the right gap is already closed, and the trapped compressive wave propagates through it without disturbance. Wave trapping between gaps is the reason wave propagation was occurring through the sets of gaps for the lumping gap study. There is a noticeable slowing of the wave front due to the reflections. The greater the distance between gaps, the more time is required for the wave to propagate through the gaps to the right end of the bar. For $\Delta\bar{x}_{gap}/\bar{t}_{wave}$ values of 0.333 and 0.444, $\bar{t} > 1.3$ when the wave front gets to the right end. Further, wave trapping increases the length of wave travel as it propagates from one end of the bar to other.

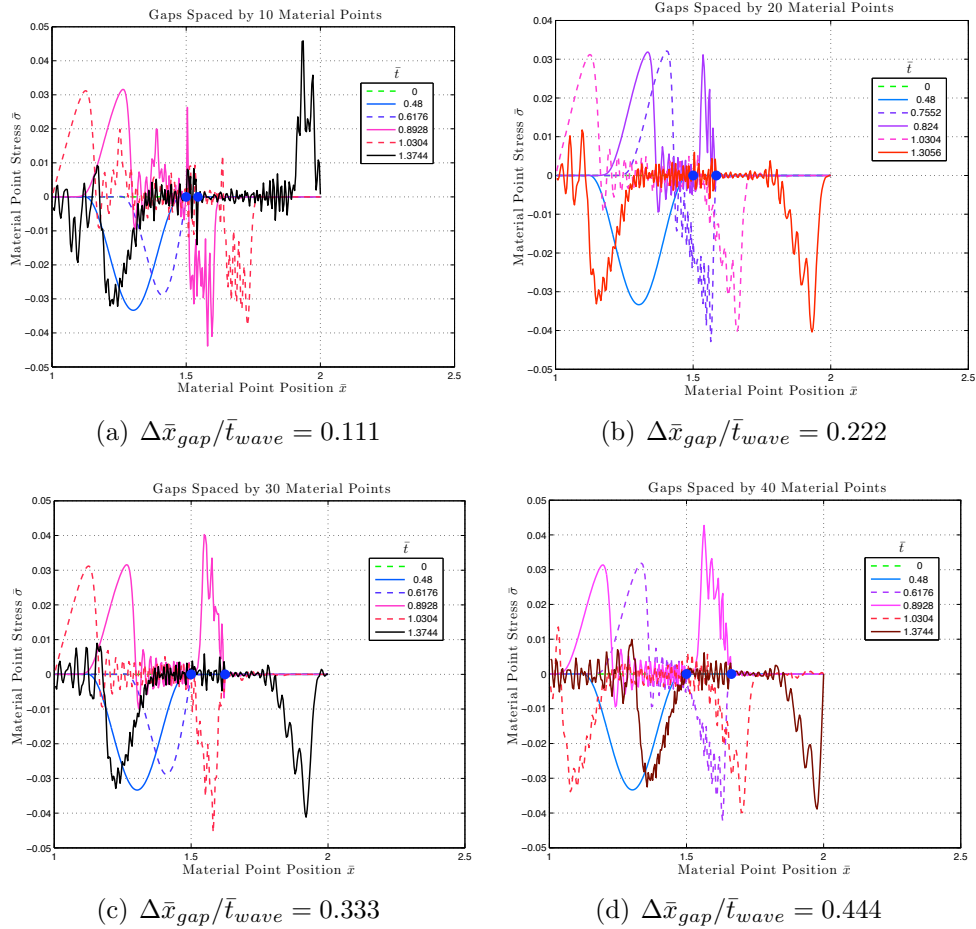


Figure 4.22: Plots of stress for different gap spacings (blue dots denote locations of gaps)

The energy transmitted through the gaps was also analyzed. Figure 4.23 shows the plots of energy transmitted through the gaps versus dimensionless time. Figures 4.23(b), 4.23(c), and 4.23(d) each show approximately 0.5 of total energy transmitted through the gaps at the end of each run. The run with a $\Delta\bar{x}_{gap}/\bar{t}_{wave}$ of value 0.111 is only 0.45 at the final time, which may be due to numerical error. When the gaps are close to one another, the discretization is not able to properly represent the wave. Nonetheless, if half of the total energy gets through the gaps, half of the wave energy is reflected off of the first gap. The second half of the wave is trapped in between the gaps then eventually propagates through the second gap. Only half of the wave is reflected in closing the first gap of size $u_p/2$. And, half of the wave is reflected at the second gap. But after wave trapping, the wave can propagate through the closed second gap.

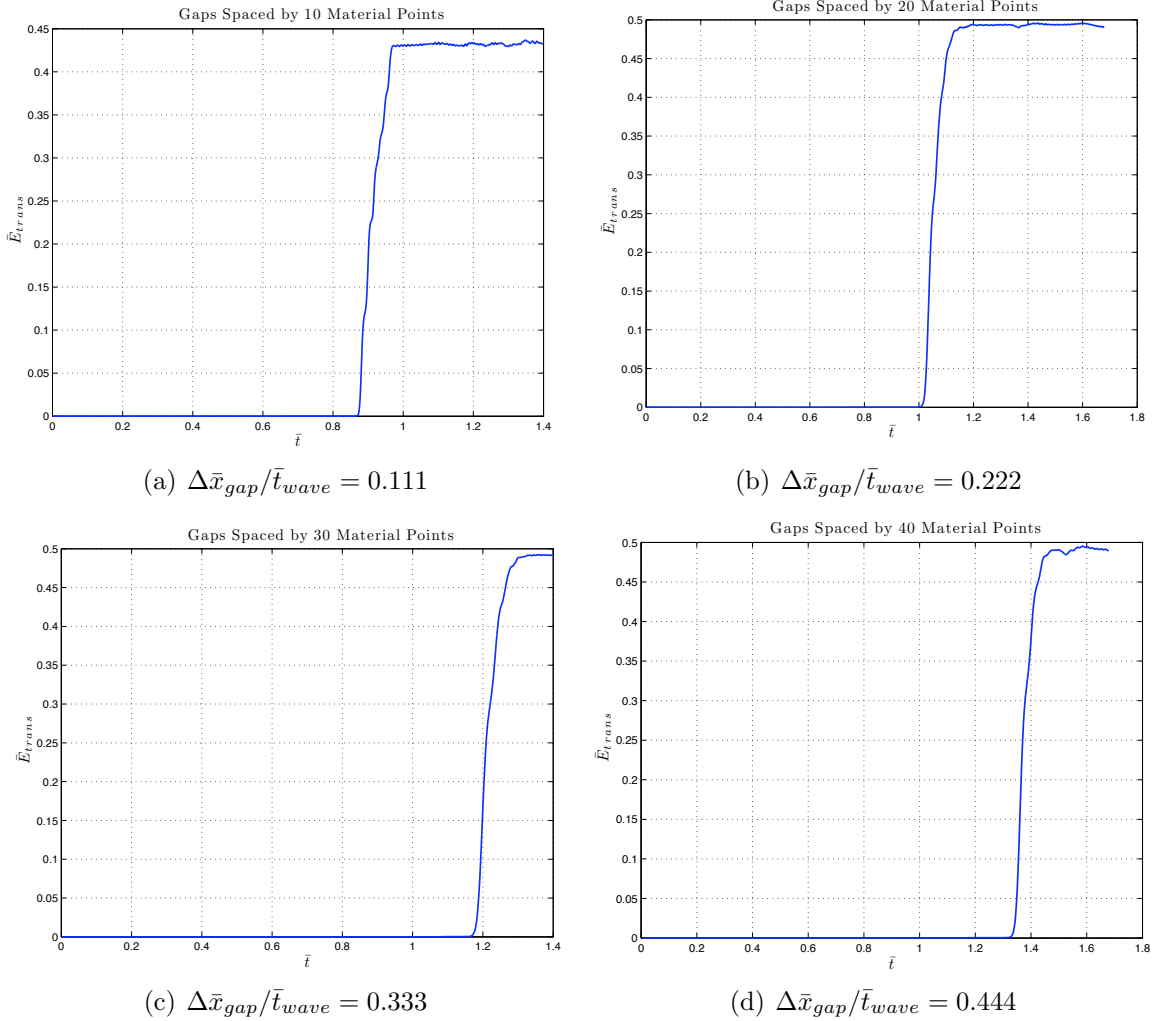


Figure 4.23: Results for transmitted energy due to gap spacing

4.5.2.2 In-Depth Details for Two Joints

The results of wave propagation through two gaps with a spacing value $\Delta\bar{x}_{gap} = 0.16$ is shown in greater detail in Figure 4.24. Each plot is the material point stress at various times. (1) is the earliest plotted time, and (6) is the latest plotted time. Beginning with (1), the process of wave propagation is:

- (1) The compressive pulse **A** originates at the left end of the bar and propagates left towards the first gap.
- (2) Wave **A** closes the first gap, splitting the wave in half. Wave **B** reflects off of the first gap as a leftward traveling tensile wave. Wave **A** propagates through the closed first gap.
- (3) Wave **B** propagates towards the left end of the bar. Wave **A** closes the second gap and reflects off of it as a leftward traveling tensile pulse.
- (4) Wave **B** begins to reflect off of the left end of the bar. Wave **A** reflects off of the first gap and becomes a rightward traveling compressive pulse. The reflection of the tensile wave on the closed gap causes the first gap to open.
- (5) Wave **B** reflects off the left end of the bar. Wave **A** propagates through the closed gap.
- (6) Wave **B** and wave **A** are rightward traveling compressive pulses. The entirety of wave **A** has propagated through both gaps.

The close-open cycle of the first (left) gap is shown in Figure 4.25(a). The first gap opens because of the tensile reflection in Figure 4.24 at (3) after initially closing at (2). Figure 4.25(b) illustrates the closing of the second (right) gap versus time. The right gap closes at (2) in Figure 4.24 and remains closed.

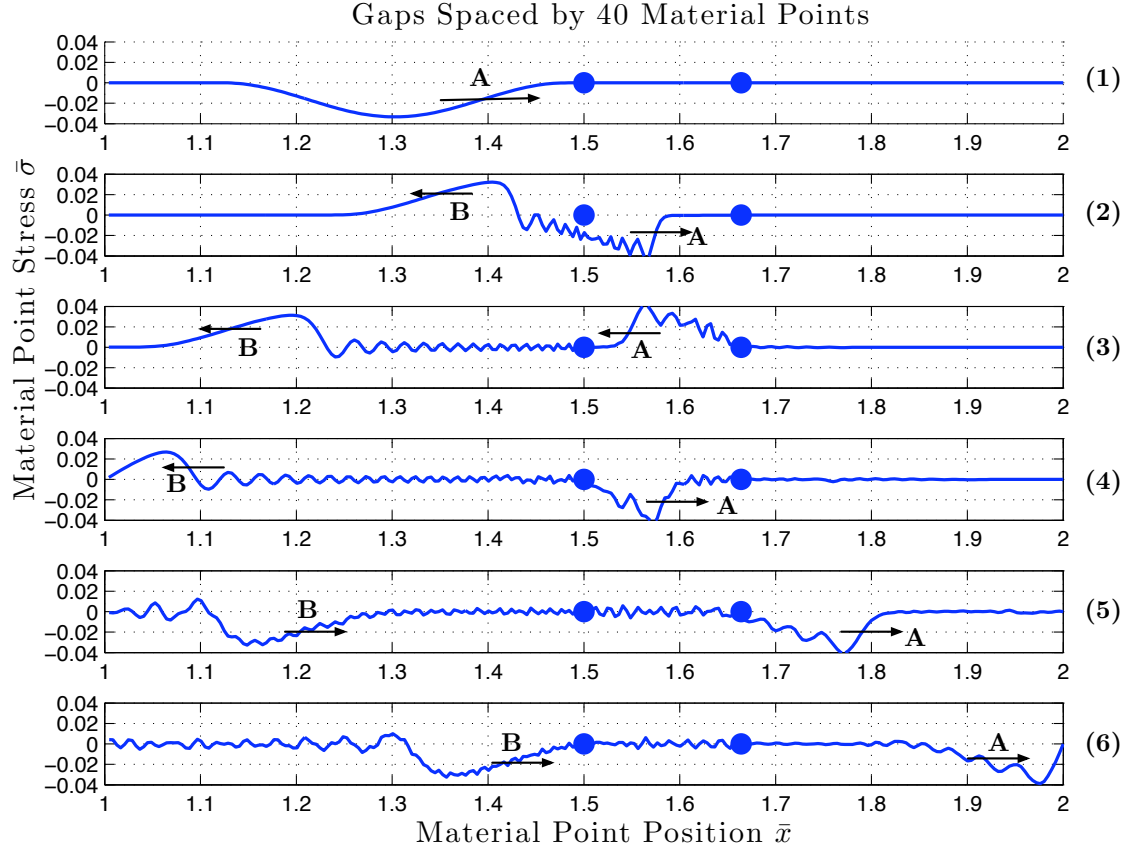


Figure 4.24: Stress plots at various time of wave propagation through two gaps spaced 40 material points apart (blue dots denote gap locations)

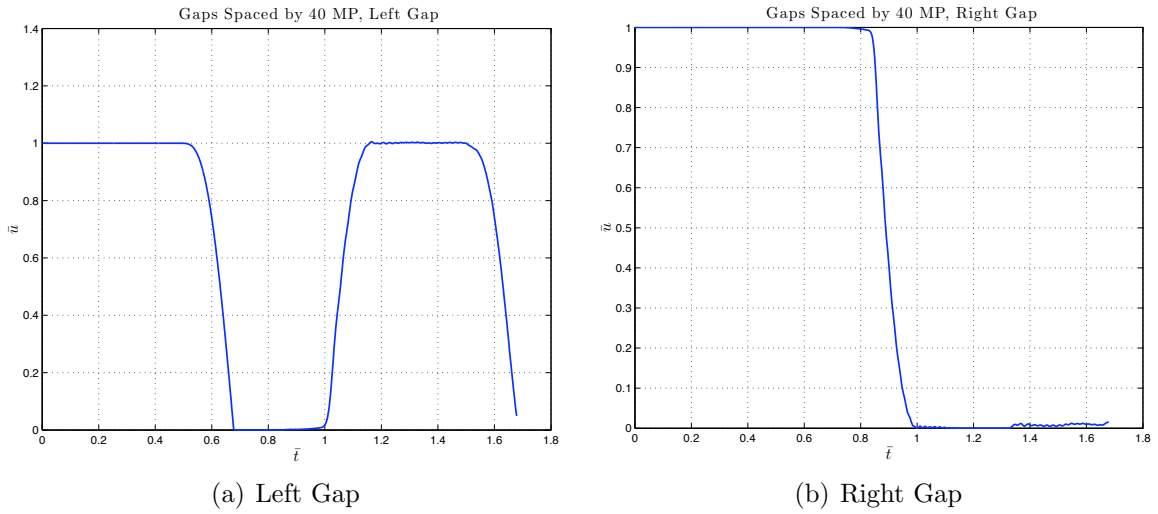


Figure 4.25: \bar{u} versus time for each gap

4.5.3 Propagation of a Wave Through Two Plastic Joints

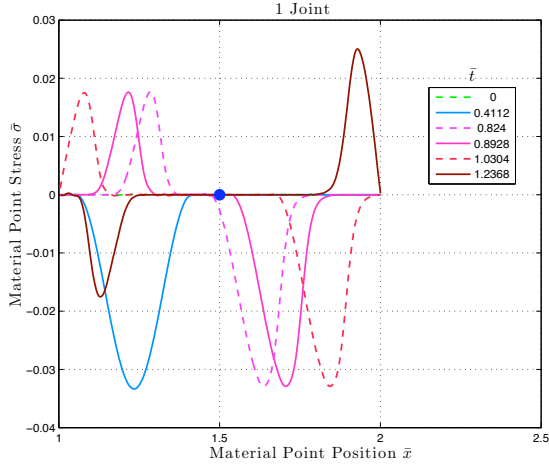
4.5.3.1 Illustrative Results

Runs with identical wave inputs to those shown in Section 4.5.2 were gathered for two plastic joints as well. Rather than analyzing a bar with two joints spaced by $\Delta\bar{x}_{joint} = 0.04$ (the first run in the two gap study), a bar with a single joint was analyzed. Comparing the single joint results with joint spacing results can give clearer insight into the possibility of joint lumping.

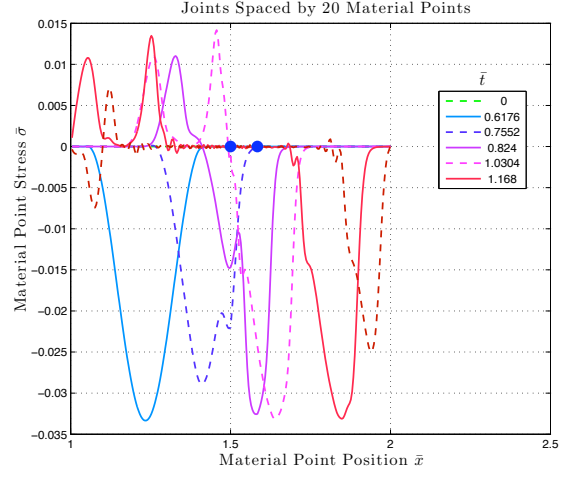
Figure 4.26 shows the plots of material point stress at various times. A single joint behaves as expected. The compressive wave is split into a tensile reflection off of the joint and a continuing compressive pulse. For two joints, wave splitting occurs twice. Therefore, the original wave will split into three separate waves after propagating through both joints. For each run, there's an initial reflection off of the first joint and a continuing compressive wave. The continuing compressive wave propagates through the second joint but part of the wave is reflected as a tensile pulse. The tensile pulse is trapped between the two joints and reflects off of the first to continue through the second joint as a compressive pulse. At this point, there are two distinct waves that have propagated through the joints. The closer the joints are to one another, the more indistinguishable the two separate waves become. Also, the time required for the wave front to reach the right end of the bar is slightly greater than the elastic propagation time because of the increase in travel distance of the wave due to wave trapping.

The energy plots were not considered for the two gap study because no energy dissipation occurs in closing gaps. For the two joint study, energy plots are important because energy is dissipated through joint closure. Figure 4.28 shows the plots of different energies versus time for each run. In each run, the kinetic and strain energy both began to alter at $\bar{t} = 0.5$. This is when the wave interacts with the first joint. For the spaced joints, a similar kinetic and strain energy attenuation occurs slightly thereafter because of the second joint. During these wave-joint interactions, the closure energy increases because the joints are being closed. Also, the sum of the kinetic and strain energies decrease, which is a result of the dissipated closure energy.

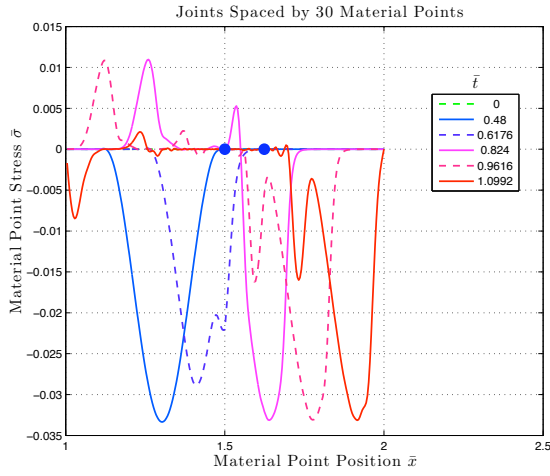
Table 4.3 displays the ratio of maximum closure energy for each run in relation to the maximum closure energy for a single equivalent joint. For a single joint, this value is one. For two joints of the prescribed spacings, the closure energy is 0.68% greater than the single joint. This implies that regardless of joint spacing, the same amount of energy will be dissipated in closing the joints. Also, if two joints only dissipate 0.68% more energy than a single joint, certain computations may warrant lumping multiple joints into fewer discontinuities to increase computing efficiency.



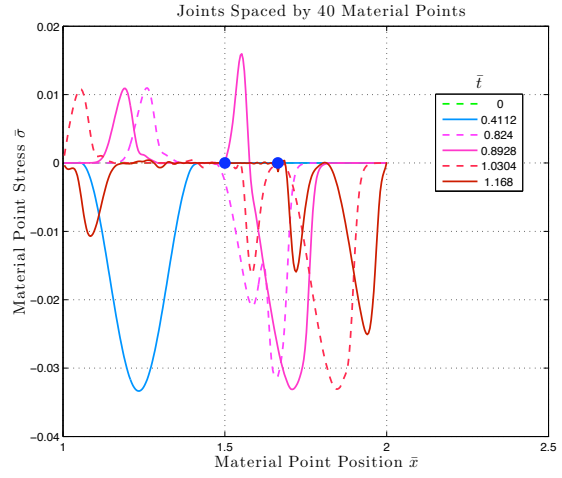
(a) 1 Joint



(b) $\Delta \bar{x}_{joint}/\bar{t}_{wave} = 0.222$



(c) $\Delta \bar{x}_{joint}/\bar{t}_{wave} = 0.333$



(d) $\Delta \bar{x}_{joint}/\bar{t}_{wave} = 0.444$

Figure 4.26: Plots of material point stress for multiple joint spacing (blue dots denote joint locations)

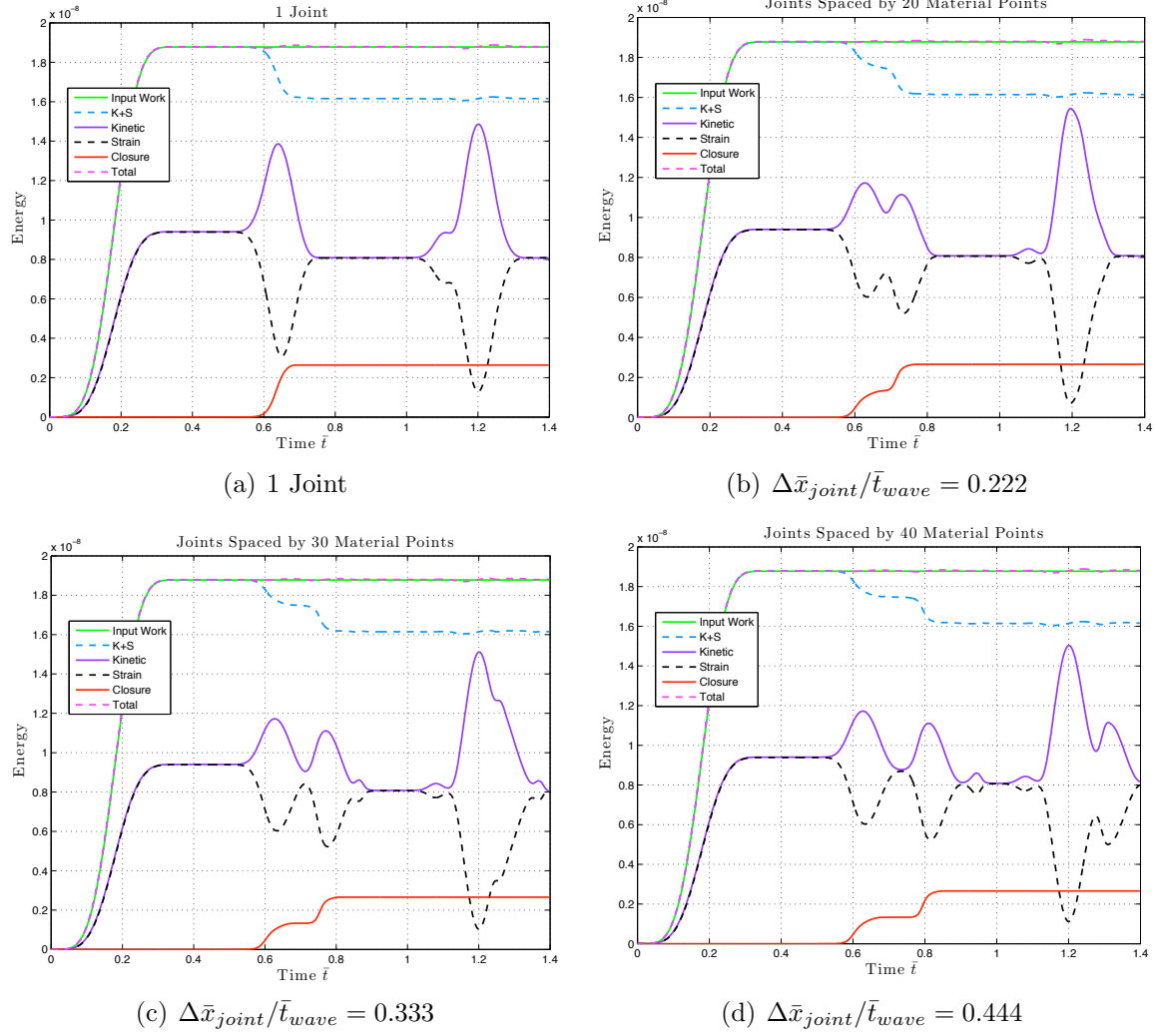


Figure 4.27: Energy versus time plots for multiple joint spacings

MP Spacing	$\bar{E}_{close} / \bar{E}_{close,1joint}$
1 Joint	1
20 MP	1.0068
30 MP	1.0068
40 MP	1.0068

Table 4.3: Energy dissipated in closing the joints

While the energy dissipated in propagating a wave through two joints is close to the energy dissipated through a single equivalent joint, the amount of energy transmitted through two joints is not the same as a single equivalent joint. Figure 4.28 illustrates the energy transmitted through the joints during wave propagation. A single joint allows approximately

73% of the total energy to be transmitted. Two joints transmit 81% to 96% of the total energy, depending on spacing. The reason is that less of the wave is reflected off of the first joint (as compared to the single joint) and the portion of the wave reflected off of the second joint is trapped between the two joints and eventually propagates through the second joint after reflecting off the first. Multiple joints split up portions of the wave multiple smaller waves which become trapped between joints and eventually propagate through. Whereas, a single joint reflects a larger portion of the wave that will not reflect back through the initial joint because there isn't another joint for the tensile wave to reflect off of again. In other words, a single joint does not produce the wave trapping effects of multiple joints.

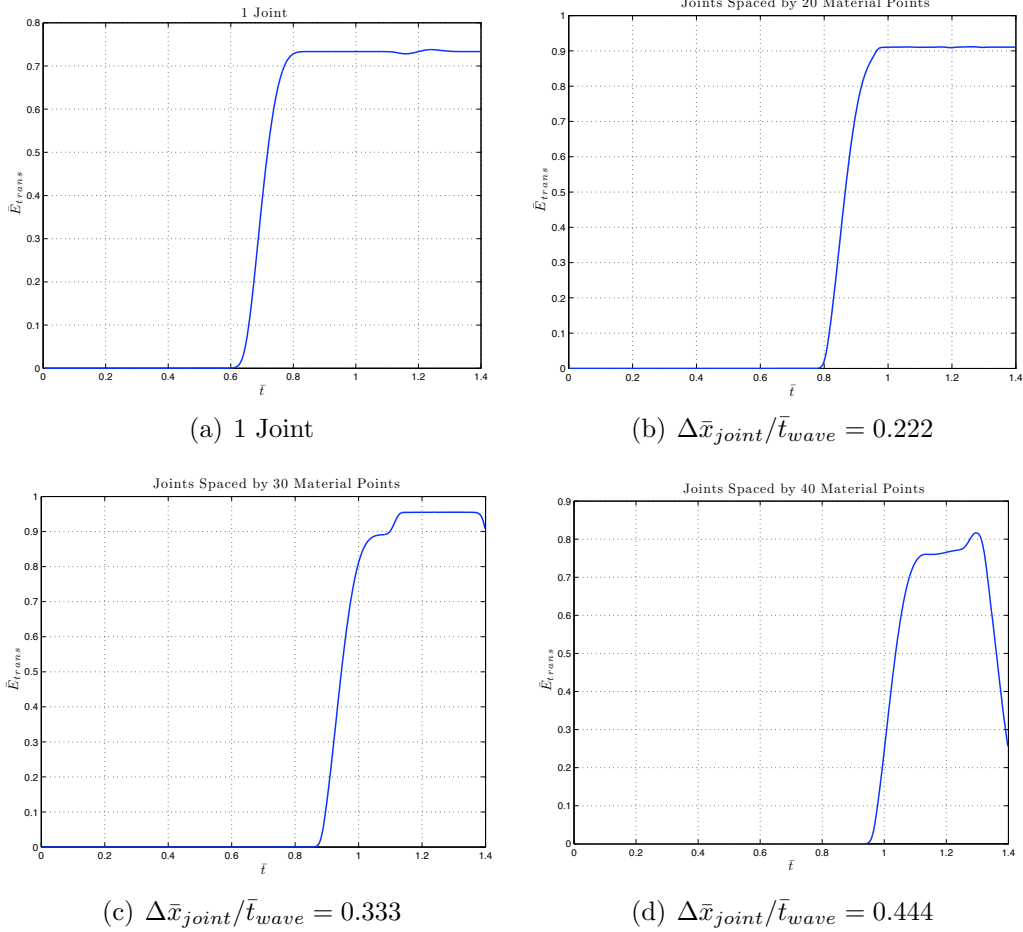


Figure 4.28: Energy transmission of multiple joint spacings

4.5.3.2 In-Depth Details for Two Joints

The run with a spacing value $\Delta \bar{x}_{joint} = 0.16$ study is further analyzed in a manner identical to the multiple gaps result of Section 4.5.2.2. Figure 4.29 shows the material point stress plotted at different times. (1) is the first time plotted. (6) is the last time plotted.

Beginning with (1), the process of wave propagation through two joints is:

- (1) The compressive pulse **A** propagates towards the first joint.
- (2) A portion of the compressive pulse **A** propagates through the joint. A smaller portion is reflected off of the joint and becomes the tensile leftward traveling wave **B**. The first joint closes to a stress state that allows wave transmission.
- (3) Wave **B** continues propagating. Wave **A** interacts with the second joint and again is broken into a continuing compressive wave **A** and a reflected wave **C**. At this current time, **C** has not reflected off of the joint fully and is still compressive. The second joint closes.
- (4) Wave **B** continues propagating. Wave **A** has propagated through the second joint and is continuing as a compressive wave. Wave **C** has reflected off of the second joint and is traveling left as a tensile pulse.
- (5) Wave **B** begins reflection off of the left end of the bar. Wave **A** continues propagating down the bar. Wave **C** reflects off of the first joint because joints have no strength in tension. Wave **C** is now a rightward traveling compressive pulse. The first joint opens because of this reflection.
- (6) Wave **B** reflects off of the end of the left bar and is traveling left as a compressive pulse. Wave **A** makes initial contact with the right end of the bar. Wave **C** propagates through the second joint with little attenuation because the joint has already closed to a stress state allowing the earlier transmission of wave **A**.

An interesting observation is that the peak stress of the tensile wave **B** is less than that of tensile wave **C**. This is most likely due to the altering of wave **A** after propagating through the first joint.

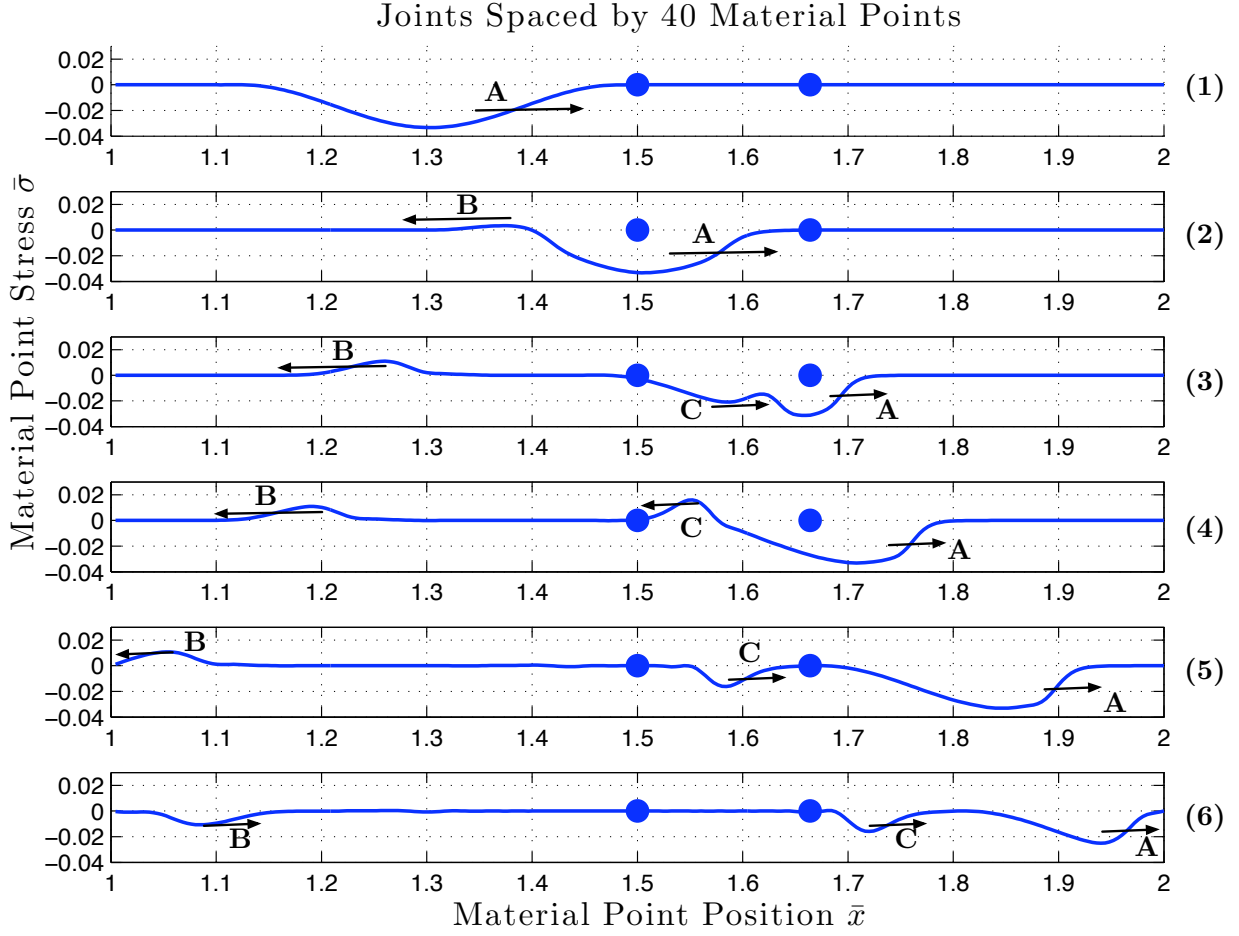


Figure 4.29: Material point stress plotted at different times (blue dots denote joint locations)

Figure 4.30 shows plots of the first and second joint sizes \bar{u} versus time. The left joint closes to approximately 0.75 from the initial propagation through the joint (Fig 4.30(a)). The wave then has a tensile reflection off of the second joint (wave **C** in Fig 4.29). When this tensile wave continues to the first joint, the joint opens up. This occurs at $\bar{t} \approx 0.85$. The second joint closes at $\bar{t} \approx 0.8$. Wave **C** propagates through the second joint without closing it further.

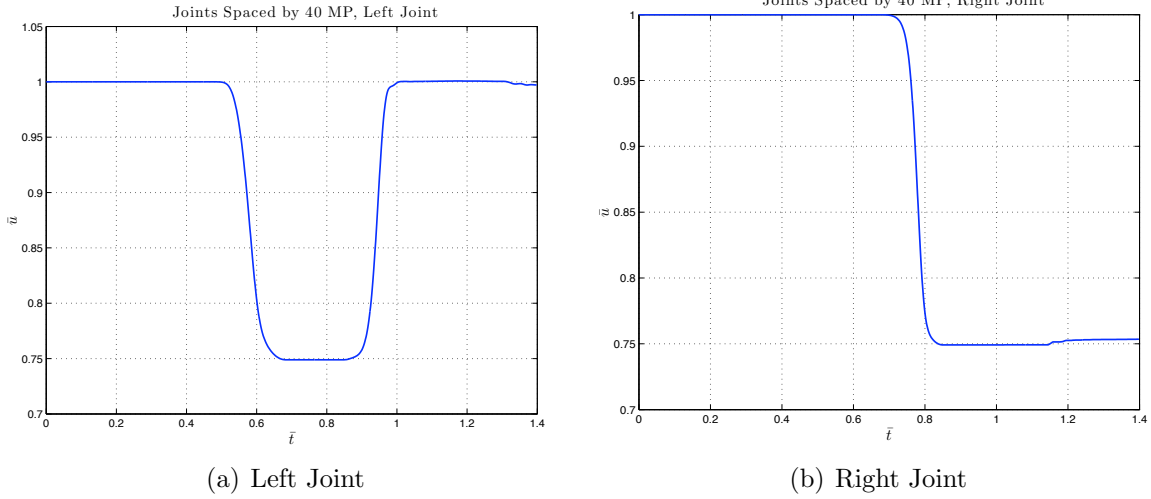


Figure 4.30: \bar{u} versus time for each joint

4.5.4 Summary of Multiple Joints

The analysis of two joints in this chapter clearly indicates that wave trapping occurs between two discontinuities, whether joints or gaps. The splitting of the initial wave at the second joint produces a tensile reflection that interacts with the first joint before propagating through the second. This phenomenon cannot be captured by a single joint. A single joint only has one tensile reflection which is not redirected back through the joint. For two joints, the second tensile reflection at the second joint does get reflected at the first joint and continues nearly uninterrupted propagation through the second joint. Therefore, more energy is transmitted through two joints than a single joint. The closure energy dissipated in two joints is very close to the energy dissipated in closing a single equivalent joint. Further, the closure energy of two joints is independent of joint spacing. Overall, the impact of two joints on wave propagation cannot be captured with a single joint.

4.6 The Utility of Lumping Gaps and Joints

4.6.1 Objective of the Chapter

To better illustrate the difference between a single lumped discontinuity and two separate discontinuities, a series of runs are analyzed similar to the analysis in Chapter 4.5. For both the gap and plastic joint constitutive model, two runs were made for a bar with a single discontinuity of initial size u_{g0} and a bar with two discontinuities initially half the size of the single discontinuity. The peak stress of the initial wave, the energy transmitted, and the energy dissipated by the discontinuities are the quantities of interest to better understand the impact of lumping two discontinuities into a single discontinuity.

4.6.2 Gaps

For the two runs with the gap constitutive model, the velocity boundary condition prescribed is the sinusoidal pulse of peak particle velocity $v_{max} = 9.92$ m/s and dimensionless wave time $\bar{t}_{wave} = 0.36$. The boundary condition has a closure potential $u_p = 1.5$ mm. For the single gap run, the gap has a prescribed initial size of $u_{g0} = 1.0$ mm in the middle of the bar. This ensures that the gap will fully close and some of the wave will propagate through during the interaction between the wave and the gap. The second run has two gaps of initial size $u_{g0} = 0.5$ mm. The sum of the initial discontinuity sizes is the initial discontinuity size for the single gap run. The first gap is located in the middle of the bar. The next gap is placed at the location from the first gap where $\Delta\bar{x}_{gap}/\bar{t}_{wave} = 0.444$. 250 material points discretize the bar.

Figure 4.31 are plots of stress at different times for the single and two gap runs. Placing the results side-by-side clearly illustrates the differences between multiple gaps and lumping them together into a single gap. The single gap case shows the wave simply propagating down the bar and reflecting off of the gap until the gap closes. Once the gap closes, the remainder of the wave transmits through the gap. The two gap case shows the wave trapping that occurs in multiple gaps. The initial wave closes the first gap. The remaining portion of the pulse transmits to the second gap, where a portion of the wave is reflected and trapped in between the two gaps. A final portion of the wave transmits through the second gap once it closes. The important conclusion of this is that the peak stress of the final wave through the single and two discontinuity simulations is approximately the same. The single gap run has a dimensionless peak stress of approximately 0.0358. And the two gap run has a dimensionless peak stress of 0.0359. Both of these values are subject to numerical dispersion due to the discontinuity in stress once the gaps close. However, they are approximately the same. Also noteworthy, the wavefront of each pulse is at approximately the same position.

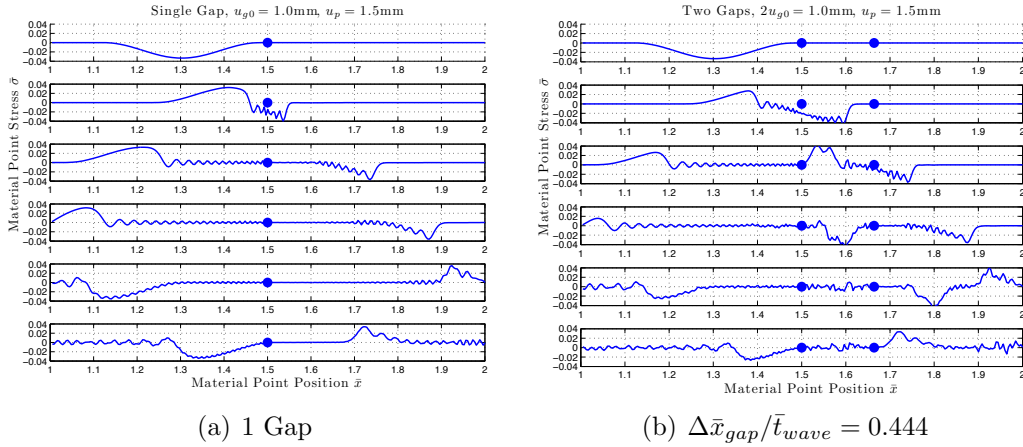


Figure 4.31: Plots of stress for a single lumped gap and two separate gaps. Blue dots denote gap locations.

Figure 4.32 is not nearly as insightful as the stress plots. However, the oscillations in

kinematic and strain energies occurs more often for the two gap case. These oscillations occur each time a pulse reflects off of a gap or free surface. Also, for both runs, the closure energy remains at zero for all time because gaps require no energy to close.

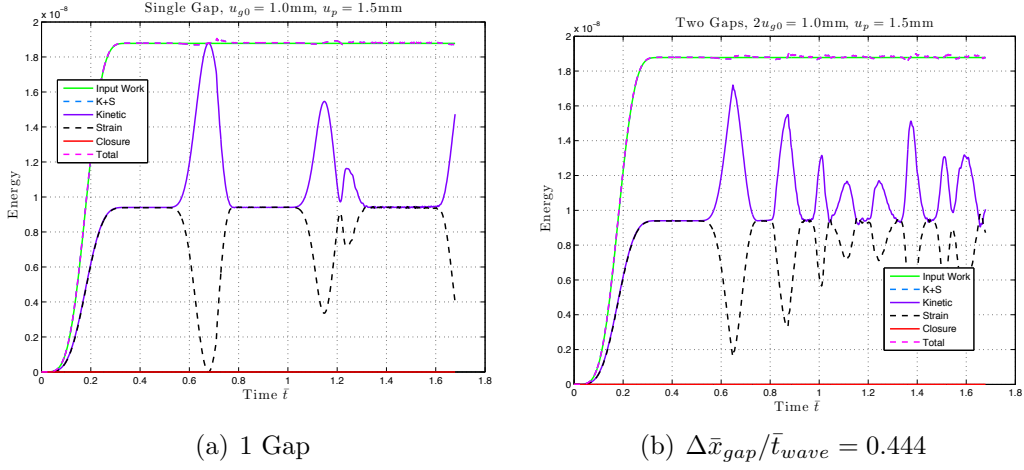


Figure 4.32: Plots of energy for a single lumped gap and two separate gaps

A key difference between multiple gaps and a single gap is the amount of energy transmitted through the discontinuities, illustrated in Figure 4.33. For a single gap, very little energy is transmitted because so much of the wave is reflected off of the gap during gap closure. However, for two gaps, more of the initial wave propagates through the first gap and then the portion that reflects off the second gap goes through wave trapping and eventually propagates past the second gap as well. In these cases, the single gap transmits approximately 0.29 of the energy in the bar through the gap. Whereas, the two gaps transmits a peak value of 0.7 of the energy through both gaps. Two gaps transmit more than twice the energy of single equivalent gap. Wave trapping allows such a large amount of energy to be transmitted through multiple gaps.

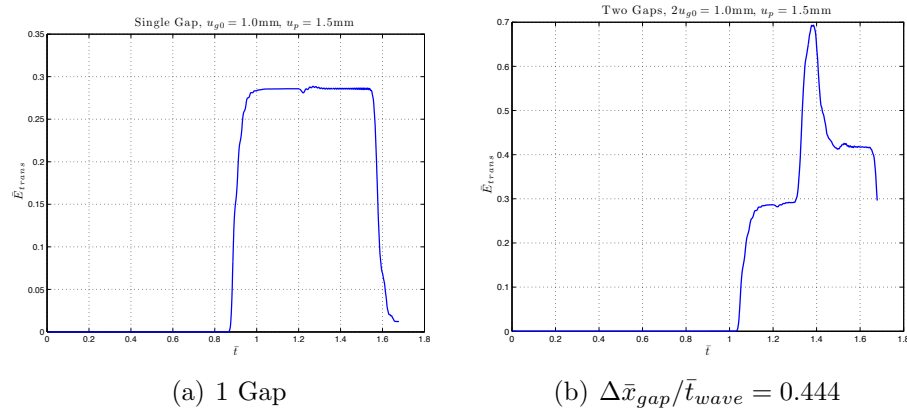


Figure 4.33: Plots of transmitted energy for a single lumped gap and two separate gaps

4.6.3 Joints

For the two runs with the plastic joint constitutive model, the velocity boundary condition prescribed is the sinusoidal pulse of peak particle velocity $v_{max} = 9.92$ m/s and dimensionless time of wave $\bar{t}_{wave} = 0.36$. The boundary condition has a closure potential $u_p = 1.5$ mm. For the single joint run, the gap has a prescribed initial size of $u_{g0} = 1.5$ mm in the middle of the bar. The second run has two gaps of initial size $u_{g0} = 0.75$ mm. The sum of the initial discontinuity sizes is the initial discontinuity size for the single joint run. The first joint is located in the middle of the bar and the next gap is placed at a $\Delta\bar{x}_{gap}$ from the first joint such that $\Delta\bar{x}_{gap}/\bar{t}_{wave} = 0.444$. 250 material points discretize the bar.

Figure 4.34 are plots of stress at different times for the single and two joint runs. The single joint run only has two separate waves form after the initial wave and joint interaction. The two joint case has three separate waves form after interacting with both joints. However, peak stress is approximately the same in the leading pulses. The single joint run has a dimensionless peak stress of 0.0329. The two joint case has a dimensionless peak stress of 0.0306. This is a minimal 0.5% difference between the two values. The wave front of the pulse through the single joint is slightly further along the bar than the pulse through the two joints because of the reflections that occur through the two joints. The shape of the propagated pulse through two joints is very similar to the shape of the pulse propagated through the single joint.

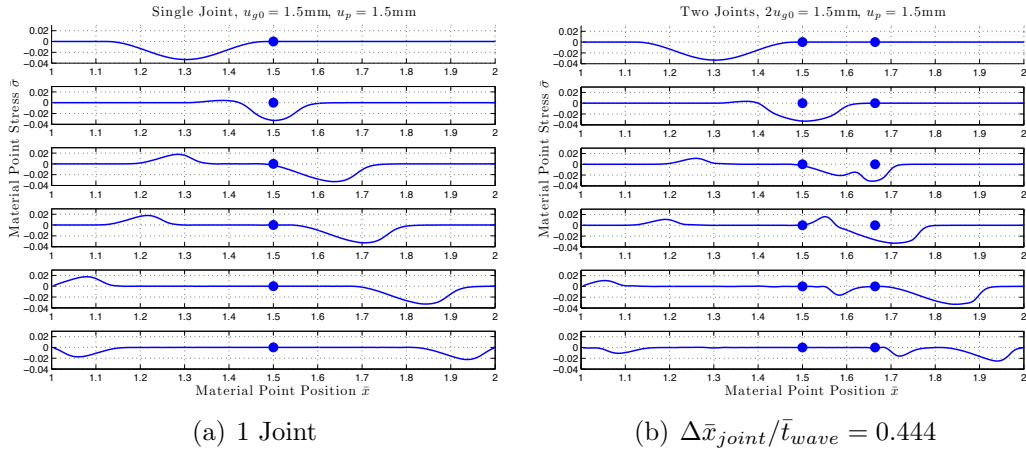


Figure 4.34: Plots of stress for a single lumped joint and two separate joints. Blue dots denote joint locations.

Figure 4.35 are plots of the calculated energies for each run. Most notably, the closure energy is approximately the same for the single joint and two joint runs. The single joint run has a peak dimensionless closure energy of $2.64\text{e-}9$, and the two joint run has a peak dimensionless closure energy of $2.66\text{e-}9$. The equates to a 0.75% difference.

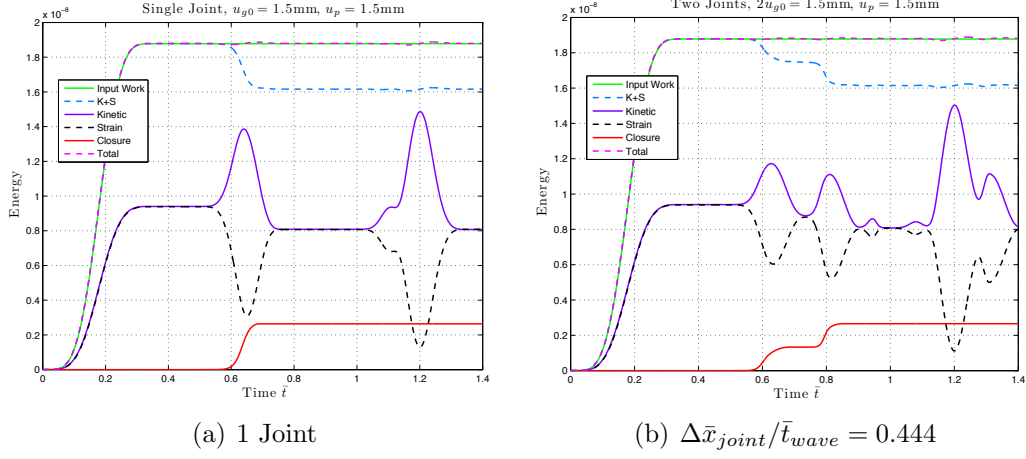


Figure 4.35: Plots of energy for a single lumped joint and two separate joints

Figure 4.36 are plots of the energy transmitted through the joints for both runs. While less drastic than the gap runs, two joints still propagate more energy through than a single joint. The single joint has a peak dimensionless energy transmission of 0.73. The two joints have a peak dimensionless energy transmission of 0.82. Between the two runs, there is a 12% difference in energy transmission between two joints and a single joint.

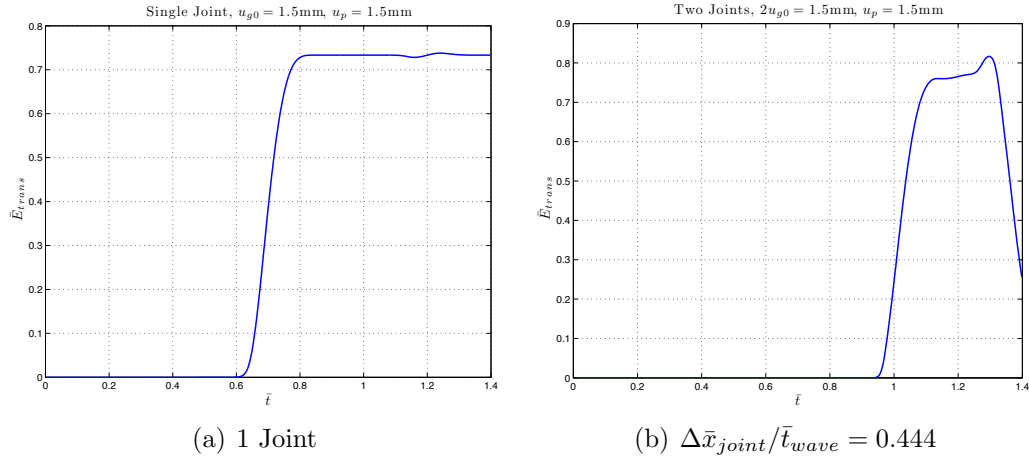


Figure 4.36: Plots of transmitted energy for a single lumped joint and two separate joints

4.6.4 Summary

The clear conclusions after analysis of the single and two gap or joint runs are:

- Both gaps and joints have negligible differences in peak stress between two discontinuities or a single equivalent discontinuity.

- Two joints dissipate an approximately equal amount of energy in joint closure as a single equivalent joint.
- Two gaps or joints transmit more energy than a single equivalent gap or joint because of wave trapping.

If energy transmission is a priority, lumping joints is not advisable. However, lumping joints is a reasonable option when the values of interest are energy dissipation and peak stress.

4.7 Conclusion

This part of the project has provided a one-dimensional constitutive equation for joints that can span the range of perfect elasticity, elasticity with plasticity, plasticity without elasticity and gaps. Representative results are given for a wave pulse transmitted through one or more joints. The key results of this effort are the effects of wave parameters and the drawbacks of lumping multiple into an equivalent joint. A gap is indifferent to wave parameters and is only influenced by the closure potential u_p of the wave. A plastic joint transmits more energy for longer waves than shorter waves when both have equal values of the closing potential u_p . The behavior of elastic-plastic and plastic joints are quite similar. Elastic unloading does not have a significant effect on transmitted and reflected waves.

The work done with multiple joints shows that lumping joints does not capture the nuances of wave propagation. As a wave propagates through individual joints, it is attenuated and split. This traps portions of the wave between joints until a certain amount of closure occurs, allowing the reflection to propagate through. Multiple joints have a net effect of allowing more of the original pulse to be transmitted in comparison with a single joint. Two joints dissipate approximately the same amount of energy as a single joint. An equivalent single joint does not transmit as much energy as multiple joints because wave trapping does not occur. The peak stress of a wave propagated through two joints or gaps is approximately the same as a single equivalent joint or gap.

Appendices

A Convergence Study with a Single Gap

The dynamic one-dimensional MPM code is specified to have a single gap in the middle of the bar. The bar is discretized with one material point per cell. Three runs are used to show convergence of the code by specifying 50, 125, and 250 material points to discretize the bar. The input wave is the sinusoidal pulse of $v_{max} = 7.14\text{m/s}$ and $\bar{t}_{wave} = 0.5$. The wave has a closure potential $u_p = 1.5\text{mm}$. The discontinuity has an initial size $u_{g0} = 0.5\text{mm}$. The gap fully closes and a portion of the pulse propagates beyond the gap. The results of each run are illustrated in Figures A.1, A.2, A.3, and A.4.

The material point stress is plotted at different times along the bar for each mesh size in Figure A.1. As the number of material points is increased, the solution converges to the expected results of zero stress after the reflected tensile wave and the abrupt face of the continuing compressive wave through the gap after closure occurs.

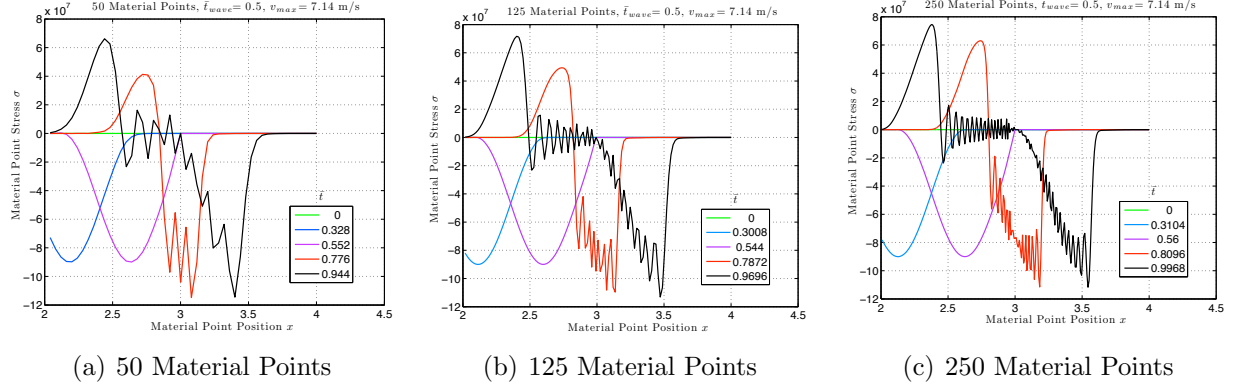


Figure A.1: Mesh refinement for wave propagation through a gap, 1 material point per cell

The energy plot converges towards a constant total energy during the initial reflection of the wave off of the gap in Figure A.2. As the mesh is refined, less of a attenuation in total bar energy occurs. This is referring to the slight increase then decrease in total bar energy at time \bar{t} from 0.5 to 0.8. Also, the closure energy remains at zero because the gap has no resistance to closure.

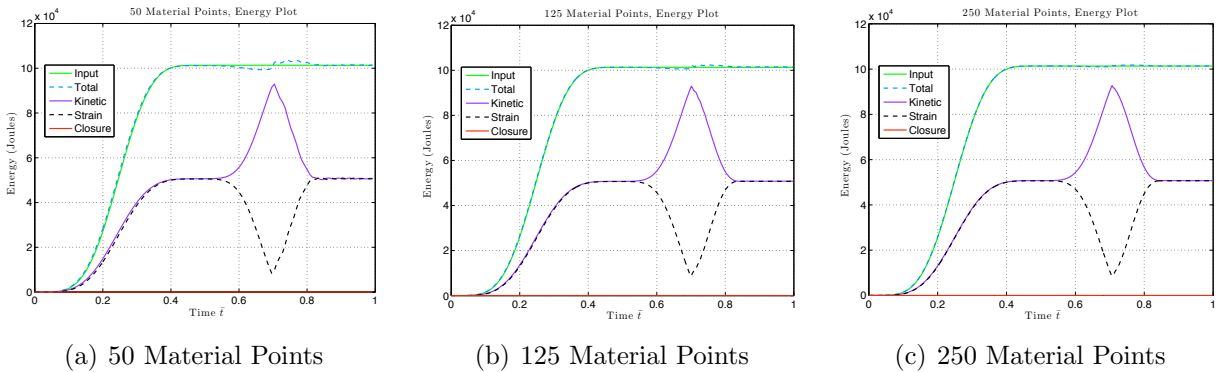


Figure A.2: Mesh refinement for wave propagation through a gap, 1 material point per cell

The energy transmitted beyond the gap versus time in Figure A.3 is almost identical for each mesh refinement. Smoothing of the curve is noticeable between the 50 material point and 125 material point meshes during the period of energy being transmitted (Figs 3(a) and 3(b), respectively). For each mesh, the transmitted energy levels off to a constant value of approximately 0.72.

The gap size versus time in Figure A.4 is almost identical for each mesh refinement. The gap begins to close at $\bar{t} \approx 0.5$ and closes fully at $\bar{t} \approx 0.7$.

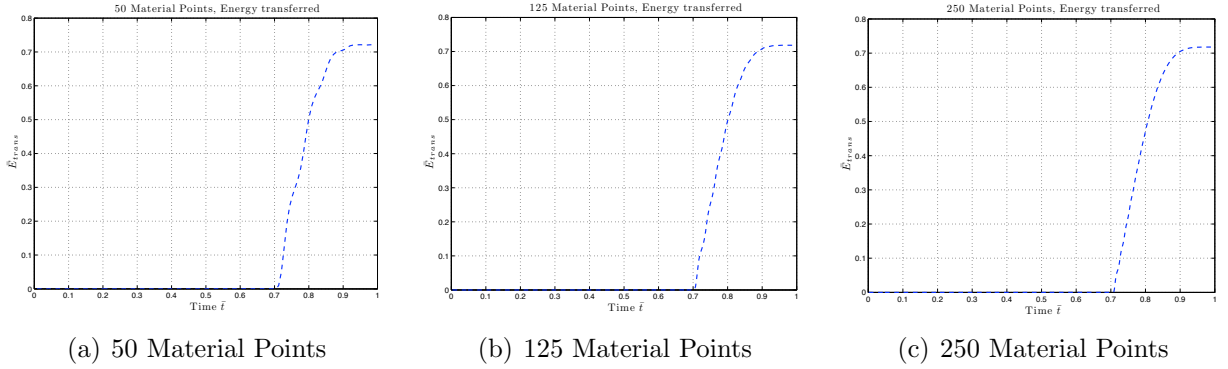


Figure A.3: Mesh refinement for wave propagation through a gap, 1 material point per cell

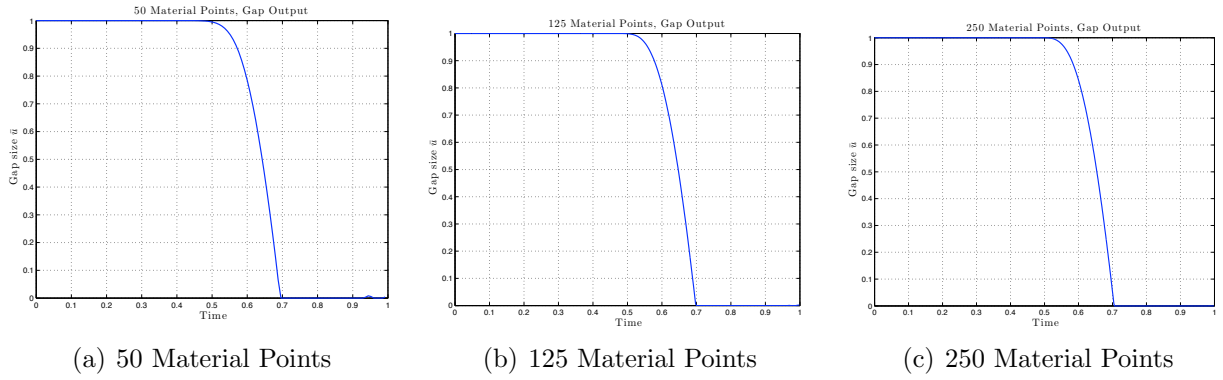


Figure A.4: Mesh refinement for wave propagation through a gap, 1 material point per cell

B Convergence Study with Two Gaps

A second convergence study was conducted to show convergence with two prescribed gaps. The input wave has parameters $v_{max} = 9.92\text{m/s}$ and $\bar{t}_{wave} = 0.36$. Figure B.1 shows convergence of stress plots when the bar discretization is refined from 125 to 250 to 500 material points. The energy plots also show smoother results due to refinement (Fig B.2). The plots of \bar{u} versus time for both the left and right gaps also converge when more material points are used (Fig B.3 and Fig B.4).

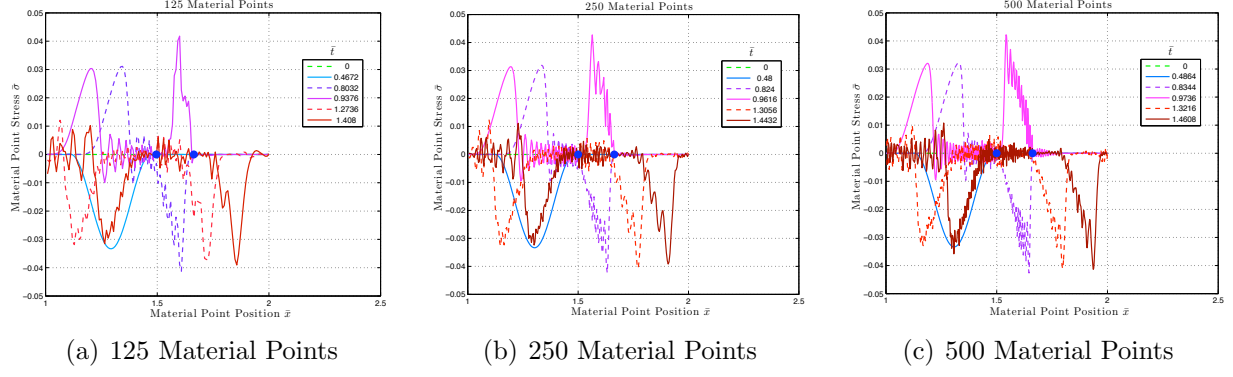


Figure B.1: Mesh refinement for wave propagation through two gaps, 1 material point per cell

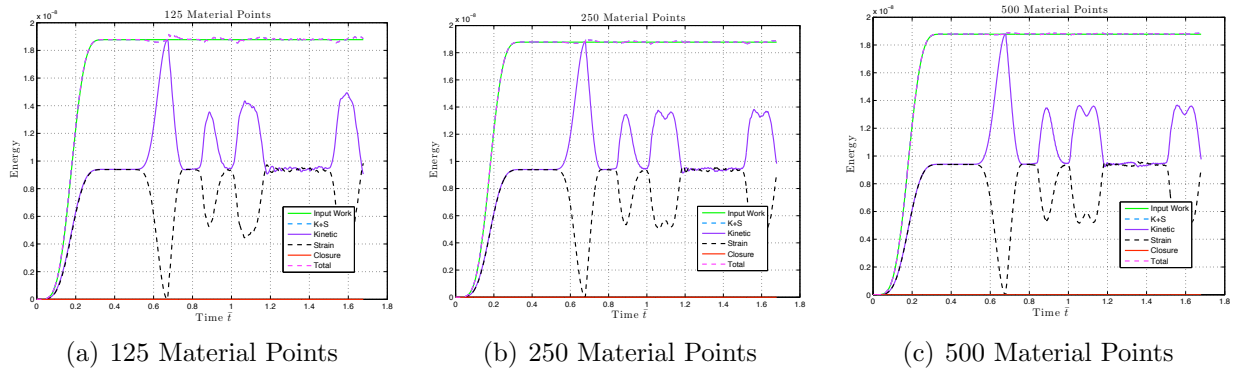


Figure B.2: Mesh refinement for wave propagation through 2 gaps, 1 material point per cell

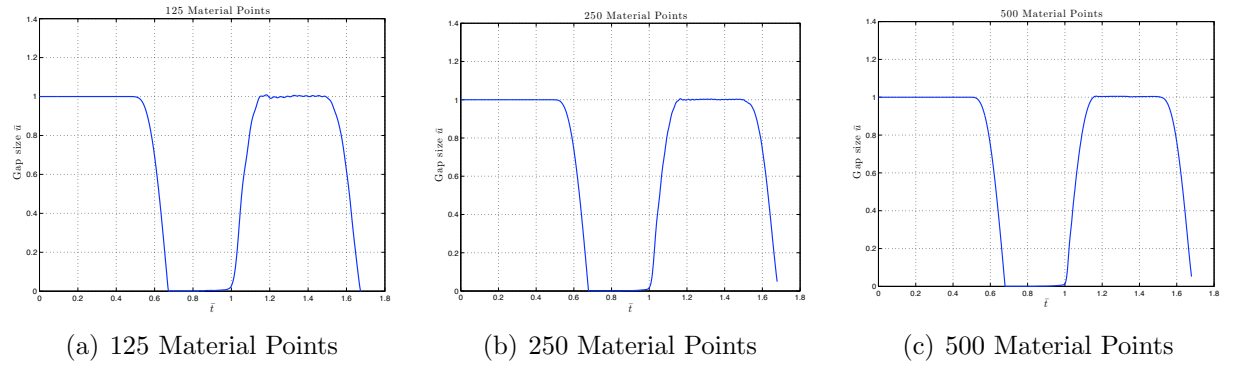


Figure B.3: \bar{u} versus time for first gap

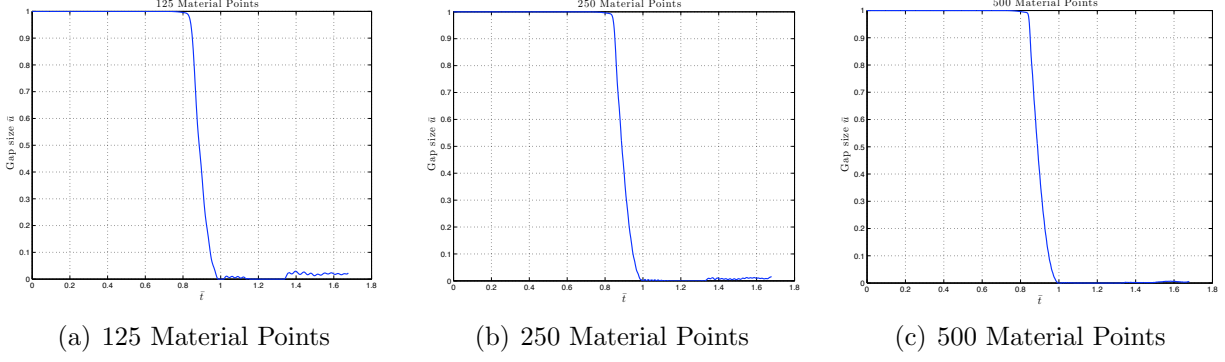


Figure B.4: \bar{u} versus time for second gap

C Nondimensionalization Scheme

The following Appendix outlines the scheme to nondimensionalize quantities for the numerical studies.

C.1 Dimensioned Quantities

The dimensioned variables of the governing equation for the one-dimensional bar problem are as follows:

1. x , the cartesian coordinate along the length of the bar with dimension meters [m]
2. u , the displacement along the length of the bar with dimension meters [m]
3. t , time with dimension seconds [s]
4. ρ , density of the bar with dimensions [kg/m³]
5. Y , Young's modulus of the bar with dimensions [kg/m s²]
6. σ , the stress in the bar with dimensions [kg/m s²]

Also, ∂ is the partial derivative operator. The partial derivative of u with respect to x is symbolically $u_{,x}$. The second partial derivative of u with respect to x is symbolically $u_{,xx}$.

C.2 Equations

Ignoring body forces, the governing equation for the motion of a bar in 1D is

$$\sigma_{,x} = \rho u_{,tt}. \quad (57)$$

The linear elastic constitutive equation in one-dimension is

$$\sigma = Y \varepsilon, \quad (58)$$

where ε is the strain in the bar. The kinematic relationship for strain in terms of displacement is

$$\varepsilon = u_{,x}. \quad (59)$$

When Equations (57), (74), and (59) are combined, the 1D wave equation is

$$(Yu)_{,x} = \rho u_{,tt}. \quad (60)$$

C.3 Proposed Dimensionless Quantities

The reference dimension quantities are

1. $x_{ref} = L$, the length of the bar
2. $\sigma_{ref} = \sigma_g/1000$, the value σ_g comes from the gap closure “hardening” function $g(\bar{u}_g)$
3. $Y_{ref} = \sigma_g$, the proposed reference Young’s modulus
4. $t_{ref} = L/c$, the reference time, where c is the elastic wave speed $\sqrt{Y/\rho}$
5. $\varepsilon_{ref} = 1000$, the reference strain

When the reference values are combined with the variables of the wave equation, the dimensionless quantities follow

1. $\bar{x} = x/L$
2. $\bar{u} = u/u_{ref}$
3. $\bar{t} = t/t_{ref}$
4. $\bar{Y} = Y/\sigma_g$
5. $\bar{\sigma} = \sigma/\sigma_g$
6. $\bar{\rho} = \rho/\rho_{ref}$

The undefined reference values u_{ref} and ρ_{ref} are determined for convenience later on. Substitute the expressions involving reference values and dimensionless variables into Equation(57) to get a dimensionless equation

$$\bar{\sigma}_{,\bar{x}} = \bar{\rho}\bar{u}_{,\bar{t}\bar{t}}. \quad (61)$$

Upon substitution of dimensionless values, Equation (57) reduces to

$$\frac{1}{1000}L\sigma_g(\bar{\sigma})_{,\bar{x}} = \frac{\rho_{ref}u_{ref}}{t_{ref}^2}\bar{\rho}(\bar{u})_{,\bar{t}\bar{t}}. \quad (62)$$

So that Equation (62) reduces to Equation (61), the the reference density ρ_{ref} comes out as,

$$\rho_{ref} = \frac{\sigma_g t_{ref}^2}{1000 L u_{ref}}. \quad (63)$$

Then with Equation (74) following a similar substitution procedure, the constitutive equation reduces to

$$\frac{\sigma_g}{1000} \bar{\sigma} = \left(\frac{\sigma_g u_{ref}}{L} \right) \bar{Y} \bar{u}_{,\bar{x}}. \quad (64)$$

u_{ref} is conveniently chosen to be

$$u_{ref} = \frac{L}{1000}, \quad (65)$$

which gives an equation of the form

$$\bar{\sigma} = \bar{Y} \bar{u}_{,\bar{x}}. \quad (66)$$

Substitute u_{ref} into (63) and simplify to get the reference density ρ_{ref} (67).

$$\rho_{ref} = \frac{t_{ref}^2 \sigma_g}{L^2} \quad (67)$$

By non-dimensionalizing the governing equation in this manner, the dimensionless elastic wave speed \bar{c} , which is $\sqrt{\bar{Y}/\bar{\rho}}$, reduces to,

$$\bar{c} = 1. \quad (68)$$

A elastic wave speed of unit value gives a dimensionless wave propagation time \bar{t}_{prop} of,

$$\bar{t}_{prop} = \bar{L}/\bar{c} \quad (69)$$

$$= \frac{L/L}{\bar{c}} \quad (70)$$

$$= 1. \quad (71)$$

A unit dimensionless wave speed and wave propagation time is easy to interpret in the plots of results.

D Material Point Placement

The material point method allows for any number of material points to be located within a cell (or element). For the one-dimensional computations exploring the effects of joints, only one material point is used per cell. Typically, the single material point is placed initially in the middle of the cell. In developing the one-dimensional material point method code, the

material points were inadvertently placed a distance ϵ from the left node of the cell. ϵ is a value slightly larger than machine precision. This placement results in unusually smooth numerical results. The effects of such a placement were further investigated compared to the typical placement of material points centered within the cells.

Considering discontinuities, the cell boundary material point locations is helpful. For small deformations, the material points map the majority of their values to a single node because the unit hat basis functions are ≈ 1 for a node and ≈ 0 for another node when evaluated at the material points. Therefore, material point information does not get mapped in front of the elastic wave as it propagates and helps to clearly identify existing discontinuities with minimal noise.

Four runs demonstrate the impact of material point location. The last two runs shown in Figures D.3 and D.4 have a zero strength gap in the middle of the bar showing the features when the material points are placed in the middle of the cells. For a zero strength gap, the wave should just reflect off of the gap. These are all one material point per cell and the values are plotted at material points (not mapped to the cells).

Also, the dimensionless times listed in the legend are $\bar{t} = t/t_{propagation}$

- Bar length $L = 2 \text{ m}$
- Density $\rho = 2000 \text{ kg/m}^3$
- Young's modulus $Y = 50 \text{ GPa}$
- Cross sectional area $A = 1 \text{ m}^2$
- Number of elements, either 50 or 128 depending on where the material points are placed in the cell, 50 when the material point is close to cell boundary, 128 when the material point is in middle of cell boundary
- 1 material point per cell
- Total run time is 1.5 wave propagations or $t_f = 0.0006 \text{ s}$
- Velocity boundary condition, left boundary $v_{left} = \frac{v_{max}}{2}(1 - \cos \frac{(2\pi t)}{t_{input}})$, where $v_{max} = 1 \text{ m/s}$ and $t_{input} = 0.0002 \text{ s}$
- $\Delta t = 0.9 h_{cell}/c$ where $c = \sqrt{Y/\rho}$

Figures D.1 and D.2 are the results for a bar without a gap in the middle. When the material point is on the cell boundary, numerical results are much smoother (Fig D.1). When the material point is centered in the cell, the results are not nearly as smooth as the cell boundary-placed material points (Fig D.2). The conclusion of this investigation is that computational results are significantly smoother when the material point is placed on the cell boundary.

Figures D.3 and D.4 are the results of placing a gap in the middle of the bar. Figure D.3 shows that material points close to the cell boundaries allow for gap behavior without noticeable numerical values passing through the open gap. But, Figure D.4 does have unrealistic

numerical values to the right of the gap. When material points are centered in the cells, material point quantities will map to two nodes equally. Similarly, nodal quantities map to two material points. This allows for quantities to propagate past the gap and allow for non-zero stresses to the right of the gap. When material points are placed on cell boundaries, the majority of material point quantities only map to one node and vice-versa. Therefore, numerical errors from the mapping are not as apparent. For this reason, the joint and gap studies place the material points close to cell boundaries during numerical discretization of the bar.

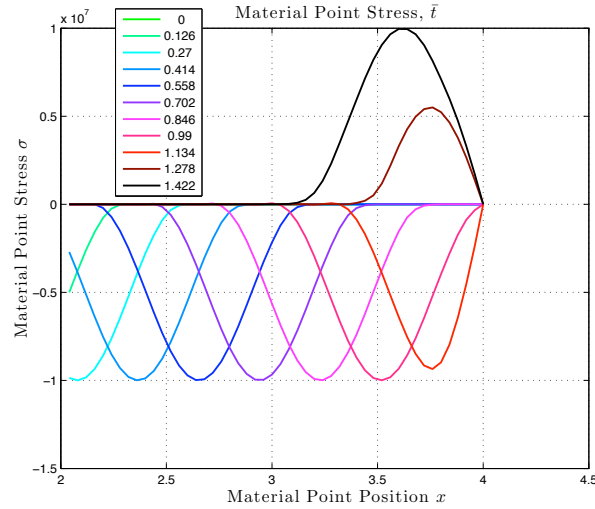


Figure D.1: Stress as a function of x for different times using 50 material points located close to the cell boundary to discretize the bar

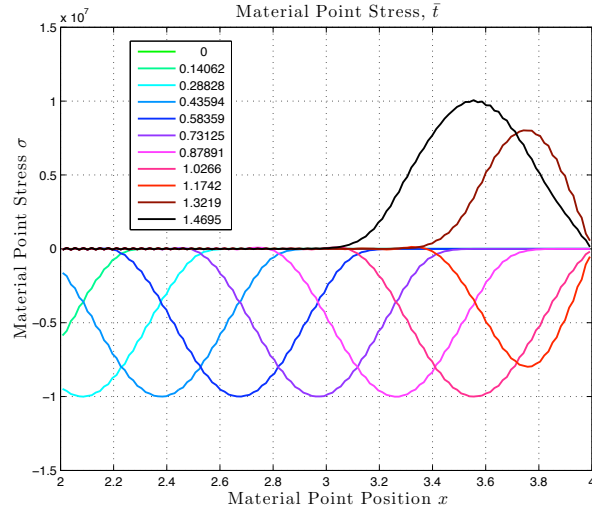


Figure D.2: Stress as a function of x for different times using 128 material points centered in the cells to discretize the bar

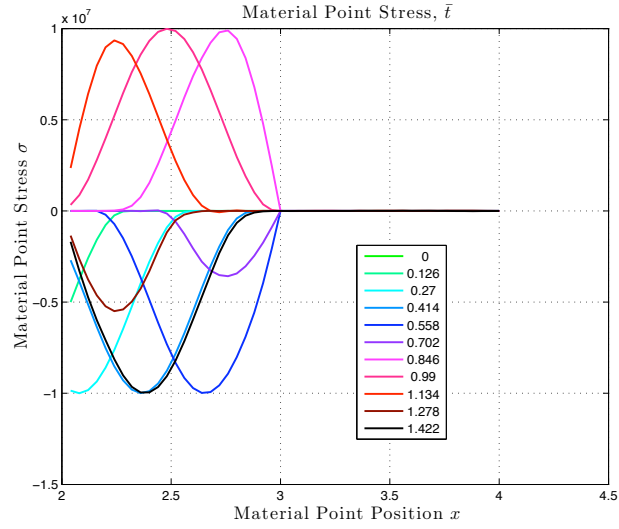


Figure D.3: Stress as a function of x for different times using 50 material points located close to the cell boundary to discretize the bar with a gap in the center of the bar

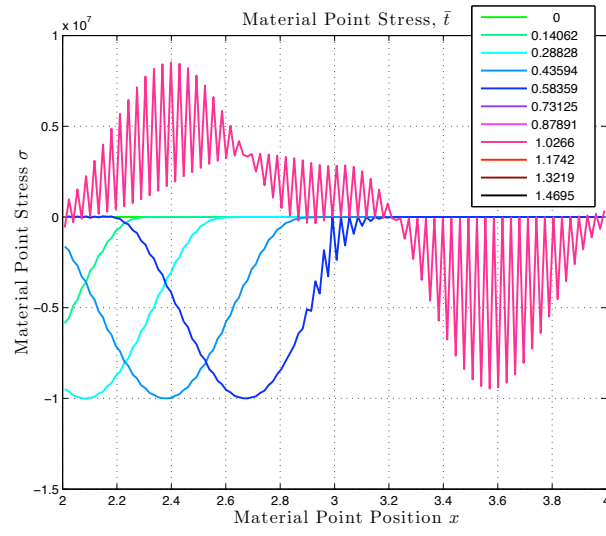
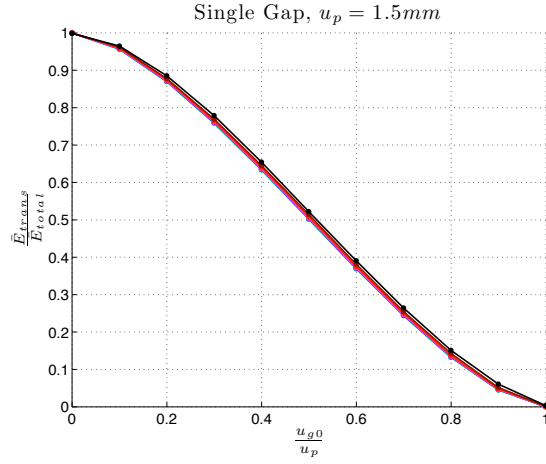


Figure D.4: Stress as a function of x for different times using 128 material points centered in the cells to discretize the bar with a gap in the center of the bar

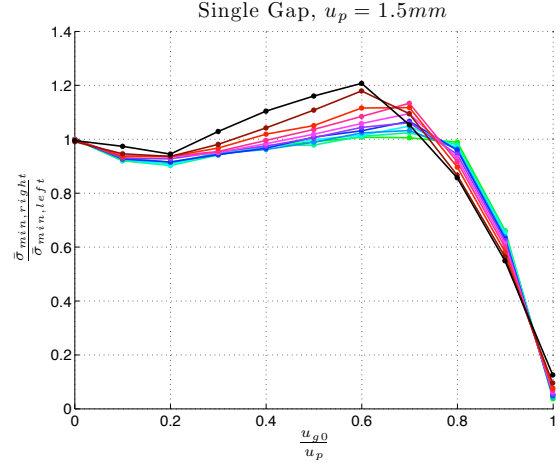
E Complete Figures

The following figures include all of runs from the single discontinuity study. In the main text, certain runs with large amounts of numerical dispersion were removed.

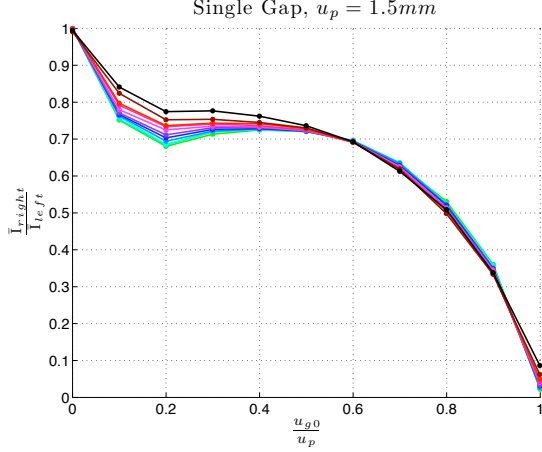
E.1 Single Gap



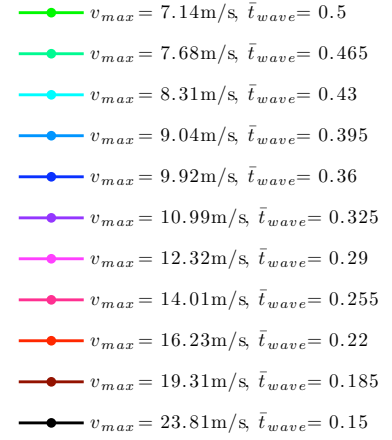
(a) Single Gap, Energy



(b) Single Gap, Peak Stress



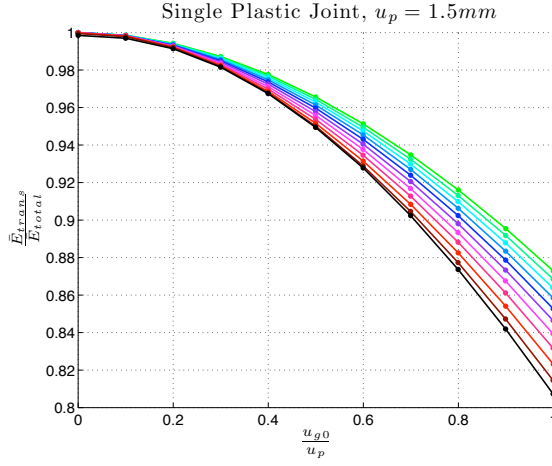
(c) Single Gap, Impulse



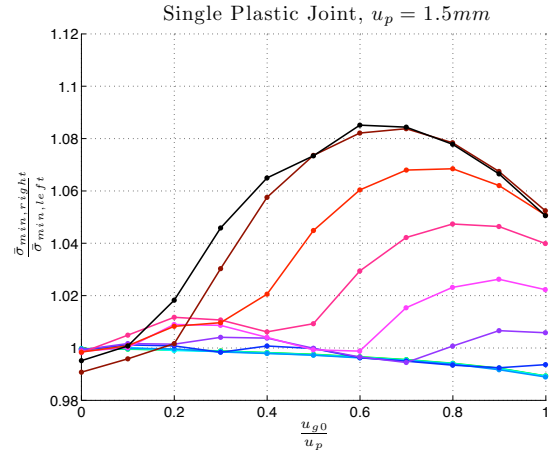
(d) Legend

Figure E.1: Results of single gap study, $u_p = 1.5\text{mm}$

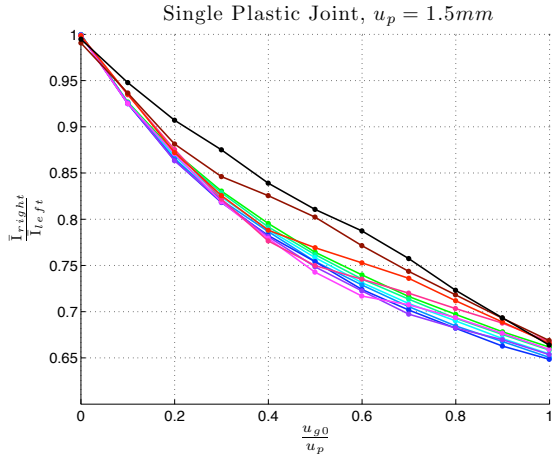
E.2 Single Plastic Joint



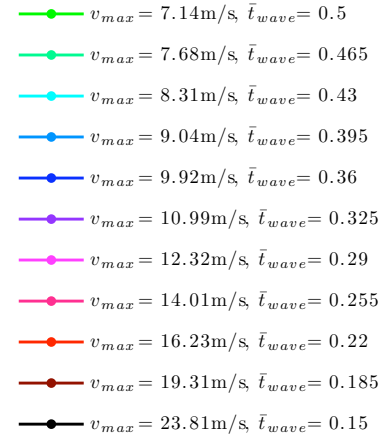
(a) Single Plastic Joint, Energy



(b) Single Plastic Joint, Peak Stress



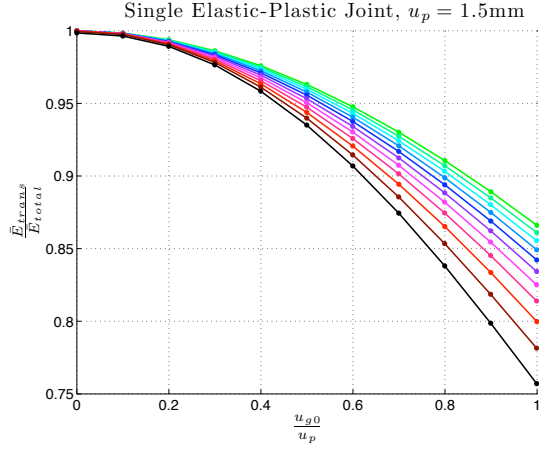
(c) Single Plastic Joint, Impulse



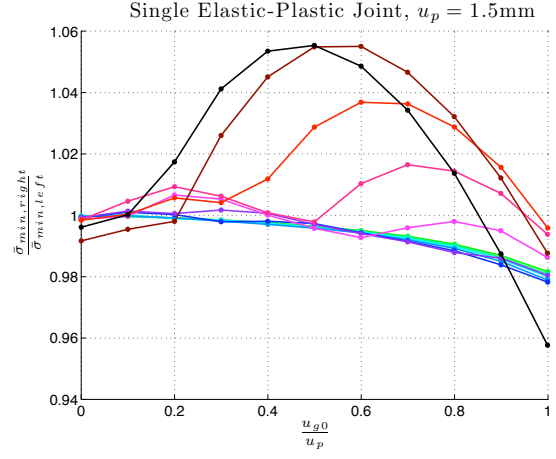
(d) Legend

Figure E.2: Results of single plastic joint study, $u_p = 1.5mm$

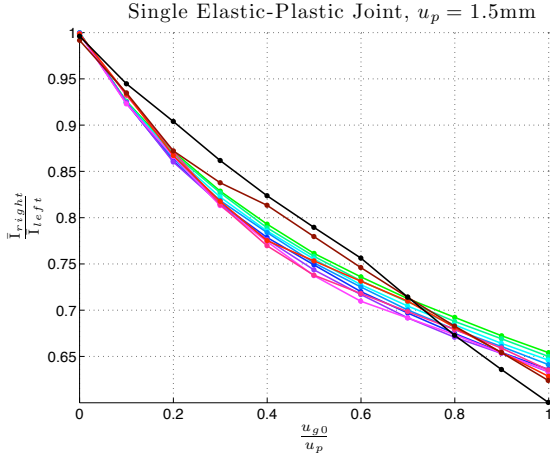
E.3 Single Elastic-Plastic Joint



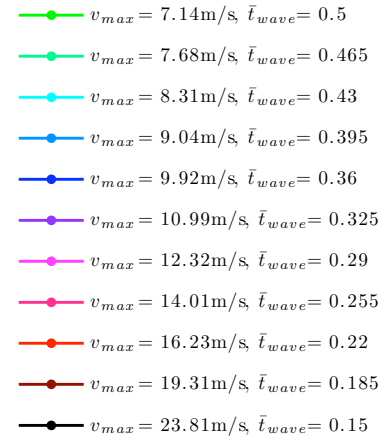
(a) Single Elastic-Plastic Joint, Energy



(b) Single Elastic-Plastic Joint, Peak Stress



(c) Single Elastic-Plastic Joint, Impulse



(d) Legend

Figure E.3: Results of single elastic-plastic joint study, $u_p = 1.5\text{mm}$

F Lumping Joints Study

Figure F.1 illustrates the investigation of the effects of multiple joints with the restriction that the sum of the initial joint lengths is a constant. This process is called lumping the joints. In this context, lumping joints places multiple discontinuities into fewer or a single discontinuity. Conversely, smearing discontinuities places a single discontinuity into multiple discontinuities. One issue of interest in connection with computing efficiency on a large scale is whether or not several joints can be modeled as one “equivalent” joint. The study will consider 16 individual discontinuities (whose initial discontinuities sum to u_{g0}) and their impact on wave propagation. Then, for the same sum of initial discontinuity, use only 14 discontinuities. The pattern continues until only one discontinuity is used with an initial size of u_{g0} . Table F.1 provides a summary of values for parameters defining the sizes of the initial joint and forcing function.

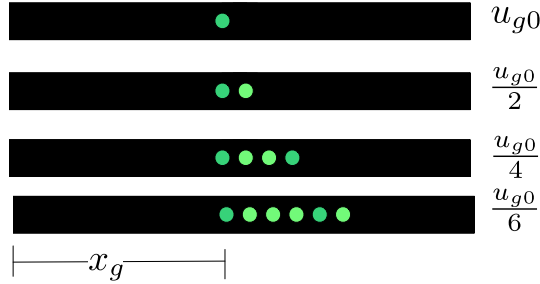


Figure F.1: Layout of Discontinuity Lumping Study

(a) Boundary Conditions, $u_p = 1.5\text{mm}$

Set	v_{max}	\bar{t}_{wave}
1	9.92 m/s	0.36
2	10.99 m/s	0.325
3	12.32 m/s	0.29
4	14.01 m/s	0.255
5	16.23 m/s	0.22
6	19.31 m/s	0.185
7	23.81 m/s	0.15

(b) Initial Discontinuity Size u_{g0}

Set	u_{g0}
1	1.5 mm
2	0.5 mm

Table F.1: Inputs used for multiple joints

The following figures are the full results of the joint lumping study. The results indicate that the fewer discontinuities used, the less energy is transmitted through. This trend applies to gaps, plastic joints, and elastic-plastic joints.

F.1 Gaps, $u_{g0} = 1.5\text{mm}$

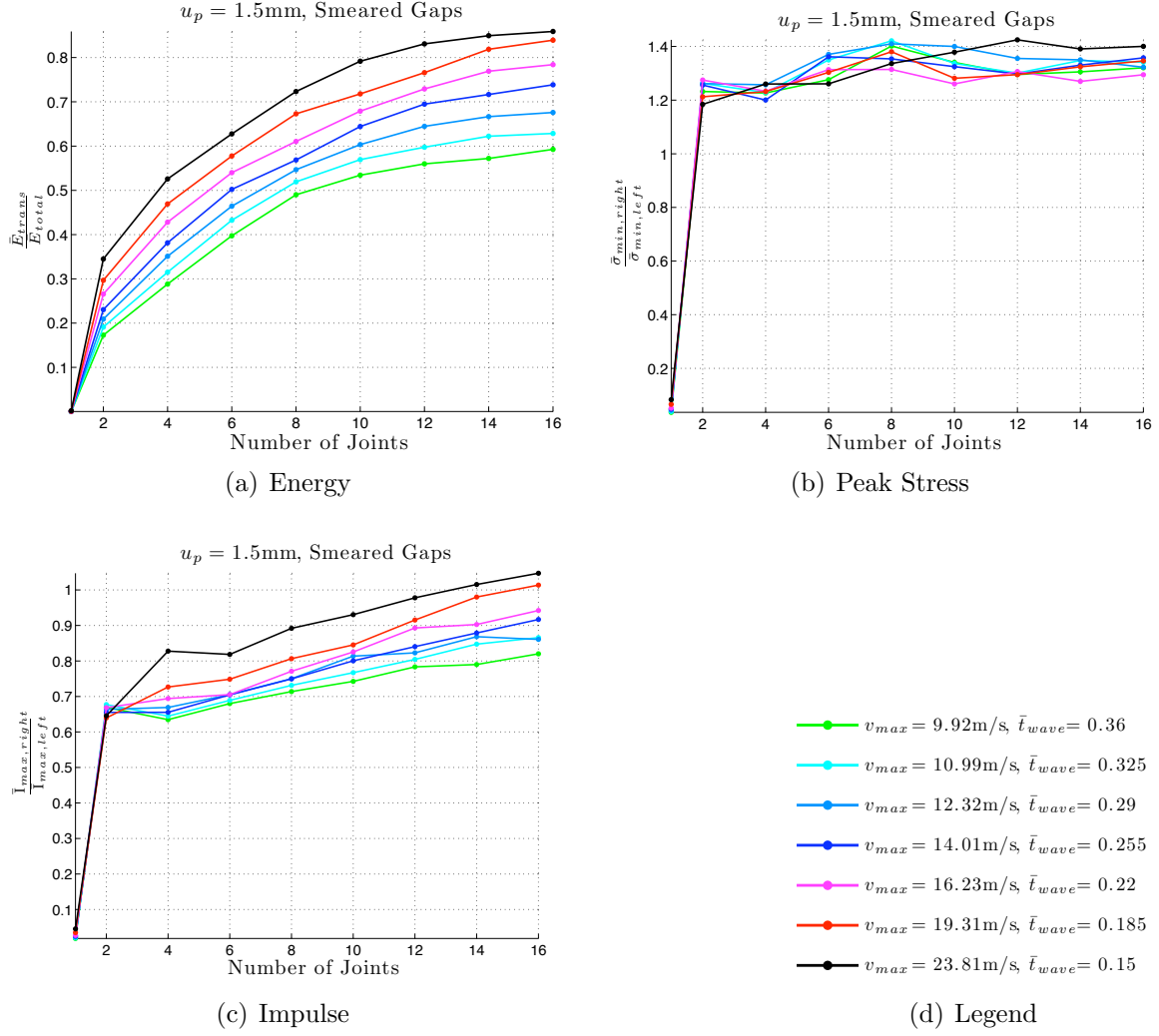


Figure F.2: Results of lumping multiple gaps, $u_{g0} = 1.5\text{mm}$

F.2 Gaps, $u_{g0} = 0.5\text{mm}$

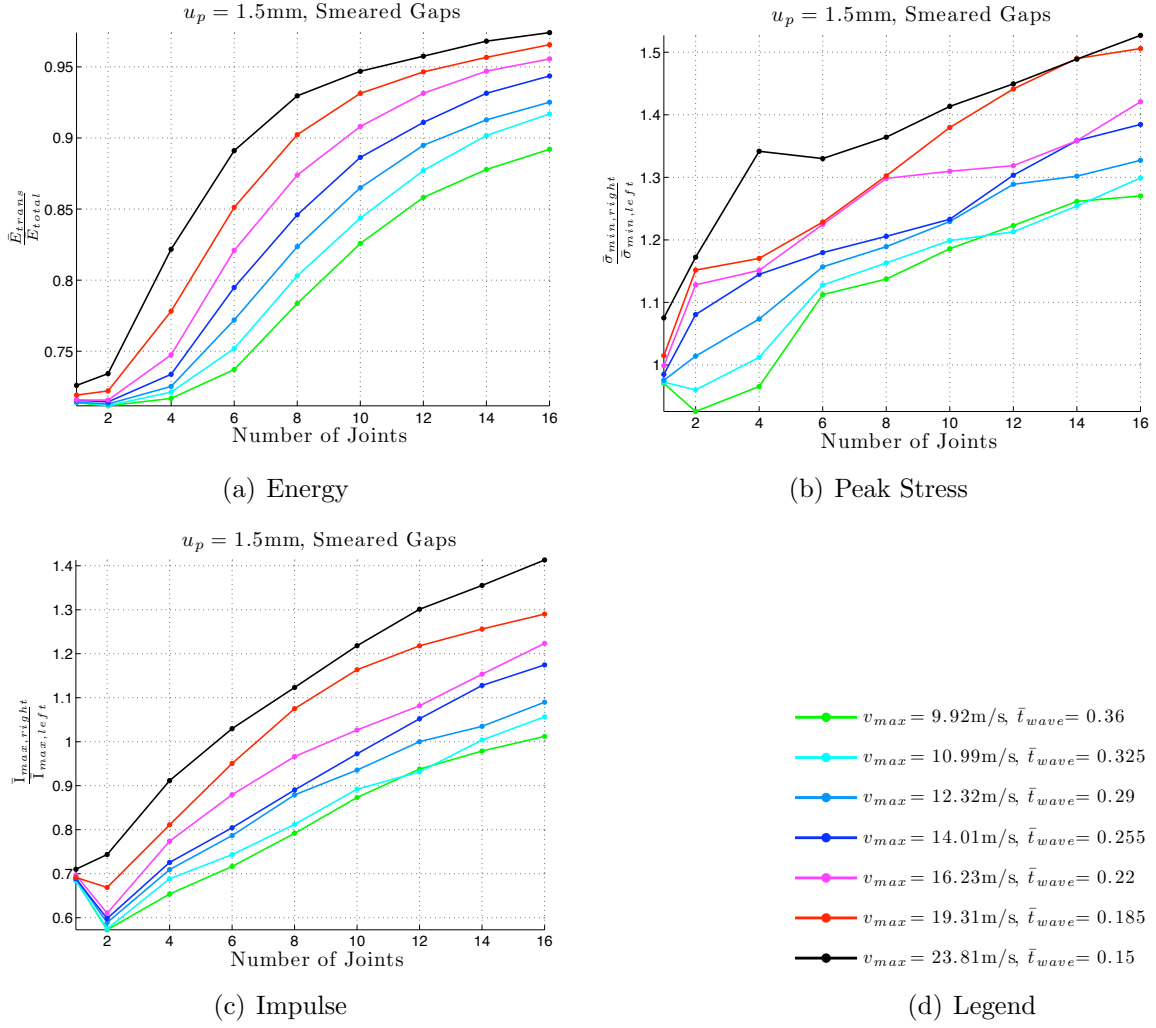


Figure F.3: Results of lumping multiple gaps, $u_{g0} = 0.5\text{mm}$

F.3 Plastic Joints, $u_{g0} = 1.5\text{mm}$

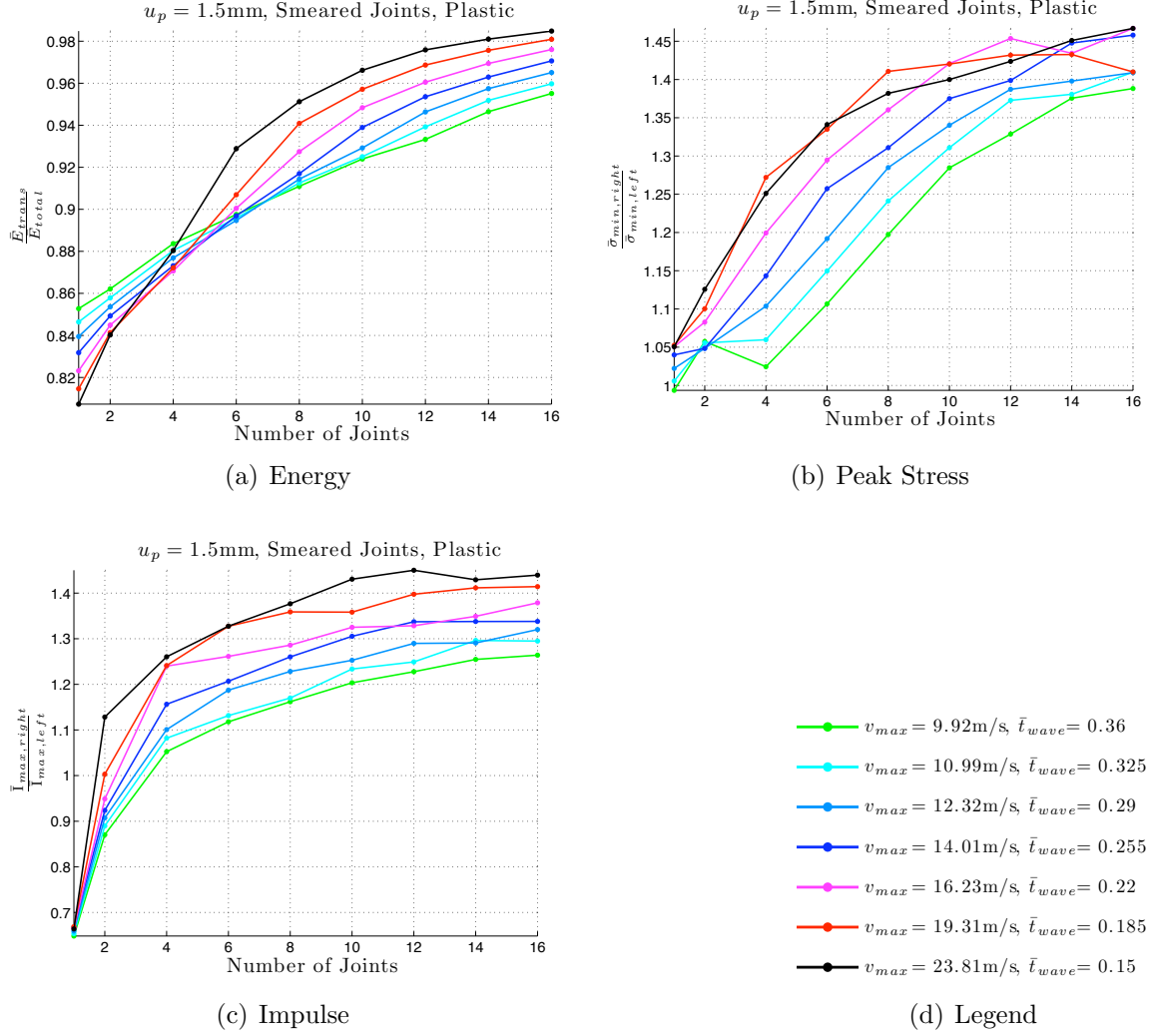


Figure F.4: Results of lumping multiple plastic joints, $u_{g0} = 1.5\text{mm}$

F.4 Plastic Joints, $u_{g0} = 0.5\text{mm}$

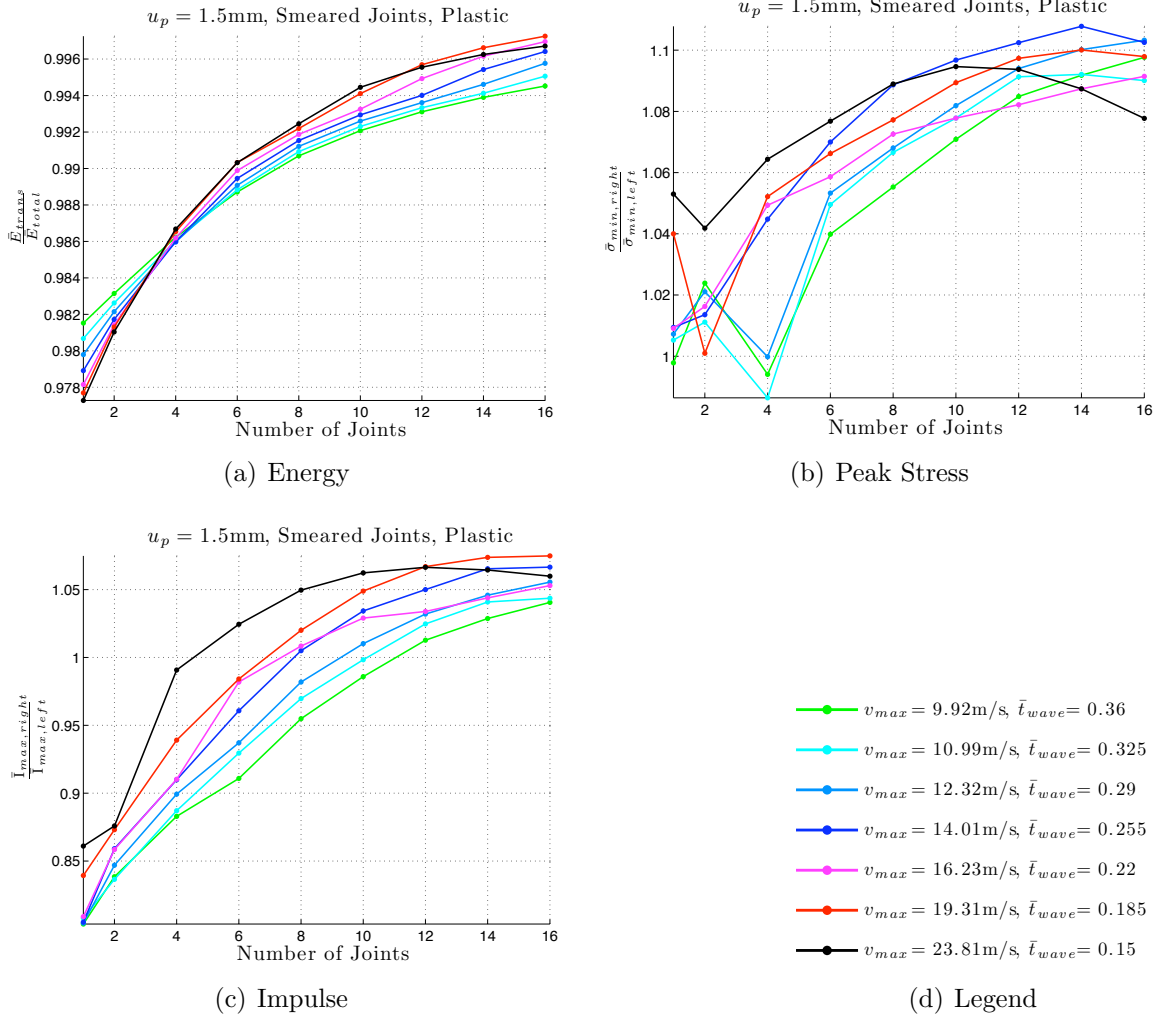


Figure F.5: Results of lumping multiple plastic joints, $u_{g0} = 0.5\text{mm}$

F.5 Elastic-Plastic Joints, $u_{g0} = 1.5\text{mm}$

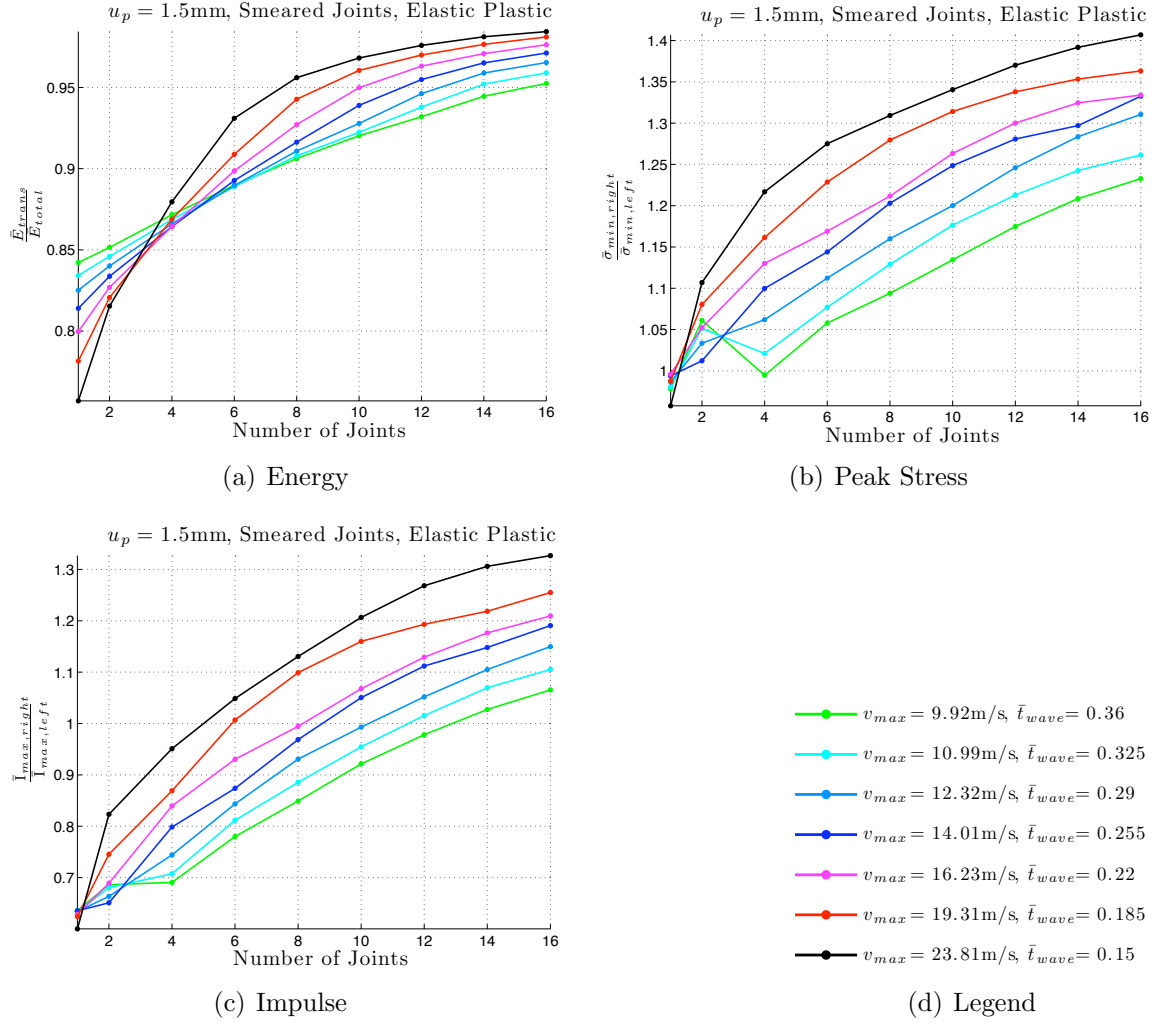


Figure F.6: Results of lumping multiple elastic-plastic joints, $u_{g0} = 1.5\text{mm}$

F.6 Elastic-Plastic Joints, $u_{g0} = 0.5\text{mm}$

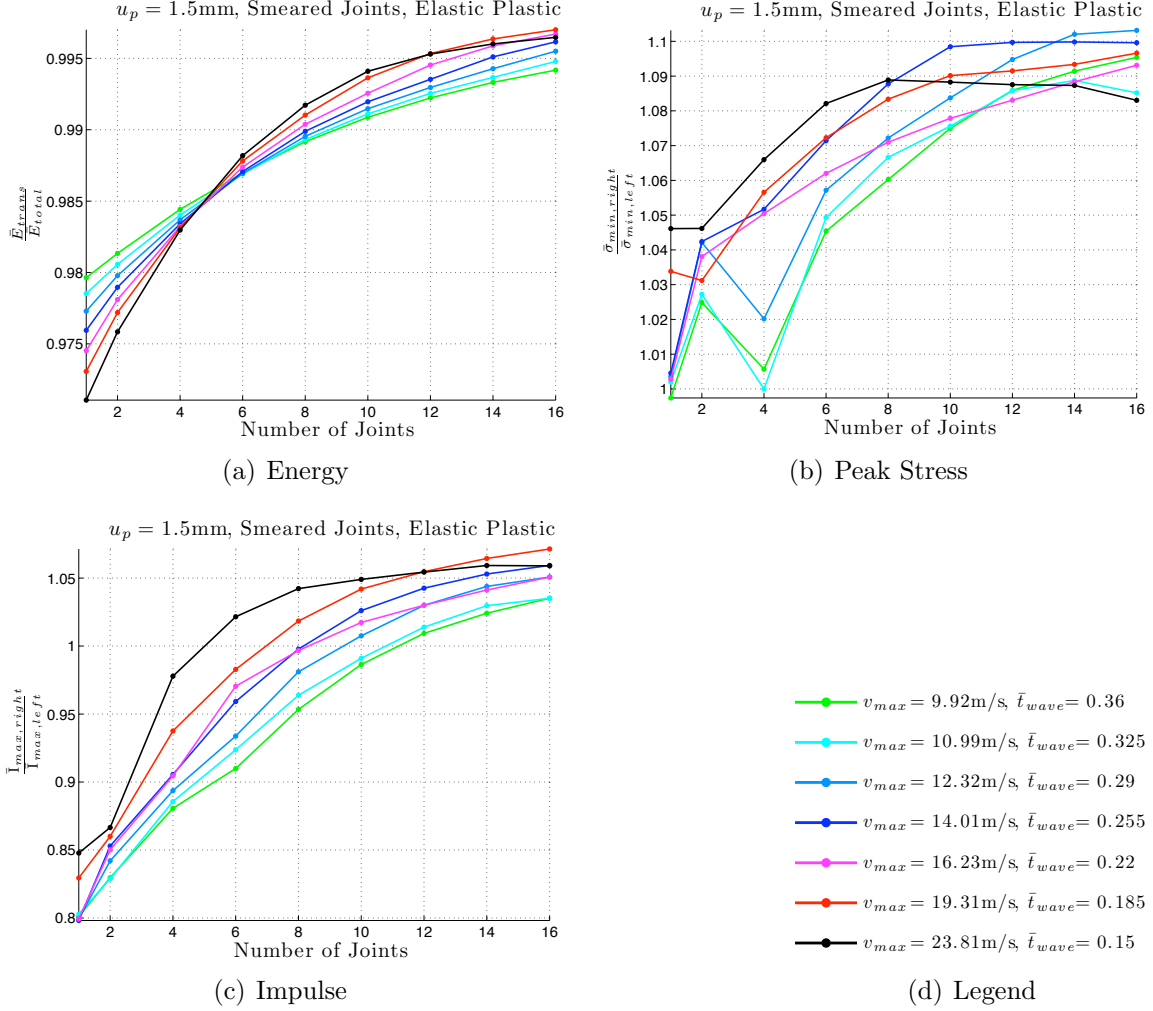


Figure F.7: Results of lumping multiple elastic-plastic joints, $u_{g0} = 0.5\text{mm}$

G Joint Spacing Study

The joint spacing study seeks to indicate the relationship between joint spacing and wave time \bar{t}_{wave} . The dimensionless parameter to relate joint spacing and wave time is as follows:

$$\Delta\bar{x} / \frac{\bar{t}_{wave}\bar{c}}{\bar{L}}. \quad (72)$$

Because the non-dimensionalizing scheme sets \bar{c} and \bar{L} to unit values, the parameter $\Delta\bar{x} / \frac{\bar{t}_{wave}\bar{c}}{\bar{L}}$ is equal to $\Delta\bar{x} / \bar{t}_{wave}$.

Figure G.1 illustrates the study. Two discontinuities with the same initial size are spaced equidistant from one another starting in the middle of the bar. The distance is increased to

determine the impact of spacing on wave propagation. Table F.1 provides the initial total discontinuity sizes and sinusoidal wave parameters for the runs in the study.

\bar{x}_{joint} is the distance between joints. And, $\bar{t}_{wave}\bar{c}/\bar{L}$ is the spatial length of the input velocity pulse.

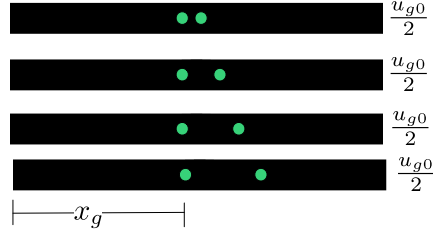


Figure G.1: Layout of Discontinuity Spacing Study

(a) Boundary Conditions, $u_p = 1.5\text{mm}$

Set	v_{max}	\bar{t}_{wave}
1	9.92 m/s	0.36
2	10.99 m/s	0.325
3	12.32 m/s	0.29
4	14.01 m/s	0.255
5	16.23 m/s	0.22
6	19.31 m/s	0.185
7	23.81 m/s	0.15

(b) Initial Discontinuity Size u_{g0}

Set	u_{g0}
1	1.5 mm

Table G.1: Inputs used for joint spacing

A tentative conclusion of these results is that the more space between gaps, the less energy is transmitted through the gaps. However, these results were collected before thoroughly understanding the implications of multiple joint wave propagation discussed in Chapter 4.5. The energy transmitted may increase if each simulation ran for a long enough time to allow the wave front to propagate to the end of the bar.

G.1 Gaps

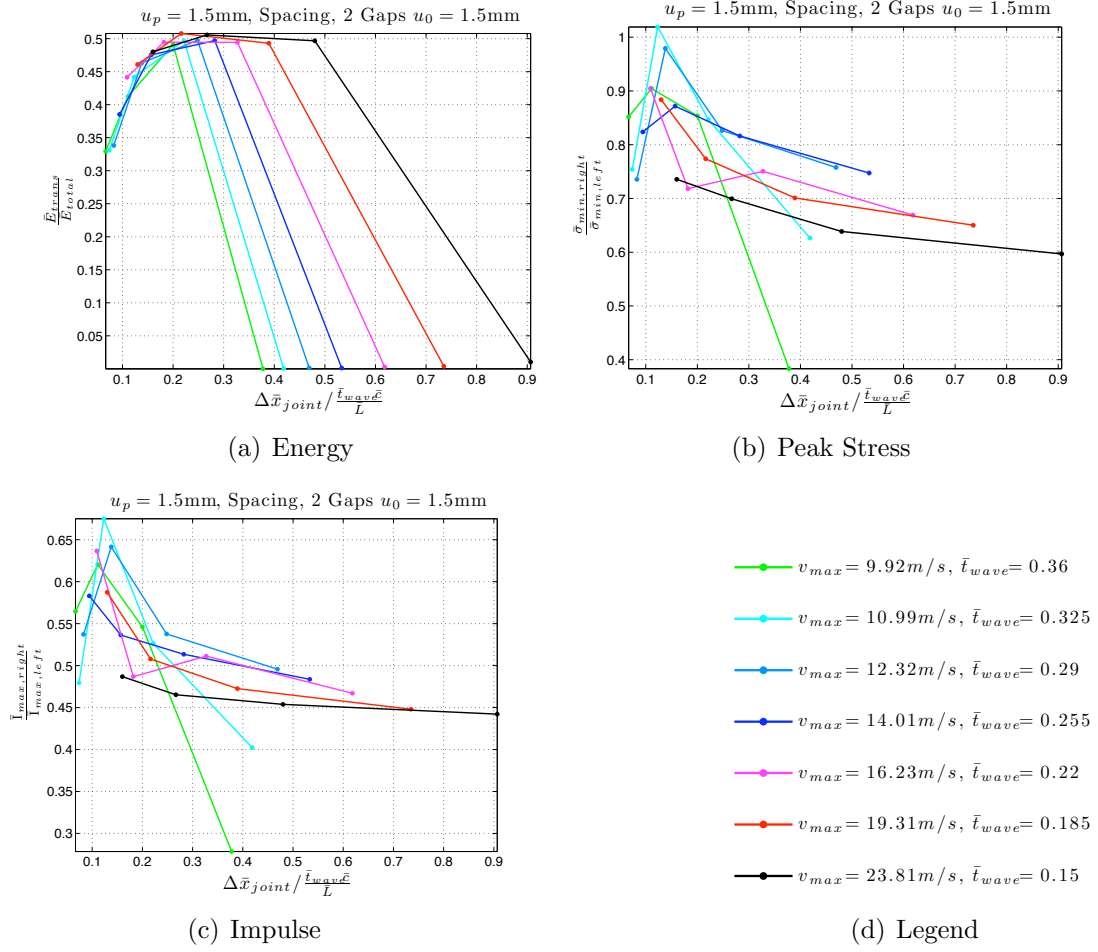


Figure G.2: Results of spacing two gaps, $u_{g0} = 1.5\text{mm}$

G.2 Plastic Joints

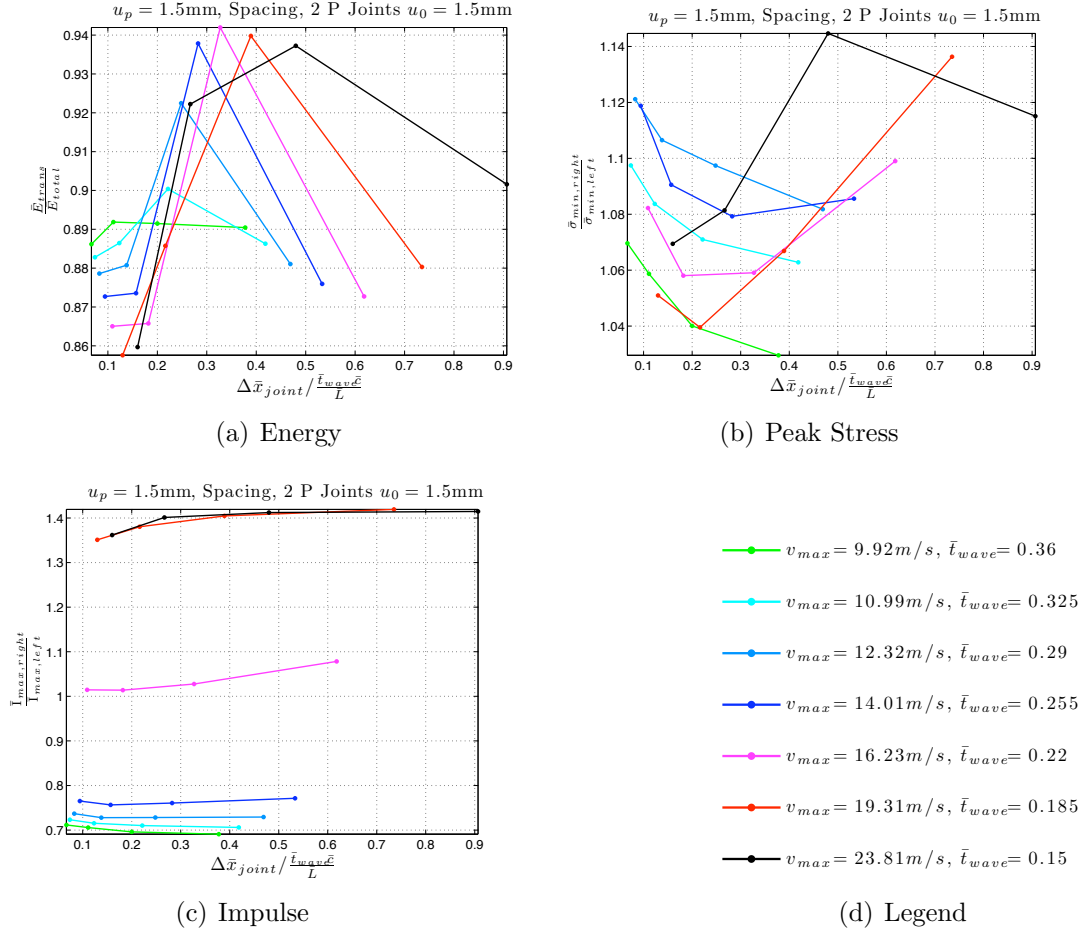


Figure G.3: Results of spacing two plastic joints, $u_{g0} = 1.5\text{mm}$

H Axisymmetric Wave Propagation

The motivation to model axisymmetric wave propagation is the direct correlation it has to a two-dimensional wave propagation from a circular pressure vessel. The axisymmetric results can be compared with the two-dimensional results as a form of validation. The motion through an axially symmetric bar is only dependent on the radial coordinate r . There is no θ or z dependence. The transient motion of the bar is defined by the governing equation of motion, the constitutive relations, and the kinematic equations. The governing equation is,

$$\frac{1}{r}(r\sigma_{rr})_{,r} - \frac{\sigma_{\theta\theta}}{r} + f = \rho u_{,tt}. \quad (73)$$

The constitutive relations are,

$$\begin{aligned}\sigma_{rr} &= E_1 \varepsilon_{rr} + E_2 \varepsilon_{\theta\theta}, \\ \sigma_{\theta\theta} &= E_2 \varepsilon_{rr} + E_1 \varepsilon_{\theta\theta}.\end{aligned}\tag{74}$$

The kinematic equations are,

$$\begin{aligned}\varepsilon_{rr} &= u_{,r}, \\ \varepsilon_{\theta\theta} &= \frac{u}{r}.\end{aligned}\tag{75}$$

For Equations (73), (74), and (75), u is the displacement, r is the radial coordinate, f is the distributed force per unit volume, ε_{rr} is the radial strain, $\varepsilon_{\theta\theta}$ is the circumferential strain, σ_{rr} is the radial stress, $\sigma_{\theta\theta}$ is the circumferential stress, E_1 and E_2 are the isotropic, linear elastic material parameters, and ρ is the density. (), is the partial derivate operator. The partial derivative of u with respect to r is symbolically $u_{,r}$. The second derivative of u with respect to r is symbolically $u_{,rr}$. The bar is confined to plane strain. The elastic material parameters E_1 and E_2 are defined by Young's modulus Y and Poisson's ratio ν as,

$$\begin{aligned}E_1 &= \frac{Y(1-\nu)}{(1+\nu)(1-2\nu)} \\ E_2 &= \frac{Y\nu}{(1+\nu)(1-2\nu)}\end{aligned}\tag{76}$$

Equations (74) and (75) are substituted into (73) to get a single differential equation in terms of u . The development of the axisymmetric numerical model from this equation uses the Finite Element Method.

H.1 Problem Layout

The numerical solution to the axially symmetric bar problem is found for three bar scenarios.

The first is for a isotropic, linearly elastic bar of length $r_{max} - r_{min}$, where $r_{min} > 0$ (Fig H.1). The bar has a traction boundary condition applied at r_{min} defined by a function $f(t)$, where $f(t)$ is a compressive, sinusoidal pulse defined over a finite time duration and by a peak amplitude. The boundary at r_{max} is free. The expected results are a stress wave in σ_{rr} propagating along the bar that has dissipation of peak stress as it moves radially and a tensile tail that develops behind the initial wave front. This numerical solution is taken as a base run to compare to the numerical results for other two solutions. Also, as r_{min} and r_{max} increase, the axisymmetric solution loses the tensile tail in the stress wave and the peak stress does not dissipate noticeably. This scenario is also modeled to using large r values in comparison to smaller values of r .

The second is for a bar that has a joint on both sides of the bar of zero strength in tension and compression that is the length of the bar oriented in the radial direction r (Fig H.2). The boundary conditions and bar length are the same as that for the first case. The presence of a joint is expected to force $\sigma_{\theta\theta}$ to zero, as the joint cannot withstand any circumferential

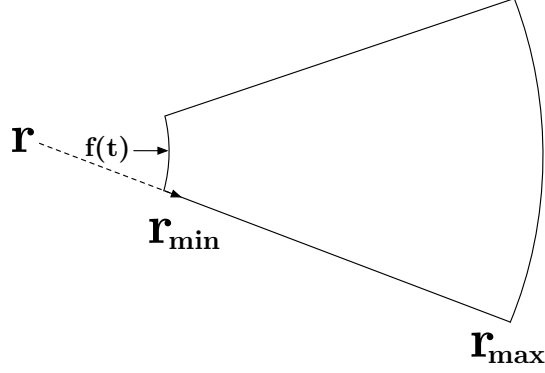


Figure H.1: Axisymmetric bar

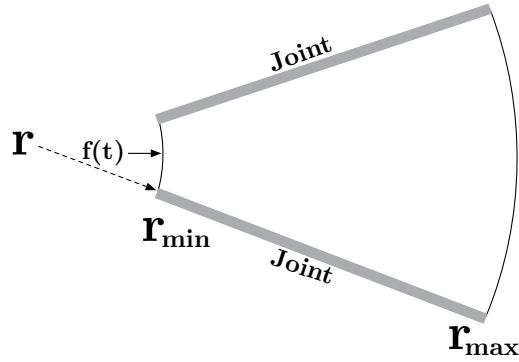


Figure H.2: Axisymmetric bar with joint parallel to radius

loading. This is enforced by setting $\sigma_{\theta\theta} = 0$ in the constitutive equation (Eq (74)), solving for $\varepsilon_{\theta\theta}$, and using this value of $\varepsilon_{\theta\theta}$ to calculate the radial stress σ_{rr} in the corresponding constitutive equation.

The third is for a bar with a joint oriented normal to the r -axis that is located halfway along the length of the bar (Fig H.3). The boundary conditions and bar length are the same for the first two cases. However, the center element is defined to have a joint that is perpendicular to the radial axis. The joint has an initial discontinuity u_0 . This discontinuity has strength in compression and zero strength in tension. The constitutive algorithm used is the same as previously implemented for a one-dimensional bar in Cartesian coordinates. It is defined by a hardening function $g(\bar{u})$, where $\bar{u} = u/u_0$. The hardening function is of the form

$$g(\bar{u}) = \sigma_g \left(1 - \frac{1}{\bar{u}^m} \right). \quad (77)$$

σ_g and m are material parameters. The expected results are an initial closure of the joint as the compressive wave propagates through and then a drop to zero stress in σ_{rr} as the tensile tail propagates into the joint. The tensile tail should not propagate past the joint because the joint cannot withstand any tensile loading.

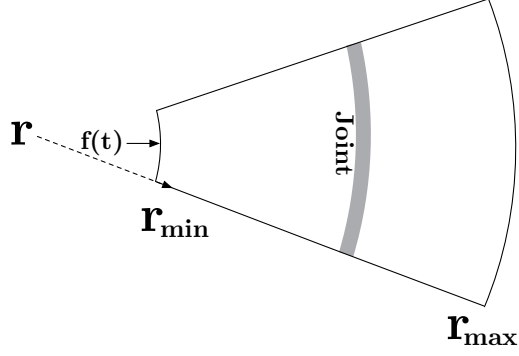


Figure H.3: Axisymmetric bar with joint perpendicular to radius

H.2 Results

H.2.1 Parameters

The three different axisymmetric bar problems have the same input parameters. These are,

- $r_{min} = 20$ m
- $r_{max} = 100$ m
- Max input force $f_{max} = 0.5$ N
- Time of wave input $t_{in} = 1.8$ s, approximately a third of the time for a wave to propagate to end of the bar
- Traction boundary condition $f(t) = f_{max} \left(1 - \cos(2\pi \frac{t}{t_{in}}) \right)$ over a time $0 < t < t_{in}$
- Bar length $L = r_{max} - r_{min}$
- Density $\rho = 1 \frac{\text{kg}}{\text{m}^3}$
- Young's Modulus $Y = 200 \frac{\text{kg}}{\text{ms}^2}$
- Hardening parameters $\sigma_g = 0.001 \frac{\text{N}}{\text{m}^2}$ and $m = 3$
- Initial joint size of $u_0 = 1.25$ mm, joint is located at a value of $r = 59.375$ m
- 64 elements are used to discretize the bar in each run

H.2.2 Plots

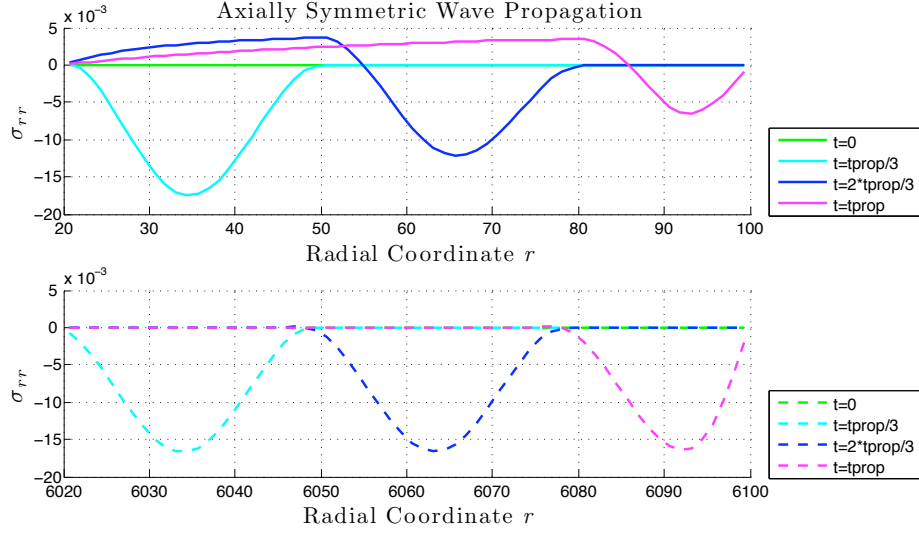


Figure H.4: Comparison of σ_{rr} when r values are large, t_{prop} is the length of time of wave propagation for the length of the bar, both cases are plotted at the same times where t_{prop} is the time of one wave propagation along the bar

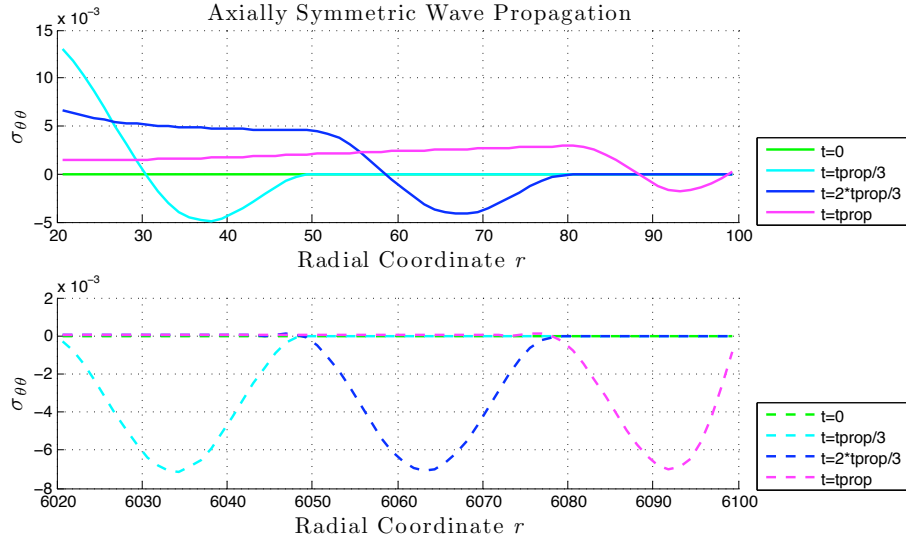


Figure H.5: Comparison of $\sigma_{\theta\theta}$ when r values are large, t_{prop} is the length of time of wave propagation for the length of the bar, both cases are plotted at the same times where t_{prop} is the time of one wave propagation along the bar

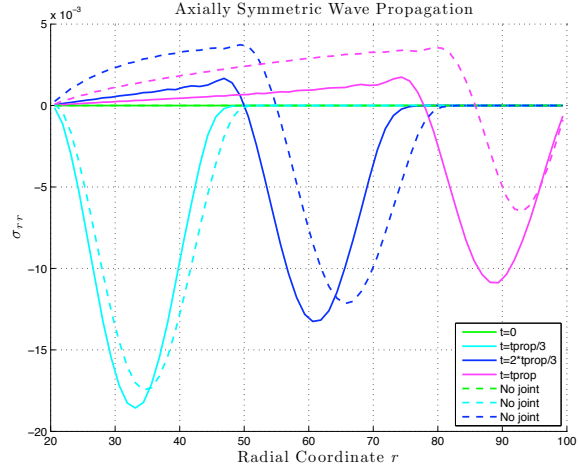


Figure H.6: Comparison of σ_{rr} when radial joint runs along bar, dashed lines are case with no joint, t_{prop} is the length of time of wave propagation for the length of the bar, both cases are plotted at the same times

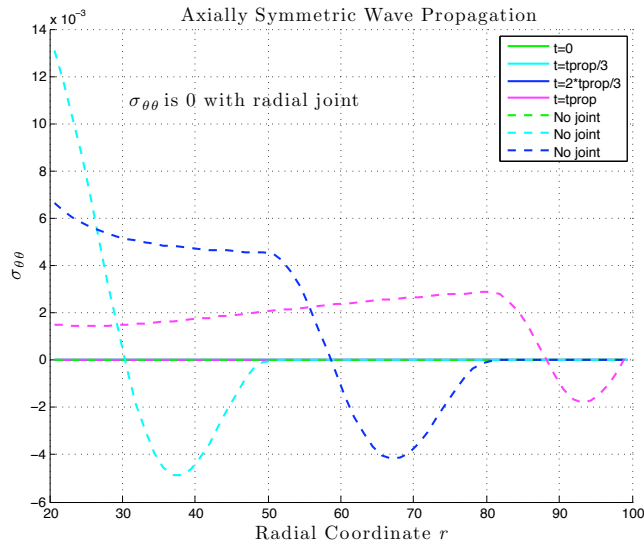


Figure H.7: Comparison of $\sigma_{\theta\theta}$ when radial joint runs along bar, dashed lines are case with no joint, t_{prop} is the length of time of wave propagation for the length of the bar, both cases are plotted at the same times

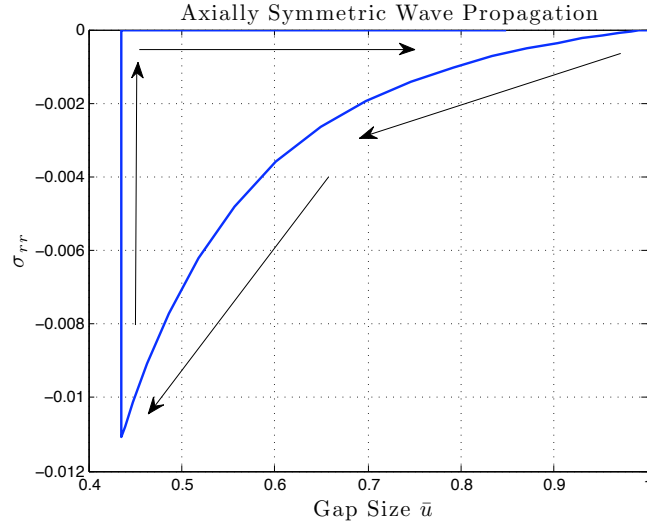


Figure H.8: Gap size versus σ_{rr} when a joint is perpendicular to r -axis in middle of bar

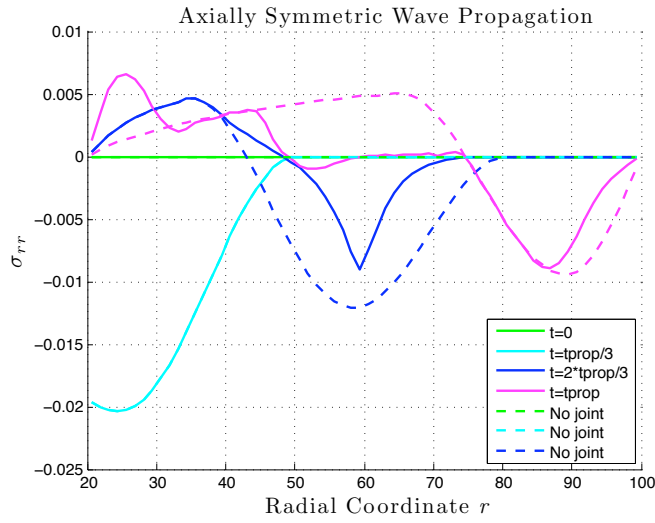


Figure H.9: Comparison of σ_{rr} when radial perpendicular to bar in middle of bar, dashed lines are case with no joint, t_{prop} is the length of time of wave propagation for the length of the bar, both cases are plotted at the same times

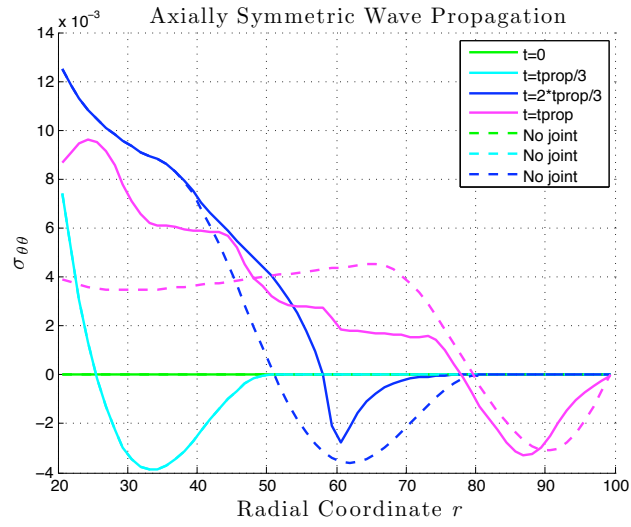


Figure H.10: Comparison of $\sigma_{\theta\theta}$ when joint perpendicular to bar in middle of bar, dashed lines are case with no joint, t_{prop} is the length of time of wave propagation for the length of the bar, both cases are plotted at the same times

H.3 Discussion

Figures H.4 and H.5 demonstrate that as the radial coordinates increase, the solution loses the tensile tail in both σ_{rr} and $\sigma_{\theta\theta}$. The length of each bar is the same but because of the dependence on r , the magnitude of peak stress dissipation decreases as r increases. Note that the values of f_{max} is not the same for both runs. f_{max} was increased for the case of large r values so that for the first time plotted the values of σ_{rr} was the same.

Figures H.6 and H.7 are the second case shown in Figure H.2. The case without a joint is also plotted to show the impact of a radial joint of zero strength. The values of σ_{rr} do not dissipate as quickly with the radial joint. Also, $\sigma_{\theta\theta}$ remains zero because of the nature of the joint strength.

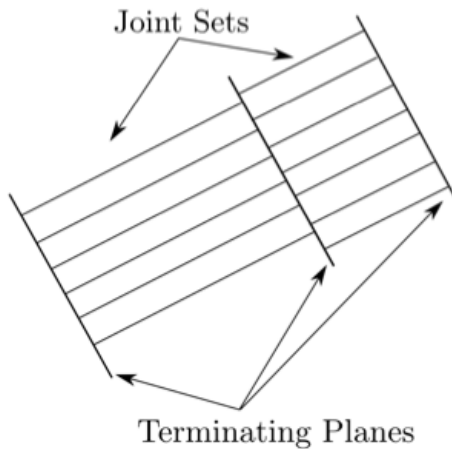
Figures H.9, H.10, and H.8 are for the third case shown in Figure H.3. Figure H.9 shows that once the compressive wave interacts with the joint, a portion of the wave energy is lost in closing the joint. Then, once the tensile tail of the stress wave hits the joint, the stress drops to zero at the joint and the joint opens. The normal joint impacts the radial strain, from which the circumferential stress comes because of the constitutive equations (Eq 74). The magnitude of the circumferential stress decreases as well with the wave-joint interaction, as shown in Figure H.10. The dimensionless size of the gap \bar{u} is given in Figure H.8. Following the arrows, the joint initially closes with the compressive wave following the hardening function. Then, the joint size remains fixed as the elastic portion of the element unloads (the vertical line). Finally, the element is unloaded and because the joint cannot withstand any tensile load, any increment in radial strain immediately opens the joint further while radial stress remains at zero.

5

Modeling of Joints and Faults

5.1 Introduction

A joint can be thought of as a weak plane between two beds of rock. Typically joints appear in sets parallel to the bedding planes of the rock. The spacing between joints within each set may vary from centimeters to 10 meters [Goodman; 1989]. One set of joints may be offset from a second set by a terminating plane as indicated in Fig. 5.1(a). It is also possible that a second set of joints may overlay the first where the normal to the joints in one set forms an arbitrary angle with respect to the normal of the second set. A photograph illustrating joints in an exposed geological structure is shown as Fig. 5.1(b).



(a) Sketch of joint sets



(b) Photograph of Jointed Rock

Figure 5.1: Jointed rock.

The object here is to develop a constitutive discrete model for an individual joint. The intent is to get the general features that are observed in experimental data into the model but not to attempt to include all possible variations because there is no way that explicit data for all joints can be obtained and utilized when a numerical simulation of waves through jointed media containing tens or hundreds of joints is being performed. If a suitable constitutive model is available, the sensitivity of predicted results to values of material parameters in the model can be performed to determine if it is necessary to better characterize a particular feature.

For a numerical simulation, the effect of a joint in an element or cell is smeared over the cell to obtain an equivalent joint strain. An alternative approach is to develop a smeared constitutive equation in which a representative volume element must be defined *a priori*. By forming a discrete constitutive equation, the step associated with smearing becomes part of the error in the numerical solution and is related to the size of the elements.

A joint can be thought of as a pre-existing crack filled with rubble. If the joint is subjected to compression, the fill provides resistance to closure where the resistance traction is a nonlinear function of the amount of crack closure. A joint is generally considered to provide little or no resistance to tensile stress.

The situation is more complicated when a joint is subjected to shear for then the effects of both asperities on the joint surfaces and frictional resistance must be taken into account. Simultaneously, the interaction of shear with normal traction must be included.

In the next section, general features associated with joint behavior are summarized. Since some features may not hold for all joints they are listed as assumptions on which the model is constructed. The following section provides a three-dimensional constitutive model for joint behavior. This is followed by constitutive equation subroutines based on the model. Finally, representative results for certain paths are presented.

5.2 Outline of the Basic Constitutive Approach

5.2.1 Preliminary Remarks

The focus of this report is to fully describe a constitutive equation that models joint deformation as represented by a discontinuity in displacement. Ultimately, a joint must be modeled in the context of its surrounding continuum material, which is often rock. Typically, numerical solutions to a structural configuration for stress and displacements are desired when static or dynamic forces applied. In this section, the constitutive equation for rock is provided. Then a detailed description of the constitutive equation for joints is incorporated. It is assumed that for the purpose of this study, the constitutive properties of joints are the dominant aspects that describe the features of wave motion through joints and rock. The next section provides the details of how rock and joint constitutive features are combined to form composite constitutive features for use in an element-based numerical algorithm.

Stress, σ , and strain, e , must be determined for the continuum, the joint and for an element involving both rock and a joint. A subscript “C” is used for the continuum, “J” for a joint, and no subscript is used for element-based variables. Superscripts “e” and “p” on strain designate elastic and plastic parts, respectively, of the strain tensor. No superscript implies total strain consisting of the sum of elastic and plastic parts. Since the joint material is nonlinear, all constitutive equations will be given in rate form so that the formulation used for numerical implementation is easily obtained with the use of stress and strain increments. A superposed dot represents a derivative with respect to time. Since the formulation is rate independent, time can be considered as any monotonically increasing variable, including time, used as a variable to describe the loading process.

5.2.2 Material between Joints and Faults

It is assumed that the continuum material between joints is elastic. Therefore the total strain for the continuum is equal to the elastic strain so the following equation will be used whenever convenient in the subsequent development:

$$e_C = e_C^e \quad (5.1)$$

In addition, the continuum is assumed to be isotropic so that the rate form of the set of continuum constitutive equations for any basis in matrix form is

$$\begin{aligned}
\begin{Bmatrix} \dot{\sigma}_{C11} \\ \dot{\sigma}_{C22} \\ \dot{\sigma}_{C33} \end{Bmatrix} &= \begin{bmatrix} E_{C1} & E_{C2} & E_{C2} \\ E_{C2} & E_{C1} & E_{C2} \\ E_{C2} & E_{C2} & E_{C1} \end{bmatrix} \begin{Bmatrix} \dot{\epsilon}_{C11} \\ \dot{\epsilon}_{C22} \\ \dot{\epsilon}_{C33} \end{Bmatrix} \\
\begin{Bmatrix} \dot{\sigma}_{C12} \\ \dot{\sigma}_{C23} \\ \dot{\sigma}_{C31} \end{Bmatrix} &= \begin{bmatrix} 2G_C & 0 & 0 \\ 0 & 2G_C & 0 \\ 0 & 0 & 2G_C \end{bmatrix} \begin{Bmatrix} \dot{\epsilon}_{C12} \\ \dot{\epsilon}_{C23} \\ \dot{\epsilon}_{C31} \end{Bmatrix}
\end{aligned} \tag{5.2}$$

in which

$$E_{C1} = \frac{Y_C(1-\nu_C)}{(1+\nu_C)(1-2\nu_C)} \quad E_{C2} = \frac{\nu_C}{(1-\nu_C)}E_{C1} \quad 2G_C = \frac{Y_C}{(1+\nu_C)} \tag{5.3}$$

with Y_C denoting Young's modulus, G_C the shear modulus, and ν_C Poisson's ratio.

5.2.3 Joints and Faults

The behavior of joints and faults are assumed to have enough similarities to warrant a constitutive formulation that can handle both cases. This development is the primary focus of this part of the project and is given Section 5.3.

5.2.4 Combination of Joints and Faults with the Surrounding Medium

For numerical simulations, the effect of a joint or fault must be included with rock in a finite region associated with a material point or finite element. The process of assimilating these two aspects results in a combined constitutive equation that is highly nonlinear and anisotropic. This is the basis for the numerical algorithm that is provided in Section 5.4. Representative results for strain paths are given in Section 5.5.

5.3 Constitutive Model for Joints and Faults

5.3.1 Initial Comments

In this section a constitutive equation for a joint or a fault is developed. A fault is defined to be similar to a joint with the key distinction that joints appear as sets and have relatively small and finite lengths whereas faults appear singly, are can be much wider than joints and are an order of magnitude longer in length. The formulation is more general than what might be considered if only joints are being considered. The constitutive equation allows for a combination of nonlinear elasticity and plasticity although each is limited in scope. The nonlinearly elastic part is associated with the

normal, or compaction, part of the deformation, and plasticity is limited to the compaction and tangential, or shear, parts. This section is limited strictly to deformation of the joint or fault.

5.3.2 Notation

Consider an orthonormal triad of vectors $(\mathbf{n}, \mathbf{t}, \mathbf{p})$ where \mathbf{t} and \mathbf{p} lie in the plane of one of the surfaces of a joint with normal \mathbf{n} as shown in Fig. 5.2. In this system the components of the strain tensor, \mathbf{e} , are $\{e_{Jnn}, e_{Jnt}, e_{Jnp}, e_{Jtt}, e_{Jpp}, e_{Jtp}\}$. Corresponding components exist for the stress tensor $\boldsymbol{\sigma}$ with the addition notation that the components of the traction, $\boldsymbol{\tau}$, are defined to be

$$\tau_{Jn} = \sigma_{Jnn} \quad \tau_{Jt} = \sigma_{Jnt} \quad \tau_{Jp} = \sigma_{Jnp} \quad (5.4)$$

The initial width of the joint is $[u_{J0}]$. The relative displacements of points originally opposite each other on the two surfaces defining a joint are $[u_{Jn}]$, $[u_{Jt}]$ and $[u_{Jp}]$. Note that the definition is based on the assumption that the initial relative displacement in shear is zero, and in the normal direction the initial normal displacement is $[u_{Jn}]_{\text{initial}} = [u_{J0}]$. Shear, or tangential motion is defined to be motion in the $\mathbf{t} - \mathbf{p}$ plane even though \mathbf{t} is defined to be the tangential direction.

Dimensionless components of displacement discontinuity are defined to be

$$\bar{u}_{Jn} = \frac{[u_{Jn}]}{[u_{J0}]} \quad \bar{u}_{Jt} = \frac{[u_{Jt}]}{[u_{J0}]} \quad \bar{u}_{Jp} = \frac{[u_{Jp}]}{[u_{J0}]} \quad (5.5)$$

Corresponding joint strains are defined to be

$$e_{Jnn} = \frac{[u_{Jn}] - [u_{J0}]}{[u_{J0}]} = \bar{u}_{Jn} - 1 \quad e_{Jnt} = \frac{[u_{Jt}]}{2[u_{J0}]} = \frac{\bar{u}_{Jt}}{2} \quad e_{Jnp} = \frac{[u_{Jp}]}{2[u_{J0}]} = \frac{\bar{u}_{Jp}}{2} \quad (5.6)$$

in which the definition of the shear components is based on the tensor formulation rather than on the definition of engineering shear.

With compaction, the value of \bar{u}_{Jn} decreases from an initial value of unity to a minimum possible value of zero. However, it is possible that the shear motion can be relatively large with the result that \bar{u}_{Jt} and \bar{u}_{Jp} may assume large values, negative or positive.

The remaining components of joint strain $\{e_{Jtt}, e_{Jpp}, e_{Jtp}\}$ are assumed to be based on the usual continuum approach and much less significant than the components defined in (5.6).

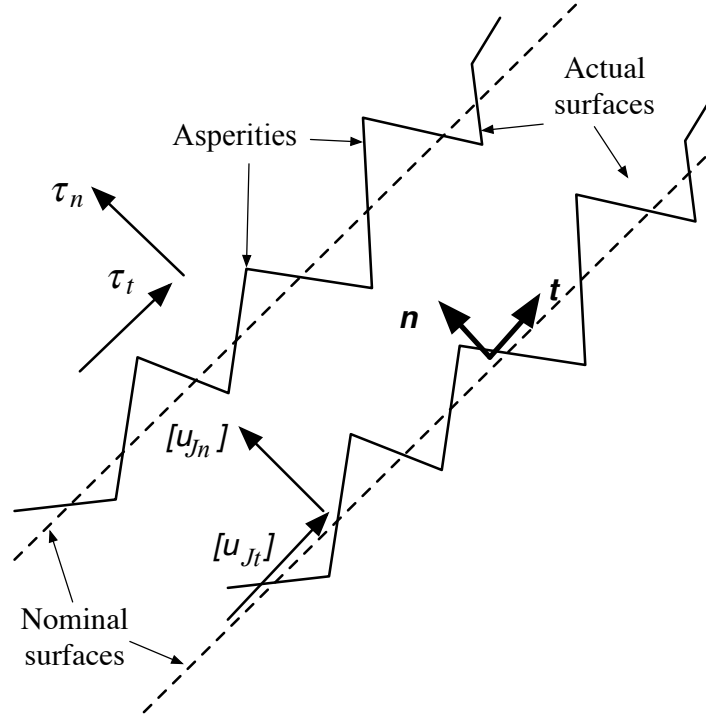


Figure 5.2: Notation for a joint.

5.3.3 Assumed Features for Joint Behavior

The joint is assumed to be a crack with an initial discontinuity in the normal direction. Closure, or compaction, is resisted by material within the joint. Resistance to opening, or to tension is small or nonexistent. Shearing motion produces tangential discontinuities. Resistance to shear may exist due to a combination of frictional resistance and the presence of asperities.

To set the groundwork on which the model is based, assumed features of joint behavior are provided in this subsection. The primary purpose is to provide the reader with a basis for determining quickly if the proposed model is appropriate or not.

The assumptions are:

Direct Closing and Opening

- (1) Under uniaxial compression, the compressive joint stress is a highly nonlinear function of the amount of closure.
- (2) The features of stress versus closure for different joints can be reflected reasonably well by a single analytical expression if dimensionless forms of stress and closure are used.
- (3) Upon unloading in the compressive regime, a nonlinear elastic response is exhibited.

- (4) A joint exhibits no strength in tension.

These features are sketched in Fig. 5.3.

Direct Shear

- (5) The amount of tangential motion may be several orders of magnitude larger than the amount of normal compaction.
- (6) After sufficiently large shear motion, the response is governed by Coulomb's friction criterion.
- (7) Even with no compressive component of traction, joints exhibit resistance to shear due to the surface roughness in the form of asperities between the mating surfaces.
- (8) After a certain amount of shear the asperities wear down and any accompanying cohesive strength is lost.

Combined Shear and Normal Deformation

- (9) Compressive traction enhance the apparent strength in shear due to asperities.
- (10) Asperities cause dilatation under shear.

These are the features incorporated into the model outlined in the next section.

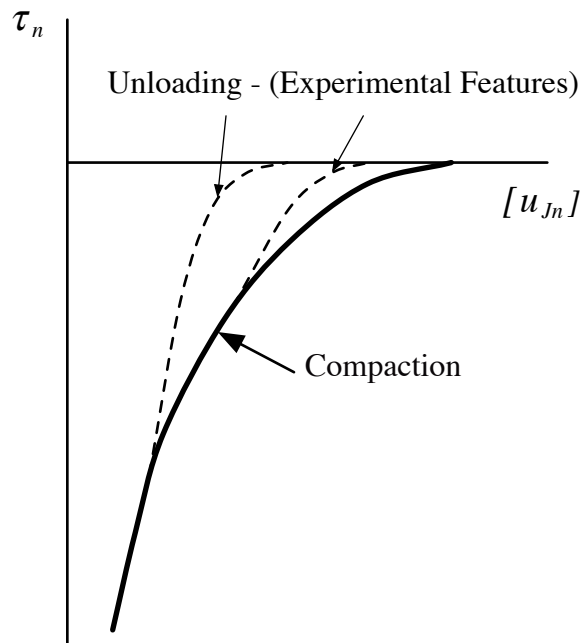


Figure 5.3: Observed features for normal compaction and unloading of a joint.

5.3.4 Basic Formulation for Compaction

Because there is a wide variety of joint geology, it is reasonable to assume that a corresponding diversity of response behavior in compression exists. There is very little information on the behavior of *in situ* joints. However, data on manufactured joints do provide some general features to serve as a guide in developing a constitutive equation.

In this subsection, we focus on just one aspect, namely that of modeling the closure, or compaction, of a joint, with no shear. For a constitutive model, the following features are assumed to be reasonable: (i) the compressive stress is a nonlinear function of the amount of compaction, (ii) closure is not elastic, (iii) unloading follows a different path and is also nonlinear, and (iv) the unloading phase appears to be mostly elastic. These features are sketched in Fig. 5.3.

To the list of generally observed features, we add the following assumption: (v) the elastic modulus of the joint under high stress cannot exceed that of the parent rock. The last point has the implication that if the inelastic part of the joint behavior is modeled as plasticity, then there is a degree of compaction beyond which the behavior is strictly elastic.

With this great degree of uncertainty, we must be careful about the objectives that can realistically be accomplished. The basic idea is to provide a general formulation which can be used to (i) obtain numerical solutions for wave propagation through joints, (ii) to provide a framework for which material parameters can be selected to approximate material data as they become available, and (iii) to allow changes to be made in a fairly straightforward way if the formulation proves to be not general enough.

We assume that with a large compaction stress, a maximum value of permanent closure can be defined and this value is taken to be the maximum possible plastic displacement, $[u_{j0}^p]$. The maximum possible elastic displacement, $[u_{j0}^e]$, is the remainder, or

$$[u_{j0}^e] = [u_{j0}] - [u_{j0}^p] \quad (5.7)$$

With this approach, the initial values of total, elastic and plastic joint displacements are

$$[u_{jn}]_{initial} = [u_{j0}] \quad [u_{jn}^e]_{initial} = [u_{j0}^e] \quad [u_{jn}^p] = [u_{j0}^p] \quad (5.8)$$

as indicated in Fig. 5.4.

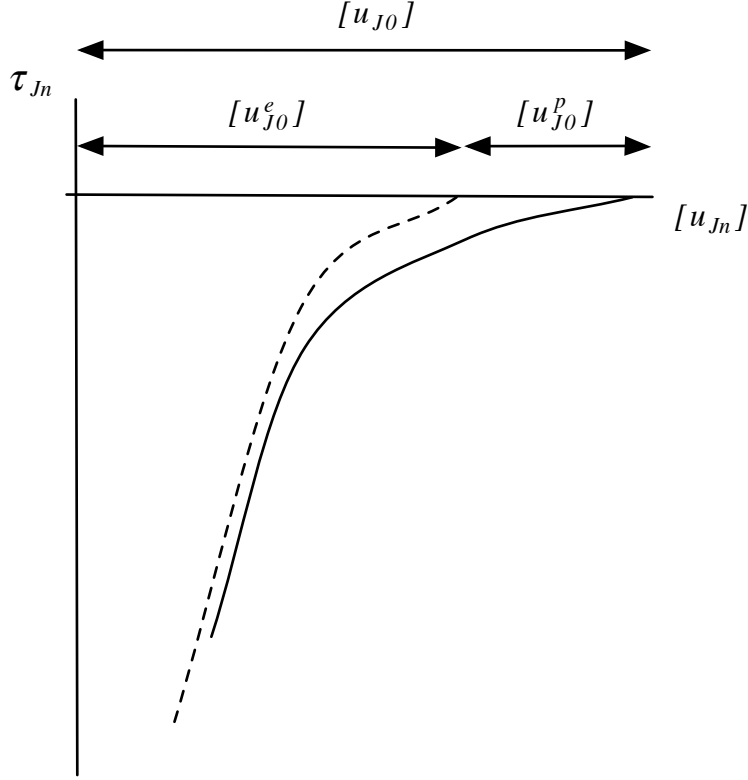


Figure 5.4: Closure of a joint.

Define the normal component of elastic and plastic strains as follows:

$$e_{Jnn}^e = \frac{[u_{Jn}^e] - [u_{J0}^e]}{[u_{J0}]} \quad e_{Jnn}^p = \frac{[u_{Jn}^p] - [u_{J0}^p]}{[u_{J0}]} \quad (5.9)$$

With these definitions, the total strain is the sum of elastic and plastic parts:

$$e_{Jnn} = e_{Jnn}^e + e_{Jnn}^p \quad (5.10)$$

and the initial values of all strains are zero. The nonzero values of strain for compaction are negative. Two of the three values $\{[u_{J0}], [u_{J0}^e], [u_{J0}^p]\}$ must be specified and can be considered joint material parameters.

Some of these details are illustrated in Fig. 5.4 in which the closure stress is plotted as a function of displacement discontinuity (solid line). Upon unloading, the stress follows the dotted line, and the function associated with the dotted line is taken to be the elastic response curve for the joint.

For convenience, introduce the following dimensionless variables:

$$\bar{u}_{J0}^e = \frac{[u_{J0}^e]}{[u_{J0}]} \quad \bar{u}_{J0}^p = \frac{[u_{J0}^p]}{[u_{J0}]} \quad (5.11)$$

Then the following relations hold:

$$\begin{aligned}
e_{Jnn} &= \bar{u}_{Jn} - I & e_{Jnn}^e &= \bar{u}_{Jn}^e - \bar{u}_{J0}^e & e_{Jnn}^p &= \bar{u}_{Jn}^p - \bar{u}_{J0}^p \\
\bar{u}_{Jn}^e + \bar{u}_{Jn}^p &= \bar{u}_{Jn} & \bar{u}_{J0}^e + \bar{u}_{J0}^p &= I
\end{aligned} \tag{5.12}$$

A similar structure for the in-plane shear strains in terms of elastic and plastic parts is assumed

$$\begin{aligned}
e_{Jnt} &= e_{Jnt}^e + e_{Jnt}^p & e_{Jnp} &= e_{Jnp}^e + e_{Jnp}^p \\
\bar{u}_{Jt} &= \bar{u}_{Jt}^e + \bar{u}_{Jt}^p & \bar{u}_{Jp} &= \bar{u}_{Jp}^e + \bar{u}_{Jp}^p
\end{aligned} \tag{5.13}$$

The remaining components of strain within the joint are assumed to be the conventional ones associated with a continuum. These components of strain are assumed to be small enough so that the plastic parts are negligible, or

$$e_{Jtt} = e_{Jtt}^e \quad e_{Jpp} = e_{Jpp}^e \quad e_{Jtp} = e_{Jtp}^e \tag{5.14}$$

5.3.5 Elasticity

The behavior of the joint is assumed to be nonlinearly elastic and the tangent elastic constitutive equation for the joint in rate form is assumed to be orthotropic as follows:

$$\begin{aligned}
\left\{ \begin{array}{c} \dot{\tau}_{Jn} = \dot{\sigma}_{Jnn} \\ \dot{\sigma}_{Jtt} \\ \dot{\sigma}_{Jpp} \end{array} \right\} &= \begin{bmatrix} E_{J11} & E_{J12} & E_{J12} \\ E_{J12} & E_{J22} & E_{J23} \\ E_{J12} & E_{J23} & E_{J22} \end{bmatrix} \left\{ \begin{array}{c} \dot{e}_{Jnn}^e \\ \dot{e}_{Jtt}^e \\ \dot{e}_{Jpp}^e \end{array} \right\} \\
\left\{ \begin{array}{c} \dot{\tau}_{Jt} = \dot{\sigma}_{Jnt} \\ \dot{\tau}_{Jp} = \dot{\sigma}_{Jnp} \\ \dot{\sigma}_{Jtp} \end{array} \right\} &= \begin{bmatrix} 2G_J & 0 & 0 \\ 0 & 2G_J & 0 \\ 0 & 0 & 2G_{Jp} \end{bmatrix} \left\{ \begin{array}{c} \dot{e}_{Jnt}^e \\ \dot{e}_{Jnp}^e \\ \dot{e}_{Jtp}^e \end{array} \right\}
\end{aligned} \tag{5.15}$$

Now the problem is to assign suitable values for the elastic parameters.

When joints are unloaded from a compressed state, the response is typically nonlinear and elastic. If the unloading path is assumed to be one of uniaxial strain, the implication is that that tangent elastic modulus E_{J11} is not constant.

Under uniaxial strain loading in the normal direction, the normal component of stress is taken to be a unique, nonlinear function of the corresponding component of elastic strain:

$$\tau_{Jn} = g^e(e_{Jnn}^e) \tag{5.16}$$

Postulate an elastic relation of the form

$$g^e = E_{J0}e_{jnn}^e - (E_{JU} - E_{J0})\frac{\bar{u}_{j0}^e}{m^e}\left\{\frac{-e_{jnn}^e}{\bar{u}_{j0}^e}\right\}^{m^e} \quad (5.17)$$

Then the elastic tangent modulus is

$$E_{J11} = \frac{\partial g^e}{\partial e_{jnn}^e} = E_{J0} + (E_{JU} - E_{J0})\left\{\frac{-e_{jnn}^e}{\bar{u}_{j0}^e}\right\}^{m^e-1} \quad (5.18)$$

The elastic modulus assumes the initial value, E_{J0} , for zero elastic strain. For large values of strain, or as $e_{jnn}^e \rightarrow -\bar{u}_{j0}^e$ the elastic modulus asymptotically approaches the ultimate value of E_{JU} . If this ultimate value equals the corresponding value of the modulus for rock, then with the use of (5.2) the following holds:

$$E_{JU} = E_{C1} \quad (5.19)$$

The result is that the nonlinear elastic response is characterized by the material parameters, $(E_{J0}, E_{C1}, \bar{u}_{j0}^e, m^e)$, of which the last two are dimensionless. It is assumed that the magnitude of the normal component of stress for the minimum possible elastic strain is much larger than any value that could be achieved in the field. The alternative approach is to utilize a more complicated form for the function g^e so that the magnitude of stress becomes infinite as $e_{jnn}^e \rightarrow -\bar{u}_{j0}^e$.

If it is assumed that the other two components of normal strain remain small, then it is reasonable to assume that the other diagonal component related to normal components of the elastic tangent stiffness described in (5.15) satisfies

$$E_{J22} = E_{J0} \quad (5.20)$$

In addition, we assume the shear component e_{jp} is small. Next the simplifying assumption is made that Poisson's ratio is a constant, ν_{J0} . In analogy with the relations that hold for isotropic materials, the remaining tangent coefficients are chosen to be

$$\begin{aligned} E_{J12} &= \frac{\nu_{J0}}{(1-\nu_{J0})}E_{J11} & E_{J23} = E_{J230} &= \frac{\nu_{J0}}{(1-\nu_{J0})}E_{J22} = \frac{\nu_{J0}}{(1-\nu_{J0})}E_{J0} \\ 2G_J &= \frac{(1-2\nu_{J0})}{(1-\nu_{J0})}E_{J11} & 2G_{Jp} = 2G_{Jp0} &= \frac{(1-2\nu_{J0})}{(1-\nu_{J0})}E_{J22} = \frac{(1-2\nu_{J0})}{(1-\nu_{J0})}E_{J0} \end{aligned} \quad (5.21)$$

in which a "0" has been appended to the subscripts of those parameters that are constant. Note that the components $(E_{J11}, E_{J12}, 2G_J)$ are not constants.

With the rock parameters assumed known, the additional elasticity parameters that must be specified consists of $(E_{J0}, \bar{u}_{j0}^e, m^e, \nu_{J0})$. The shear modulus for the nt- and np-components can become large under compaction. The only relation that is completely and linearly elastic is the one relating σ_{Jp} and e_{Jp}^e .

5.3.6 Plasticity

Basic Structure

A conventional plasticity model requires a yield surface and evolution equations for plastic strains and other internal variables. A particular model requires the choice of specific forms for a yield function and the evolution functions.

Define an effective shear stress for the joint to be

$$\tau_{Js} = [\tau_{Jt}^2 + \tau_{Jp}^2]^{1/2} \quad (5.22)$$

The proposed yield function is assumed to depend on τ_{Jn} and τ_{Js} . A yield function for the joint, F_J , is proposed for which $F_J < 0$ indicates elastic behavior, yielding occurs if $F_J = 0$, and $F_J > 0$ is not allowed theoretically. The yield surface $F_J = 0$ is taken to be a combination of three individual yield surfaces for compaction, effective shear and tension:

$$F_C = 0 \quad F_S = 0 \quad F_T = 0 \quad (5.23)$$

For numerical simulations it is desirable to use dimensionless variables denoted with an over-bar. If dimensionless stress and yield functions are used, the proposed forms for the yield surfaces of (5.23) are illustrated in Fig. 5.5.

In this subsection, detailed descriptions for each individual yield surface is given. Possible coupling between yield functions is also considered.

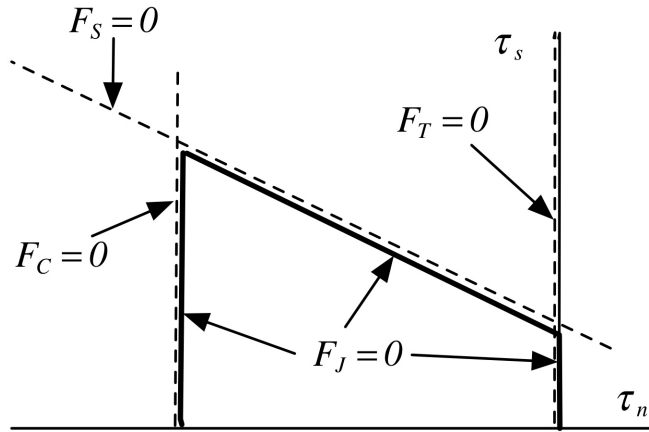


Figure 5.5: Yield surface for joint in space of traction components.

Compaction

For compaction, it is assumed that the dominant effect is captured through the use of normal components of stress, τ_{Jn} , and plastic strain, e_{Jnn}^p . Coupling with shear such

as shear-enhanced compaction is not included. The yield function for compaction only is assumed to be

$$F_C = \tau_{Jcy} - \tau_{Jn} \quad (5.24)$$

where the yield stress in compaction, τ_{Jcy} , is given in the following generic form:

$$\tau_{Jcy} = g^p(<-e_{Jnn}^p>) \quad (5.25)$$

The function g^p is chosen to be negative for negative values of e_{Jnn}^p . Therefore $F_C < 0$ if $\tau_{Jn} > \tau_{Jcy}$. The bracket on the strain is used to imply that the yield function is zero for positive values of plastic strain, which is also used to track joint opening. For convenience, the bracket will be dropped with the understanding that the yield function is zero for positive plastic strain.

A feature consistent with that of elastic behavior for large compaction is obtained by choosing the yield stress to become infinite as $\bar{u}_{Jn}^p \rightarrow \bar{u}_{J0}^p$ or $e_{Jnn}^p \rightarrow -\bar{u}_{J0}^p$. One possible form is the following:

$$g^p = E_{J0}^p \frac{\bar{u}_{J0}^p}{m^p} \left[1 - \left\{ \frac{\bar{u}_{J0}^p}{e_{Jnn}^p + \bar{u}_{J0}^p} \right\}^{m^p} \right] \quad (5.26)$$

in which the value zero for g^p has been imposed for zero plastic strain because experimental data indicate a very small value for the initial yield stress. Additional material parameters are E_{J0}^p and m^p of which the latter is dimensionless. The yield stress becomes infinitely large and negative as $e_{Jnn}^p \rightarrow -\bar{u}_{J0}^p$. The tangent plastic modulus is defined to be

$$E_J^p \equiv \frac{\partial g^p}{\partial e_{Jnn}^p} = E_{J0}^p \left\{ \frac{\bar{u}_{J0}^p}{e_{Jnn}^p + \bar{u}_{J0}^p} \right\}^{m^p-1} \quad (5.27)$$

so that E_{J0}^p can be interpreted as the plastic modulus for zero plastic strain.

Suppose compaction is followed by unloading to a negative or zero value of normal stress. Upon immediate reloading the response is purely elastic. Suppose the unloading to zero stress is followed by further unloading specified by further positive increments in joint displacement. The elastic joint strain remains zero but the plastic strain is allowed to increase (decrease in absolute value) with a corresponding reduction in absolute value of yield stress. With even more unloading the total joint discontinuity \bar{u}_{Jn} is larger than unity and a gap forms. The elastic part of the gap opening is fixed at $\bar{u}_{Jn}^e = \bar{u}_{J0}^e$, and does not change until a reverse in loading causes the gap to close so that $\bar{u}_{Jn} = 1$. Then upon further compaction, the original stress-strain curve is recovered.

If experimental data indicate that cyclic loading causes a change in the stress-strain curve, then a kinematic feature must be incorporated into the formulation.

The evolution equation for plastic strain is assumed to be based on an associated flow rule, or

$$\dot{\epsilon}_{Jnn}^p = \dot{\bar{u}}_{Jn}^p = \dot{\omega}_c \frac{\partial F_C}{\partial \tau_{Jn}} = -\dot{\omega}_c \quad (5.28)$$

in which ω_c is considered to be a monotonically increasing parameter so that $\dot{\omega}_c \geq 0$ and, therefore, $\dot{\epsilon}_{Jnn}^p \leq 0$. To obtain ω_c the consistency condition $\dot{F}_C = 0$ is invoked. With the use of (5.25), (5.27) and the first of (5.27), the result is

$$\begin{aligned} \dot{\tau}_{Jcy} - \dot{\tau}_{Jn} &= 0 \\ E_J^p \dot{\epsilon}_{Jnn}^p - E_{J11} \dot{\epsilon}_{Jnn}^e - E_{J12} (\dot{\epsilon}_{Jtt}^e + \dot{\epsilon}_{Jpp}^e) &= 0 \\ E_J^p \dot{\epsilon}_{Jnn}^p - E_{J11} (\dot{\epsilon}_{Jnn} - \dot{\epsilon}_{Jnn}^p) - E_{J12} (\dot{\epsilon}_{Jtt} + \dot{\epsilon}_{Jpp}) &= 0 \\ (E_J^p + E_{J11}) \dot{\epsilon}_{Jnn}^p - E_{J11} \dot{\epsilon}_{Jnn} - E_{J12} (\dot{\epsilon}_{Jtt} + \dot{\epsilon}_{Jpp}) &= 0 \end{aligned} \quad (5.29)$$

or

$$\dot{\epsilon}_{Jnn}^p = \frac{I}{(E_J + E_{J11}^p)} \{ E_{J11} \dot{\epsilon}_{Jnn} + E_{J12} (\dot{\epsilon}_{Jtt} + \dot{\epsilon}_{Jpp}) \} = -\dot{\omega}_c \quad (5.30)$$

Therefore, if the normal components of total strain rate are prescribed, the corresponding normal component of plastic strain rate is obtained from (5.30). Recall that the other two normal components of plastic strain rate are assumed to be zero. Since both the normal components of traction and of rate of plastic strain are always positive, plastic compaction results in positive dissipation.

In summary, an outline has been given for describing the response of a joint to compaction. The additional plastic material parameters that must be specified are $\{[u_{J0}], [u_{J0}^p], E_{J0}^p, m^p\}$.

If the yield condition indicates that unloading is elastic in the compressive regime then the total strain components equal the elastic strain components and the unloading phase is governed by

$$\dot{\tau}_{Jn} = E_{J11} \dot{\epsilon}_{Jnn}^e + E_{J12} (\dot{\epsilon}_{Jtt}^e + \dot{\epsilon}_{Jpp}^e) \quad (5.31)$$

where the elastic tangent components must be evaluated for the current value of normal elastic strain.

Shear

Consider the case where the normal component of traction is negative or zero. If τ_{Js} denotes the effective shear defined in (5.22) and τ_{Jsy} represents the yield stress in shear, then the corresponding yield function for shear is chosen to be

$$F_S = \tau_{Js} - \tau_{Jsy} \quad (5.32)$$

Note that $\tau_{Js} \geq 0$ so we impose the restriction that $\tau_{Jsy} \geq 0$ as well. Then $F_S \geq 0$ if $\tau_{Js} \geq \tau_{Jsy}$.

There is assumed to be some inherent resistance in shear, or cohesion τ_{Jas} , due to the asperities of matching surfaces. After these asperities are worn off, it is assumed further that the tangential motion is governed by the Mohr-Coulomb criterion. The result is that the yield stress in shear is represented as follows:

$$\tau_{Jsy} = \tau_{Jas} - \mu_J \tau_{Jn} \quad (5.33)$$

in which μ_J is a material constant, the friction coefficient for material in the joint. Recall that τ_{Jn} is negative.

Next we define a measure of the inelastic motion in shear. Effective plastic strain and dimensionless displacement in shear are defined to be

$$\begin{aligned} \bar{e}_{Js}^p &= \int \dot{e}_{Js}^p dt & \dot{e}_{Js}^p &= \{ \dot{e}_{Jnt}^p + \dot{e}_{Jnp}^p \}^{1/2} \\ \bar{u}_{Js}^p &= \int \dot{u}_{Js}^p dt & \dot{u}_{Js}^p &= 2\dot{e}_{Js}^p = \{ \dot{u}_{Jt}^p + \dot{u}_{Jp}^p \}^{1/2} \end{aligned} \quad (5.34)$$

For any given problem consisting of cyclic tangential motion it is quite possible that $\bar{u}_{Js}^p \gg 1$ even if the components of final tangential displacement are small.

The cohesion is assumed to decay monotonically with an increase in the effective inelastic shear displacement. For simplicity, a linear relation is assumed:

$$\tau_{Jas} = \tau_{Ja0} \left\langle 1 - \frac{\bar{u}_{Js}^p}{\bar{u}_{Ja}} \right\rangle \quad (5.35)$$

in which τ_{Ja0} denotes the initial shear strength due to asperities and \bar{u}_{Ja} is the effective tangential displacement at which the strength due to asperities is lost.

Suppose an associated flow rule is used to obtain evolution equations for the plastic components of shear strain, e_{Jnt}^p , e_{Jnp}^p , and normal plastic joint strain, e_{Jnn}^p , or

$$\begin{aligned} \dot{e}_{Jnt}^p &= \dot{\omega}_s \frac{\partial F_S}{\partial \tau_{Jt}} = \dot{\omega}_s \frac{\tau_{Jt}}{\tau_{Js}} \\ \dot{e}_{Jnp}^p &= \dot{\omega}_s \frac{\partial F_S}{\partial \tau_{Jp}} = \dot{\omega}_s \frac{\tau_{Jp}}{\tau_{Js}} \\ \dot{e}_{Jnn}^p &= \dot{\omega}_s \frac{\partial F_S}{\partial \tau_{Jn}} = \mu_J \dot{\omega}_s \end{aligned} \quad (5.36)$$

in which ω_s is a monotonically increasing plasticity parameter and the following equation has been used for the derivative with respect to τ_{Jt} :

$$\frac{\partial F_S}{\partial \tau_{Jt}} = \frac{\partial F_S}{\partial \tau_{Js}} \frac{\partial \tau_{Js}}{\partial \tau_{Jt}} = \frac{\tau_{Jt}}{\tau_{Js}} \quad (5.37)$$

with a corresponding relation for the other component of shear. It follows from (5.34) and (5.36) that

$$\dot{\bar{e}}_{Js}^p = \dot{\omega}_s \frac{\partial \bar{F}_S}{\partial \bar{\tau}_{Js}} = \dot{\omega}_s = \dot{\bar{u}}_{Js} \quad (5.38)$$

Note that \dot{e}_{Jnn}^p is always positive which indicates that plastic dilatation is occurring under shear motion. With dilatation, the current yield strength for compaction is reduced and represents a coupling effect between shear and normal motion. This is a result expected due to the effect of asperities and is included in the combined model.

Once the asperities have worn off, it is assumed that the result is simple Mohr-Coulomb friction, in which case no more dilatation is expected. To reflect the pure-slip case after the asperities are eliminated, a non-associated flow rule is proposed whereby the rate of the normal component of plastic strain is taken to be zero. To provide a smooth transition from dilatation to zero normal component, the last evolution equation of (5.36) is replaced with

$$\dot{e}_{Jnn}^p = \dot{\omega}_s \frac{\partial F_S}{\partial \tau_{Jn}} \left\langle 1 - \frac{\bar{u}_{Js}}{\bar{u}_{Ja}} \right\rangle = \dot{\omega}_s \mu_J \left\langle 1 - \frac{\bar{u}_{Js}}{\bar{u}_{Ja}} \right\rangle \quad (5.39)$$

The implication is that the evolution equation is non-associative for both regimes of asperity decay and Mohr-Coulomb friction.

The consistency equation becomes

$$\begin{aligned} \dot{F}_S &= 0 \\ \dot{\tau}_{Js} - \dot{\tau}_{Jsy} &= 0 \\ \dot{\tau}_{Js} - \dot{\tau}_{Jas} + \mu_J \dot{\tau}_{Jn} &= 0 \end{aligned} \quad (5.40)$$

The rates of the stress variables are

$$\begin{aligned} \dot{\tau}_{Jn} &= E_{J11}(\dot{e}_{Jnn} - \dot{e}_{Jnn}^p) + E_{J12}(\dot{e}_{Jnt} + \dot{e}_{Jpp}) \\ \dot{\tau}_{Js} &= \frac{I}{\tau_{Js}} [\tau_{Jt} \dot{\tau}_{Jt} + \tau_{Jp} \dot{\tau}_{Jp}] \\ \dot{\tau}_{Jt} &= 2G_J(\dot{e}_{Jnt} - \dot{e}_{Jnt}^p) \\ \dot{\tau}_{Jp} &= 2G_J(\dot{e}_{Jnp} - \dot{e}_{Jnp}^p) \\ \dot{\tau}_{Jas} &= -\tau_{Ja0} \frac{\dot{\bar{u}}_s}{\bar{u}_{Ja}} H \left[1 - \frac{\bar{u}_{Js}}{\bar{u}_{Ja}} \right] \end{aligned} \quad (5.41)$$

Using the elastic constitutive relations of (5.15) with (5.10), (5.13) and (5.36), it follows that

$$\begin{aligned}
\dot{\tau}_{Jn} &= E_{J11}\dot{e}_{Jnn} + E_{J12}(\dot{e}_{Jtt} + \dot{e}_{Jpp}) - E_{J11}\dot{\omega}_s\mu_J \left\langle 1 - \frac{\bar{u}_{Js}}{\bar{u}_{Ja}} \right\rangle \\
\dot{\tau}_{Jt} &= 2G_J\dot{e}_{Jnt} - 2G_J\dot{\omega}_s \frac{\tau_{Jt}}{\tau_{Js}} \\
\dot{\tau}_{Jp} &= 2G_J\dot{e}_{Jnp} - 2G_J\dot{\omega}_s \frac{\tau_{Jp}}{\tau_{Js}} \\
\dot{\tau}_{Js} &= \frac{2G_J}{\tau_{Js}} [\dot{\tau}_{Jt}\dot{e}_{Jnt} + \dot{\tau}_{Jp}\dot{e}_{Jnp}] - 2G_J\dot{\omega}_s \\
\dot{\tau}_{Jas} &= -\tau_{Ja0} \frac{\dot{\omega}_s}{\bar{u}_{Ja}} H \left[1 - \frac{\bar{u}_{Js}}{\bar{u}_{Ja}} \right]
\end{aligned} \tag{5.42}$$

The result is

$$\begin{aligned}
\dot{\tau}_{Js} - \dot{\tau}_{Jas} + \mu_J \dot{\tau}_{Jn} &= 0 \\
\frac{2G_J}{\tau_{Js}} [\dot{\tau}_{Jt}\dot{e}_{Jnt} + \dot{\tau}_{Jp}\dot{e}_{Jnp}] - 2G_J\dot{\omega}_s + \tau_{Ja0} \frac{\dot{\omega}_s}{\bar{u}_{Ja}} H \left[1 - \frac{\bar{u}_{Js}}{\bar{u}_{Ja}} \right] \\
+ \mu_J \left[E_{J11}\dot{e}_{Jnn} + E_{J12}(\dot{e}_{Jtt} + \dot{e}_{Jpp}) - E_{J11}\dot{\omega}_s\mu_J \left\langle 1 - \frac{\bar{u}_{Js}}{\bar{u}_{Ja}} \right\rangle \right] &= 0
\end{aligned} \tag{5.43}$$

Now solve for the rate of plasticity parameter $\dot{\omega}_s$ to obtain

$$\begin{aligned}
\dot{\omega}_s &= \frac{A}{B} \\
A &= \frac{2G_J}{\tau_{Js}} [\dot{\tau}_{Jt}\dot{e}_{Jnt} + \dot{\tau}_{Jp}\dot{e}_{Jnp}] + \mu_J [E_{J11}\dot{e}_{Jnn} + E_{J12}(\dot{e}_{Jtt} + \dot{e}_{Jpp})] \\
B &= 2G_J + E_{J11}\mu_J^2 \left\langle 1 - \frac{\bar{u}_{Js}}{\bar{u}_{Ja}} \right\rangle - \frac{\tau_{Ja0}}{\bar{u}_{Ja}} H \left[1 - \frac{\bar{u}_{Js}}{\bar{u}_{Ja}} \right]
\end{aligned} \tag{5.44}$$

This equation requires that the total strain rates of both normal and shear components of joint strain be specified. The plasticity loading criterion is based on the assumption that $A > 0$. The term with the negative sign in the expression for B is associated with softening and implies there is the possibility that $B \leq 0$, a situation we call material instability. It is assumed that the material parameters are chosen such that instability does not occur.

During the softening regime, the asperities may cause dilatation, $\dot{e}_{Jnn}^p > 0$, and this will have an effect of changing the location of the yield surface used for compaction. After the effect of asperities has been erased, the denominator in (5.44) reduces simply to $B = 2G_J$. The shear yield condition becomes one of perfect plasticity with a nonassociated flow law that yields $\dot{e}_{Jnn}^p = 0$ and is consistent with a Mohr-Coulomb criterion.

Tensile State

If $\tau_{Jn} = 0$, it is assumed the joint offers no resistance to motion in either the normal or tangential directions. Positive values for τ_{Jn} are not allowed to exist. This case is handled by defining a yield function, F_T , for the tensile state as follows:

$$F_T = \tau_{Jn} \quad (5.45)$$

With the assumption that the components of shear (τ_{Jt} , τ_{Jp}) must also be zero when the normal component of traction is zero, the evolution equations on plastic strain are chosen simply to be one for which the plastic strain rates maintains zero for these stress components. Recall that the relevant elastic constitutive equations are

$$\begin{aligned} \dot{\tau}_{Jn} &= E_{J11}(\dot{\epsilon}_{Jnn} - \dot{\epsilon}_{Jnn}^p) + E_{J12}(\dot{\epsilon}_{Jtt} + \dot{\epsilon}_{Jpp}) \\ \dot{\tau}_{Jp} &= 2G_J(\dot{\epsilon}_{Jnp} - \dot{\epsilon}_{Jnp}^p) \\ \dot{\tau}_{Jt} &= 2G_J(\dot{\epsilon}_{Jtp} - \dot{\epsilon}_{Jtp}^p) \end{aligned} \quad (5.46)$$

with the total strain rates prescribed. The solutions for the plastic strain rates that yield zero stress rates are

$$\begin{aligned} \dot{\epsilon}_{Jnn}^p &= \dot{\epsilon}_{Jnn} + \frac{E_{J12}}{E_{J11}}(\dot{\epsilon}_{Jtt} + \dot{\epsilon}_{Jpp}) = \dot{\epsilon}_{Jnn} + \frac{\nu_{J0}}{(1 - \nu_{J0})}(\dot{\epsilon}_{Jtt} + \dot{\epsilon}_{Jpp}) \\ \dot{\epsilon}_{Jnt}^p &= \dot{\epsilon}_{Jnt} \\ \dot{\epsilon}_{Jnp}^p &= \dot{\epsilon}_{Jnp} \end{aligned} \quad (5.47)$$

in which (5.21) has been used for the term involving Poisson's ratio.

For the sake of completeness, the remaining stress rates become

$$\begin{aligned} \dot{\sigma}_{Jtt} &= E_{J12}\dot{\epsilon}_{Jnn}^e + E_{J22}\dot{\epsilon}_{Jtt}^e + E_{J230}\dot{\epsilon}_{Jpp}^e \\ \dot{\sigma}_{Jpp} &= E_{J12}\dot{\epsilon}_{Jnn}^e + E_{J230}\dot{\epsilon}_{Jtt}^e + E_{J22}\dot{\epsilon}_{Jpp}^e \\ \dot{\sigma}_{Jtp} &= 2G_{Jtp0}\dot{\epsilon}_{Jtp}^e \end{aligned} \quad (5.48)$$

Recall that ($\dot{\epsilon}_{Jtt}^e = \dot{\epsilon}_{Jtt}$, $\dot{\epsilon}_{Jpp}^e = \dot{\epsilon}_{Jpp}$, $\dot{\epsilon}_{Jtp}^e = \dot{\epsilon}_{Jtp}$). If (5.47) is substituted in (5.48), the result is

$$\begin{aligned} \dot{\sigma}_{Jtt} &= D_1\dot{\epsilon}_{Jtt} + D_2\dot{\epsilon}_{Jpp} \\ \dot{\sigma}_{Jpp} &= D_2\dot{\epsilon}_{Jtt} + D_1\dot{\epsilon}_{Jpp} \\ \dot{\sigma}_{Jtp} &= 2G_{Jtp0}\dot{\epsilon}_{Jtp} \end{aligned} \quad (5.49)$$

where the use of (5.20) and (5.21) provides the following expressions for the material parameters D_1 and D_2 :

$$\begin{aligned}
D_1 &= E_{J0} - \left\{ \frac{\nu_{J0}}{1 - \nu_{J0}} \right\}^2 E_{J11} \\
D_2 &= \left\{ \frac{\nu_{J0}}{1 - \nu_{J0}} \right\} \left(E_{J0} - \left\{ \frac{\nu_{J0}}{1 - \nu_{J0}} \right\} E_{J11} \right)
\end{aligned} \tag{5.50}$$

The result is that the formation of a gap is handled through a constitutive equation with the gap opening related to a positive value for the normal component of plastic strain.

5.3.7 Composite Yield Function

With the three yield functions defined above, the composite yield function, F_J , is defined to be

$$F_J = \max(F_C, F_S, F_T) \tag{5.51}$$

where

$$F_C = \tau_{Jny} - \tau_{Jn} \quad F_S = \tau_{Js} - \tau_{Jsy} \quad F_T = \tau_{Jn} \tag{5.52}$$

The composite yield surface is given simply by $F_J = 0$.

To illustrate how the composite yield surface behaves under a couple of paths, sketches are provided in Fig. 5.6. Because the initial yield stress is very small, the surfaces $F_C = 0$ and $F_T = 0$ are nearly coincident as indicated in Fig. 5.6(a). With loading in compaction, with or without some shear as suggested by the paths shown in Fig. 5.6(b), the surface $F_C = 0$ moves to the left with the other segments of the surface stationary.

Next, consider the path identified as 0-(i)-(ii)-(iii) with “0” denoting the origin as shown in Fig. 5.6(c). First the compaction yield surface is pushed out to configuration (a). Then for the next segment of loading, the normal component of traction is reduced but the shear part is increased so that the shear yield surface, designated (c), is reached. Shear softening occurs because of ablation of asperities. While softening, dilatation is occurring which causes the compaction surface to move inward to location (b). The yield surface decays until the Mohr-Coulomb surface designated as (d), is reached after which the yield surface in shear remains stationary. When unloading, the three components of traction satisfy the elastic relation.

There is the possibility that the revised location of the compaction yield surface will cause both yield surfaces to be simultaneously activated. The approach proposed here is to simply apply the yield conditions one at a time until both are satisfied. A mathematically rigorous approach is to satisfy both criteria simultaneously.

Once the effect of asperities is gone it is assumed that cohesion is lost, there is no further dilatation and the shear surface is associated with sliding only.

In summary, after some compaction with small or no shear, the composite yield surface appears as shown in Fig. 5.7(a). After compaction with sufficient shear, the composite yield surface is illustrated in Fig. 5.7(b).

5.3.8 Closing Comments

This section provides the description of a basic constitutive model for a joint and includes both compaction and shear. The effects of shear enhanced compaction and dilatation due to asperities are included.

In the next section, the structure for handling a joint in a finite element framework is given for the case of when the adjacent material is governed by isotropic elasticity.

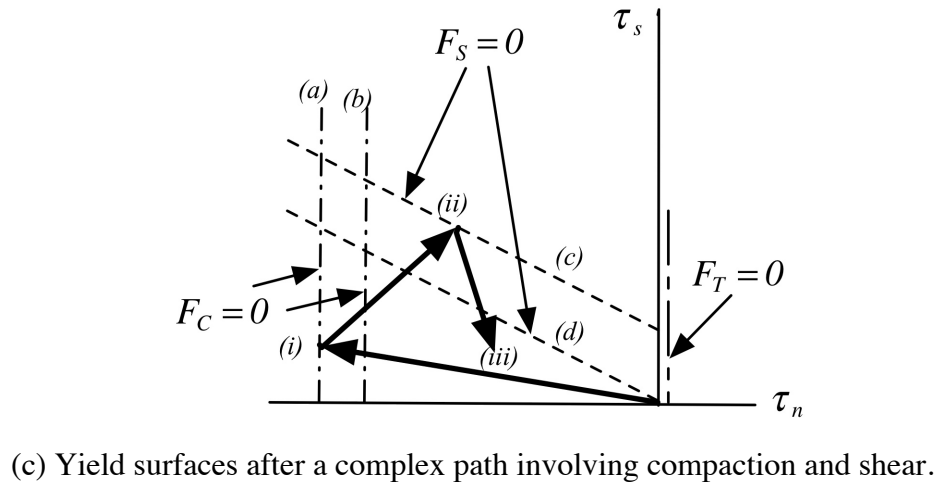
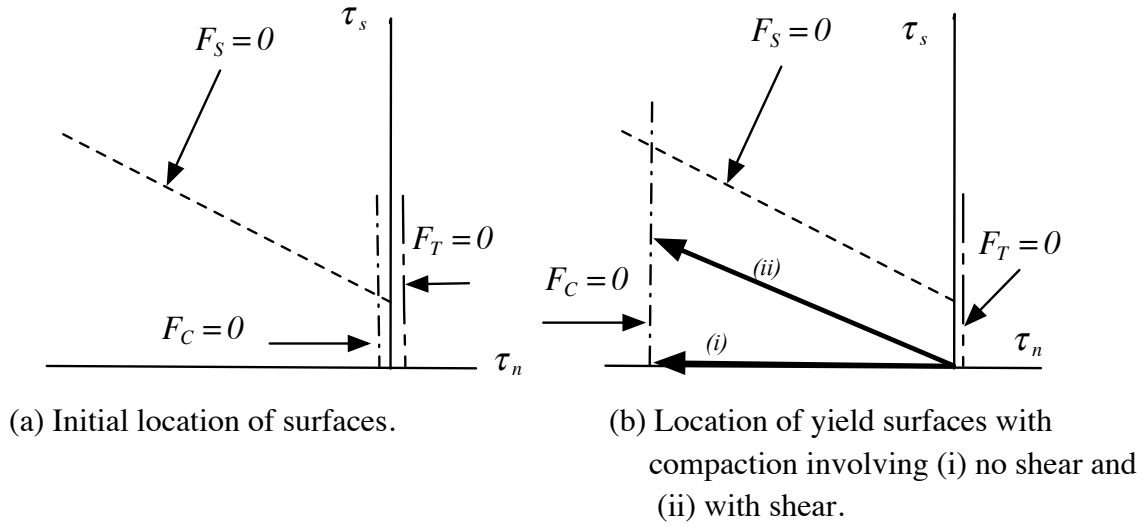


Figure 5.6: Evolution of yield surfaces in space of traction components.

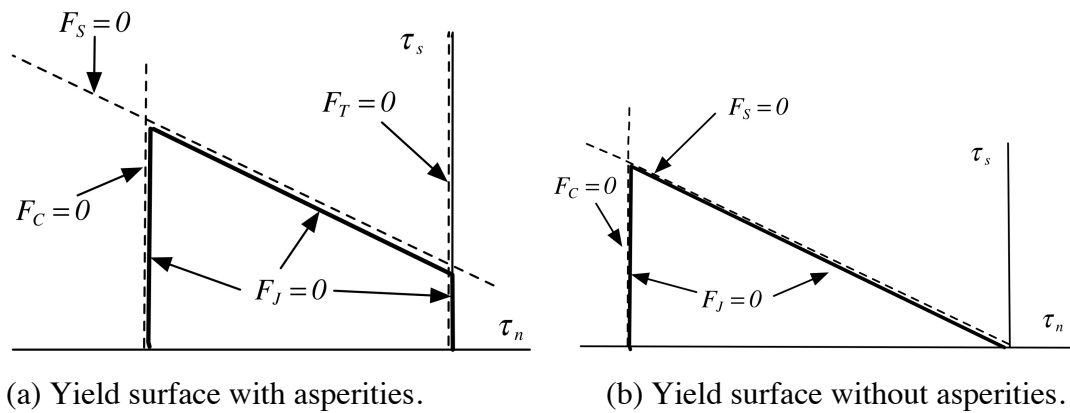


Figure 5.7: Yield surface with and without asperities.

5.4 Strains Related to the Use of Finite Elements

5.4.1 Preliminary Remarks

Here, the displacements associated with a joint are smeared over an element in the form of joint strains. In a manner similar to decohesion, it is assumed element strain components are prescribed and the joint displacements or strains, are adjusted so that the deformation is compatible, equilibrium (traction) is satisfied, and the yield condition is not violated.

The numerical algorithm is based on obtaining a trial stress under the assumption that the step is elastic so this part of the constitutive equation is discussed in detail.

5.4.2 Strain and Stress Associated with Joints, Continuum and Elements

An elementary, but efficient, approach for representing the effect of a joint using the finite element method is to smear the effect of the joint over an element. The basic approach adopted here is to construct a local element with size h and sides parallel to the joint as illustrated in Fig. 5.8(a).

Consider the relative movement of nodes on opposite sides of an element in the \mathbf{n} -direction to be u_n as shown in Fig. 5.8(b). The normal strain in the continuum is e_{Cnn} and the normal strain in the joint is e_{Jnn} . The stretch of the continuum and of the joint within an element is obtained by multiplying the strains by the respective lengths of the segments so that

$$u_n = e_{Cnn}\{h - [u_{J0}]\} + e_{Jnn}[u_{J0}] \quad (5.53)$$

The element strain is defined to be

$$e_{nn} = \frac{u_n}{h} \quad (5.54)$$

Define dimensionless length parameters to be

$$\bar{L}_J = \frac{[u_{J0}]}{h} \quad \bar{L}_C = \frac{\{h - [u_{J0}]\}}{h} = 1 - \bar{L}_J \quad (5.55)$$

with the result that

$$\bar{L}_J + \bar{L}_C = 1 \quad (5.56)$$

Smeared joint and continuum strains are defined as follows:

$$e_{Cnn}^{sm} = \bar{L}_C e_{Cnn} \quad e_{Jnn}^{sm} = \bar{L}_J e_{Jnn} \quad (5.57)$$

The result is that the element strain is the sum of the smeared continuum and joint strains:

$$e_{nn} = e_{Cnn}^{sm} + e_{Jnn}^{sm} \quad (5.58)$$

For most applications, $\bar{L}_C \approx 1$. However, for characterizing joint behavior, element strains can be interpreted as joint strains by choosing $\bar{L}_C = 0$.

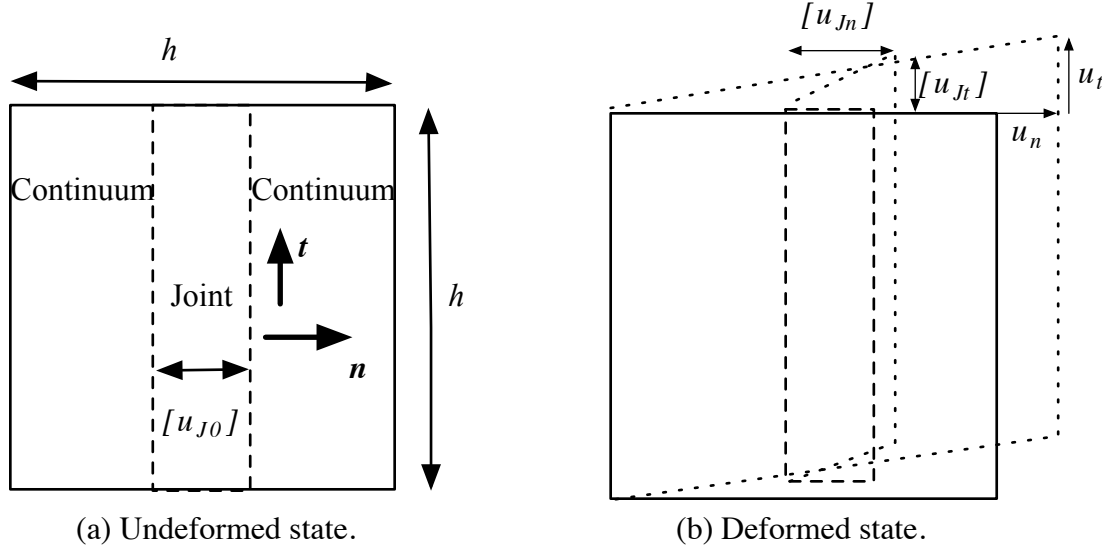


Figure 5.8: Notation associated with joint and element.

Consider the relative tangential motion on the two sides of the element in the \mathbf{t} -direction to be u_t and in the \mathbf{p} -direction to be u_p . Similarly to the argument used to obtain(5.53), the result is

$$\begin{aligned} u_t &= 2e_{Cnt}\{h - [u_{J0}]\} + 2e_{Jnt}[u_{J0}] \\ u_p &= 2e_{Cnp}\{h - [u_{J0}]\} + 2e_{Jnp}[u_{J0}] \end{aligned} \quad (5.59)$$

Define smeared shear-strain components for the continuum and the joint to be

$$\begin{aligned} e_{Cnt}^{sm} &\equiv \bar{L}_C e_{Cnt} & e_{Jnt}^{sm} &\equiv \bar{L}_J e_{Jnt} \\ e_{Cnp}^{sm} &\equiv \bar{L}_C e_{Cnp} & e_{Jnp}^{sm} &\equiv \bar{L}_J e_{Jnp} \end{aligned} \quad (5.60)$$

Then the element shear strain components become

$$\begin{aligned} e_{nt} &= \frac{u_t}{2h} = e_{Cnt}^{sm} + e_{Jnt}^{sm} \\ e_{np} &= \frac{u_p}{2h} = e_{Cnp}^{sm} + e_{Jnp}^{sm} \end{aligned} \quad (5.61)$$

The normal components of strain in the \mathbf{t} and \mathbf{p} directions, and the remaining shear-strain component for the joint are defined to be identical to the corresponding components for the continuum and, hence the element, so that

$$e_{Jt} = e_{Ct} = e_{tt} \quad e_{Jpp} = e_{Cpp} = e_{pp} \quad e_{Jtp} = e_{Ctp} = e_{tp} \quad (5.62)$$

This construction allows the remaining strain components in the element to be written in a form similar to (5.58), and (5.61), or

$$\begin{aligned} e_{tt} &= e_{Ctt}^{sm} + e_{Jtt}^{sm} & e_{pp} &= e_{Cpp}^{sm} + e_{Jpp}^{sm} & e_{tp} &= e_{Ctp}^{sm} + e_{Jtp}^{sm} \\ e_{Ctt}^{sm} &= \bar{L}_C e_{tt} & e_{Cpp}^{sm} &= \bar{L}_C e_{pp} & e_{Ctp}^{sm} &= \bar{L}_C e_{tp} \\ e_{Jtt}^{sm} &= \bar{L}_J e_{tt} & e_{Jpp}^{sm} &= \bar{L}_J e_{pp} & e_{Jtp}^{sm} &= \bar{L}_J e_{tp} \end{aligned} \quad (5.63)$$

in which the smeared form of the normal components of strain have been defined. The result is that all components of strain can be treated similarly or, in direct notation,

$$\mathbf{e} = \mathbf{e}_C^{sm} + \mathbf{e}_J^{sm} \quad (5.64)$$

In summary, recall from (5.6) that three components of the joint strains are defined to be

$$e_{Jnn} = \frac{[u_{Jn}] - [u_{J0}]}{[u_{J0}]} = \bar{u}_{Jn} - 1 \quad e_{Jnt} = \frac{[u_{Jt}]}{[u_{J0}]} = \bar{u}_{Jt} \quad e_{Jnp} = \frac{[u_{Jp}]}{[u_{J0}]} = \bar{u}_{Jp} \quad (5.65)$$

The result is that these components of the smeared joint strain can be given in the following alternative forms:

$$e_{Jnn}^{sm} = \frac{[u_{Jn}] - [u_{J0}]}{h} \quad e_{Jnt}^{sm} = \frac{[u_{Jt}]}{2h} \quad e_{Jnp}^{sm} = \frac{[u_{Jp}]}{2h} \quad (5.66)$$

Now consider the components of stress that compose the traction acting on the joint. Based on equilibrium, the following equalities hold:

$$\dot{\sigma}_{nn} = \dot{\sigma}_{Cnn} = \dot{\sigma}_{Jnt} \equiv \dot{\tau}_{Jn} \quad \dot{\sigma}_{nt} = \dot{\sigma}_{Cnt} = \dot{\sigma}_{Jnt} \equiv \dot{\tau}_{Jt} \quad \dot{\sigma}_{np} = \dot{\sigma}_{Cnp} = \dot{\sigma}_{Jnp} \equiv \dot{\tau}_{Jp} \quad (5.67)$$

These relations are analogous to those used for the complementary components of strain as given in (5.62). The three remaining components of stress rate for the element are assumed to be the following weighted averages:

$$\dot{\sigma}_{tt} \equiv \bar{L}_J \dot{\sigma}_{Jtt} + \bar{L}_C \dot{\sigma}_{Ctt} \quad \dot{\sigma}_{pp} \equiv \bar{L}_J \dot{\sigma}_{Jpp} + \bar{L}_C \dot{\sigma}_{Cpp} \quad \dot{\sigma}_{tp} \equiv \bar{L}_J \dot{\sigma}_{Jtp} + \bar{L}_C \dot{\sigma}_{Ctp} \quad (5.68)$$

in a manner used for the alternative components of strain used in (5.58) and (5.61).

5.4.3 Tangent Components

So far we have described the relationships between joint, continuum and element measures of stress and strain. Here we use the elasticity relations for the joint and the continuum to obtain the corresponding elastic constitutive equation between element-based components of stress and strain rate.

Recall that the rate form of the continuum constitutive equation is elastic, and from (5.2), is repeated here for convenience in the $(\mathbf{n}, \mathbf{t}, \mathbf{p})$ basis

$$\begin{aligned}
\begin{Bmatrix} \dot{\sigma}_{Cnn} \\ \dot{\sigma}_{Ctt} \\ \dot{\sigma}_{Cpp} \end{Bmatrix} &= \begin{bmatrix} E_{C1} & E_{C2} & E_{C2} \\ E_{C2} & E_{C1} & E_{C2} \\ E_{C2} & E_{C2} & E_{C1} \end{bmatrix} \begin{Bmatrix} \dot{e}_{Cnn} \\ \dot{e}_{Ctt} \\ \dot{e}_{Cpp} \end{Bmatrix} \\
\begin{Bmatrix} \dot{\sigma}_{Cnt} \\ \dot{\sigma}_{Cnp} \\ \dot{\sigma}_{Ctp} \end{Bmatrix} &= \begin{bmatrix} 2G_C & 0 & 0 \\ 0 & 2G_C & 0 \\ 0 & 0 & 2G_C \end{bmatrix} \begin{Bmatrix} \dot{e}_{Cnt} \\ \dot{e}_{Cnp} \\ \dot{e}_{Ctp} \end{Bmatrix}
\end{aligned} \tag{5.69}$$

Similarly, the rate form of the elastic constitutive equations for joints is repeated from (5.15):

$$\begin{aligned}
\begin{Bmatrix} \dot{\tau}_{Jn} = \dot{\sigma}_{Jnn} \\ \dot{\sigma}_{Jtt} \\ \dot{\sigma}_{Jpp} \end{Bmatrix} &= \begin{bmatrix} E_{J11} & E_{J12} & E_{J12} \\ E_{J12} & E_{J0} & E_{J230} \\ E_{J12} & E_{J230} & E_{J0} \end{bmatrix} \begin{Bmatrix} \dot{e}_{Jnn}^e \\ \dot{e}_{Jtt}^e \\ \dot{e}_{Jpp}^e \end{Bmatrix} \\
\begin{Bmatrix} \dot{\tau}_{Jt} = \dot{\sigma}_{Jnt} \\ \dot{\tau}_{Jp} = \dot{\sigma}_{Jnp} \\ \dot{\sigma}_{Jtp} \end{Bmatrix} &= \begin{bmatrix} 2G_J & 0 & 0 \\ 0 & 2G_J & 0 \\ 0 & 0 & 2G_{Jtp0} \end{bmatrix} \begin{Bmatrix} \dot{e}_{Jnt}^e \\ \dot{e}_{Jnp}^e \\ \dot{e}_{Jtp}^e \end{Bmatrix}
\end{aligned} \tag{5.70}$$

in which the elasticity components that are constants from (5.21) are noted.

In summary, the strain components of joint and continuum are related as follows:

$$\begin{aligned}
e_{nn} &= \bar{L}_C e_{Cnn} + \bar{L}_J e_{Jnn} & e_{nt} &= \bar{L}_C e_{Cnt} + \bar{L}_J e_{Jnt} & e_{np} &= \bar{L}_C e_{Cnp} + \bar{L}_J e_{Jnp} \\
e_{tt} &= e_{Ctt} = e_{Jtt} & e_{pp} &= e_{Cpp} = e_{Jpp} & e_{tp} &= e_{Ctp} = e_{Jtp}
\end{aligned} \tag{5.71}$$

The corresponding relationships for components of stress rate are

$$\begin{aligned}
\dot{\sigma}_{tt} &= \bar{L}_J \dot{\sigma}_{Jtt} + \bar{L}_C \dot{\sigma}_{Ctt} & \dot{\sigma}_{pp} &\equiv \bar{L}_J \dot{\sigma}_{Jpp} + \bar{L}_C \dot{\sigma}_{Cpp} & \dot{\sigma}_{tp} &\equiv \bar{L}_J \dot{\sigma}_{Jtp} + \bar{L}_C \dot{\sigma}_{Ctp} \\
\dot{\sigma}_{nn} &= \dot{\sigma}_{Cnn} = \dot{\sigma}_{Jnt} \equiv \dot{\tau}_{Jn} & \dot{\sigma}_{nt} &= \dot{\sigma}_{Cnt} = \dot{\sigma}_{Jnt} \equiv \dot{\tau}_{Jt} & \dot{\sigma}_{np} &= \dot{\sigma}_{Cnp} = \dot{\sigma}_{Jnp} \equiv \dot{\tau}_{Jp}
\end{aligned} \tag{5.72}$$

First, consider the nt-component of shear

$$\dot{e}_{nt}^e = \bar{L}_J \dot{e}_{Jnt}^e + \bar{L}_C \dot{e}_{Cnt}^e = \frac{\bar{L}_J}{2G_J} \dot{\sigma}_{Jnt} + \frac{\bar{L}_C}{2G_C} \dot{\sigma}_{Cnt} = \frac{(G_C \bar{L}_J + G_J \bar{L}_C)}{2G_C G_J} \dot{\sigma}_{nt} \tag{5.73}$$

A similar relation holds for the np-component. The remaining shear component satisfies

$$\begin{aligned}
\dot{\sigma}_{tp} &\equiv \bar{L}_J \dot{\sigma}_{Jtp} + \bar{L}_C \dot{\sigma}_{Ctp} \\
&= \bar{L}_J 2G_{Jtp0} \dot{e}_{Jtp}^e + \bar{L}_C 2G_C \dot{e}_{Ctp}^e \\
&= (2G_{Jtp0} \bar{L}_J + 2G_C \bar{L}_C) \dot{e}_{tp}^e
\end{aligned} \tag{5.74}$$

In summary, for the shear components the tangent elastic rate equations are:

$$\dot{\sigma}_{nt} = 2G_{nt}\dot{e}_{nt}^e \quad \dot{\sigma}_{np} = 2G_{nt}\dot{e}_{np}^e \quad \dot{\sigma}_{tp} = 2G_{tp}\dot{e}_{tp}^e \quad (5.75)$$

where the element shear moduli are defined to be

$$G_{nt} = \frac{G_C G_J}{(G_C \bar{L}_J + G_J \bar{L}_C)} \quad G_{tp0} = G_{Jtp0} \bar{L}_J + G_C \bar{L}_C \quad (5.76)$$

Note that because G_J varies, the first shear modulus varies with elastic normal strain while the second modulus is a constant.

Next, consider the tt- and pp-normal components of stress:

$$\begin{aligned} \dot{\sigma}_{tt} &= \bar{L}_J \dot{\sigma}_{Jtt} + \bar{L}_C \dot{\sigma}_{Ctt} \\ &= \bar{L}_J \{ E_{J12} \dot{e}_{Jnn}^e + E_{J22} \dot{e}_{Jtt}^e + E_{J23} \dot{e}_{Jpp}^e \} + \bar{L}_C \{ E_{C2} \dot{e}_{Cnn}^e + E_{C1} \dot{e}_{Ctt}^e + E_{C2} \dot{e}_{Cpp}^e \} \\ &= \bar{L}_J E_{J12} \dot{e}_{Jnn}^e + \bar{L}_C E_{C2} \dot{e}_{Cnn}^e + \{ \bar{L}_J E_{J0} + \bar{L}_C E_{C1} \} \dot{e}_{tt}^e + \{ \bar{L}_J E_{J230} + \bar{L}_C E_{C2} \} \dot{e}_{tt}^e \\ \dot{\sigma}_{pp} &= \bar{L}_J \dot{\sigma}_{Jpp} + \bar{L}_C \dot{\sigma}_{Cpp} \\ &= \bar{L}_J \{ E_{J12} \dot{e}_{Jnn}^e + E_{J23} \dot{e}_{Jtt}^e + E_{J22} \dot{e}_{Jpp}^e \} + \bar{L}_C \{ E_{C2} \dot{e}_{Cnn}^e + E_{C2} \dot{e}_{Ctt}^e + E_{C1} \dot{e}_{Cpp}^e \} \\ &= \bar{L}_J E_{J12} \dot{e}_{Jnn}^e + \bar{L}_C E_{C2} \dot{e}_{Cnn}^e + \{ \bar{L}_J E_{J230} + \bar{L}_C E_{C2} \} \dot{e}_{tt}^e + \{ \bar{L}_J E_{J0} + \bar{L}_C E_{C1} \} \dot{e}_{tt}^e \end{aligned} \quad (5.77)$$

We need expressions for the terms \dot{e}_{Jnn}^e and \dot{e}_{Cnn}^e . To this end, use (5.70) and (5.71) to obtain

$$\begin{aligned} \dot{\sigma}_{nn} &= \dot{\sigma}_{Cnn} = \dot{\sigma}_{Jnn} \\ \dot{\sigma}_{Cnn} &= E_{C1} \dot{e}_{Cnn}^e + E_{C2} \dot{e}_{tt}^e + E_{C2} \dot{e}_{pp}^e \\ \dot{\sigma}_{Jnn} &= E_{J11} \dot{e}_{Jnn}^e + E_{J12} \dot{e}_{tt}^e + E_{J12} \dot{e}_{pp}^e \\ \dot{e}_{nn}^e &= \bar{L}_J \dot{e}_{Jnn}^e + \bar{L}_C \dot{e}_{Cnn}^e \end{aligned} \quad (5.78)$$

If the right sides of the second and third equations of (5.78) are equated and the last equation of (5.78) is rewritten, the resulting two equations are solved for \dot{e}_{Jnn}^e and \dot{e}_{Cnn}^e :

$$\begin{aligned} \dot{e}_{Cnn}^e &= \frac{1}{(\bar{L}_J E_{C1} + \bar{L}_C E_{J11})} \left[E_{J11} \dot{e}_{nn}^e + \bar{L}_J (E_{J12} - E_{C2}) (\dot{e}_{tt}^e + \dot{e}_{pp}^e) \right] \\ \dot{e}_{Jnn}^e &= \frac{1}{(\bar{L}_J E_{C1} + \bar{L}_C E_{J11})} \left[E_{C1} \dot{e}_{nn}^e - \bar{L}_C (E_{J12} - E_{C2}) (\dot{e}_{tt}^e + \dot{e}_{pp}^e) \right] \end{aligned} \quad (5.79)$$

Again, we seek expressions for the rates of normal components of stress in terms of elastic strain rates for the element. If (5.79) is substituted in the following expressions from (5.77) and (5.78)

$$\begin{aligned} \dot{\sigma}_{nn} &= \dot{\sigma}_{Jnn} = E_{J11} \dot{e}_{Jnn}^e + E_{J12} \dot{e}_{tt}^e + E_{J12} \dot{e}_{pp}^e \\ \dot{\sigma}_{tt} &= \bar{L}_J \dot{\sigma}_{Jtt} + \bar{L}_C \dot{\sigma}_{Ctt} \\ &= \bar{L}_J E_{J12} \dot{e}_{Jnn}^e + \bar{L}_C E_{C2} \dot{e}_{Cnn}^e + \{ \bar{L}_J E_{J0} + \bar{L}_C E_{C1} \} \dot{e}_{tt}^e + \{ \bar{L}_J E_{J230} + \bar{L}_C E_{C2} \} \dot{e}_{tt}^e \\ \dot{\sigma}_{pp} &= \bar{L}_J \dot{\sigma}_{Jpp} + \bar{L}_C \dot{\sigma}_{Cpp} \\ &= \bar{L}_J E_{J12} \dot{e}_{Jnn}^e + \bar{L}_C E_{C2} \dot{e}_{Cnn}^e + \{ \bar{L}_J E_{J230} + \bar{L}_C E_{C2} \} \dot{e}_{tt}^e + \{ \bar{L}_J E_{J0} + \bar{L}_C E_{C1} \} \dot{e}_{tt}^e \end{aligned} \quad (5.80)$$

the result is

$$\begin{aligned}
\dot{\sigma}_{nn} &= H_{nn}\dot{e}_{nn}^e + H_{nt}\dot{e}_{tt}^e + H_{np}\dot{e}_{pp}^e \\
\dot{\sigma}_{tt} &= H_{nt}\dot{e}_{nn}^e + H_{tt}\dot{e}_{tt}^e + H_{tp}\dot{e}_{pp}^e \\
\dot{\sigma}_{pp} &= H_{nt}\dot{e}_{nn}^e + H_{tp}\dot{e}_{tt}^e + H_{pp}\dot{e}_{pp}^e
\end{aligned} \tag{5.81}$$

where

$$\begin{aligned}
H_{nn} &= \frac{E_{J11}E_{C1}}{(\bar{L}_J E_{C1} + \bar{L}_C E_{J11})} \\
H_{nt} = H_{np} &= \frac{(\bar{L}_C E_{J11}E_{C2} + \bar{L}_J E_{J12}E_{C1})}{(\bar{L}_J E_{C1} + \bar{L}_C E_{J11})} \\
H_{tt} = H_{pp} &= (\bar{L}_J E_{J0} + \bar{L}_C E_{C1}) - \bar{L}_C \bar{L}_J \frac{(E_{J12} - E_{C2})^2}{(\bar{L}_J E_{C1} + \bar{L}_C E_{J11})} \\
H_{tp} &= (\bar{L}_J E_{J230} + \bar{L}_C E_{C2}) - \bar{L}_C \bar{L}_J \frac{(E_{J12} - E_{C2})^2}{(\bar{L}_J E_{C1} + \bar{L}_C E_{J11})}
\end{aligned} \tag{5.82}$$

Now we summarize the elastic rate constitutive equations in terms of stress and strain rate components for the element:

$$\begin{aligned}
\begin{Bmatrix} \dot{\sigma}_{nn} \\ \dot{\sigma}_{tt} \\ \dot{\sigma}_{pp} \end{Bmatrix} &= \begin{bmatrix} H_{nn} & H_{nt} & H_{nt} \\ H_{nt} & H_{tt} & H_{tp} \\ H_{nt} & H_{tp} & H_{tt} \end{bmatrix} \begin{Bmatrix} \dot{e}_{nn}^e \\ \dot{e}_{tt}^e \\ \dot{e}_{pp}^e \end{Bmatrix} \\
\begin{Bmatrix} \dot{\sigma}_{nt} \\ \dot{\sigma}_{np} \\ \dot{\sigma}_{tp} \end{Bmatrix} &= \begin{bmatrix} 2G_{nt} & 0 & 0 \\ 0 & 2G_{nt} & 0 \\ 0 & 0 & 2G_{tp0} \end{bmatrix} \begin{Bmatrix} \dot{e}_{nt}^e \\ \dot{e}_{np}^e \\ \dot{e}_{tp}^e \end{Bmatrix}
\end{aligned} \tag{5.83}$$

where

$$\begin{aligned}
H_{nn} &= E_{J11}E_{C1}D^{in} \\
H_{nt} &= (\bar{L}_C E_{J11}E_{C2} + \bar{L}_J E_{J12}E_{C1})D^{in} \\
H_{tt} &= (\bar{L}_J E_{J0} + \bar{L}_C E_{C1}) - \bar{L}_C \bar{L}_J (\bar{E}_{J12} - E_{C2})^2 D^{in} \\
H_{tp} &= (\bar{L}_J E_{J230} + \bar{L}_C E_{C2}) - \bar{L}_C \bar{L}_J (\bar{E}_{J12} - E_{C2})^2 D^{in} \\
G_{nt} &= \frac{G_C G_J}{(G_C \bar{L}_J + G_J \bar{L}_C)} \\
G_{tp0} &= G_{Jtp0} \bar{L}_J + G_C \bar{L}_C \\
D^{in} &\equiv \frac{1}{(\bar{L}_J E_{C1} + \bar{L}_C E_{J11})}
\end{aligned} \tag{5.84}$$

If $(\bar{L}_C = 0, \bar{L}_J = 1)$ and $(\bar{L}_J = 0, \bar{L}_C = 1)$ the elasticity parameters reduce to those for the joint and the continuum, respectively, as they should.

Note that since the elastic joint parameter \bar{E}_{JII} is not constant if nonlinear elasticity is used for the joint, many of these element parameters will also change and must be re-evaluated for each loading step. The tangent matrix of (5.83) represents tetragonal 6-symmetry with respect to the **n**-axis.

5.5 Numerical Procedure for Constitutive Equation

5.5.1 Preliminary Remarks

In this section, the numerical procedure is developed for obtaining new values of stress when increments in strain are prescribed for the element. Elastic behavior is relatively straightforward whereas plasticity involves a much more complicated process. In addition there is the possibility of joint separation, and this is incorporated within the plasticity framework.

Only the variables specific to the constitutive equation framework for an element are considered here. There are other variables such as nodal displacements and velocities that must also be stored in a general computational code. It is assumed that increments in element strain are made available for the constitutive equation subroutine.

For easy reference the various variables of interest are listed next. Discontinuous displacement variables associated with joints are:

$$\{[u]\} = \{[u_{Jn}], [u_{Jt}], [u_{Jp}]\} \quad (5.85)$$

Because of the assumptions placed on the kinematics of element deformation and on the constitutive equations, we have the following relations among components of the strain tensors:

$$\begin{aligned} e_{Jtt}^p &= 0 & e_{Jpp}^p &= 0 & e_{Jtp}^p &= 0 \\ e_{Jtt}^e &= e_{Jtt} & e_{Jpp}^e &= e_{Jpp} & e_{Jtp}^e &= e_{Jtp} \\ e_{tt}^p &= 0 & e_{pp}^p &= 0 & e_{tp}^p &= 0 \\ e_{tt}^e &= e_{tt} & e_{pp}^e &= e_{pp} & e_{tp}^e &= e_{tp} \\ e_{nn}^p &\equiv \bar{L}_J e_{Jnn}^p & e_{nt}^p &\equiv \bar{L}_J e_{Jnt}^p & e_{np}^p &\equiv \bar{L}_J e_{Jnp}^p \\ e_{nn}^e &\equiv \bar{L}_J e_{Jnn}^e + \bar{L}_C e_{Cnn} & e_{nt}^e &\equiv \bar{L}_J e_{Jnt}^e + \bar{L}_C e_{Cnt} \\ & & e_{np}^e &\equiv \bar{L}_J e_{Jnp}^e + \bar{L}_C e_{Cnp} \end{aligned} \quad (5.86)$$

The result is that the total, elastic and plastic joint strain components are:

$$\begin{aligned} \{e_J\} &= \{e_{Jnn}, e_{Jtt}, e_{Jpp}, e_{Jnt}, e_{Jnp}, e_{Jtp}\} \\ \{e_J^e\} &= \{e_{Jnn}^e, e_{Jtt}^e, e_{Jpp}^e, e_{Jnt}^e, e_{Jnp}^e, e_{Jtp}^e\} \\ \{e_J^p\} &= \{e_{Jnn}^p, 0, 0, e_{Jnt}^p, e_{Jnp}^p, 0\} \end{aligned} \quad (5.87)$$

Element total strain, elastic strain and plastic strain components are:

$$\begin{aligned} \{e\} &= \{e_{nn}, e_{tt}, e_{pp}, e_{nt}, e_{np}, e_{tp}\} \\ \{e^e\} &= \{e_{nn}^e, e_{tt}^e, e_{pp}^e, e_{nt}^e, e_{np}^e, e_{tp}^e\} \\ \{e^p\} &= \{e_{nn}^p, 0, 0, e_{nt}^p, e_{np}^p, 0\} \end{aligned} \quad (5.88)$$

Finally, a list of the corresponding stress variables is:

$$\begin{aligned}
\{\sigma\} &= \{\tau_n = \sigma_{nn}, \sigma_{tt}, \sigma_{pp}, \tau_t = \sigma_{nt}, \tau_p = \sigma_{np}, \sigma_{tp}\} \\
\sigma_{nn} &= \sigma_{Jnn} = \sigma_{Cnn} \quad \sigma_{nt} = \sigma_{Jnt} = \sigma_{Cnt} \quad \sigma_{np} = \sigma_{Jnp} = \sigma_{Cnp} \\
\sigma_{tt} &= \bar{L}_J \sigma_{Jtt} + \bar{L}_C \sigma_{Ctt} \quad \sigma_{pp} = \bar{L}_J \sigma_{Jpp} + \bar{L}_C \sigma_{Cpp} \\
\sigma_{tp} &= \bar{L}_J \sigma_{Jtp} + \bar{L}_C \sigma_{Ctp}
\end{aligned} \tag{5.89}$$

The length of the element, h , must be specified as well as the joint parameters $[u_{J0}], [u_{J0}^e], [u_{J0}^p]$ with

$$[u_{J0}^e] + [u_{J0}^p] = [u_{J0}] \tag{5.90}$$

Then we obtain

$$\begin{aligned}
\bar{L}_J &= \frac{[u_{J0}]}{h} & \bar{L}_C &= \frac{\{h - [u_{J0}]\}}{h} = 1 - \bar{L}_J \\
\bar{u}_{J0}^e &= \frac{[u_{J0}^e]}{[u_{J0}]} & \bar{u}_{J0}^p &= \frac{[u_{J0}^p]}{[u_{J0}]}
\end{aligned} \tag{5.91}$$

The following relations hold:

$$\begin{aligned}
e_{Jnn} &= \bar{u}_{Jn} - I & e_{Jnn}^e &= \bar{u}_{Jn}^e - \bar{u}_{J0}^e & e_{Jnn}^p &= \bar{u}_{Jn}^p - \bar{u}_{J0}^p \\
\bar{u}_{Jn} &= \bar{u}_{Jn}^e + \bar{u}_{Jn}^p & \bar{u}_{Jt} &= \bar{u}_{Jt}^e + \bar{u}_{Jt}^p & \bar{u}_{Jp} &= \bar{u}_{Jp}^e + \bar{u}_{Jp}^p \\
e_{Jnn} &= e_{Jnn}^e + e_{Jnn}^p & e_{Jnt} &= e_{Jnt}^e + e_{Jnt}^p & e_{Jnp} &= e_{Jnp}^e + e_{Jnp}^p
\end{aligned} \tag{5.92}$$

The elasticity constants for the continuum, (E_{C1}, E_{C2}, ν_C) , and for the joint, $(E_{J0}, E_{C1}, \bar{u}_{J0}^e, m^e, \nu_0)$, must be specified.

It is assumed that values of the various contributions to stress and strain are available at the end of each load step. However, the normal stress component may have to be obtained using (5.17):

$$\sigma_{Jnn} = E_{J0} e_{Jnn}^e - (E_{C1} - E_{J0}) \frac{\bar{u}_{J0}^e}{m^e} \left\{ \frac{-e_{Jnn}^e}{\bar{u}_{J0}^e} \right\}^{m^e} \tag{5.93}$$

and the elastic tangent modulus for the joint is a variable from (5.18)

$$E_{J11} = E_{J0} - (E_{C1} - E_{J0}) \left\{ \frac{-e_{Jnn}^e}{\bar{u}_{J0}^e} \right\}^{m^e-1} \tag{5.94}$$

Note that there is an inherent contradiction. The use of (5.93) was initiated under the assumption of uniaxial strain. Now the relation is assume to hold for the general three-dimensional case. With the use of (5.20) and (5.21), the remaining elastic parameters that depend on this variable are

$$\begin{aligned}
E_{J22} &= E_{J0} \\
E_{J12} &= \frac{\nu_{J0}}{(1-\nu_{J0})} E_{J11} & E_{J230} &= \frac{\nu_{J0}}{(1-\nu_{J0})} E_{J0} \\
2G_{Jnt} &= \frac{(1-2\nu_{J0})}{(1-\nu_{J0})} E_{J11} & 2G_{Jtp0} &= \frac{(1-2\nu_{J0})}{(1-\nu_{J0})} E_{J0}
\end{aligned} \tag{5.95}$$

From(5.84), the finite element elasticity parameters are

$$\begin{aligned}
H_{nn} &= E_{J11} E_{C1} D^{in} \\
H_{nt} &= (\bar{L}_C E_{J11} E_{C2} + \bar{L}_J E_{J12} E_{C1}) D^{in} \\
H_{tt} &= (\bar{L}_J E_{J0} + \bar{L}_C E_{C1}) - \bar{L}_C \bar{L}_J (\bar{E}_{J12} - E_{C2})^2 D^{in} \\
H_{tp} &= (\bar{L}_J E_{J230} + \bar{L}_C E_{C2}) - \bar{L}_C \bar{L}_J (\bar{E}_{J12} - E_{C2})^2 D^{in} \\
G_{nt} &= \frac{G_C G_J}{(G_C \bar{L}_J + G_J \bar{L}_C)} \\
G_{tp0} &= G_{Jtp0} \bar{L}_J + G_C \bar{L}_C \\
D^{in} &\equiv \frac{1}{(\bar{L}_J E_{C1} + \bar{L}_C E_{J11})}
\end{aligned} \tag{5.96}$$

Finally, the plasticity constants that must be specified are $(E_{J0}^p, \bar{u}_{J0}^p, m^p, \mu_J, \tau_{Ja0}, \bar{u}_{Ja})$,

5.5.2 Initial Step to Obtain a Trial Stress

It is assumed that the first step, as far as the call to a constitutive equation subroutine is concerned, consists of prescribed values of increments in components of element strain $\{\Delta e\}$. These increments are assumed to be elastic for the first step. The total and elastic strain components can be immediately updated and stored as indicated by the following:

$$\{e\} \leftarrow \{e\} + \{\Delta e\} \quad \{\Delta e^e\} = \{\Delta e\} \quad \{e^e\} \leftarrow \{e^e\} + \{\Delta e^e\} \tag{5.97}$$

Trial values for stress are obtained using the element elastic constitutive equations. Instead of labeling the stress components as “trial” the approach is to simply consider these components as merely updated with the understanding that further adjustments or updating may be necessary within the current loading step. To be specific, the constitutive equations for this step are:

$$\begin{aligned}
\tau_n &\leftarrow \tau_n + \Delta\tau_n & \Delta\tau_n &= H_{nn}\Delta e_{nn} + H_{nt}\Delta e_{tt} + H_{nt}\Delta e_{pp} \\
\sigma_{tt} &\leftarrow \sigma_{tt} + \Delta\sigma_{tt} & \Delta\sigma_{tt} &= H_{tt}\Delta e_{tt} + H_{tp}\Delta e_{pp} + H_{nt}\Delta e_{nn} \\
\sigma_{pp} &\leftarrow \sigma_{pp} + \Delta\sigma_{pp} & \Delta\sigma_{pp} &= H_{tt}\Delta e_{pp} + H_{nt}\Delta e_{nn} + H_{tp}\Delta e_{tt} \\
\tau_t &\leftarrow \tau_t + \Delta\tau_t & \Delta\tau_t &= 2G_{nt}\Delta e_{nt} \\
\tau_p &\leftarrow \tau_p + \Delta\tau_p & \Delta\tau_p &= 2G_{nt}\Delta e_{np} \\
\sigma_{tp} &\leftarrow \sigma_{tp} + \Delta\sigma_{tp} & \Delta\sigma_{tp} &= 2G_{tp}\Delta e_{tp}
\end{aligned} \tag{5.98}$$

We also need to monitor the elastic strain in the joint because of the nonlinearity. Recall that the joint elastic constitutive equations from (5.15) are

$$\begin{aligned}
\dot{\tau}_{Jn} &= E_{J11}\dot{e}_{Jnn}^e + E_{J12}(\dot{e}_{Jtt}^e + \dot{e}_{Jpp}^e) \\
\dot{\tau}_{Jt} &= 2G_J\dot{e}_{Jnt}^e \\
\dot{\tau}_{Jp} &= 2G_J\dot{e}_{Jnp}^e
\end{aligned} \tag{5.99}$$

Recall that increments in the tt- and pp-components for the joint strain contain no plasticity parts and equal the corresponding increments in element strain. We obtain from (5.99) the increments and updates in elastic strain:

$$\begin{aligned}
\Delta e_{Jnn}^e &= \frac{1}{E_{J11}}[\Delta\tau_{Jn} - E_{J12}(\Delta e_{Jtt} + \Delta e_{Jpp})] & e_{Jnn}^e &\leftarrow e_{Jnn}^e + \Delta e_{Jnn}^e \\
\Delta e_{Jnt}^e &= \frac{\Delta\tau_{Jt}}{2G_J} & e_{Jnt}^e &\leftarrow e_{Jnt}^e + \Delta e_{Jnt}^e \\
\Delta e_{Jnp}^e &= \frac{\Delta\tau_{Jp}}{2G_J} & e_{Jnp}^e &\leftarrow e_{Jnp}^e + \Delta e_{Jnp}^e
\end{aligned} \tag{5.100}$$

The next step is to check for plasticity by obtaining the value of the composite yield function. If the value is negative, the conclusion is that the step is elastic and the updated stresses are indeed the final stress components for the step. No updating for plastic strain components is required.

An elastic step occurs if the joint has been compacted previously, and the current step is one of either unloading or reloading with an existing yield stress that is sufficiently large.

The composite yield function is formed as the maximum of three separate yield functions:

$$F_J = \max(F_C, F_S, F_T) \tag{5.101}$$

where

$$F_C = \tau_{Jny} - \tau_{Jn} \quad F_S = \tau_{Js} - \tau_{Sny} \quad F_T = \tau_{Jn} \tag{5.102}$$

It is possible to have simultaneous yield based on two or more yield functions. The procedure adopted for this situation is to first obtain the deformation based on the

yield function displaying the largest value of the yield function. Then invoke the plasticity associated with the next largest positive yield function and continue until all yield criteria are satisfied.

Now we proceed to look at the implications of each yield condition in turn.

5.5.3 Case where the Compressive Cap Governs

Here it is assumed that with the trial stress, $F_C > 0$ where

$$F_C = \tau_{Jy} - \tau_{Jn} \quad \tau_{Jy} = g^p = E_{J0}^p \frac{\bar{u}_{J0}^p}{m^p} \left[1 - \left\{ \frac{\bar{u}_{J0}^p}{e_{Jnn}^p + \bar{u}_{J0}^p} \right\}^{m^p} \right] \quad (5.103)$$

Now the Newton-Raphson scheme is used to force F_C to zero by allowing sub-increments in plastic strain with the total strain held fixed. The procedure is summarized as follows:

$$\begin{aligned} \delta\omega_c &= -\frac{F_C}{\partial F_C / \partial \omega_c} \\ \delta e_{Jnn}^p &= -\delta\omega_c & e_{Jnn}^p &\leftarrow e_{Jnn}^p + \delta e_{Jnn}^p \\ \delta e_{nn}^p &= \bar{L}_J \delta e_{Jnn}^p & e_{nn}^p &\leftarrow e_{nn}^p + \delta e_{nn}^p \\ \delta e_{nn}^e &= -\delta e_{nn}^p & e_{nn}^e &\leftarrow e_{nn}^e + \delta e_{nn}^e \\ \delta \tau_n &= H_{nn} \delta e_{nn}^e & \tau_n &\leftarrow \tau_n + \delta \tau_n \\ \delta \sigma_{tt} &= H_{nt} \delta e_{nn}^e & \sigma_{tt} &\leftarrow \sigma_{tt} + \delta \sigma_{tt} \\ \delta \sigma_{pp} &= H_{nt} \delta e_{nn}^e & \sigma_{pp} &\leftarrow \sigma_{pp} + \delta \sigma_{pp} \\ \Delta e_{Jnn}^e &= \frac{\Delta \tau_n}{E_{J11}} & e_{Jnn}^e &\leftarrow e_{Jnn}^e + \Delta e_{Jnn}^e \\ \tau_{Jn} &= \tau_n \\ \tau_{Jy} &= g^p(e_{Jnn}^p) \end{aligned} \quad (5.104)$$

To obtain the denominator in the first equation, use (5.103) and (5.86) with the total strain components of the element considered fixed to obtain

$$\begin{aligned} \dot{F}_C &= \dot{\tau}_{Jcy} - \dot{\tau}_{Jn} = E_J^p \dot{e}_{Jnn}^p - H_{nn} \dot{e}_{nn}^e \\ &= E_J^p \dot{e}_{Jnn}^p + H_{nn} \dot{e}_{nn}^p = (E_J^p + H_{nn} \bar{L}_J) \dot{e}_{Jnn}^p \\ &= (E_J^p + H_{nn} \bar{L}_J) \dot{\omega}_c \end{aligned} \quad (5.105)$$

or

$$\begin{aligned}
\frac{\partial F_C}{\partial \omega_c} &= -(E_J^p + \bar{L}_J H_{mn}) \\
&= -E_{J0}^p \left\{ \frac{\bar{u}_{J0}^p}{e_{Jmn}^p + \bar{u}_{J0}^p} \right\}^{m^p-1} - \bar{L}_J H_{mn}
\end{aligned} \tag{5.106}$$

The steps of (5.104) with (5.106) are repeated until the value of \bar{F}_C is less than a prescribed small positive value. There is no alteration of the shear components of stress and strain.

5.5.4 Case where Shear Governs

Here it is assumed that the use of the trial stress results in a value for the shear yield function that satisfies $F_S > 0$ where

$$\begin{aligned}
F_S &= \tau_{Js} - \tau_{Jsy} \\
\tau_{Js} &= (\tau_{Jt}^2 + \tau_{Jp}^2)^{1/2} \\
\tau_{Jsy} &= \tau_{Jas} - \mu_J \tau_{Jn} \\
\tau_{Jas} &= \tau_{Ja0} \left\langle 1 - \frac{\bar{u}_{Js}^p}{\bar{u}_{Ja}} \right\rangle \\
\dot{e}_{Js}^p &= \{ \dot{e}_{Jnt}^{p2} + \dot{e}_{Jnp}^{p2} \}^{1/2} \\
\dot{\bar{u}}_{Js}^p &= 2\dot{e}_{Js}^p = \{ \dot{\bar{u}}_{Jt}^{p2} + \dot{\bar{u}}_{Jp}^{p2} \}^{1/2} \\
\bar{u}_{Js}^p &= \int \dot{\bar{u}}_{Js}^p dt
\end{aligned} \tag{5.107}$$

Similarly for the compaction case, the elastic part of the joint strain must be updated using (5.100).

Again, the Newton-Raphson scheme is used to force F_S to zero by allowing sub-increments in plastic strain with the total strain held fixed. The procedure is summarized as follows:

$$\begin{aligned}
\delta\omega_s &= -\frac{F_S}{\partial F_S / \partial \omega_s} \\
\delta e_{Jnt}^p &= \delta\omega_s \frac{\tau_{Jt}}{\tau_{Js}} & e_{Jnt}^p &\leftarrow e_{Jnt}^p + \delta e_{Jnt}^p \\
\delta e_{Jnp}^p &= \delta\omega_s \frac{\tau_{Jp}}{\tau_{Js}} & e_{Jnp}^p &\leftarrow e_{Jnp}^p + \delta e_{Jnp}^p \\
\delta e_{Jnn}^p &= \mu_J \delta\omega_s \left\langle 1 - \frac{\bar{u}_{Js}}{\bar{u}_a} \right\rangle & e_{Jnn}^p &\leftarrow e_{Jnn}^p + \delta e_{Jnn}^p \\
\delta e_{nt}^p &= \bar{L}_J \delta e_{Jnt}^p & e_{nt}^p &\leftarrow e_{nt}^p + \delta e_{nt}^p \\
\delta e_{np}^p &= \bar{L}_J \delta e_{Jnp}^p & e_{np}^p &\leftarrow e_{np}^p + \delta e_{np}^p \\
\delta e_{nn}^p &= \bar{L}_J \delta e_{Jnn}^p & e_{nn}^p &\leftarrow e_{nn}^p + \delta e_{nn}^p \\
\delta e_{nt}^e &= -\delta e_{nt}^p & e_{nt}^e &\leftarrow e_{nt}^e + \delta e_{nt}^e \\
\delta e_{np}^e &= -\delta e_{np}^p & e_{np}^e &\leftarrow e_{np}^e + \delta e_{np}^e \\
\delta e_{nn}^e &= -\delta e_{nn}^p & e_{nn}^e &\leftarrow e_{nn}^e + \delta e_{nn}^e \\
\delta \tau_t &= G_{nt} \delta e_{nt}^e & \tau_t &\leftarrow \tau_t + \delta \tau_t \\
\delta \tau_p &= G_{nt} \delta e_{np}^e & \tau_p &\leftarrow \tau_p + \delta \tau_p \\
\delta \tau_n &= H_{nn} \delta e_{nn}^e & \tau_n &\leftarrow \tau_n + \delta \tau_n \\
\delta \sigma_{tt} &= H_{nt} \delta e_{nn}^e & \sigma_{tt} &\leftarrow \sigma_{tt} + \delta \sigma_{tt} \\
\delta \sigma_{pp} &= H_{nt} \delta e_{nn}^e & \sigma_{pp} &\leftarrow \sigma_{pp} + \delta \sigma_{pp} \\
\Delta e_{Jnn}^e &= \frac{\Delta \tau_n}{E_{J11}} & e_{Jnn}^e &\leftarrow e_{Jnn}^e + \Delta e_{Jnn}^e \\
\tau_{Js} &= (\tau_t^2 + \tau_p^2)^{1/2} \\
\delta e_{Js}^p &= \{(\delta e_{Jnt}^p)^2 + (\delta e_{Jnp}^p)^2\} & \bar{u}_{Js}^p &\leftarrow \bar{u}_{Js}^p + 2\delta e_{Js}^p \\
\tau_{Jas} &= \tau_{Ja0} \left\langle 1 - \frac{\bar{u}_{Js}^p}{\bar{u}_{Ja}} \right\rangle \\
\tau_{Jsy} &= \tau_{Jas} - \mu_J \tau_{Jn}
\end{aligned} \tag{5.108}$$

To obtain the denominator in the first equation, use (5.43) with the total strain rates equal zero to obtain

$$\dot{F}_S = -2G_{Jnt} \dot{\omega}_s + \tau_{Ja0} \frac{\dot{\omega}_s}{\bar{u}_{Ja}} H \left[1 - \frac{\bar{u}_{Js}}{\bar{u}_{Ja}} \right] - E_{J11} \dot{\omega}_s \mu_J^2 \left\langle 1 - \frac{\bar{u}_{Js}}{\bar{u}_{Ja}} \right\rangle \tag{5.109}$$

from which it follow that

$$\frac{\partial F_S}{\partial \omega_s} = -2G_{Jnt} - E_{J11} \mu_J^2 \left\langle 1 - \frac{\bar{u}_{Js}}{\bar{u}_{Ja}} \right\rangle + \frac{\tau_{Ja0}}{\bar{u}_{Ja}} H \left[1 - \frac{\bar{u}_{Js}}{\bar{u}_{Ja}} \right] \tag{5.110}$$

The procedure of (5.108) with (5.110) is repeated until the value of F_S is less than a prescribed small positive value. Again, the parameters must satisfy the restriction that $\partial F_S / \partial \omega_s < 0$. The critical case occurs when \bar{u}_{Js} is just slightly less than \bar{u}_{Ja} at which time we require

$$2G_{Jnt} - \frac{\tau_{Ja0}}{\bar{u}_{Ja}} > 0 \quad (5.111)$$

Recall from (5.95) and (5.94) that

$$2G_{Jnt} = \frac{(1-2\nu_{J0})}{(1-\nu_{J0})} E_{J11} \quad E_{J11} = E_{J0} - (E_{C1} - E_{J0}) \left\{ \frac{-e_{Jnn}^e}{\bar{u}_{J0}^e} \right\}^{m^e-1} \quad (5.112)$$

The worst case is when the joint has undergone only a small amount of compaction for then $E_{J11} = E_{J0}$ and (5.111) reduces to

$$\frac{(1-2\nu_J)}{(1-\nu_J)} E_{J0} - \frac{\tau_{Ja0}}{\bar{u}_{Ja}} > 0 \quad (5.113)$$

For $\nu_J = 0.25$, this restriction becomes

$$\frac{2}{3} E_{J0} - \frac{\tau_{Ja0}}{\bar{u}_{Ja}} > 0 \quad (5.114)$$

The initial intercept of the Mohr-Coulomb surface with the shear axis at zero normal stress is τ_{Ja0} which is generally available from experimental data. Therefore (5.114) places a restriction on \bar{u}_{Ja} .

5.5.5 Case of Zero Normal Traction

Suppose the increments in total element strain components result in a trial state for which $\tau_n > 0$. The procedure to force the traction components, including shear, to zero is to simply prescribe sub-increments in plastic strain components to force the corresponding traction components to zero. Since the total strains for the element are fixed, sub-increments in total strain must be zero for this step and, therefore, the plastic strain sub-increments must be the negative of the elastic sub-increments. First, we perform the operation on element strains and then obtain the corresponding sub-increments for joint strains. The difference between this case and the two previous ones involving plasticity is that this is a one-step procedure and only one sub-increment is required. The sub-increments in traction components are chosen to be

$$\delta\tau_n = -\tau_n \quad \delta\tau_t = -\tau_t \quad \delta\tau_p = -\tau_p \quad (5.115)$$

Now, we use the appropriate subset of (5.98) as follows:

$$\begin{aligned}
\delta e_{nn}^e &= \frac{\delta \tau_n}{H_{nn}} & \delta e_{nt}^e &= \frac{\delta \tau_t}{2G_{nt}} & \delta e_{np}^e &= \frac{\delta \tau_p}{2G_{nt}} \\
\delta \sigma_{tt} &= H_{nt} \delta e_{nn}^e & \delta \sigma_{pp} &= H_{nt} \delta e_{nn}^e & & \\
\delta e_{nn}^p &= -\delta e_{nn}^e & \delta e_{nt}^p &= -\delta e_{nt}^e & \delta e_{np}^p &= -\delta e_{np}^e \\
e_{nn}^e &\leftarrow e_{nn}^e + \delta e_{nn}^e & e_{nt}^e &\leftarrow e_{nt}^e + \delta e_{nt}^e & e_{np}^e &\leftarrow e_{np}^e + \delta e_{np}^e \\
e_{nn}^p &\leftarrow e_{nn}^p + \delta e_{nn}^p & e_{nt}^p &\leftarrow e_{nt}^p + \delta e_{nt}^p & e_{np}^p &\leftarrow e_{np}^p + \delta e_{np}^p
\end{aligned} \tag{5.116}$$

Finally, the corresponding strains for the joint are found using (5.100) as follows:

$$\begin{aligned}
\delta e_{Jnn}^e &= \frac{\Delta \tau_{Jn}}{E_{J11}} & \delta e_{Jnn}^p &= -\delta e_{Jnn}^e & e_{Jnn}^e &\leftarrow e_{Jnn}^e + \delta e_{Jnn}^e & e_{Jnn}^p &\leftarrow e_{Jnn}^p + \delta e_{Jnn}^p \\
\delta e_{Jnt}^e &= \frac{\delta \tau_{Jt}}{2G_J} & \delta e_{Jnt}^p &= -\delta e_{Jnt}^e & e_{Jnt}^e &\leftarrow e_{Jnt}^e + \delta e_{Jnt}^e & e_{Jnt}^p &\leftarrow e_{Jnt}^p + \delta e_{Jnt}^p \\
\delta e_{Jnp}^e &= \frac{\delta \tau_{Jp}}{2G_J} & \delta e_{Jnp}^p &= -\delta e_{Jnp}^e & e_{Jnp}^e &\leftarrow e_{Jnp}^e + \delta e_{Jnp}^e & e_{Jnp}^p &\leftarrow e_{Jnp}^p + \delta e_{Jnp}^p
\end{aligned} \tag{5.117}$$

5.5.6 Concluding Remarks

In this section, the basic set of constitutive equations for joint deformation have been provided together with an algorithmic approach for the corresponding constitutive equation subroutine. The essential assumption of the algorithm is that the total strain increments are given. The equations for an element containing a joint or fault have been presented. The next item is a constitutive equation subroutine and sample paths that illustrate the properties of the proposed model.

5.6 Constitutive Equation Algorithm and Features

5.6.1 Preliminary Remarks

The purpose here is to write a general-purpose subroutine that can be used by a general code for obtaining numerical solutions to problems involving wave propagation in jointed and faulted media. A driver program has been constructed to provide strain increments for a number of paths in order to test the subroutine and to show the general features of the model. In turn, the constitutive equation subroutine assumes strain increments are provided to update values of the components of stress and internal variables.

5.6.2 Features of the Assumed Response Functions

To illustrate the features of the proposed model, a number of paths are simulated. Stress and stress moduli have been scaled so that the maximum stress is of order ten, and length parameters scaled so that the width of the element is $h = 0.1$. The results of 8 example paths are provided in the next subsection.

The following values for material parameters were used for all examples:

$$\begin{aligned}
 Y_C &= 18 & \nu_C &= 0.2 & E_{CI} &= 20. \\
 E_{J0} &= 1.0 & \nu_{J0} &= 0.2 & m^e &= 1.5 \\
 E_{J0}^p &= 4.0 & m^p &= 2.0 & \mu_J &= 0.4 \\
 \tau_{Ja0} &= 0.6 & \bar{u}_{Ja} &= 1.0 & &
 \end{aligned} \tag{5.118}$$

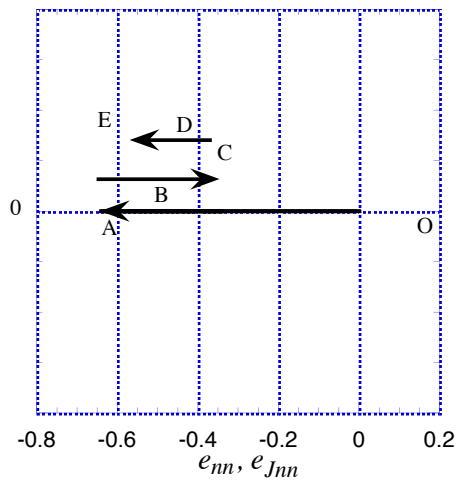
The geometrical parameter $[u_{J0}]$ and the material parameter $[u_0^p]$ were selected as follows:

$$\begin{aligned}
 [u_{J0}] &= h & [u_0^p] &= 0.9[u_{J0}] & \text{Examples 1 \& 2} \\
 [u_{J0}] &= h & [u_0^p] &= 0.5[u_{J0}] & \text{Examples 3,4 \& 5} \\
 [u_{J0}] &= 0.5h & [u_0^p] &= 0.9[u_{J0}] & \text{Examples 6} \\
 [u_{J0}] &= 0.1h & [u_0^p] &= 0.9[u_{J0}] & \text{Examples 7\&8}
 \end{aligned} \tag{5.119}$$

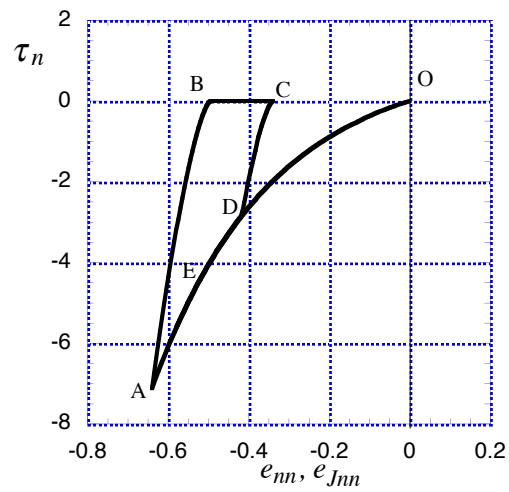
Since $[u_{J0}] = h$ for the first 5 cases, these examples demonstrate the properties of the joint model. For Example 6, the joint represents one-half the element, and for the last two examples, the joint represents just one-tenth of the element. Therefore, it is to be expected that for these three cases the properties of the continuum, at least in compression, become more important in comparison to the properties of the joint.

Example 1

The first sample problem is a load path involving compaction and release only. The strain path is shown in Fig. 5.9(a) and the corresponding stress-strain plot is shown in Fig. 5.9(b). Initially, the strain is reduced from the origin (Point O) to the strain at point A. The stress-strain behavior is nonlinear based on both the elastic and plastic behavior. Then the strain is reduced to point B where the stress is zero. This reduction is strictly elastic and the shape of the curve shows the behavior is nonlinear. The relaxation is continued with zero stress to point C at which time the strain increments are reversed to cause re-compaction. The loading is elastic until the yield surface is reached at point D. With further compaction, plasticity is invoked and the original path is followed until loading is terminated at point E.



(a) Prescribed strain path.

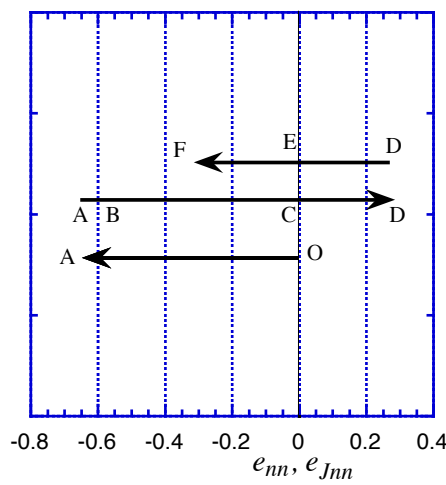


(b) Stress versus strain.

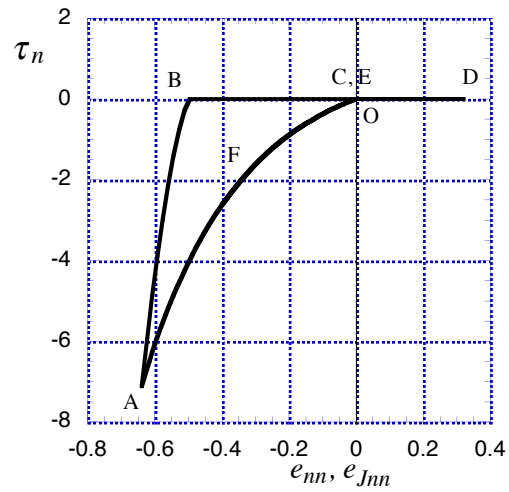
Figure 5.9: Path showing compaction, unloading and re-compaction.

Example Problem 2

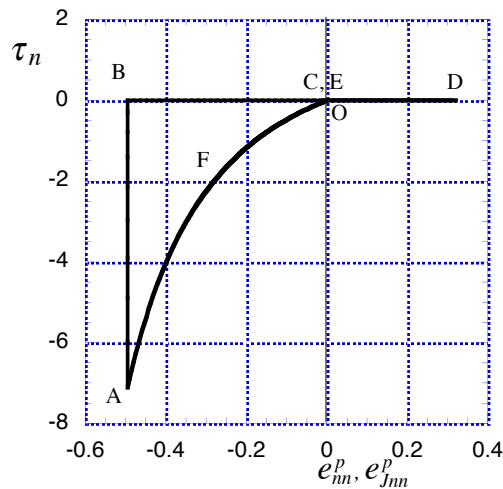
Example Problem 2 is a case where the unloading portion is extended further. The strain path is shown in Fig. 5.10(a) and the corresponding stress-strain path in Fig. 5.10(b). The sample is compacted to point A, and then unloaded to zero stress at point B. With additional positive increments in strain, the joint is unloaded to its original configuration at point C. With even further positive increments, a gap is formed to the maximum value illustrated as point D. The width of the gap is tracked through the use of a positive joint plastic strain. Then the strain increments are reversed and the gap is closed at point E at which time the joint plastic strain is zero. The model has been formulated so that re-compaction follows the original loading curve as indicated by the segment E-F. A plot of stress versus joint plastic strain is given in Fig. 5.10(c).



(a) Prescribed strain path.



(b) Stress versus strain.



(c) Stress versus element and joint plastic strain.

Figure 5.10: Plots of stress and strain for uniaxial strain with gap formation and closing.

Example 3

Example 3 is similar to that for Example 1 but with the choice of $[u_0^p] = 0.5[u_{J0}]$ instead of $[u_0^p] = 0.9[u_{J0}]$ used previously. This simple change causes a rather dramatic change in the nonlinear behavior. The stress-strain plot shown in Fig. 5.11 becomes significantly steeper as the magnitude of the strain becomes larger. At the same time the elastic unloading part of the curve shows significantly greater nonlinearity.

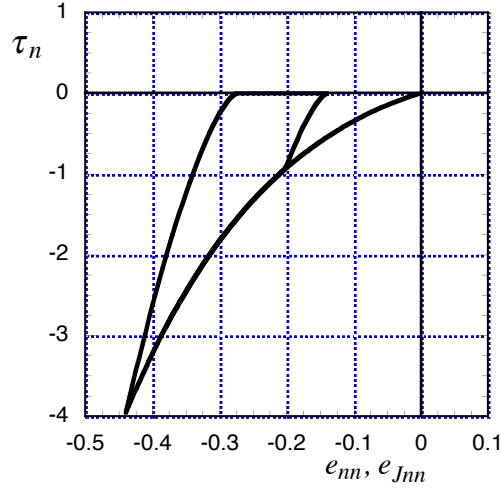


Figure 5.11: Plot of stress versus strain for a path similar to that of Example 1 but with $[u_0^p] = 0.5[u_{J0}]$.

Example 4

The next problem, with results plotted in Fig. 5.12, consists of a combination of normal and shear components of strain and stress. Fig. 5.12(a) shows the path in strain space while Fig. 5.12(b) shows the corresponding path in stress space. First the joint is compacted by path 0-A to push the compaction yield surface to the left. Then an elastic unloading step in the normal direction is performed along path A-B. From then on the joint is loaded strictly with increments in shear strain to obtain the path B-C-D-E. The initial part of the shear segment, B-C, is elastic until the initial yield surface in shear is activated. After that, both inelastic shear and plastic dilatation occur. However, because the normal strain is held fixed, the plastic strain increments (dilatation) are positive so the the normal component of elastic strain increments are negative and the normal component of stress also becomes more negative. This is the reason why the stress path goes from C to D. Simultaneously, the compaction surface is moving to the right because of dilatation, and the yield curve is softening because of shear deformation. At point D, the compaction yield surface has moved sufficiently to the right to become activated. For the strain path from D to E, the combination of plastic dilatation due to shear and plastic compaction has the net effect of small motion of the compaction yield surface. The drop in shear along path D-E is due to the softening of the shear yield surface. Ultimately the effect of the shear deformation on asperities is removed, no additional dilatation occurs, and the yield surface remains fixed on the surface that passes through the origin and is shown as the final Mohr-Coulomb yield surface.

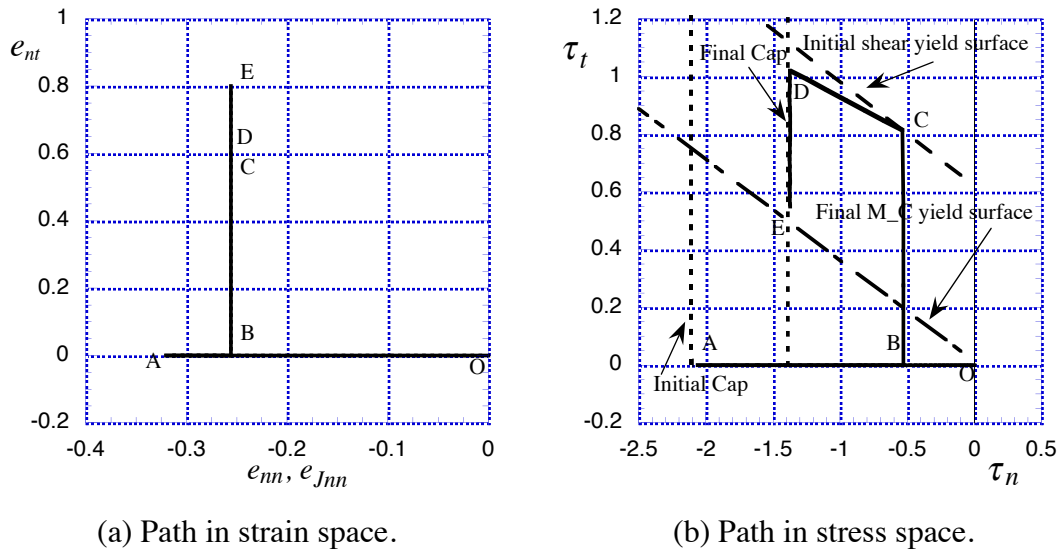


Figure 5.12: Path showing the interactive effects of shear and normal stress.

Example 5

The strain path is shown in 14a. In this example the joint is first loaded in compression under uniaxial strain as illustrated by leg OA. Then positive increments in both axial and shear strain are prescribed to obtain leg AB. Finally, leg BC is obtained by specifying negative increments in axial strain and positive increments in shear.

The corresponding path in stress space is shown in 14b. In this space, leg O-A represents the compaction of the joint as illustrated by negative values of normal stress. The portion of leg A-B, denoted by A-a, is elastic and holds until the initial yield surface in shear is reached at point a. With further loading, shown by segment a-b, the normal component of stress decreases further because of elastic unloading, and the shear stress reduces because of softening of the shear yield surface. Meanwhile the cap has moved in from the value of normal stress associated with point A. For the step illustrated by b-c, both yield surfaces are active. Softening due to dilatation from shear dominates hardening of the cap. The normal component of stress reduces to zero, and consequently the shear stress also reduces to zero at point c. The joint has returned to its original width. At point B, the normal strain is positive with the implication that a gap has formed. The segment B-d of the leg B-C corresponds to closing the gap. Then d-e represents elastic reloading in shear until the yield surface for shear is reached at point e. The yield surface softens further until the maximum softening has been attained and the yield surface becomes a Mohr-Coulomb frictional surface at point f. For the remaining part of the leg B-C as defined by the segment f-C, the stress point is merely moving along the Mohr-Coulomb surface while the cap is governed by hardening.

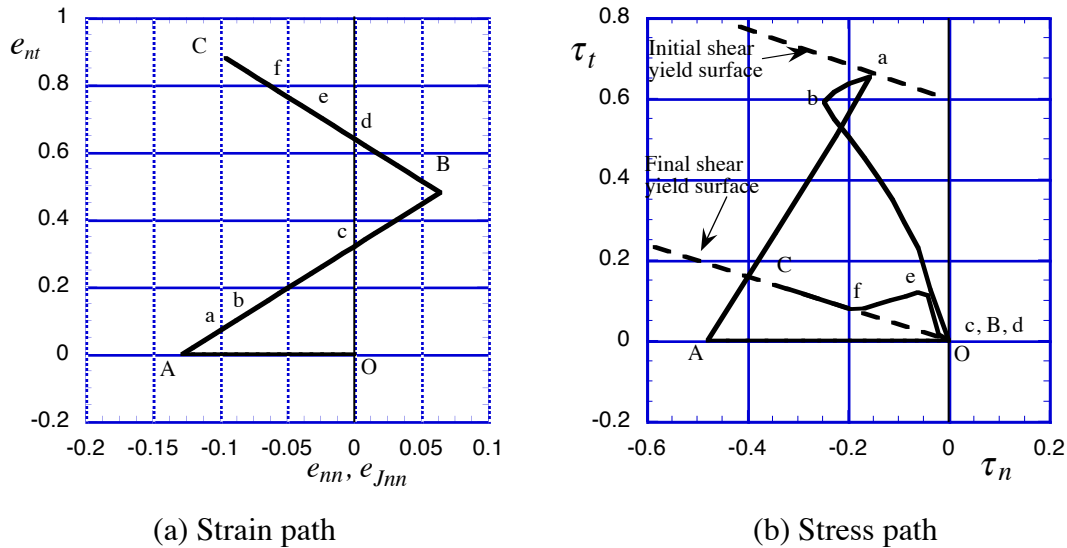


Figure 5.13: Path showing compaction, unloading into gap opening with shear, and reloading in compression with shear.

Example 6.

Example 6 is intended to show a case where the joint represents one-half the width of an element, or $[u_0] = 0.5h$, and $[u_0^p] = 0.9[u_{J0}] = 0.045$ so that the properties of the continuum on either side of the joint come into play. The normal component of the element strain is prescribed. The corresponding plots of the elastic and plastic parts of joint strain are shown in Fig. 5.5(a) and the normal components of stress in the **n**- and **t** directions are given in Fig. 5.14(b). All segments consist of loading and unloading in uniaxial strain in the normal direction. First, compaction is prescribed as indicated by the segment from the origin O to point A on the plots. Then the material is unloaded elastically shown as segment A-B. Further unloading on segment B-C results in a reduction in the plastic strain of the joint to zero. Positive plastic strain of the joint corresponds to opening of the joint. Upon reversal of the loading, the joint closes (segment C-D) and then the joint goes into compression again. Note that the normal component of stress, σ_{nn} , does not reduce to zero when the joint opens. This residual component of stress also affects when reloading occurs because the normal component of elastic strain in the continuum does not reduce to zero even though the normal component of stress is zero when the gap forms.

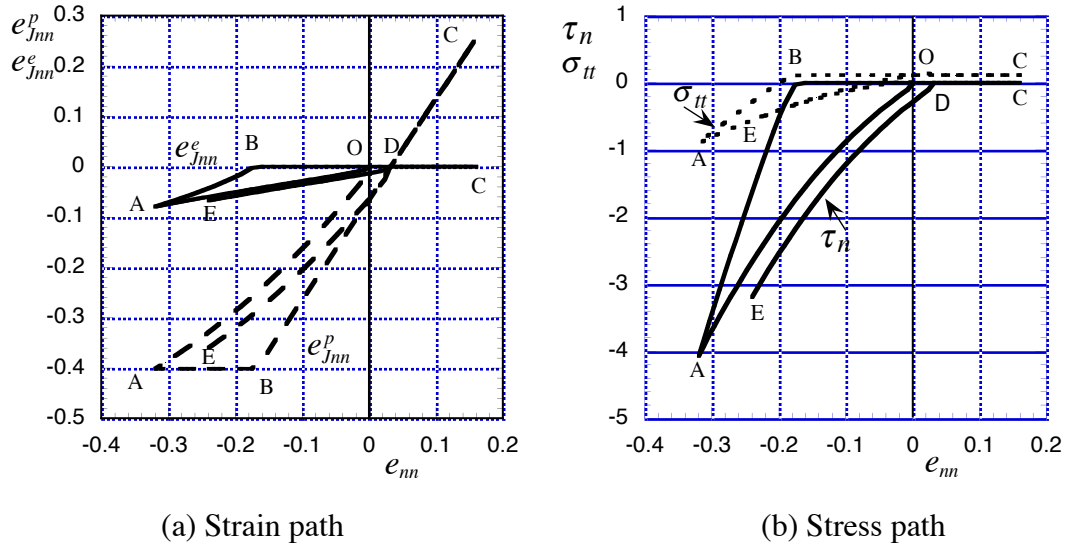


Figure 5.14: Path showing compaction, unloading to include a gap formation, and reloading in compression for a joint half the width of an element.

Example 7.

This example is intended to show the effect of reducing the joint width to one-tenth the width of the element, or $[u_0] = 0.1[u_{J0}]$, $[u_0^p] = 0.9[u_{J0}^p]$ and the load path is the same as that used for Example 6. Fig. 5.15 shows the results. The key point is that for a given amount of element strain, the strain of the joint and, hence, the maximum compressive stress is higher in comparison to corresponding quantities when the joint width is a small fraction of the element size. This is simply a manifestation of the fact that the continuum material that makes up the majority of the material represented by an element is much stiffer than the joint, at least for the range of stress considered in these examples. Again, the presence of a residual value of the stress, σ_{tt} , and of the strain, e_{nn}^e , results in reloading when the strain e_{nn} reduces to a nonzero positive value.

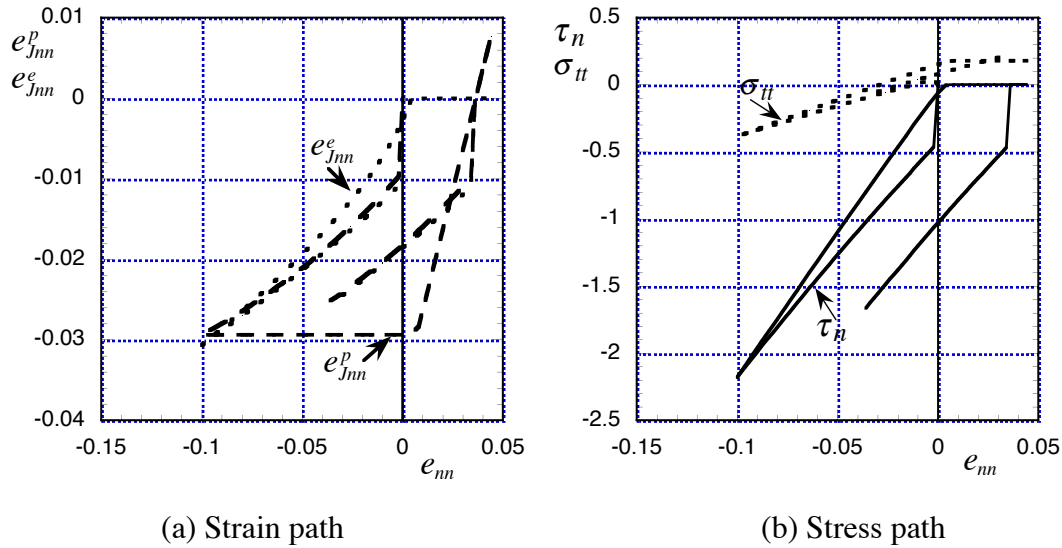


Figure 5.15: Path showing compaction, unloading to include a gap formation, and reloading in compression for a joint one-tenth the width of an element.

Example 8.

This example represents a case of combined normal and shear loading with the joint width one-tenth of the element width. The strain path is illustrated in Fig. 5.16(a) and the corresponding stress path is shown in Fig. 5.16(b). The joint is compacted by performing the segment of strain given as O-A. Then unloading in the normal direction is combined with shear loading. The segment A-B is elastic while step B-C represents softening of the shear yield surface. At point C the maximum amount of softening has occurred and from then on the shear yield surface is fixed and designated the Mohr-Coulomb (M-C) yield surface in Fig. 5.16(b). There is no further dilatation due to shear. Segment C-D represents further unloading in the normal direction with the shear yield surface continuously active. Finally, the segment D-E represents loading in the normal direction while simultaneously staying on the M-C shear yield

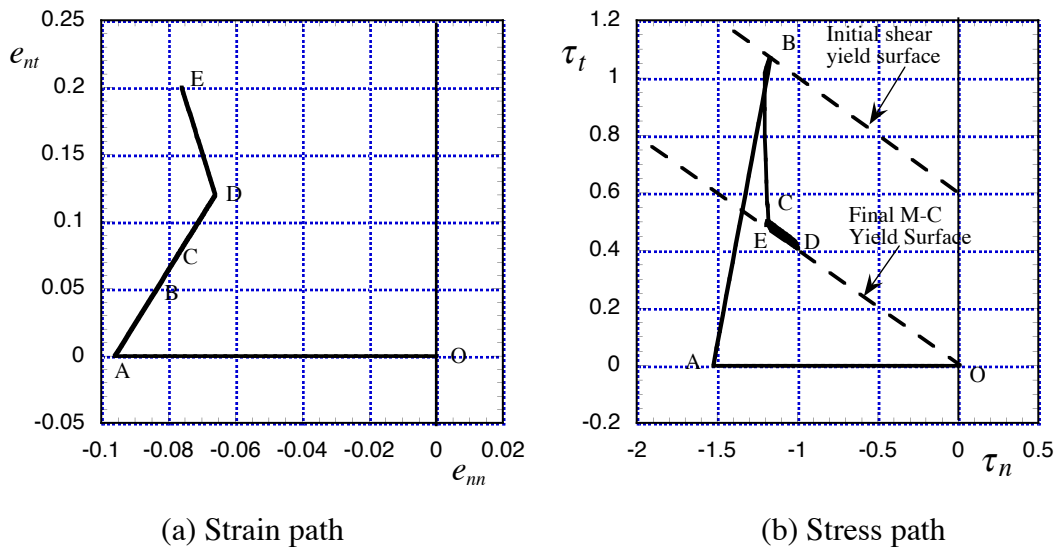


Figure 5.16: Path showing compaction, unloading to include a gap formation, and reloading in compression for a joint one-tenth the width of an element.

5.6.3 Concluding Remarks

In this section sample paths have been specified in the driver program to test various segments of the constitutive equation subroutines. Although not comprehensive, the set of paths illustrate essential features of the joint constitutive equation and how these features can be combined with a joint through the deformation of an element.

5.7 Summary

In this section a constitutive equation has been proposed for joints and faults, a formulation provided for combining this constitutive equation with elastic behavior of surrounding continuum, and a numerical algorithm described for obtaining stress when increments in strain are provided for an element. The continuum is assumed to behave as a linearly isotropic elastic material. Under compaction, the joint and fault material is assumed to be nonlinearly elastic-plastic with no strength in tension. An initial cohesion in shear is assumed to exist because of the presence of asperities. A coupling effect between compaction and shear exists for two reasons: (i) the yield stress in shear increases with the magnitude of the normal compressive stress, and (ii) initial deformation in shear is accompanied by dilatation, again due to asperities, and the dilatation reduces the yield strength for the normal compressive stress. With a large enough motion in shear, the effect of the asperities diminishes to the point that no additional dilatation occurs, and the yield strength in shear is only due to Coulomb friction.

It is assumed that joints and faults cannot sustain a tensile component in the normal direction. Therefore, under certain kinematic conditions a gap can form. Tangential motion can then occur with no resistance in shear. Furthermore, it is possible that the gap can close and resistance to shear motion can exist due to friction if the normal component of stress is compressive. Often gaps and gap closure are modeled numerically with contact algorithms. A unique aspect of the numerical formulation is that gap opening and closing together with tangential motion, if any, handled within the constitutive equation formulation through the definition of “pseudo” components of plastic strain that force the pertinent components of stress to zero while simultaneously reflecting a record of the amount of gap opening and tangential slip experienced by the joint or fault. This feature is of particular value for problems involving large dynamic loads with stress waves that can exhibit significant tensile components of stress at certain times.

Overall, the important aspect of this phase of the research is that a nonlinearly elastic-plastic framework has been established for modeling the essential features of joints and faults under a variety of loads. Relatively minor modifications should be needed if experimental data suggest that certain features should be represented in more detail.

Bibliography

- Alfaiate, J., Simone, A., and Sluys, L. (2003). Non-homogeneous displacement jumps in strong embedded discontinuities. *Int. J. of Solids and Structures*, 40:5799–5817.
- Barton, N. (1972). A model study of rock-joint deformation. *International Journal of Rock Mechanics and Mining Sciences*, 9:579–602.
- Brannon, R. (January, 2010). A homogenized rock-joint (fault) formulation for computational material models. In *Ground Shock in Faulted Media Workshop, University of Utah*.
- Cai, M. and Horii, H. (1992). A constitutive model of highly jointed rock masses. *Mechanics of Materials*, 13:217–246.
- Chalhoub, M. and Pouya, A. (2008). Numerical homogenization of a fractured rock mass: A geometrical approach to determine the mechanical representative elementary volume. *Electronic Journal of Geotechnical Engineering*, 13.
- Chitty, D. E. (2010). Problems of joints and faults. In *Ground Shock in Faulted Media Workshop, Washington, D.C.*
- Desai, C. and Ma, Y. (1992). Modelling of joints and interfaces using the disturbed-state concept. *International Journal for Numerical and Analytical Methods in Geomechanics*, 16:623–653.
- Goodman, R. E. (1989). *Introduction to rock mechanics*. Number 0-471-81200-5. John Wiley, 2nd edition.
- Grasselli, G. and Egger, P. (2003). Constitutive law for the shear strength of rock joints based on three-dimensional surface parameters. *International Journal of Rock Mechanics and Mining Sciences*, 40:25–40.
- Huang, T., Chang, C., and Chao, C. (2002). Experimental and mathematical modeling for fracture of rock joint with regular asperities. *Engineering Fracture Mechanics*, 69:1977–1996.
- Lade, P. (2001). Modeling sea ice as an elasto-plastic frictional material. In *IUTAM Symposium on Scaling Laws in Ice Mechanics and Ice Dynamics*, pages 227–238. Kluwer Academic Publishers.

- Larsson, R. and Runesson, K. (1996). Element-based localization band based on regularized displacement discontinuity. *J. of Engineering Mechanics*, 122:402–411.
- Lee, U. (1998). A theory of smeared continuum damage mechanics. *Journal of Mechanical Science and Technology*, 12(2):233–243.
- Li, J. and Ma, G. (2009). Experimental study of stress wave propagation across a filled rock joint. *International Journal of Rock Mechanics and Mining Sciences*, 46:471–478.
- Moes, N., Dolbow, J., and Belytschko, T. (1999). A finite element method for crack growth without remeshing. *Int. J., Numer. Meth. Engng.*, 46:131–150.
- Peterson, K. and Sulsky, D. (2011). Towards a new elastic-decohesive model of Arctic sea ice. *Physica D*. doi:10.1016/j.physletb.2003.10.071.
- Planas, J., Elices, M., Guinea, G., Gomez, F., Cendon, D., and Arbillá, I. (2003). Generalizations and specializations of cohesive crack models. *Engineering Fracture Mechanics*, 70:1759–1776.
- Plesha, M. (1987). Constitutive models for rock discontinuities with dilatancy and surface degradation. *International Journal for Numerical and Analytical Methods in Geomechanics*, 11:345–362.
- Rashid, Y. (1968). Analysis of prestressed concrete pressure vessels. *Nuclear Engineering and Design*, 7:334–355.
- Schreyer, H. (1976). Impulse attenuation of waves emanating from a cylindrical cavity in anisotropic media. *Int. J. of Mechanical Sci.*, 18:487–495.
- Schreyer, H. (2001). Modeling failure initiation in sea ice based on loss of ellipticity. In *IUTAM Symposium on Scaling Laws in Ice Mechanics and Ice Dynamics*, pages 239–250. Kluwer Academic Publishers, The Netherlands.
- Schreyer, H. (2007). Modelling surface orientation and stress at failure of concrete and geological materials. *J. for Numerical and Analytical Methods in Geomechanics*, 31:141–171.
- Schreyer, H., Monday, L., Sulsky, D., Coon, M., and Kwok, R. (2006). Elastic-decohesive constitutive model for sea ice. *Journal of Geophysical Research*, 111:C11S26.
- Schreyer, H., Sulsky, D., and Zhou, S.-J. (2002a). Modeling delamination as a strong discontinuity with the material point method. *Computer Methods in Applied Mechanics and Engineering*, 191:2483–2508.
- Schreyer, H. L., Sulsky, D., and Zhou, S.-J. (2002b). Modeling delamination as a strong discontinuity with the material point method. *Comput. Meths. Appl. Mech. Engrg.*, 191:2463–2481.

- Schulson, E. (2004). Compressive shear faults within arctic sea ice: Fracture on scales large and small. *J. Geophys. Res.*, 109:C07016.
- Sulsky, D., Chen, Z., and Schreyer, H. L. (1994). A particle method for history-dependent materials. *Comput. Methods Appl. Mech. Engrg.*, 118:179–196.
- Sulsky, D. and Schreyer, H. (2004). MPM simulation of dynamic material failure with a decohesive constitutive model. *European Journal of Mechanics A/Solids*, 23:423–445.
- Sulsky, D., Schreyer, H., Peterson, K., Kwok, R., and Coon, M. (2007). Using the material-point method to model sea ice dynamics. *J. Geophys. Res.*, 112:C02S90, doi:10.1029/2005JC003329.
- Sulsky, D. and Schreyer, H. L. (1996). Axisymmetric form of the material point method with applications to upsetting and Taylor impact problems. *Comput. Meths. Appl. Mech. Engrg.*, 139:409–429.
- Sulsky, D., Zhou, S.-J., and Schreyer, H. L. (1995). Application of a particle-in-cell method to solid mechanics. *Comput. Phys. Commun.*, 87:236–252.
- Wang, J., Ichikawa, Y., and Leung, C. (2003). A constitutive model for rock interfaces and joints. *International Journal of Rock Mechanics and Mining Sciences*, 40:41–53.
- Wells, G. and Sluys, L. (2001a). Analysis of slip planes in three-dimensional solids. *Comput. Methods Appl. Mech. Engrg.*, 190:3591–3606.
- Wells, G. and Sluys, L. (2001b). A new method for modelling cohesive cracks using finite elements. *Int. J. Numer. Meth. Engrg.*, 190:2667–2682.
- Wells, G. and Sluys, L. (2001c). Three-dimensional embedded discontinuity model for brittle fracture. *Int. J. of Solids and Structures*, 138:897–913.

**DISTRIBUTION LIST
DTRA-TR-14-4**

DEPARTMENT OF DEFENSE

DEFENSE THREAT REDUCTION
AGENCY
8725 JOHN J. KINGMAN ROAD
STOP 6201
FORT BELVOIR ,VA 22060
ATTN: J. REED

DEFENSE TECHNICAL
INFORMATION CENTER
8725 JOHN J. KINGMAN ROAD,
SUITE 0944
FT. BELVOIR, VA 22060-6201
ATTN: DTIC/OCA

**DEPARTMENT OF DEFENSE
CONTRACTORS**

EXELIS, INC.
1680 TEXAS STREET, SE
KIRTLAND AFB, NM 87117-5669
ATTN: DTRIAC